Determination of Two-Phase Flow Parameters for Nuclear Fuel Channels using a Real-Time Neutron Radiography Method

By

Glenn David Harvel, B.Eng., M. Eng.

A Thesis
Submitted to the School of Graduate Studies
in Partial Fulfillment of the Requirements
for the Degree
Doctor of Philosophy

McMaster University

Determination of Two-Phase Flow Parameters for Nuclear Fuel Channels using a Real-Time Neutron Radiography Method

DOCTOR OF PHILOSOPHY (1995) MCMASTER UNIVERSITY
(Engineering Physics) Hamilton, Ontario

Title: Determination of Two-Phase Flow Parameters for Nuclear Fuel Channels using a Real-Time Neutron Radiography Method

AUTHOR: Glenn David Harvel, B. Eng., M. Eng.

SUPERVISORS: Dr. J.S. Chang and Dr. V.S. Krishnan

NUMBER OF PAGES: xxv,227

Summary

Multi-dimensional modelling of two-phase flow requires accurate constitutive relationships for interfacial parameters such as interfacial heat transfer, void fraction distribution, interfacial area, etc. However, existing diagnostic systems for measurement of two-phase flow parameters have difficulty measuring two or three-dimensional void distributions required for determination of interfacial parameters.

In this work, a Real-Time Neutron Radiography(RTNR) system is developed for non-intrusive measurement of two-phase flow parameters in nuclear fuel channels at low thermal neutron fluxes (on the order of $10^6 n/cm^2\text{-}s$). This advanced radiation technique has the advantage of measuring two-phase flow in $3^1/_2$ dimensions$(x,\int dy,z,t)$ where the $^1/_2$ dimension refers to an integrated or averaged space dimension. Pipe flow channels, annulus flow channels, MAPLE-type nuclear fuel flow channels, and CANDU-type nuclear fuel flow channels are investigated. Measurements of flow regime, void fraction, void fraction distribution, bubble diameter, bubble velocity, and interfacial area are conducted.

The RTNR system is compared to ultrasonic and optical video measurement systems in pipe flow channels. Good agreement is obtained for flow regime, void fraction, bubble diameter, and interfacial area measurements.

The RTNR system is compared to High-Speed X-ray Computed Tomography (X-CT) and optical video measurement systems in the annulus flow channel. Good agreement is obtained for the determination of flow regime, void fraction, void fraction distribution, and bubble velocity measurements.

Application of the RTNR system to the vertical MAPLE-type 37 rod hexagonal finned fuel bundle and the horizontal CANDU-type 37 rod cylindrical fuel bundle is conducted. Measurements of flow regime, void fraction, and void fraction distribution are obtained and interfacial wave motion is observed. Flow regime observations in the MAPLE-type nuclear fuel channel show good agreement with previous work whereas flow regime observations in the CANDU-type nuclear fuel channel show significant discrepancies with previous work. A new large amplitude stratified wavy (LASW) flow regime is observed by the RTNR images in the CANDU-type nuclear fuel channel. The MAPLE-type nuclear fuel channel is shown to inhibit void migration and bubble coalescence at the entrance to the bundle and significantly affect the flow. The CANDU-type nuclear fuel channel is also observed to influence the cross flow in the core of the rod bundle.

Based on this work, an RTNR diagnostic technique is shown to be successful in measuring two-phase flow parameters in nuclear fuel channels.

Acknowledgements

This work has been completed with the assistance of several different groups of people. The High Speed X-ray CT work was carried out at Mitsubishi Heavy Industries in Japan. The Real-Time Neutron Radiography work was carried out in the McMaster Nuclear Reactor. I have much appreciation for both these facilities to allow me to complete my work.

This work has been sponsored in part by Mitsubishi Heavy Industries Ltd. of Japan, NUPEC corporation of Japan(Nuclear Power Engineering Centre), NSERC (Natural Sciences and Engineering Council of Canada), and the Ontario Ministry of Universities and Colleges URIF program. Without the kind assistance of these organizations, this work could not have been completed.

In addition, the Canadian Department of National Defense is acknowledged for the loan of the Image Processing system and Atomic Energy of Canada Ltd. (AECL-Research) is acknowledged for the loan of the heavy water used in this work.

I would like to thank Dr. E.A. Ballik, Dr. M. Dokainish, Dr. J.E. Kowalski, Dr. A. Tsuge, Dr. K. Hori, Mr. K. Kawanishi, and Mr. M.P. Butler for their valuable discussions and comments.

I acknowledge the assistance provided by the technical staff of the Takasago Research Laboratory in Japan and the technical staff of the Thermalhydraulics and Electro-Hydrodynamics Laboratory at McMaster University in completing the experiments. In particular, Mr. Murakami was most helpful during both the experimental and analysis phases of the High Speed X-ray CT work. Mr. Hamamura is acknowledged for assistance in code development for the High Speed X-ray CT

system. Mr. Paul Looy provided excellent technical support in the area of electrical instrumentation and just plain help.

My colleagues in the Thermalhydraulic and Electromagnetic Hydrodynamics Laboratory provided assistance, comments, and humour even when not asked. Those deserving special recognition are Mr. John Campeau, Mr. Thomas Beuthe, Mr. Izuh Obinelo, Mr. P. Busono, Mr. Dave Novog, and Mr. Paul Looy.

Of great importance, has been the strong support and guidance received from my supervisors: Dr. J.S. Chang and Dr. V.S. Krishnan. Their efforts will always be remembered.

My family has been instrumental in providing patience, an attempt at understanding what it is I do, and general support. My mother, my wife, and my two children, (Amanda and Alexandre) deserve recognition.

This work is dedicated to my wife, Barbara, for all she has done to enrich my life.

Table of Contents

List of Figures

List of Tables

Nomenclature

Roman

A	atomic weight[g/mole], annular flow
A,a	area
A(y)	non-dimensional intensity
B	bubbly flow
BU	build-up term
C_p	capacitance
C	churn flow
D,d	diameter, separation distance
DB	dispersed bubble flow
f(x,y)	density function of object in image plane[cm^{-1}]
G	RTNR camera gain
I	intensity[#/cm^2-s], intermittent flow
L(y)	chordal path length along path y[cm]
N	Avogadro's number[#/mole]
p(θ,x)	projection function
PL	plug flow
Q	volumetric flow rate, charge
r	radial coordinate

SS	stratified smooth flow
SL	slug flow
SW	stratified wavy flow
t	temporal coordinate
U	velocity
u,v	fourier coordinates of image plane
V	volume, potential
x,y,z	Cartesian Coordinates of Image Plane
z	Atomic Number

Greek

α	void fraction
β	RTNR camera constant = 0.465
γ	[cm^2/g] mass attenuation coefficient
ϵ	dielectric constant
μ	[cm^{-1}] linear attenuation coefficient
ρ	[kg/m^3] material density
σ	[cm^4] atomic attenuation coefficient, microscopic cross-section
Σ_t	[cm^{-1}] macroscopic cross-section
θ	[°] X-ray beam path angle relative to reconstruction coordinates
ω	filter function
ψ	convolution function

Subscripts

b	base (reference) data, bubble
cs	cross-section
D	dark current noise
eq	equivalent
g	gas
gs	superficial gas
h	hydraulic
i	interfacial
k	phase number
l	liquid
ls	superficial liquid
m	measured data
o	incident

Chapter 1

1. Introduction

This chapter discusses the background of this topic, introduces two-phase flow parameters, and their definitions, and describes the basic objectives of this thesis.

1.1 Background

Two-phase gas-liquid flow is found in several industries such as nuclear power plants, oil, gas, and, other power and process industries. Two-phase flow affects the pressure drop, heat transfer, and mass transfer in any system where it occurs. Knowledge of the correct behaviour of two-phase flow is necessary to ensure the safe operation of nuclear power plants, efficient mixing in vessels, and enhanced mass transfer rates in chemical reactors. Currently, safety analysis and design uses computer models for two-phase flow, however, the interfacial phenomena and void distribution behaviour are not well modelled. To improve the numerical models, more detailed experimental knowledge of two-phase flow parameters is necessary.

The study of two-phase gas-liquid flow requires accurate measurement of each phase velocity and phase fraction. Most instrumentation available today provides this type of information but have various disadvantages ranging from poor sensitivity to geometrical limitations[1,2].

1.2 Two-Phase Flow Parameters

The void fraction or liquid holdup is the volume fraction of the test section occupied by a given phase. This value is expressed either as a percentage or as a value between 0 and 1. The sum of all volume fractions of each phase is 1 as expressed below where α_k is the void fraction for phase k.

$$\sum_k \alpha_k = 1 \tag{1.1}$$

For example, the void fraction (α_g) and liquid holdup (α_l) of gas-liquid two-phase flow can be defined by;

$$\alpha_g = \frac{V_g}{V_g + V_l} \tag{1.2}$$

$$\alpha_l = \frac{V_l}{V_g + V_l} = 1.0 - \alpha_g \tag{1.3}$$

for gas-liquid two-phase pipe flow as shown in Figure 1.1.

Hence, we can obtain phase velocities from gas and liquid volumetric flow rates (Q_g and Q_l $[m^3/s]$) as follows:

$$U_g = \frac{Q_g}{\alpha_g A_{cs}} = \frac{U_{gs}}{\alpha_g} \ [m/s] \tag{1.4}$$

$$U_l = \frac{Q_l}{\alpha_l A_{cs}} = \frac{U_{ls}}{\alpha_l} \ [m/s] \tag{1.5}$$

where A_{cs} is the cross-sectional area [m^2] of the flow channel, and U_{gs} and U_{ls} are the superficial velocities of the gas and liquid phases. These phase velocities are local cross-sectional or volume averaged phase velocities, since the void fraction is not always constant along the flow tubes.

The phases may or may not distribute evenly throughout the test volume. Different patterns of distribution may occur as shown in Figures 1.2 and 1.3 for horizontal gas-liquid, and vertical gas-liquid two-phase pipe flow systems respectively. These distribution patterns are known as flow regimes. The flow regimes that can occur depend primarily on the phase velocities, test geometry, and orientation with respect to gravity. For example, in horizontal gas-liquid two-phase flow, we observe stratified smooth (SS), stratified wavy (SW), annular (A), dispersed bubble (DB), slug (SL), and plug (PL) flow depending on the gas and liquid superficial velocities.

Stratified smooth flow occurs when the liquid is at the bottom of the pipe and the gas flows along the top. The surface of the liquid is smooth; however, for stratified wavy flow, the gas-liquid interface is wavy. Both plug flow and slug flow are defined by Taitel and Dukler [3] as intermittent flow (I) and are characterized by the liquid bridging the gap between the gas-liquid interface and the top of the pipe. The difference between slug and plug flow depends on the degree of agitation of the bridge. Plug flow is considered the limiting case of slug flow where no entrained bubbles exist in the liquid slug.

Annular flow occurs when the walls are wetted by a thin film of liquid, while the gas flows at high velocity through the centre of the pipe. Liquid droplets are usually entrained in this gas. When the upper walls are wetted periodically by large aerated waves, it is neither slug flow requiring a complete fluid bridge nor annular flow requiring a stable film. Taitel and Dukler [3] designated this flow pattern as wavy annular flow. This region, however, was not recognized by Mandhane et al. [4] and was considered slug flow.

In the dispersed bubble or bubbly regime, small gas bubbles are distributed throughout the liquid phase which otherwise completely fills the pipe. The transition to this regime is characterized by the gas bubbles losing contact with the top of the

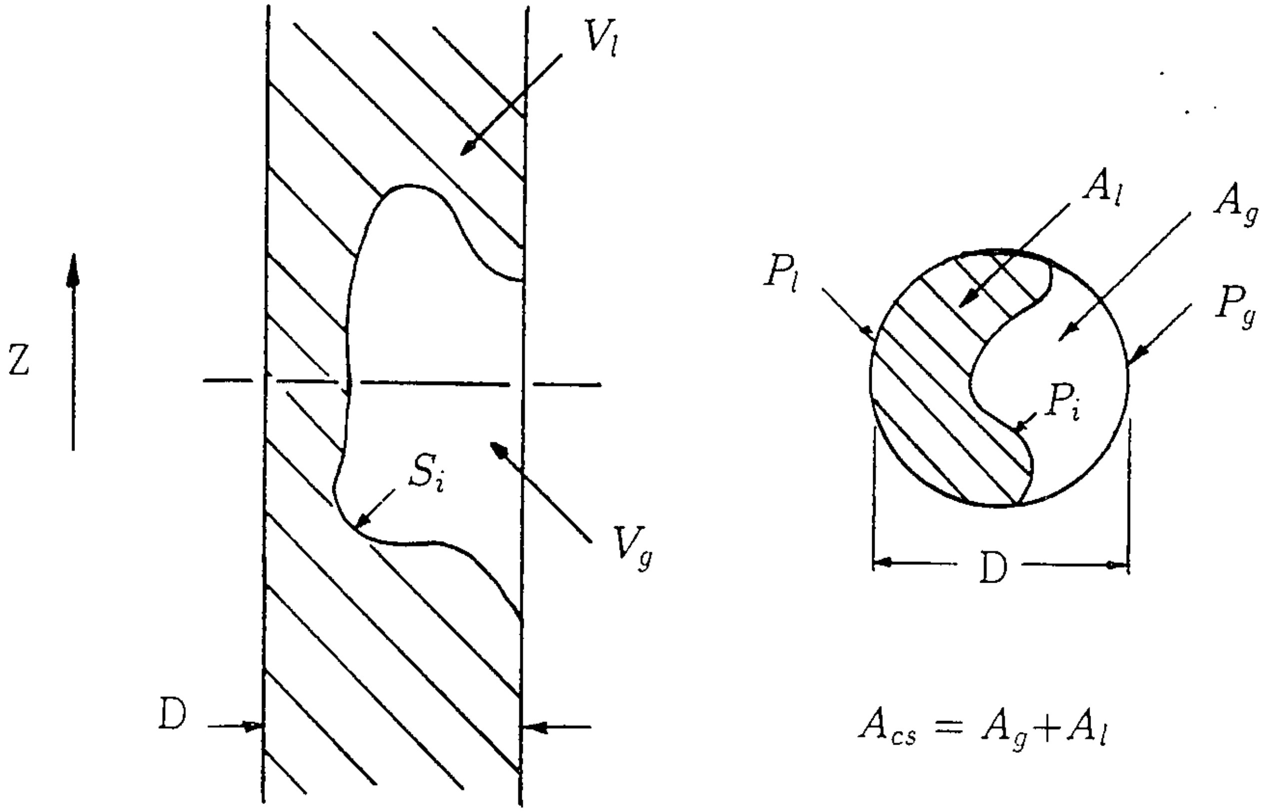

Figure 1.1: Two-phase pipe flow definitions: A is the area, V is the volume, P is the perimeter, l denotes liquid, g denotes gas, i denotes interface, S_i is the interfacial area, D is the diameter, and z is the axial position.

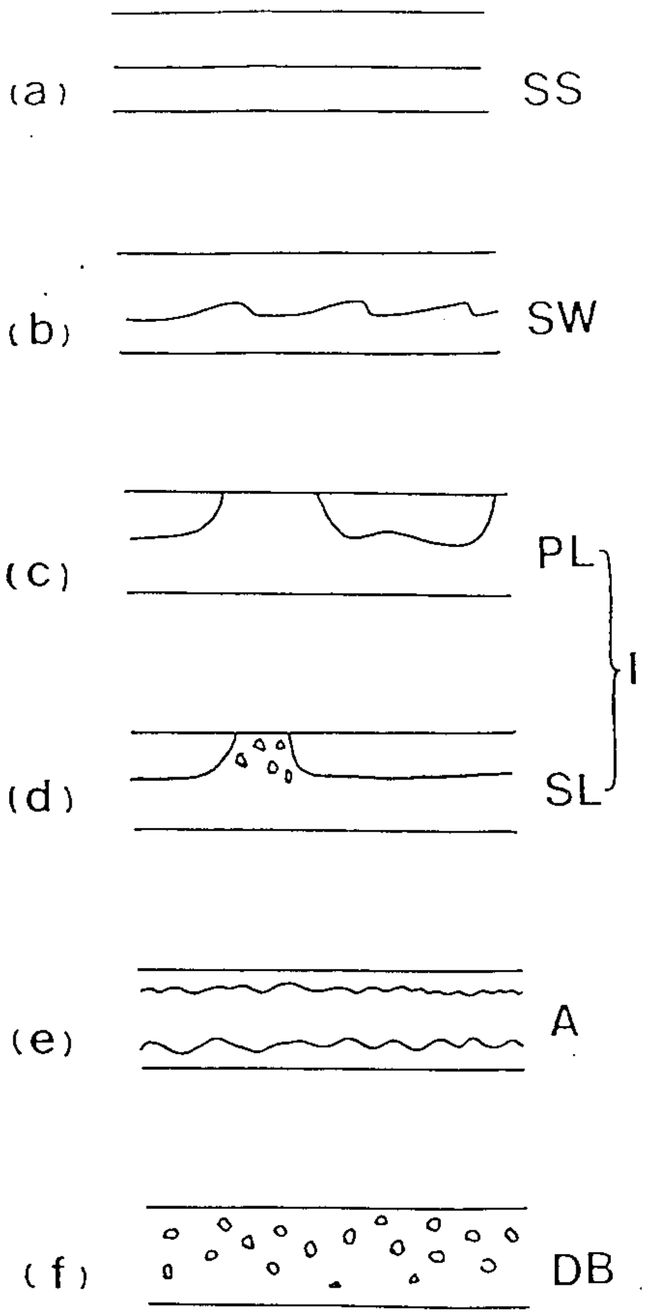

Figure 1.2: Typical horizontal gas-liquid flow regime patterns: SS is Stratified smooth flow, SW is stratified wavy flow, PL is plug flow, SL is slug flow, I is intermittent flow, A is annular flow, and DB is dispersed bubble.

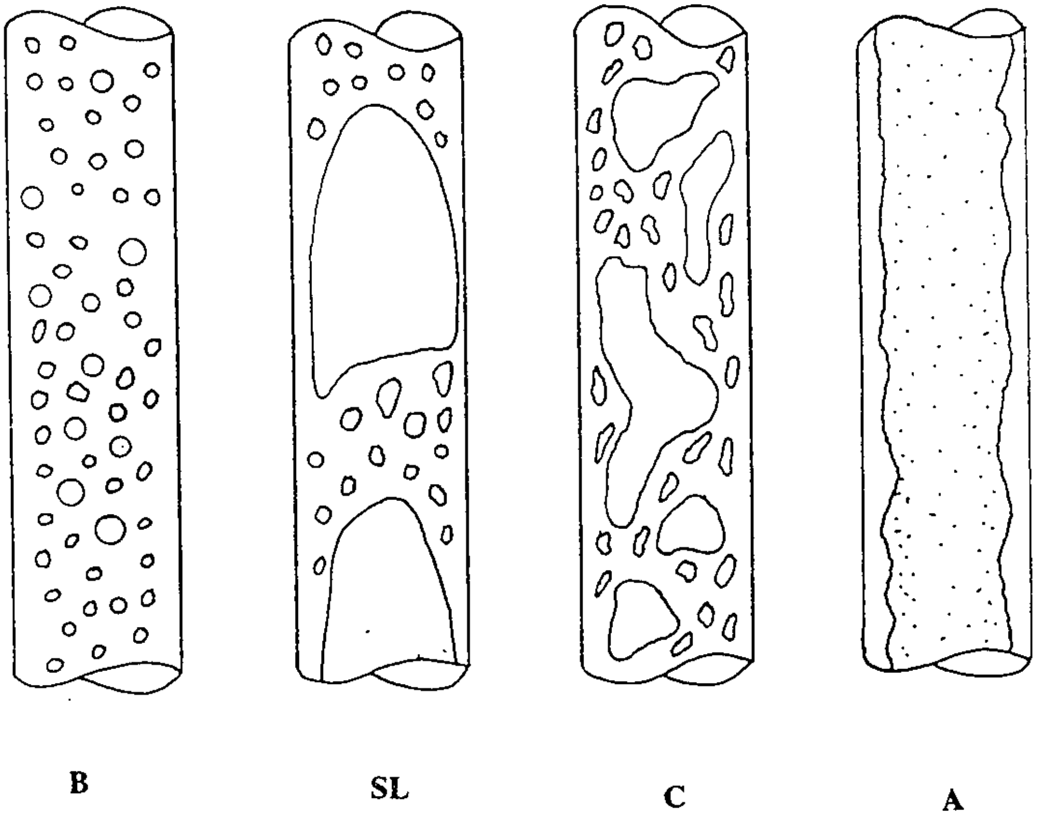

Figure 1.3: Typical vertical gas-liquid flow regime patterns: B is bubbly flow, SL is slug flow, C is churn flow, A is annular flow.

tube. At first, the bubbles are near the upper portion of the pipe, but at higher liquid flow rates, become uniformly distributed throughout the system.

The flow regimes which may occur in a vertical gas-liquid two-phase flow system are bubbly flow, slug flow, churn flow, and annular flow as shown in Figure 1.3.

Typical flow regime maps based upon the superficial velocities are shown in Figures 1.4 and 1.5 for horizontal gas-liquid and vertical gas-liquid two-phase flow respectively.[5,6]

Different flow regimes have a significant effect on the momentum, heat, and mass transfer behaviour and can also influence most of the two-phase flow instrumentation since the response time and the phase fraction ranges significantly vary. Identification of these flow regimes is important in understanding both the influence on the flow and for thermal design of the system.

Two other important two-phase flow parameters are the bubble diameter (d_b) and the interfacial area (a_i). The bubble diameter is usually measured and defined as the mean bubble diameter. The interfacial area is generally determined from the void fraction and the mean bubble diameter as shown below:

$$a_i = \frac{6\alpha_g}{d_b} \quad [m^{-1}] \tag{1.6}$$

1.3 Objectives of this Work

Several techniques exist to measure two-phase flow parameters, however, each technique is limited in application and sensitivity. Most void fraction measurement techniques are either intrusive devices or do not provide full detail of the two-phase behaviour inside a metal pipe flow system as discussed in chapter 2.

The objective of this work is to develop a new diagnostic technique based on a Real-Time Neutron Radiography (RTNR) system for the determination of two-phase flow parameters for use in complex nuclear fuel channels. An experimental

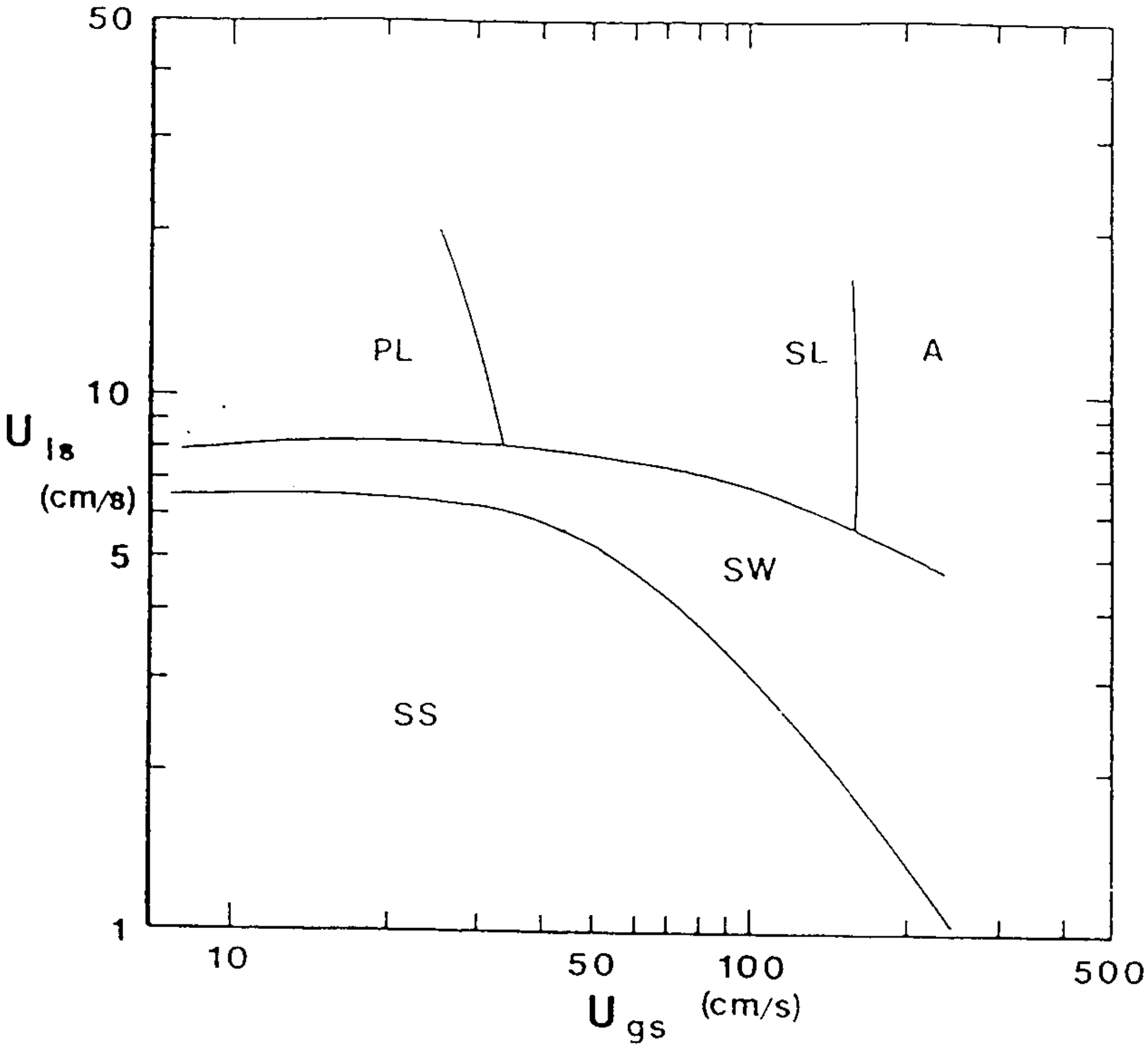

Figure 1.4: Typical gas-liquid flow regime map for horizontal flow.[5]

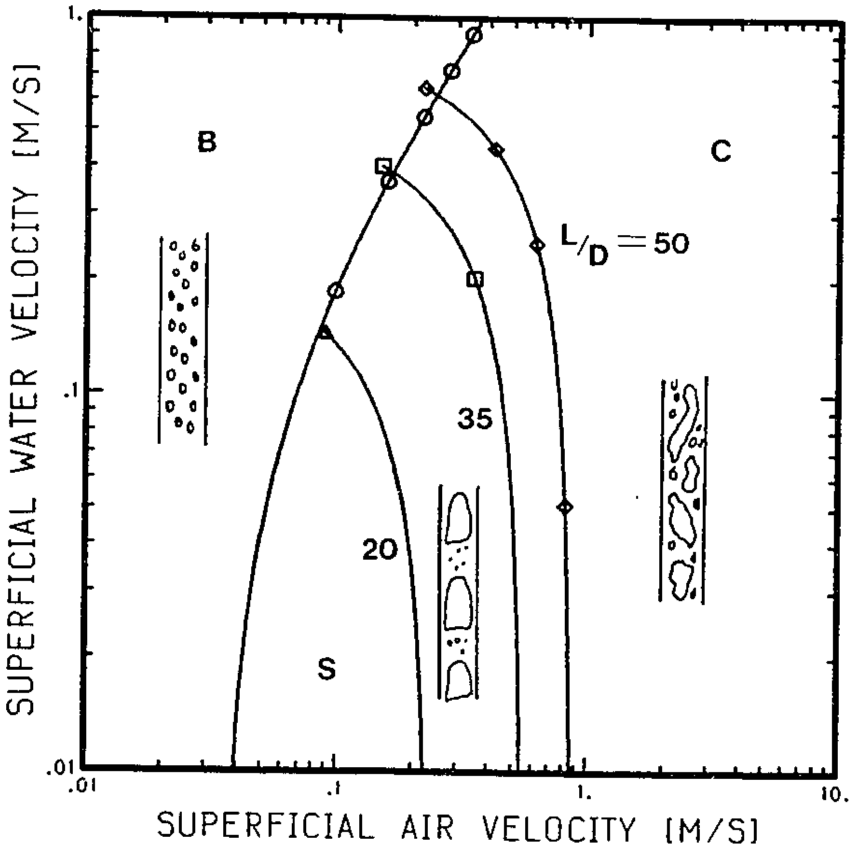

Figure 1.5: Typical Gas-Liquid Flow Regime Map for Vertical Pipe Flow.[6]

study is performed to examine the characteristics of the developed RTNR system and to examine application to various two-phase flow systems. The two-phase flow systems examined include a vertical natural circulation pipe flow, a bubble column pipe flow, a vertical annulus flow channel, a horizontal CANDU-type fuel rod bundle flow channel, and a vertical MAPLE-type hexagonal finned bundle flow channel.

Chapter 2 describes existing techniques for the measurement of two-phase flow parameters. Chapters 3 and 4 describes the advanced diagnostic techniques developed in this work and chapters 5 to 7 describe the experimental studies of this work. Concluding remarks and recommendations for future work can be found in chapters 8 and 9 respectively.

Chapter 2

2. Review of Conventional Diagnostic Techniques for Two-Phase Flow Parameters

This chapter reviews existing techniques for measuring two-phase flow parameters. A summary table of all techniques is shown in Table 2.2 at the end of this chapter.

2.1 Electrostatic Devices

Recent studies have developed several two-phase flow meters based upon electrostatics principles. These flow meters have increased sensitivity to the measurement of the flow velocity and the void fraction yet have their own limitations. One important advantage of these devices is the fast time response that allows these devices to be used for analyzing fast transient phenomena. The following sections will discuss the basic physical principles behind the electrostatic flow meters, design considerations, and potential applications.

Most of the electrostatic multiphase flow measurement techniques inherently measure the impedance of the flow or some aspect of it. The electrical impedance of the flow essentially falls into a conductance term or a capacitance term. Conductance is simply the inverse resistance of the two-phase flow and best applies where one phase has higher electrical conductivity than the other and is fairly continuous as is the case in most solid-liquid and gas-liquid flow. Capacitance measurement is based upon each gas and liquid phase having a different dielectric constant.

Electrostatic principles are also used in the detectors of other multiphase flow measurement techniques. For example, piezo-electric transducers can be used to measure ultrasonic waveforms that have interacted with multiphase flow. Another example uses ionization (charge) chambers for the detection of radiation attenuation. Examples of these devices will be discussed later in the chapter.

The various techniques for measurement of two-phase flow parameters such as void fraction, phase distribution, and phase velocity will be discussed for gas-liquid two-phase flow applications. Several techniques are mentioned to ensure a fairly complete list with particular strengths and weaknesses addressed.

2.1.1 Measurement of Phase Fraction

Both AC and DC devices exist which can measure the volume fraction or void fraction occupied by either phase in a two-phase system. The DC based devices rely mainly on the principle of conduction of electricity through the phases and the AC based techniques rely mainly on the principle of capacitance or inductance of the phases depending on the operating frequency.

A conductance transducer has been used to determine the local phase fraction in pipe flow [7,8,9]. The transducer is influenced by the conductivity of each phase. For a constant applied voltage, the variation in conductance between the probe tip and the sheath alters the current measured. From the time response in the current signal, information can be obtained for the interfacial frequency and void fraction of each phase which passes the tip of the transducer.

Cross-sectional or volume averaged type conductance transducers have been examined by Andreussi et al. [10] and Tsochatzidis et al. [11]. This technique uses ring-type sensors that are in contact with the fluid flow and are embedded in the walls of the pipe. The ring-type device is somewhat superior to the probe-type device [12] since the sensors are flush mounted and will not have as strong an influence on the flow. However, the technique provides volume averaged information regarding void fraction and not local void fraction.

Andreussi et al.[10] utilize a three-ring sensor where the first two rings act as a fast response meter for detecting sudden changes in the void fraction. The third ring is used with one of the first two rings to obtain volume averaged void fraction information. Andreussi et al. [10] clearly state the separation of the second and third rings should be large. This improves the linearity of the device but inherently averages the flow.

Although Andreussi et al.[10] name their technique an impedance technique, they operate the device in a conductance mode by applying a frequency of ≈ 100 kHz. At frequencies ≤ 0.5 MHz, capacitance and inductance effects are small and the conductance term is dominant, and for frequencies $\geq$ 0.5 MHz the capacitance term is dominant [12]. However, the conductivity of the liquid often changes as a function of time and applied voltages.

Tsochatzidis et al. [11] provide more detailed theory of this device and have applied the technique to two-phase gas-liquid flow in a packed bed reactor.

Several authors have examined capacitance techniques for the measurement of void fraction in gas-liquid flow as shown in Figure 2.1 [13,14]. Chang et al. [13] used ring type sensors around the periphery of a non-conducting pipe. Cimorelli and Evangelisti [14] used a shell and tube annulus test section with the shell and the tube as the electrodes. Although the fluids are able to contact the sensors, appropriate instrumentation is used to separate the capacitive and conductive components.

The capacitance transducer uses a dielectric constant difference between the gas and liquid, where the specific dielectric constant, ϵ_s, of gases which include steam and other liquid vapours are close to 1, and the specific dielectric constant of liquids range from 2 to 100. The electrodes can be placed inside or outside the flow tubes depending on sensitivity and response time requirements.

The primary advantage of the capacitance transducer lies in its ability to

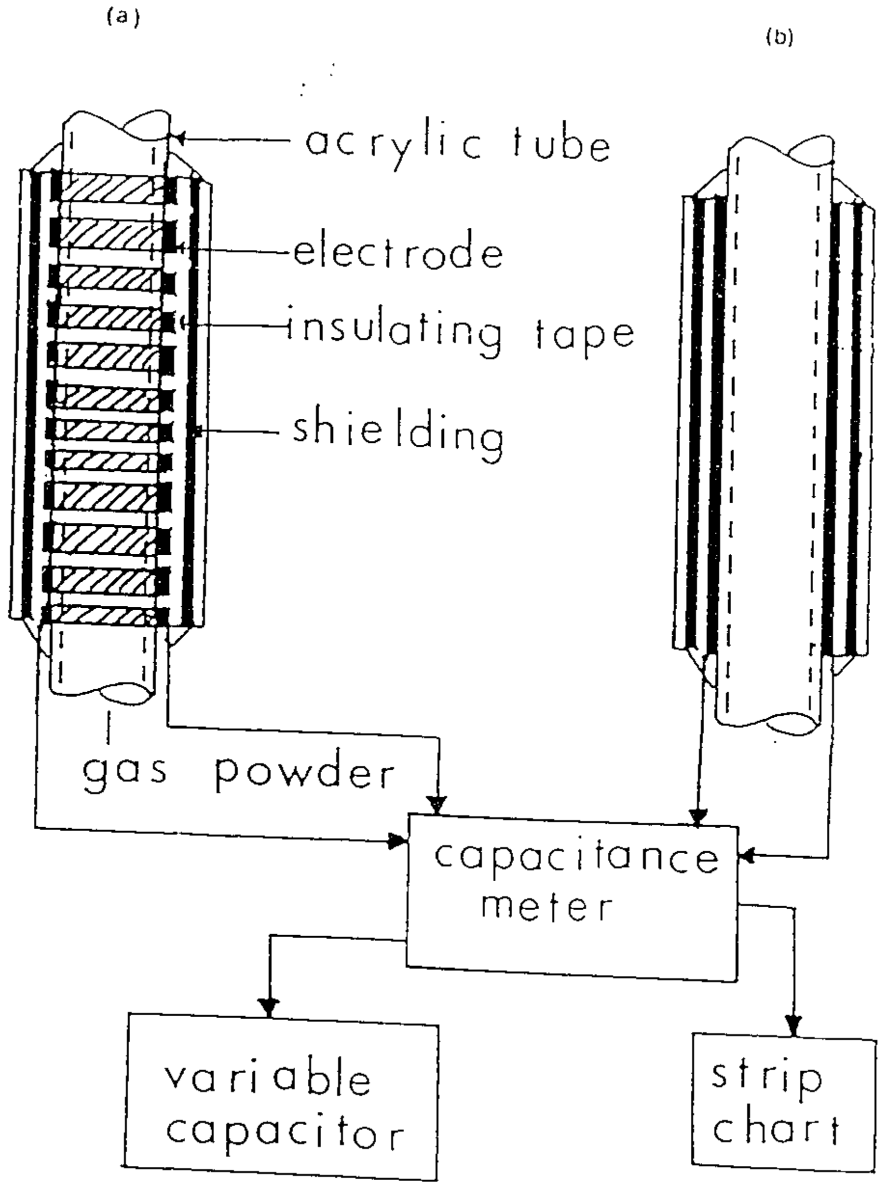

Figure 2.1: Capacitance Transducer Concept:(a) ring type; (b) strip type[15]

capture fast transient phenomena (1ms) non-intrusively and at low cost. This is an improvement over other techniques which have difficulty in either responding to rapidly changing input or intrusively disturb the flow measurement. In addition, the transducer is easy to manufacture, and can be configured to any geometrical shape.

The capacitance measured by a transducer for two-phase fluids can be treated as an approximation of a parallel plate capacitor. Typical equivalent plate capacitance circuits for various flow regimes in gas-liquid two-phase flow are shown in Figure 2.2 [13]. The capacitance is related to the charge (Q_E) on the plates and is inversely related to the Electric Potential (V_E) between them. This relationship is equivalent to the dependence on the dielectric nature of the material (ϵ), the cross-sectional area between the plates (A), and the inverse relationship to the separation distance (d). The two or more phases present in an experimental system will have different dielectric constants and will occupy different regions in the control volume. The equivalent circuit for the capacitance transducer in two-phase flow is then a selection of series and parallel capacitors of different dielectric constants.

$$C_p = \frac{Q_E}{V_E} = \frac{\epsilon_s \epsilon_o A}{d} \tag{2.1}$$

The void fraction will affect either the cross-sectional area or the separation distance depending on the orientation with respect to the capacitance transducer. This orientation will reveal two general and distinct relationships between the void fraction and the capacitance of the transducer.

For the parallel and series circuits, the void fraction and capacitance are related by Equation 2.2 and 2.3 respectively;

$$C_p = \frac{\epsilon_1 A_1}{d} + \frac{\epsilon_2 A_2}{d} = \frac{A}{d}\left(\epsilon_1 \alpha_1 + \epsilon_2 (1 - \alpha_1)\right) \tag{2.2}$$

$$C_p=\frac{1}{\frac{d_1}{\epsilon_1 A}+\frac{d_2}{\epsilon_2 A}}=\frac{A\epsilon_1\epsilon_2}{d(\epsilon_2\alpha_1+\epsilon_1(1-\alpha_1))} \tag{2.3}$$

,where α_1 is the void fraction of phase 1.

Detailed theoretical considerations for a capacitance transducer have been developed by Chang et al. [13] for various gas-liquid flow regimes. Chang et al.[13] use a linear difference theory as a first order approximation to calculate the void fraction based upon a non-dimensional capacitance value as shown below;

$$\alpha=C_p'=\frac{C_{TP}-C_l}{C_g-C_l} \tag{2.4}$$

,where this relationship may change with geometry and transducer design.

A Faraday shield is used to reduce the influence of the external environment, namely the local electromagnetic fields and the electronic equipment [15]. Guard rings are used to suppress the electric field along the axial length of the test section. This ensures the capacitance transducer is sensing a local measurement. The dielectric insulator isolates the Faraday shield from the sensing ring electrodes.

Capacitance and impedance probes are also recommended to use together with a temperature sensor, since the dielectric constant and conductivity of the fluid are functions of the temperature.

Shielding from stray capacitance and electric fields is important and with proper calibration this device will provide accurate information. Disadvantages of the capacitance method are sensitivity to the moisture and the electrostatic discharge as discussed in detail by Sugaya et al.[16]

2.1.2 Measurement of Void Distribution

Void distribution is an important consideration both spatially and temporally. The void fraction transducers previously discussed can be used to obtain temporal

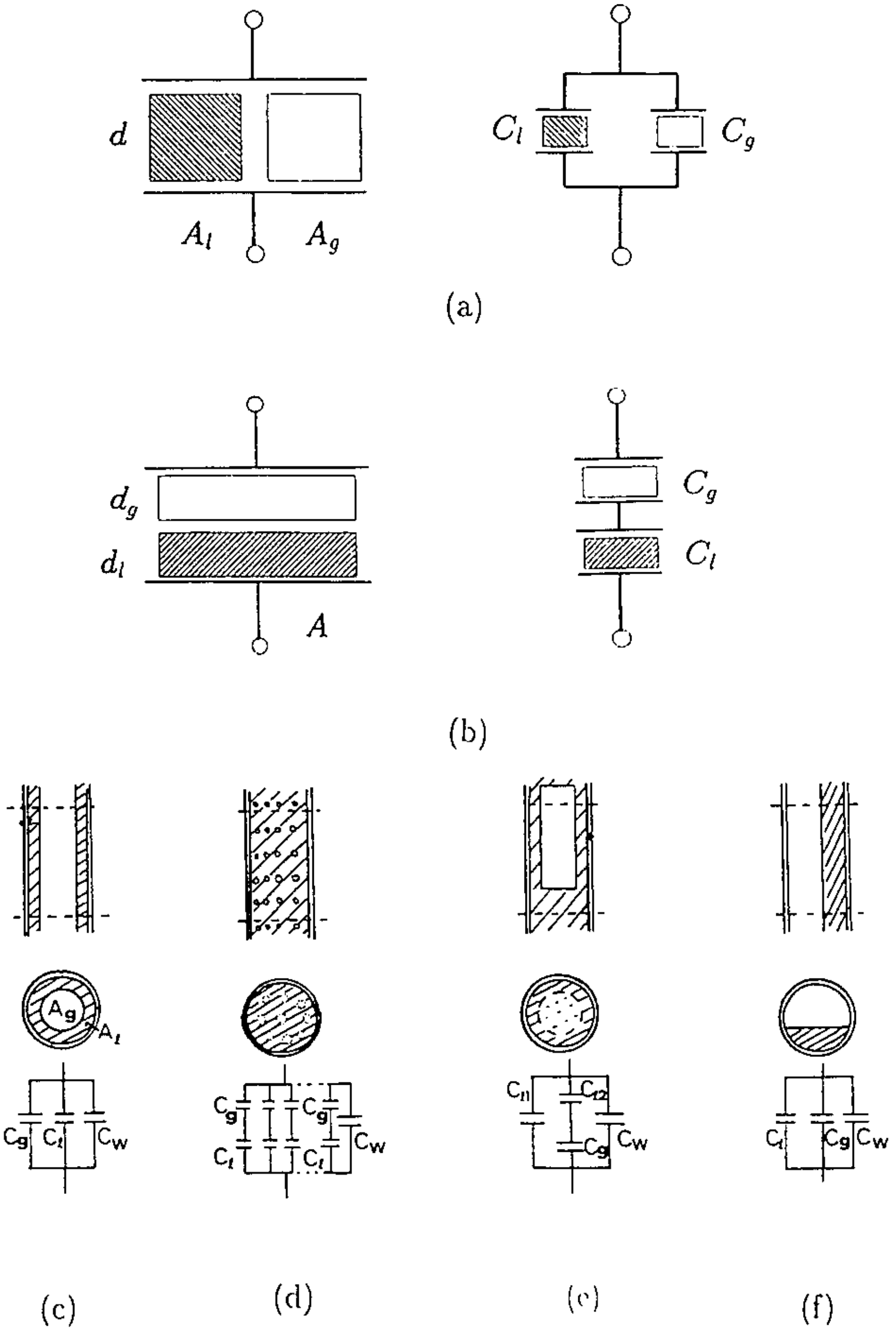

Figure 2.2: Equivalent circuits for capacitance transducers:(a) parallel arrangement, (b) series arrangement, (c) annular flow, (d) bubbly flow, (e) slug flow, and (f) stratified smooth flow;; where $A_l$is the flow area occupied by the liquid, A_g is the flow area occupied by the gas, C_l is the capacitance of the liquid, C_g is the capacitance of the gas, C_w is the capacitance of the wall, d_l is the separation distance between electrodes occupied by the liquid, and d_g is the separation distance occupied by the gas.[13]

variations in the void fraction signal as shown in Figures 2.3 [17] for gas-liquid flow regimes. Capacitance waveforms show that the flow regime can be well characterized for these void fraction waveforms. The waveform produced by such a signal is unique for each flow regime or phase distribution that can occur.

Huang et al.[18] and Xie et al.[19], have developed a tomographic approach to imaging the void distribution by using an 8-electrode sensor capacitance technique placed peripherally around a non-conducting region of the pipe. The capacitance is measured between any two plates and a linear backprojection algorithm is used to reconstruct the void distribution. The measurement area is interpreted by the 8-electrode system as a collection of pixel regions each sensed by several capacitance electrodes. The pixel regions will have different sizes due to the arrangement of the electrodes in a ring. This will influence the local accuracy of the measurement. However, since the transducer concept is considered as measuring presence or absence of each phase and not relative quantity, the influence of pixel size will not be significant. However, due to the signal processing, time and space resolutions of the transducer are poor at this moment ($\approx$ few seconds and centimetres).

Other researchers have been investigating a similar concept based upon the conductance between the electrodes as opposed to the capacitance. Seagar et al. [20] have examined electrical impedance imaging on the human body to illustrate the phase differences which can be imaged. Lin et al.,[21] have performed similar work in gas-liquid two-phase flow. The results are similar to the capacitance tomography system with possibly better accuracy. However, the essential difference is due to the stage of development of the two techniques and the number of electrodes used.

2.1.3 Measurement of Phase Velocity

There are several electrostatic techniques which can be used for the measurement of phase velocity. The most common technique is the double resistivity probe or conductance transducer as shown in Figure 2.4 and as discussed by Sekoguchi et al.[7] Capacitance techniques can be used in two approaches to measure phase velocity. The waveforms from two transducers separated along the pipe could be cross-correlated to determine the phase velocity. The other method is to directly calculate the phase velocity from the measured void fraction and knowledge of the entrance mass flow rate.[15,22] Brodowicz et al.[23] developed a two-phase velocity meter for the measurement of average flow velocity and mass flow rate based upon capacitive techniques.

Sekoguchi et al.[24] discuss two techniques and several analysis methods for the measurement of a liquid slug in a gas-liquid system. Both techniques are electrical double sensing devices which respond to the liquid void fraction in the test section.

The first technique uses a double resistivity probe as shown in Figure 2.4 and employs a direct time delay measuring method. Sekoguchi et al.[7] provides more detail about the operation and fundamentals of this instrument. Other work has been done on this technique by Ishii and Revankar[9], and Sekoguchi et al.[25]. This device measures the local resistivity of the probe volume that corresponds to the type of material present. Use of two probes in one device provides the time of flight information required to measure bubble or wave velocity parallel to the probe. This technique has demonstrated good local measurements for forward flow but is intrusive to the flow. Also, measurement of the wave velocity in annular flow is difficult by this technique since position of the probe is very important and the film thickness does vary with time.

The second technique uses two terminals to inject a current through the test section as shown in Figure 2.5.[24] Between these terminals, two double ring electrode sensors are placed which receive an induced voltage proportional to the water content in their sensing region. Sekoguchi et al.[24] discuss both cross-correlation and cross-spectrum-coherence methods. This system allows for the measurement of the transit time of the liquid slugs as they pass the sensors for both forward and reverse flows depending on the correlation method used. Sekoguchi et al.[24] showed excellent agreement of liquid slug or wave velocity for slug to annular flow regimes.

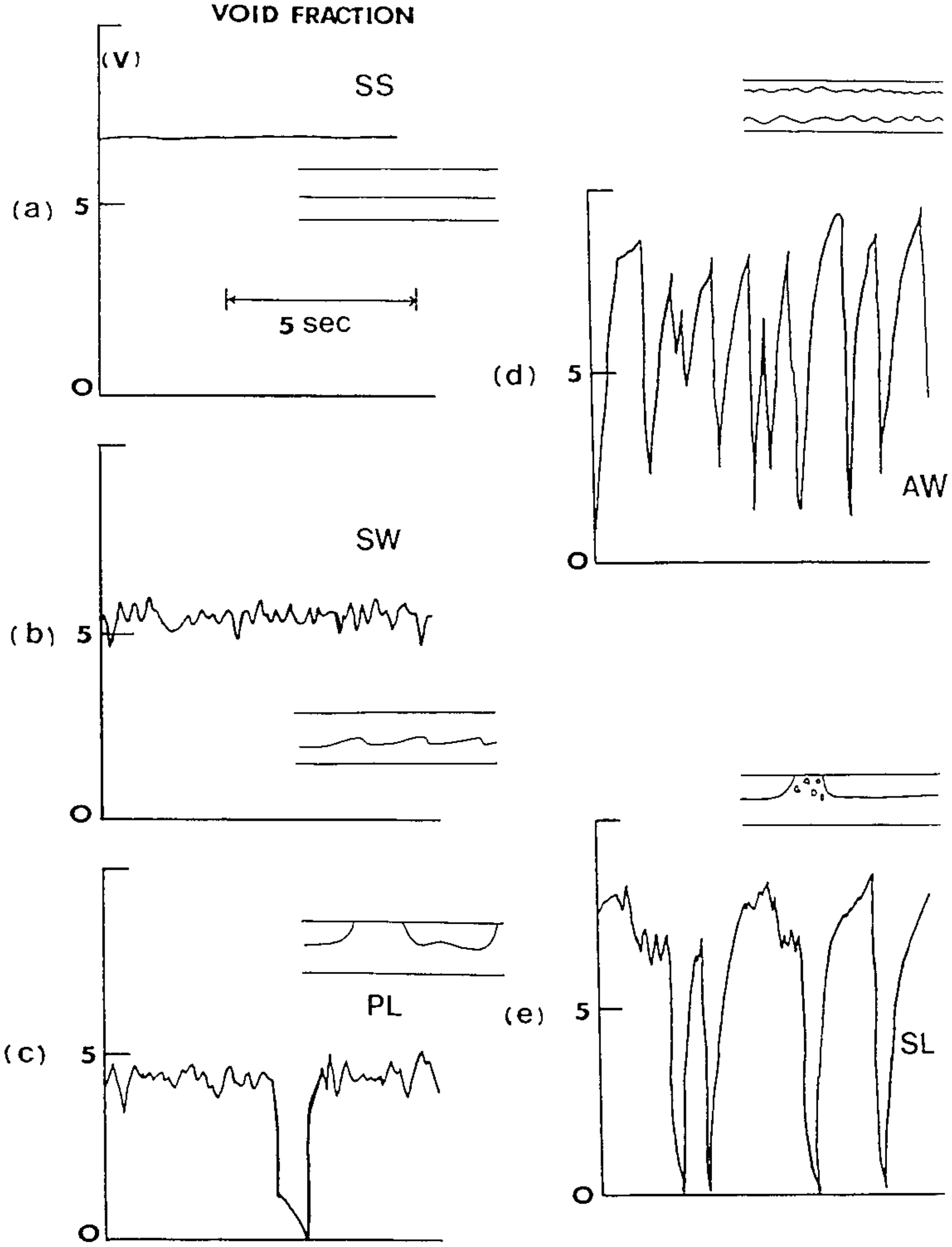

Figure 2.3: Typical transient response of capacitance transducers for various gas-liquid flow regimes.[17]

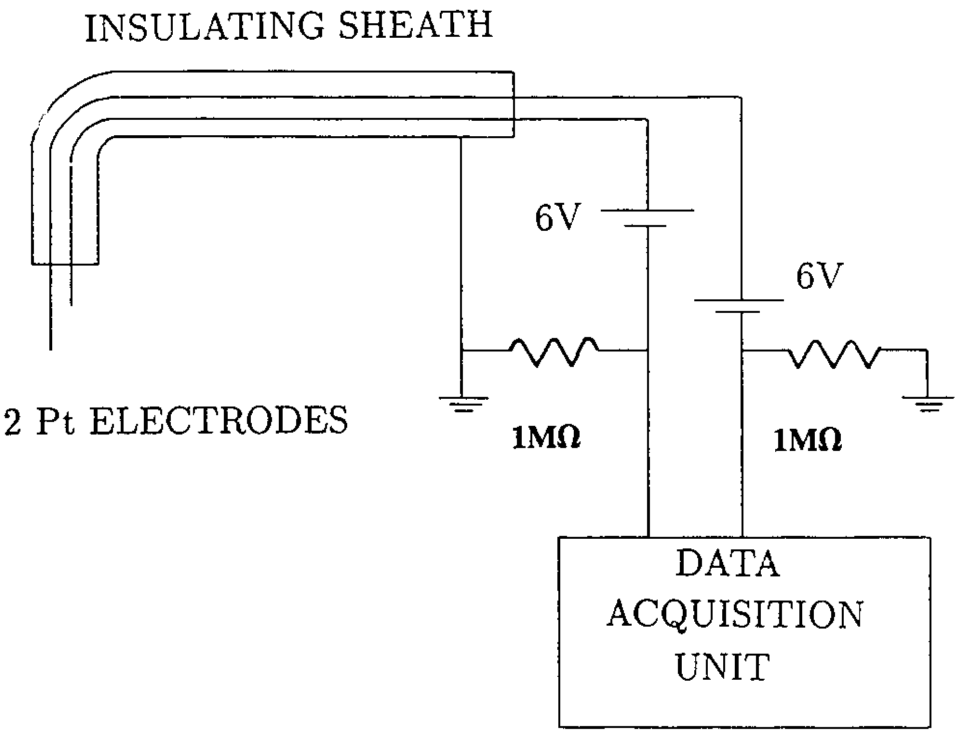

Figure 2.1: Double resistivity probe for phase velocity measurement.[7]

2.1.4 Measurement of Film Thickness and Interfacial Area

Other two-phase flow parameters are possible to measure using electrostatic techniques. Applications to film thickness and interfacial area will be mentioned here but not discussed in detail as many of the techniques already discussed have been used by various authors to examine these two parameters.

Keska and Fernando [26] and Ozgu and Chen [27] have examined the application of a capacitance technique for the measurement of liquid film thickness in gas-liquid flow. Although both authors used the impedance type probes that contact the liquid, their devices were set into a capacitance mode. The use of ring-type non-contact transducers could also be used with similar results. The authors have demonstrated remarkable accuracy for the measurement of film thickness, however, this type of device inherently averages the film thickness across the separation length of the ring sensors. For smooth and constant film thicknesses, such as liquid levels, this technique is satisfactory, but the inherent averaging is a serious disadvantage when film thickness varies either with time or axial length. The use of film thickness to calculate the interfacial area will lead to significant errors for certain flow regimes such as stratified wavy or annular as the wavy interface will have an interfacial area significantly greater than the averaged value measured in this manner. It is possible some merit could be achieved for heat conduction models of thin films but the lack of accurate dynamic information at the interface will not allow for an accurate heat convection model to be ascertained, seriously weakening the results. The film thickness measurement by this technique is only considered valid for application to liquid level measurements.

The ring and strip type capacitance transducer has been demonstrated for the measurement of interfacial area[17]. The results were noted to agree well with the theory.

Kataoka et al. [8] and Ishii and Revankar [9] examined the use of a double resistivity (conductance) probe for applications to interfacial area in gas-liquid flow.

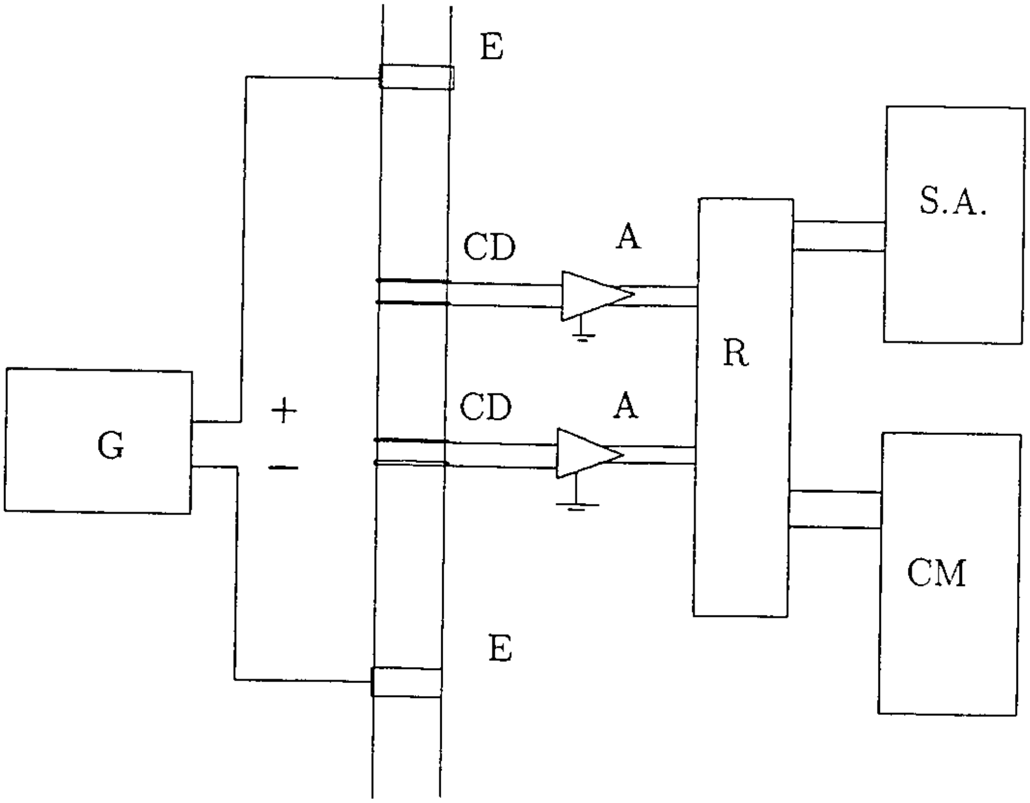

Figure 2.5: Conductance method for phase velocity measurement: E is an electrode, CD is the conductance detector electrode, A is an amplifier, G is a dc constant current generator, R is the data recorder, S.A. is a spectrum analyzer, and CM is a computer.[24]

In their work, a double sensor is necessary to obtain not only the gas bubble frequency but also the interfacial velocity as well. This technique is based on the assumption that the bubble intersects the probe along the normal to the bubble surface and in the direction of flow.

Kang and Kim [28] demonstrated a flush-wire probe for the measurement of liquid film thickness. This device is simply a conductance transducer with one electrode flush mounted on the wall of the test section and the other electrode as a wire some known distance normal to the wall. The authors suggest the flush-wire probe enhances spatial resolution over other conductance transducers yet the device remains an intrusive technique.

2.2 Ultrasonic Techniques

Ultrasonic techniques using a piezo-electric type transducer are often used for multiphase flow measurements. An AC pulsed signal is applied to the piezo-electric material causing a vibration in the crystal lattice. The transmitted sound pulse interacts differently with each phase. The interfaces between phases with different acoustic impedances reflect the sound pulses back towards the transducer. Vibration in the crystal induces an electrical pulse in the transducer detecting the sound wave.

Two methods are possible with ultrasonic devices for multiphase flow measurement. The pulse echo method is used primarily for film thickness measurements, and the transmission method is used for phase fraction measurements. Chang and Morala [29], used these methods to determine the void fraction, phase distribution, interfacial areas and bubble diameter in a gas liquid two-phase flow. Matikainen et al. [30] used the pulse echo technique for the detection of gas-liquid interface locations in two-phase flow. Ultrasonic techniques have indicated an excellent time response and excellent spatial accuracy.

The major limitations for the ultrasonic techniques are the transducer curie point and false echoes scattered from the walls or the rod bundle surfaces. The curie point is the temperature at which the signal is lost in the transducer and transducers must be cooled if they are to operate in temperature fields above their curie point. Typical curie points for most ultrasonic transducers is approximately 90°C. False echoes from vibration, tube walls, and other surfaces such as bundle rods can render the gas-liquid interface difficult to detect.

2.3 Gamma Densitometry

Radiation usually interacts with matter in the forms of absorption or scattering. This interaction can be useful for determining the void fraction. For example, a gamma densitometer uses a beam of gamma radiation and a gamma sensitive detector.[31] In gas-liquid two-phase flow, the gamma beam is exponentially reduced by the mass of the liquid in the test section. For a linear radiation beam in pure materials, gamma-ray attenuation normally decreases as follows:

$$I(x) = I_o exp(-\mu x) \tag{2.5}$$

,where I(x) is the attenuated gamma-ray beam strength, I_o is the incident gamma-ray beam strength, μ is the linear attenuation coefficient of the material, and x is the thickness of the material.

The void fraction is determined by measuring the attenuation of the gamma beam signal under two-phase conditions as follows:

$$\alpha = \frac{\ln\left(\frac{I_{2\phi}}{I_l}\right)}{\ln\left(\frac{I_g}{I_l}\right)} \tag{2.6}$$

,where α is the void fraction, $I_{2\phi}$ is the two-phase gamma signal, I_g is the gamma signal with only gas phase present, and I_l is the gamma signal with only liquid phase present.

For this application, measurement of the radiation flux is achieved by an electrostatic type detector. Examples of these detectors are ionization chambers and photomultiplier tubes.[32] Each of these detectors relies on an interaction between the radiation and some medium to produce electrons or charged particles. For example, the ionization chamber uses a pressurized gas which is ionized by the radiation flux. The ions are collected at the cathode or anode. Each collection of ions produces a voltage pulse. Counting electronics are used to determine the number of pulses that is directly proportional to the radiation field.

The single beam gamma densitometer is only applicable to small homogeneous channels. This approach assumes a one-dimensional model is valid and averages the void fraction distribution. The averaged void fraction distribution results in a strong flow regime effect. Multiple beam gamma densitometry provides improved information regarding the void fraction distribution and is less affected by the flow regime. Hori et al. developed a gamma-ray computed tomography system which greatly reduced the flow regime effect but could only perform time averaged measurements.[33]

2.4 High-Speed X-ray Computed Tomography

The X-ray Technique operates on the same principle as the gamma-ray technique. As with gamma-ryas, X-ray attenuation is proportional to Z^5, where Z is the atomic number since X-rays interact with the electron clouds. The two main differences are that X-rays are usually lower in energy than gamma-rays and are typically generated by an accelerator instead of a radio-isotope.

Some investigators have studied the single beam X-ray densitometer. More recently though, investigators have applied multiple beam X-ray techniques for the measurement of void fraction and void distribution.[34,35,36,37,38,39] Narabayashi et al. discussed in detail a scanning X-ray system for measurement of void fraction in pipe flow.[34,36] Morooka et al. discussed application of computed tomography to the X-ray technique[35,37]. Each investigator improved the spatial measurement of void fraction using the multiple beam X-ray technique, but usually at the expense of temporal resolution. Hori et al.[38] developed a High-Speed X-ray system for measurement of void fraction in a pipe which has both good spatial and good temporal resolution.

2.5 Real-Time Neutron Radiography

A detailed description regarding the RTNR system used in this work is given in the next chapter. This section reviews previous work by other researchers in the development and application of this techniques.

The RTNR method is based upon thermal neutron interaction with one or more fluids in the flow channel. Neutron interaction usually takes one of four forms: scattering, absorption, fission, and transmission.

Scattering occurs when a neutron and a nucleus collide without a nuclear reaction. The result of such a collision is generally a transfer of energy from the neutron to the atom and a change in momentum of the neutron.

Absorption occurs when the neutron is captured by the nucleus yet the nucleus does not split apart. Absorption is a mechanism which removes neutrons from the neutron beam.

In a fission interaction, a neutron is captured into the nucleus and causes the nucleus to split into two or more different nuclei in a fission reaction. This reaction is limited to fissile and fissionable material and is generally unimportant to neutron radiography.

Transmission occurs when a neutron passes through a material without either a fission, absorption, or scattering event occurring.

The interactions are described by a parameter known as the neutron cross-section that represents the probability of neutron attenuation by a specific material. Neutron cross-sections for typical materials found in two-phase flow research are shown in Table 2.1.[32] Unlike X-ray interactions, neutron interactions are isotope specific. The difference between the X-ray and neutron interactions allows for visualization of different types of materials. Metals such as steel and Aluminium have very low neutron cross-sections but greatly attenuate an X-ray beam. Gases usually have low cross-sections but this is quite often due to their low density. Water, which contains a high degree of hydrogen, is known to be a very good scattering material for neutrons. The reason is essentially that both neutron and hydrogen particles have roughly the same mass; then a billiard ball type scatter will result in nearly 100% energy loss from the neutron to the hydrogen atom. The net result is a very efficient attenuation which larger molecules cannot duplicate.

Flow channels constructed from steel or aluminium are virtually transparent to thermal neutrons and allow for a good imaging of the material inside the pipe. Conversely, the water inside the flow channel highly attenuates the neutron beam presenting a black image. The presence of void or gas decreases the attenuating power of the water providing a brighter image. In this manner, the neutron image represents the void fraction in the flow channel by producing a reconstructed image of the fluid density.

For RTNR applications, a collimated projected beam of neutrons is transmitted through the material. Build-up phenomena can occur where a neutron is scattered out of the beam and then scattered back into the beam.

These physical reactions are represented by the material's microscopic cross-sections and are related to the neutron intensity as shown in Equation 2.7 below:

$$I(x) = I_o Bu(\mu x) e^{-\sigma N x} \tag{2.7}$$

,where $Bu(\mu x)$ is the build-up factor representing the amount of neutron scatter back into the beam. Build-up is only significant for thick materials which produce a large amount of scattering.

Most industrial radiography is still performed today with film radiography. Although the film techniques provide excellent resolution, they are time consuming and usually involve high radiation exposures. The use of a Real-Time Neutron Radiography system has been discussed for a relatively long time but has only recently been applied to two-phase flow. The essential reasoning is that the image intensifier screens have only recently allowed for a good quality image to be developed.

Mishima et al.[40] have delineated flow regimes and calculated average void fractions for two-phase flow in a rectangular duct. Cimbala et al.[41] used a TRIGA type reactor for both pulsed and continuous analysis of two-phase images by neutron radiography. Robinson and Wang[42] also used a pulsed or flash radiography for visualization of two-phase flow. In each case, some "snap shot" information was obtained at higher resolutions than continuous beam RTNR. Other flow visualization work has been performed by Jones et al.[43] who examined the flow of oil inside internal combustion engines.

The RTNR system has a distinct advantage over other methods in that the system allows for global visualization of fluid flow inside metal containers. Other techniques are either intrusive or can only act in a localized area. X-ray radiography is another global method but is too sensitive to metal in the material of the test section.

2.6 Other Radiation Based Techniques

Additional forms of radiation exist such as photons, non-thermal neutrons, and beta particles which can interact with matter. Of these forms, only photons and high energy neutrons have been extensively studied for application to two phase flow.

The photon or light techniques include light scattering[44], light transmission [45,46,47], and imaging techniques[48]. In general, photon techniques are limited to transparent test sections, a limited number of gas-liquid interfaces, and the need to account for changes in the index of refraction.

Neutron techniques include fast neutron scattering[49], pulsed neutron activation[50], and fast neutron radiography[51]. Neutrons have the distinct advantage of easily penetrating metals and are best applied to complex flow geometries such as nuclear fuel channels with bundles. The main limiting factor with

Table 2.1: Thermal Neutron Cross-Sections for Some Materials

Material	Microscopic Absorption Cross-Section	Microscopic Scattering Cross-Section	Total Macroscopic Cross-Section
	σ_a	σ_s	Σ_t
	Barns	Barns	(cm^{-1})
H	0.33	38	0.002
Li	71	1.4	3.35
Be	0.01	7.0	0.865
C	0.004	4.8	0.385
Na	0.525	4.0	0.115
Al	0.241	1.4	0.099
Fe	2.62	11.0	1.15
Ni	4.6	17.5	2.02
Cu	3.85	7.2	0.937
Water - H_2O	0.66	103.0	3.45
Heavy Water D_2O	0.001	13.6	0.449

neutron techniques is the poor neutron detection efficiency. This means that for good signal to noise ratios, a strong neutron source is required and hence a large amount of shielding material is necessary for personnel protection.

Table 2.2: Summary of Existing Two-Phase Diagnostic Techniques

Diagnostic Technique	Application of Technique								
	Interfering	Steady State	Slow Transient	Fast Transient	Local Void Fraction	Averaged Void Fraction	Void Distribution	Bubble Velocity	Flow Regime
Capacitance	No	Yes	Yes	Yes	No	Yes	*	Yes	Yes
Conductance	Yes	Yes	Yes	Yes	Yes	No	*	Yes	No
Ultrasonic	No	Yes	Yes	Yes	†	Yes	*	Yes	Yes
Gamma Densitometer	No	Yes	Yes	Require Strong Source	No	Yes	*	Yes	Yes
Pulsed Neutron Activation	No	Yes	Yes	No	No	Yes	No	Yes	?
Fast Neutron Scattering	No	Yes	No	No	No	Yes	No	Yes	Yes

Table 2.2: Summary of Existing Two-Phase Diagnostic Techniques

Diagnostic Technique	Application of Technique								
	Interfering	Steady State	Slow Transient	Fast Transient	Local Void Fraction	Averaged Void Fraction	Void Distribution	Bubble Velocity	Flow Regime
X-ray Computed Tomography	No	Yes	No, Memory Limited	Yes	Yes	Yes	Yes	No	Yes
Real-Time Neutron Radiography	No	Yes	Yes	No	No, Chordal	Yes	Yes	Yes	Yes

* Application is Currently Limited.

† Requires Tomography.

Chapter 3

3. Two-Phase Diagnostic Systems and Experimental Flow Systems

This work uses three independent measurement techniques for two-phase flow parameters. They are the RTNR system, the X-CT system, and the ultrasonic system. An optical video camera system is also used for flow regime visualization. The RTNR and ultrasonic systems are used at the McMaster University Nuclear Reactor (MNR) facility. The X-CT system is used at the Mitsubishi Heavy Industries Takasago Research and Development Centre with the test section constructed at McMaster University. The experimental systems studied in this work include a natural circulation flow loop (pipe flow), a bubble column (pipe flow), an annulus flow channel, a CANDU-type nuclear fuel flow channel, and a MAPLE-type nuclear fuel flow channel.

3.1 MNR Neutron Radiography Facility

The neutron radiography facility at the McMaster Nuclear Reactor(MNR) is shown in Figure 3.1. The neutron flux for the MNR radiography facility is approximately $10^6 n/(cm^2\text{-}s)$ when the reactor is operated at 2.0 MW_{th} power. The beam is well thermalized and well collimated to ensure clear imaging of the test apparatus. A Bismuth block (gamma-ray filter) and a lead-boron carbide collimator produces a square aperture high purity neutron beam. The gamma content (neutron to gamma ratio) of the beam is approximately $5X10^6 n/(cm^2 mrem)$ and the collimator ratio (L/D) is approximately 70.6. The RTNR camera and test apparatus are contained inside a "cave" like chamber to provide a safe operating environment and also to reduce noise in the neutron beam. The collimated neutron beam is attenuated by fluid and the test apparatus, then absorbed by the neutron to photon converter in the camera head of the Real-Time Neutron Radiography system.

3.2 RTNR Camera System

The RTNR system developed in this work is shown in Figure 3.2. An LTV Co., model NRTV-2 Real-Time Neutron Radiography Camera is used as the central component of the RTNR system. The other components in the system include a time code generator (Telcom Research Model T5010), a Mitsubishi video cassette recorder (VHS and S-VHS), an image processing board (Data Translation DT2853, DT2861), and a personal computer (IBM 486 AT Compatible). The image processing board and the personal computer comprise the Image Processing system.

The RTNR camera outputs a standard RS-330 video signal to a VCR for video storage at a sample rate of 30 frames/second. The video can then be acquired by the Image Processing board for enhancement and analysis by computer.

The RTNR camera can produce a variable resolution in horizontal lines by jumping the electronic raster scan chips in the camera control unit. Currently, the camera is set to the lowest level of 570 lines resolution to match conventional storage devices and image processing equipment. The image processing board can only image 480 lines by 512 pixels per image. Essentially, there is little need to increase the resolution of the camera unless examination of finer detail is required.

The RTNR Camera operates under relatively low thermal neutron fluxes; on the order from 10^4-$10^6 n/(cm^2$-$s)$[52]. To do neutron imaging at these low flux levels, the system contains two special features: a neutron to photon converter screen and a Silicon Intensified Target. The neutron to photon converter (a Li^6 doped ZnS

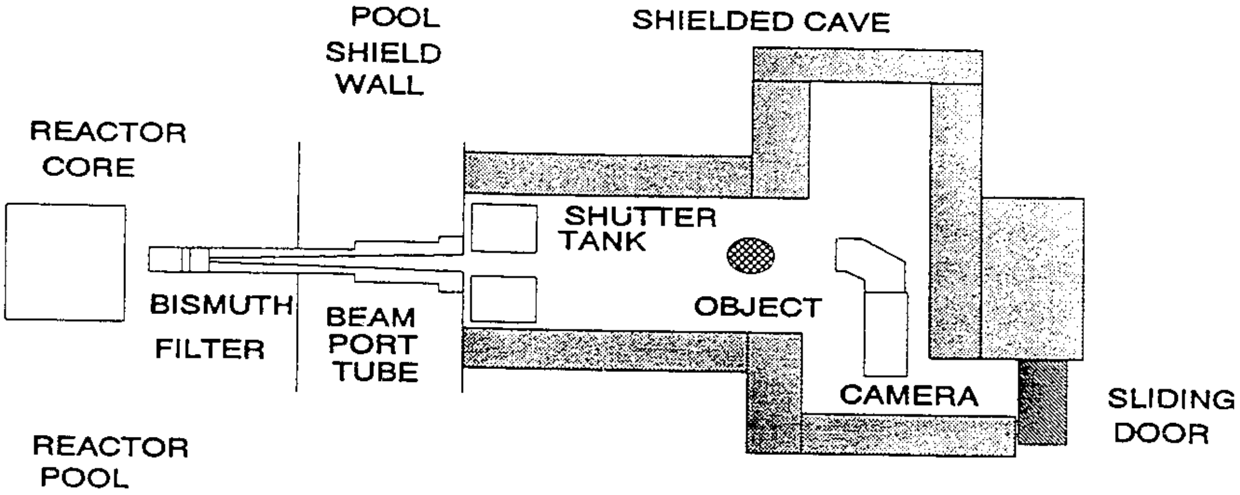

Figure 3.1: Schematic of Neutron Radiography Facility at the McMaster University Nuclear Reactor (Beam Port #2)

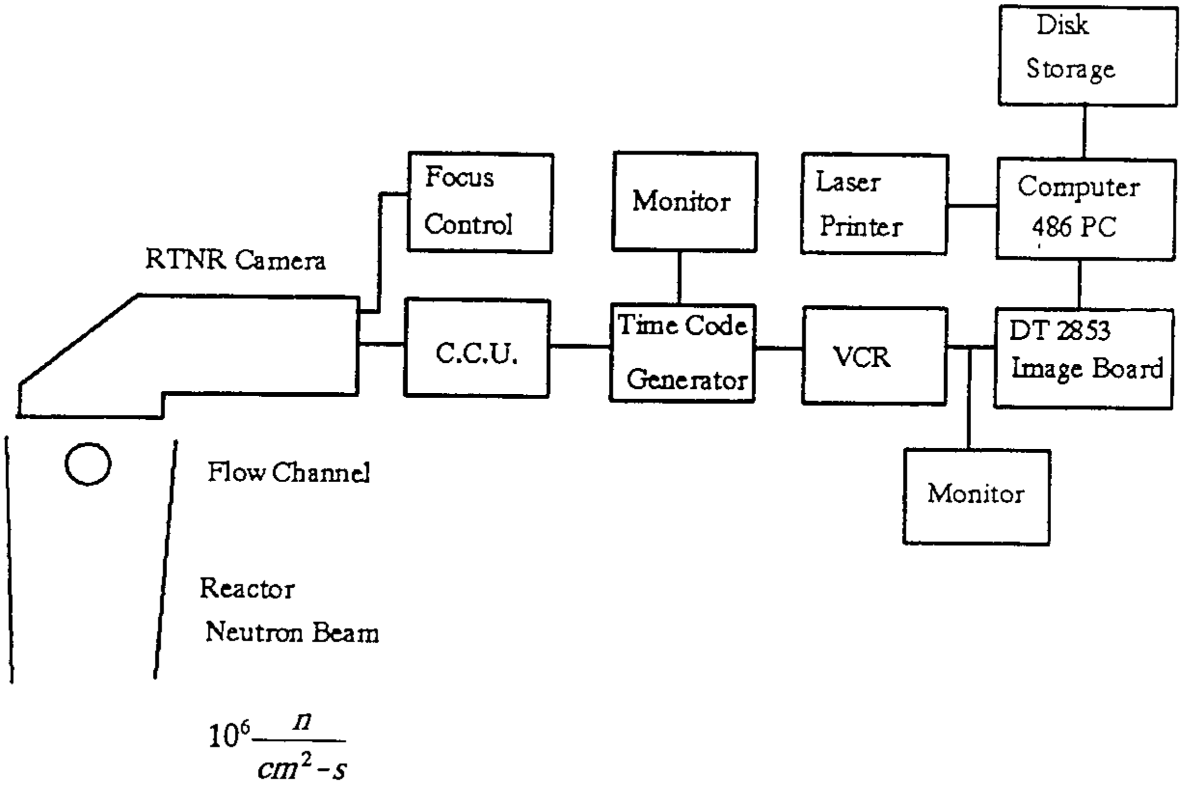

Figure 3.2: Schematic of the Real-Time Neutron Radiography System: CCU is the Camera Control Unit

screen) allows for high efficiency conversion of the neutron particles into photons and the low light level silicon intensified target (SIT) provides higher sensitivity to photon detection than other systems.[53] The RTNR Camera contains a 45° mirror that deflect the photon beam into the target to reduce potential damage to the electronic components from the radiation beam and reduce gamma induced noise in the image[54]. A cooling jacket of dry nitrogen allows for noise reduction, thermal insulation and electrical insulation of the target.

The spatial resolution of the RTNR camera is limited, by the lens system and by the converter screen doping, providing a typical resolution on the order of 1 mm for a high contrast image. It is possible to increase the resolution of the camera system but it would be exceedingly difficult to achieve micron resolution and still maintain image quality.

The temporal resolution of the RTNR system is limited by the sampling rate of 30 frames/second or 33.0 ms. The exposure time for each image is also 33.0 ms as the camera uses a continuous exposure feature. This value can be changed but a faster acquisition time or faster exposure time would require a higher neutron flux so as not to degrade image quality by the corresponding decrease in observed neutrons. As a result, the effect of the exposure time is to produce blurred images of moving objects as the image is inherently averaged over 33.0 ms.

The radiographic image is scanned by the camera in an interlaced mode, which means that the image pixel lines are acquired alternately. These alternate sets of pixel lines are called a field, where two fields combine to make one image. For a 480 pixel line image, the odd pixel lines correspond to field 1 and the even pixel lines correspond to field 2. Field 1 is completely scanned first, followed by field 2. This means there is a time difference of 16.5 ms between each field.

3.2.1 Beam Uniformity and Target Integration

Experimental studies have been performed by other researchers to determine the uniformity of the neutron flux in the imaging plane of the MNR Neutron

Radiography Facility. The results indicate the image plane is relatively square and quite uniform in neutron intensity with a dramatic decrease in the neutron flux at the edges of the beam.[55] The neutron converter has been assured uniform by the LTV company.

The video image however, results in a non-uniformity suggesting a maximum intensity in the centre of the screen with a cutoff on the left edge of the video display. These artifacts are created by the camera itself and are not due to the neutron beam on the converter screen. The left edge cutoff is created by either some misalignment of the camera tube with the internal optics or by masking the target. Each camera tube is aligned by hand and shimmed into place, hence alignment with the optics and the mirror to image squarely on the converter screen is quite difficult. Also, it is common practise to cover sections of the vidicon target to create square images as these covered areas usually are not required for the video output.

3.2.2 Video Image Gain Mechanisms

The RTNR camera can output an image in either a preset or auto gain mode. The choice of gain mode can be critical and is usually application specific.

The preset gain is determined by a screwdriver potentiometer on the camera control unit. The gain can be varied at any time and will be consistent until the next adjustment is made. I.e., Gain drift has not been noted to occur in the camera.

The auto gain mode averages the intensity across the image and boosts the gain on the image automatically to a predetermined level. Although the auto gain mode provides higher intensities and greater range than the preset mode, each image is now unique with it's own average intensity. This renders analysis from image to image difficult unless gain corrections are considered.

3.2.3 Spatial Calibration Experiment

A 5.057 cm X 5.055 cm Cadmium square was placed in the centre of the neutron converter screen to do a spatial calibration of the image pixels with respect to the outer frame of the camera. This is important as most experiments performed use the outer frame of the camera as the reference location for the experimental apparatus. Once the spatial calibration is known, liquid levels inside pipes can be easily cross-referenced.

The spatial calibration shows that 14.8 horizontal pixels is equivalent to 1.0 cm and 19.8 vertical pixels is equal to 1.0 cm. The camera is calibrated relative to the lower left corner of the converter screen. This corner also corresponds to near the lower left corner of the image. Equations 3.1 and 3.2 give the spatial calibration as follows:

$$L_{hor} = 0.0701 P_{ix} - 4.922 \quad [cm] \tag{3.1}$$

$$L_{ver} = -0.0561 P_{ix} + 27.503 \quad [cm] \tag{3.2}$$

,where P_{ix} is the pixel number and L is the length in centimetres from the lower left corner of the neutron to photon converter frame.

Pixel number (0,0) is traditionally the top left of the image.

3.2.4 Time Code Generator and VCR

The time code generator is used to mark each video frame with a time code and an experiment code. The time code and experiment code catalogue each frame which simplifies temporal analysis as the time code provides detailed information regarding frame number and time of acquisition and the experiment code identifies each different experimental condition.

Both a VHS format and a S-VHS format video cassette recorder (VCR) have been used as a storage medium. Although the S-VHS VCR has better resolution than the VHS VCR, both are the limiting resolution factor in the RTNR System.

Typical considerations for the video signal are bandwidth limitations, synchronous abberations, and line resolution. These phenomena can cause distortions or pixel shifts in the image.

Test patterns developed using the image processing system were passed through the VCR to examine the sync abberation and pixel shift phenomena. The results show intensity variations as high as 20% in the video signal and pixel shifts of 3 or 4 pixels due to this phenomena. Two essential factors were found to be the cause of these variations. The first factor is the band width limitation which cuts out the higher frequencies in the video signal. The VHS VCR has a bandwidth limitation of 3 MHz and the image processing board has a bandwidth limitation of 4 MHz. The other factor is due to an unstable sync signal.

In the RTNR system, there are three devices which are generating synchronization pulses, The camera generates the original pulses and the video information. The VCR generates another set with which the camera is synchronized for recording purposes. Lastly, the image processing board generates its own set of pulses with which the incoming pulses (from the VCR or directly from the camera) are synchronized for frame grabbing. This duplication of synchronization pulses allows for phase error in the synchronization of the two signals. If there was a slight error in the synchronization of the camera and the VCR, in one frame but not in the consecutive frame, the images could have slight differences even though there have been no change in the objects being radiographed. These changes would be invisible to the eye but could show up when the images are further processed.

An error in horizontal synchronization is far more likely than an error in vertical synchronization (simply because of the higher frequency of the horizontal sync-pulses) and this would account for the small changes in position and intensity.

3.3 RTNR Image Processing System

The image processing system allows for some key image manipulation such as frame averaging, filtering, image subtraction, and contrast imaging. The ability to average many frames and to pass the images through various filters greatly reduces the noise associated with the radiographs. Image subtraction can then be applied to remove the image detail according to the neutron beam and the test geometry. Contrast imaging allows for the enhancement of the image to aid in visualizing either very weak or very strong attenuating materials. By combining these image processing features in the correct manner, it is possible to clearly visualize various two-phase flow pattern fluid density maps.

3.3.1 Image Processing Boards

Two image processing boards are available for use with the custom-built software and commercial software used in this work. The DT2853 image processing board currently supports DT-IRIS and IPPLUS commercial software. The image processing board is limited to two frame buffers but can acquire and display images. The DT2861 image processing board is a more advanced version of the DT2853 image processing board containing 16 image buffers numbering from 0 to 15. The custom software developed in this project was designed to take advantage of the 16 image buffers for temporal analysis of the images.

3.3.2 Commercial Software Packages

Two commercial software packages are currently available for use with each image processing board. The image processing boards come with the DT-IRIS software. The IPPLUS software is capable of supporting either image processing board or a super-VGA card and monitor.

The DT-IRIS software promotes the use of macros to streamline operations and is the only package which currently can acquire 16 consecutive frames. The IPPLUS software is currently the only system which can manipulate the images using a S-VGA card and is a user friendly menu driven system which allows for advanced image processing concepts such as filtering, contouring, image equalization, etc. The advantage of using the S-VGA card is the ability to use false colour imaging to help clarify various details in the images.

The IPPLUS software can print out the images to a HP Laserjet II+ printer(300DPI) or a HP PaintJet colour printer(180DPI).

3.3.3 Processing Speed Considerations

Certain applications will require high speed processing such as acquiring consecutive frames, frame averaging and intensive image manipulation. A simple code was used to test the speed capabilities of certain routines and computers. The routine *RWBUF.ASM* transfers data from computer memory to the frame buffer memory. The call statement can handle any size of information. If the image was transferred pixel by pixel, the time to complete the file transfer could be over 1 hour. By transferring 64 lines of information at one time, loading an image file into the frame buffer memory will take 30 seconds on a 386-25MHz machine.

The code *SKELETON.FOR* was operated on both a 386-25MHz computer and a 486-33MHz computer. The 386 machine did not contain a math coprocessor chip while the 486 machine has an integral math coprocessor chip. The time for the code to complete processing the image on the 386 was slightly greater than 4 minutes real time. The 486 computer took approximately 18 seconds to complete the same image manipulation. This corresponds to approximately a factor of 10 increase in speed. Faster computers are always more desirable for image processing but the 486-33MHz PC computer is fast enough to perform most tasks.

3.4 High-Speed X-ray CT System

Part of the experimental study for the annulus flow channel is carried out at the Mitsubishi Heavy Industries Takasago Research and Development Centre. At this facility, a High-Speed X-ray Computed Tomography system (X-CT) and an engineering work station are used to determine various two-phase flow parameters.

The High-Speed X-ray CT scanner is shown in Figure 3.3. Design parameters for the High-Speed X-ray CT system are shown in Table 3.1. A 100 kV grid accelerates an electron beam in a vacuum chamber to strike a target and produce 100 keV X-rays. Most of the X-rays from a source are distributed into a 30^{o} fan beam. A detector array measures the X-ray beam strength using Cadmium Tungstenate ($CdWO_4$) scintillators and silicon photodiodes. To increase temporal resolution, 18 X- ray sources and 122 $CdWO_4$ detectors are arranged around the test channel. The sources and detectors are stationary and numerous enough to eliminate the need to rotate either source or detector array. Eliminating the rotation improves the temporal resolution; then the temporal resolution is limited by the photon decay time in the scintillation crystal, the number of X-ray sources, and the electronic timing circuit[38]. The current cross-section sampling time is 4.0 ms(250 cross-section/s).

The High Speed X-ray CT scanner has a total height of 62.5 cm. The scanner is physically separated into an X-ray generator unit and an X-ray detector unit. The X-ray generator unit surrounds a pipe channel with a diameter of 7.0 cm and a height of 38.8 cm. The channel is widened at the top to allow for placement of the X-ray detector unit with a height of 9.8 cm. The X-ray detector unit has a total height of 23.7 cm. Assuming gas injection occurs at an elevation equivalent to the bottom of the X-ray generator unit, the minimum X-ray measurement elevation is 47.0 cm as the scanner is currently operated in a vertical upright position. In future work, it may be possible to invert the X-ray scanner to eliminate this problem.

3.5 Ultrasonic Data Acquisition System

As part of this work, an advanced ultrasonic data acquisition system is developed. The advanced system is based on an earlier design [29] and is modified to include more memory and a second data channel on the IBM PC interface card as shown in Figure 3.4. Two transducer signals can be acquired simultaneously by two independent memory circuits(ECM). A controller circuit (CU) will act as a sync generator to both drivers and activate the memory circuits. The computer interface(CIU-2) and software acquire data into both channels. The controller, 2

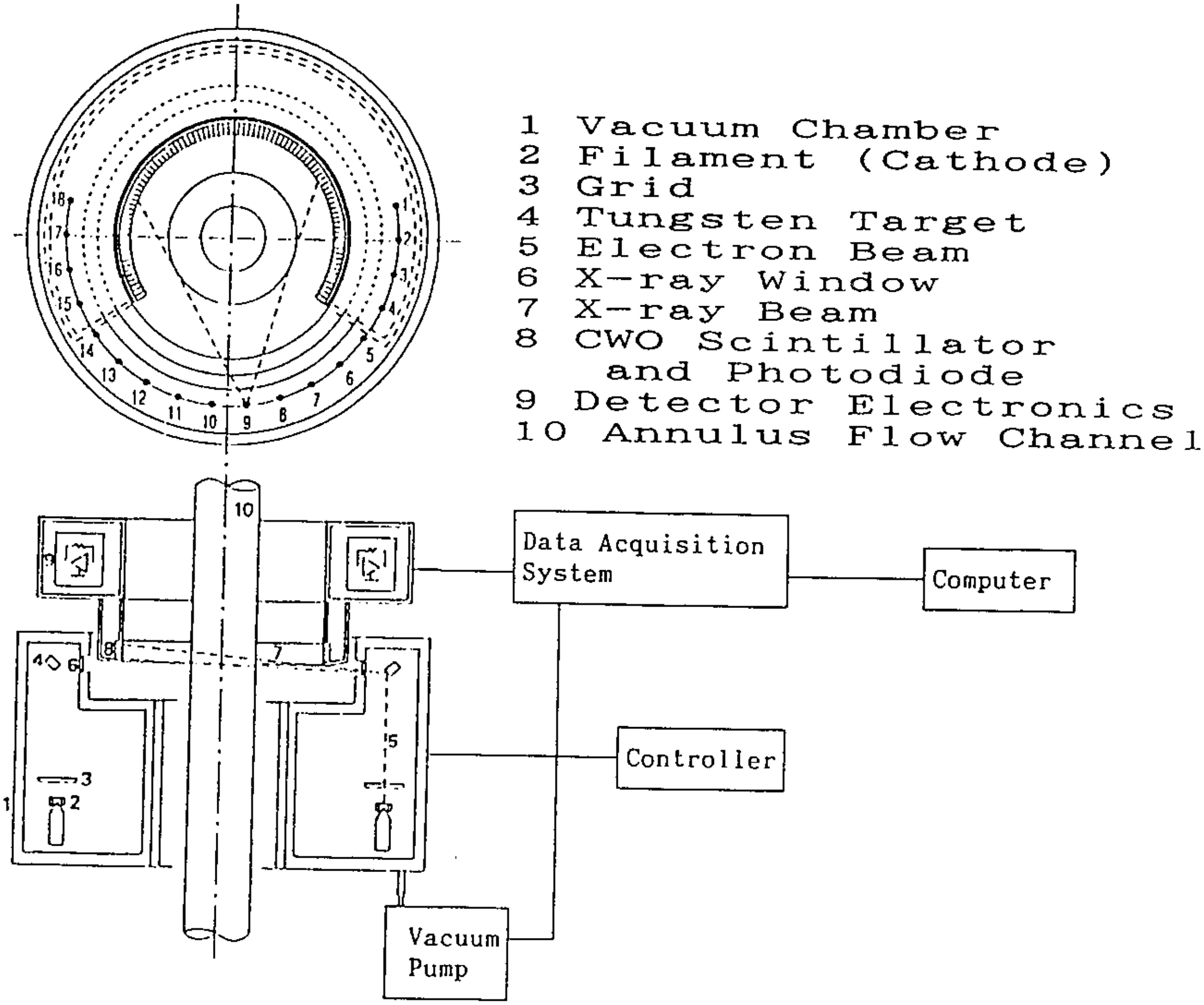

Figure 3.3: Schematic of the High Speed X-ray CT Scanner

Table 3.1: Design Parameters of X-ray CT System

X-ray Source	
Number of Sources	18
Accelerating Voltage	100.0 kV
Beam Current	20.0 mA
Target	Tungsten (W)
Fan Angle	24
Scan Rate	4.0 ms
Detector Array	
Number of Detectors	122
Samples per Views	32
Scintillator Type	$CdWO_4$
Detector Type	Silicon PhotoDiode
Image Quality	
Maximum Object Diameter	50.0 mm
Pixel Grid Size	256X256
Memory Size	16.0 MB

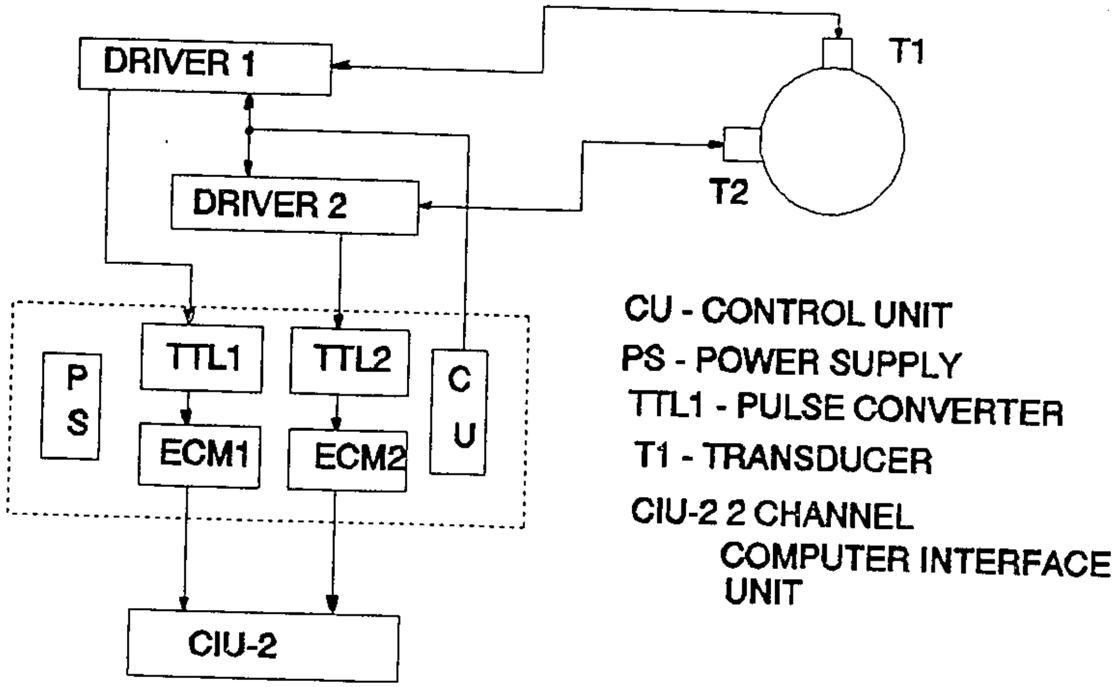

Figure 3.4: Advanced Ultrasonics System for Pulse-Echo Analysis of Two-Phase Flow

TTL pulse converters, 2 memory circuits, and a power supply are contained in one unit with appropriate electromagnetic shielding. The two TTL Pulse Converters have adjustable trigger levels to reduce false echo triggering. The memory circuits have 32 kBytes of memory, counters, and associated switches. This allows for data acquisition for a 2.0 second period. The IBM PC interface with two channels is operated by an 8255 IC controller.

3.6 Experimental Flow Loops

Several different flow loops are studied in this work. The natural circulation flow loop and the bubble column flow loop represent pipe flow geometries. Other test sections studied in this work are the annulus flow channel, the CANDU-type nuclear fuel flow channel and the MAPLE-type nuclear fuel flow channel. These additional test sections provide insight into measuring void fraction distribution in complex geometries.

3.6.1 Natural Circulation Flow Loop

The natural circulation flow loop consists of a mixer section, a test section, a gas-liquid separation tank and a reservoir tank as shown in Figure 3.5. The test section is a 50.0 cm long vertical tube with an inner diameter of 1.0 cm. Two tubes were used : - one fabricated from glass for visual observations; - the other fabricated from stainless steel for neutron radiography. The loop is filled with either light water (H_2O) or heavy water (D_2O). Normal air is used for the gas. Gas is injected into the lower mixer section of the test facility. The gas rises to the separator causing the fluid to circulate naturally about the loop. The gas flow rate is measured by a rotameter. The induced liquid flow rate is measured by a turbine flowmeter and also by the liquid level of the upper gas-liquid separation tank as determined by ultrasonic liquid level measurements[29]. Video camera, RTNR, and Ultrasonic pulse-echo measurements are taken on the two-phase vertical leg of the apparatus.

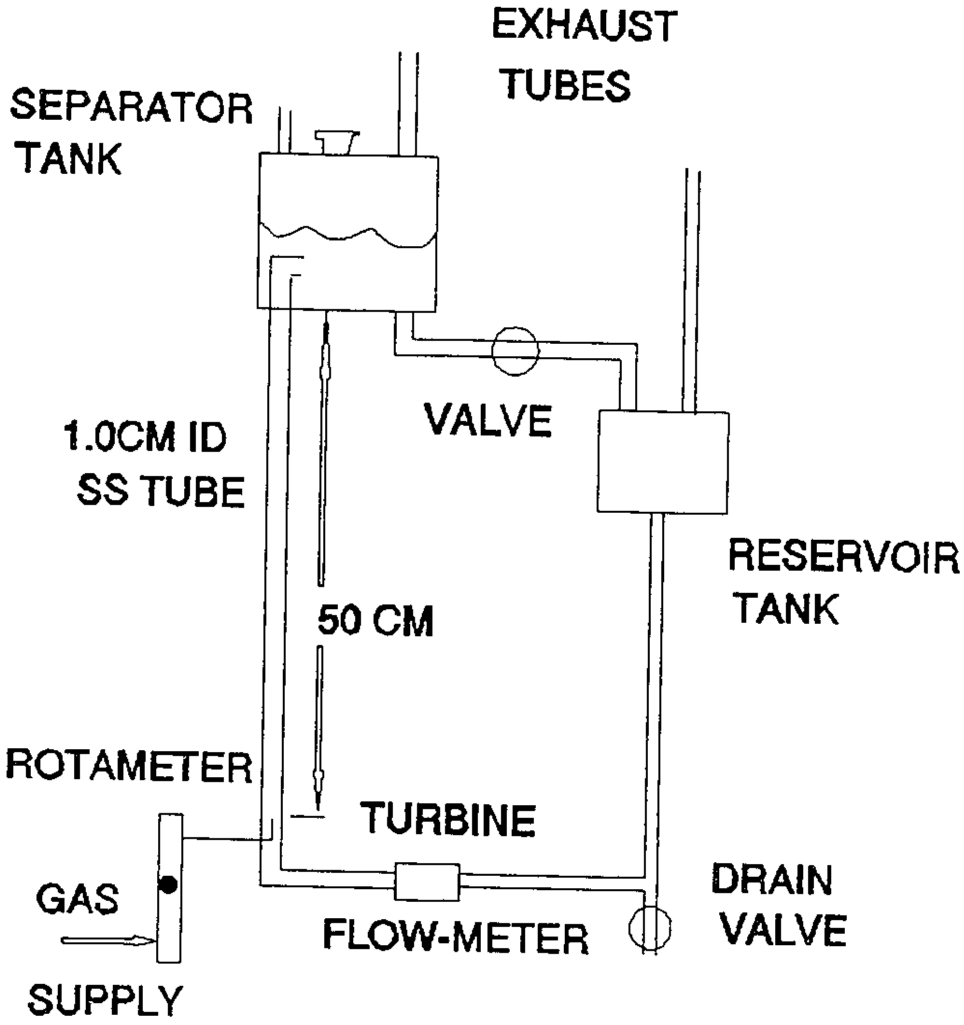

Figure 3.5: Experimental Natural Circulation Flow Loop

3.6.2 Bubble Column Flow Loop

The bubble column experimental flow loop is shown in Figure 3.6. Air is used for the gas phase and is injected into a packed bed mixer. Glass beads are used to mix the gas with the liquid and a sieve plate is used to generate the bubbles in a homogeneous distribution with a constant bubble diameter. A small lucite pipe section is used to provide an interface between the mixer and the aluminium channel. The lucite interface allows for optical flow visualization of the bubbles. The aluminium test section is 5.40 cm in diameter (2R) with a thin wall to reduce wall attenuation of the neutron beam. The channel is 61.0 cm in length and water levels are varied from 30.0 cm to 40.0 cm from the sieve plate exit. The gas flow rate is monitored by a rotameter and liquid level measurements are observed by neutron flow visualization. Void fraction measurements are performed using the relative intensities of the neutron radiographic images.

3.6.3 Annulus Channel Flow Loop

The annulus test section is shown in Figure 3.7. The gas used in these tests is atmospheric air and the liquid used in these tests is light water or heavy water. Gas supply is provided by an air compressor and is regulated to 5.0 kg/cm^2. A rotameter type gas flow meter (Osaka Flowmeter) is used to monitor the gas flow rate. Two pressure gauges are used. The first gauge monitors the gas flow meter pressure to correct the gas flow rate and the second gauge monitors the system pressure at the inlet of the gas injector. A glass bead packed bed is used to thoroughly mix the gas and a sieve plate is used to generate small bubbles uniformly distributed in the annulus. An overflow flange is used to ensure the instrumentation remains dry at high gas flow rates. Sponge supports are used to centre the test section inside the X-ray CT scanner. An adjustable stand is used to vary the axial measurement location.

One annulus is manufactured from acrylic resin to allow for visualization by both X-rays and the naked eye. Visualization with the optical video camera uses the same experimental apparatus with the High-Speed X-ray CT system removed.

The experiments with the Real-Time Neutron Radiography system uses Aluminium tubes as the wall material for the annulus test section for static liquid levels greater than 30.0 cm and both Quartz and Aluminium tubes are used for static liquid levels less than 30.0 cm. Two boronated rubber shields are used on either side of the annulus test section to reduce neutron scattering components in the image and to eliminate high frequency electronic noise.

The length of the test section for the Lucite and Aluminium tubes is 1.0 m and is 0.50 m for the Quartz tubes. The inner diameter of the outer tube is approximately 4.54 cm and the outer diameter of the inner tube is approximately 1.9 cm for the Lucite tubes which gives a flow area of the annulus of 0.00133 m^2 and a hydraulic diameter of 2.63 cm for both the High Speed X-ray CT study and the optical video study. For the Quartz tubes, the hydraulic diameters and flow areas are the same as for the Lucite tubes. With the Aluminium tubes used in the RTNR study, the inner diameter of the outer tube is 4.75 cm and the outer diameter of the inner tube is 1.9 cm which gives the flow area as 0.00145 m^2 and the hydraulic diameter as 2.84 cm for the Aluminium tubes.

3.6.4 CANDU-Type Nuclear Fuel Channel Flow Loop

A 37 rod bundle in a circular channel as shown in Figure 3.8 is used for the CANDU-type nuclear fuel channel loop. Both the rod bundle and the flow channel are made of aluminium for better flow visualization by neutrons. The flow channel is a cylindrical pipe with a diameter of 10.16 cm and a tube thickness of 1.0 cm. The length of the flow channel is 1.5 m to ensure a greater length than the bundle. This type of bundle is used in the fuel channel of a CANDU type nuclear power plant.

Figure 3.9 shows the detailed geometry of the CANDU type bundle. The

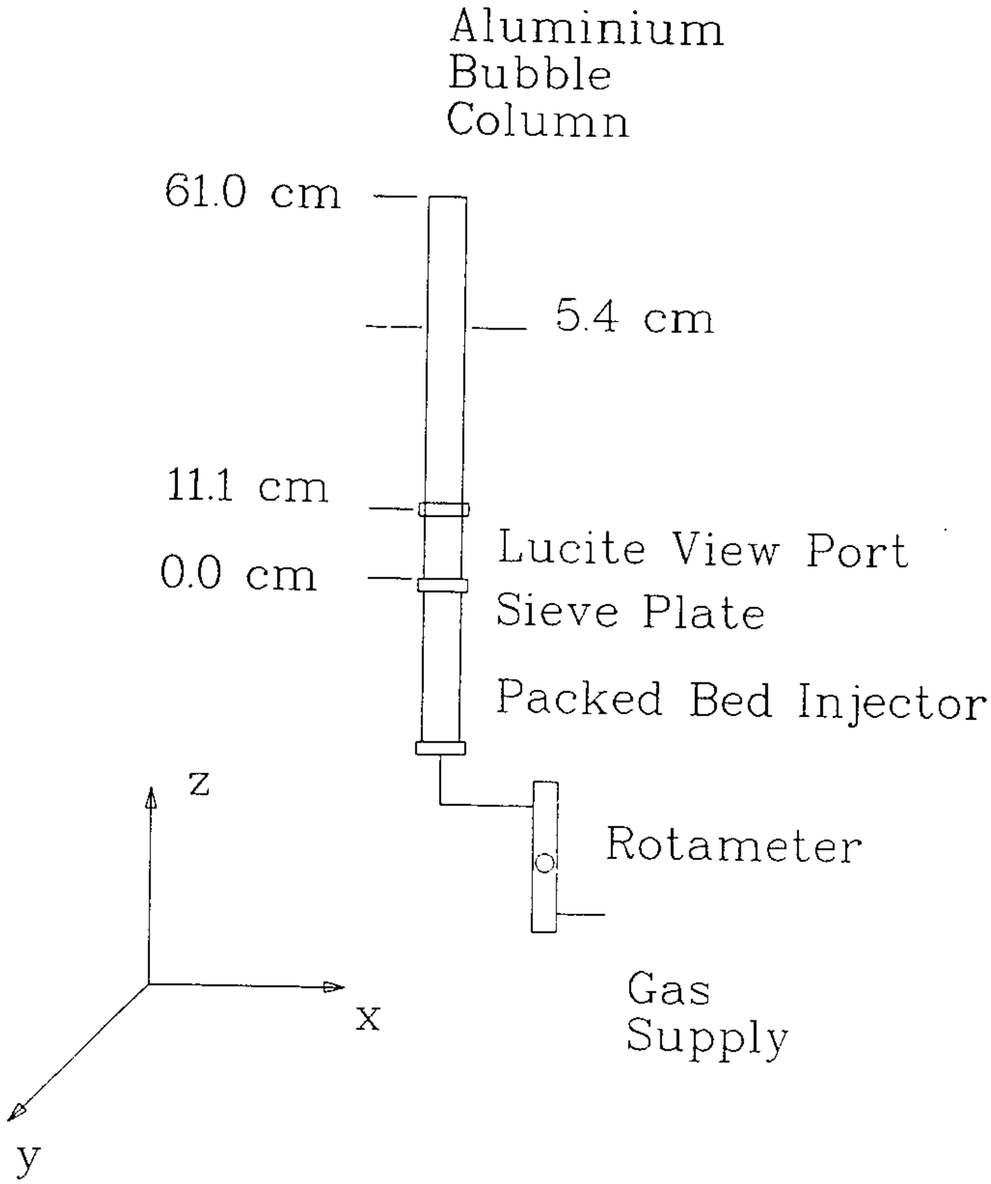

Figure 3.6: Experimental Bubble Column Flow Loop

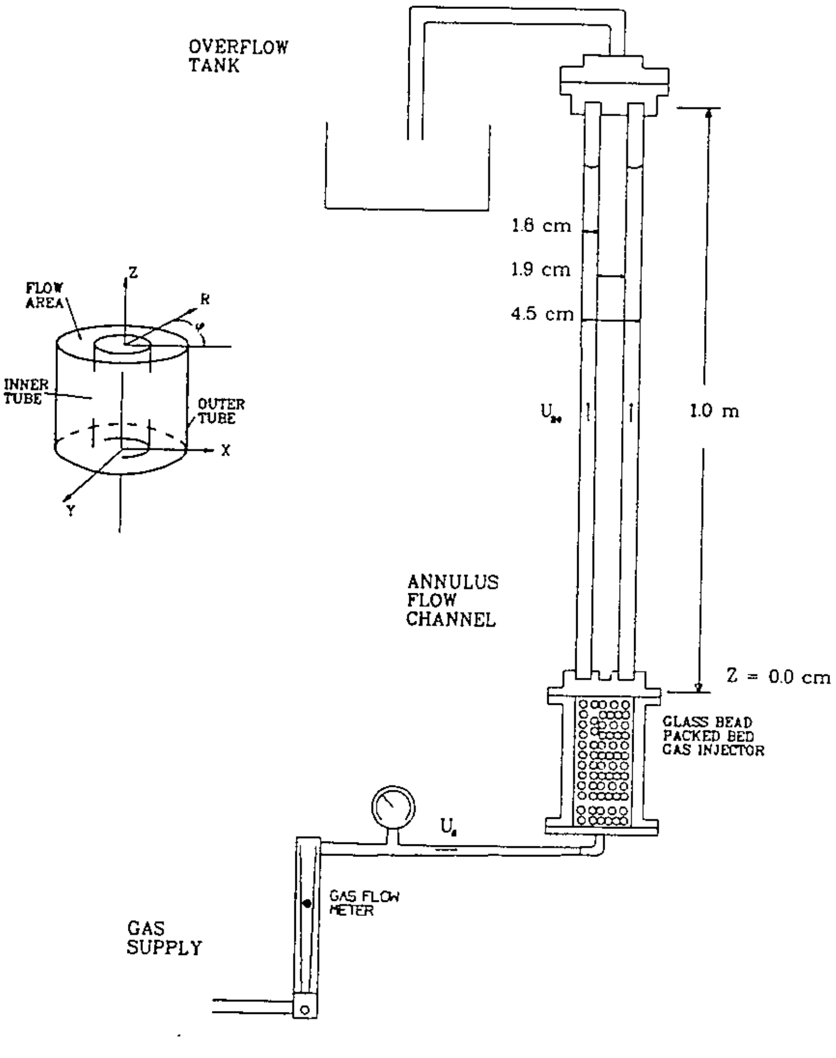

Figure 3.7: Experimental Apparatus of the Annulus Flow Channel

bundle is patterned with three concentric rings of tubes. Each tube or rod has a diameter of 1.27 cm. The gap separation between rods varies from 1.79 to 1.96 mm. The hydraulic diameter of the flow channel with the 37 rod CANDU-type bundle is 3.05 cm. The bundle length is 1.0 m with two endplates holding the rods in position.

Air is used as the gas and is measured by two Brooks rotameters (models 1110-08H2A1D, 1110-10H3A1D). Heavy water is used as the working fluid and the liquid flow rate is measured by a turbine flow meter (Pottermeter LSC-450-10037-1).

3.6.5 MAPLE-Type Nuclear Fuel Channel Flow Loop

The bundle examined in this study is of hexagonal shape with 36 finned rods and a central support shaft, as shown in Figure 3.10. Each rod contains 8 longitudinal fins with a fin height of 1.02 mm. The bundle has a finned length of 0.65 m with end plates at each end, and a seating plug located in the lower end.

The finned hexagonal bundle is placed at the bottom of an Aluminium hexagonal flow channel that has a side length of 42.7 mm. The hydraulic diameters of the hexagonal flow channel with and without the finned hexagonal bundle are 7.44 mm and 75.61 mm, respectively.

The flow loop consists of an inlet plenum, outlet plenum, and pump as shown in Figure 3.11. The inner diameters of the inlet and outlet plenums are 25 cm and 23 cm, respectively. A Validyne model DP15TL pressure transducer is placed in the inlet plenum to measure the system pressure drop. The bulk air injector located inside the bottom of the inlet plenum generates an inlet flow pattern with a homogeneous void mixture across the flow channel, where Matheson 604 and Matheson 605 rotameters measure the gas flow rate.

The liquid flow rate is controlled by a constant power pump and valves. A turbine flow meter (Flow Technology model FT-12M20-LB) measures the liquid flow rate before the liquid enters the inlet plenum.

The experiments are conducted for superficial velocities of each phase from 0.0 to 0.22 m/s at one atmosphere pressure. The flow regimes are observed just

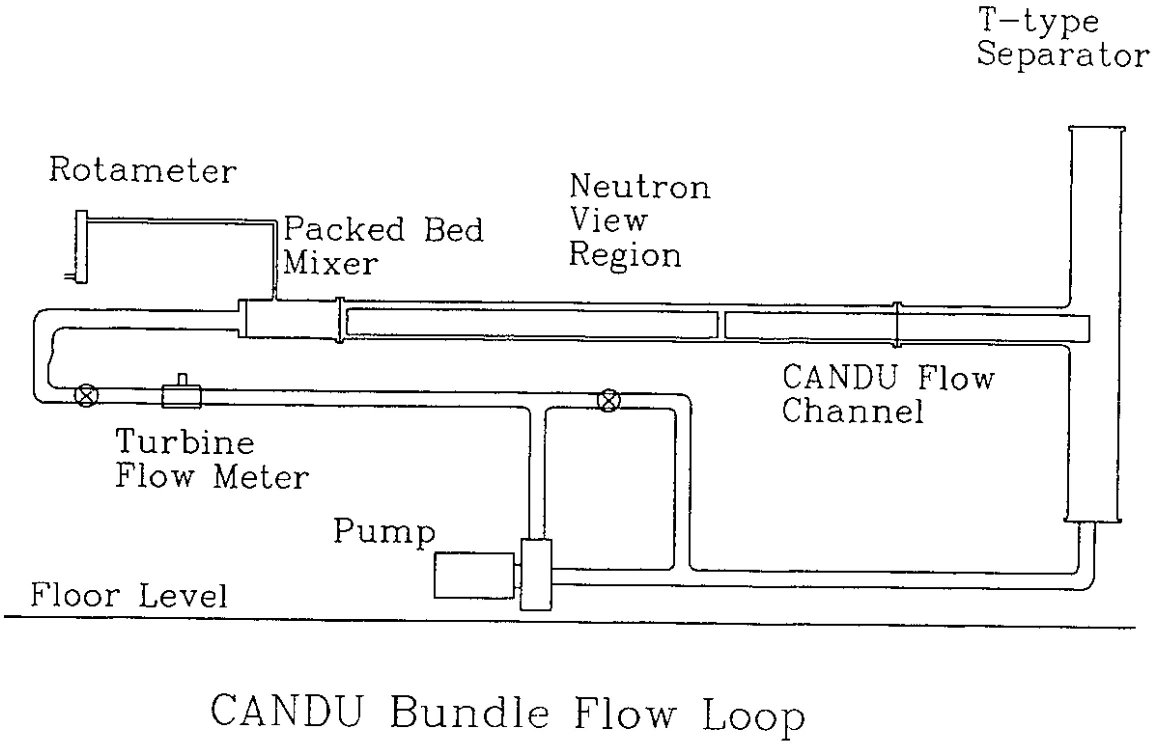

Figure 3.8: CANDU-Type Nuclear Fuel Channel Flow Loop

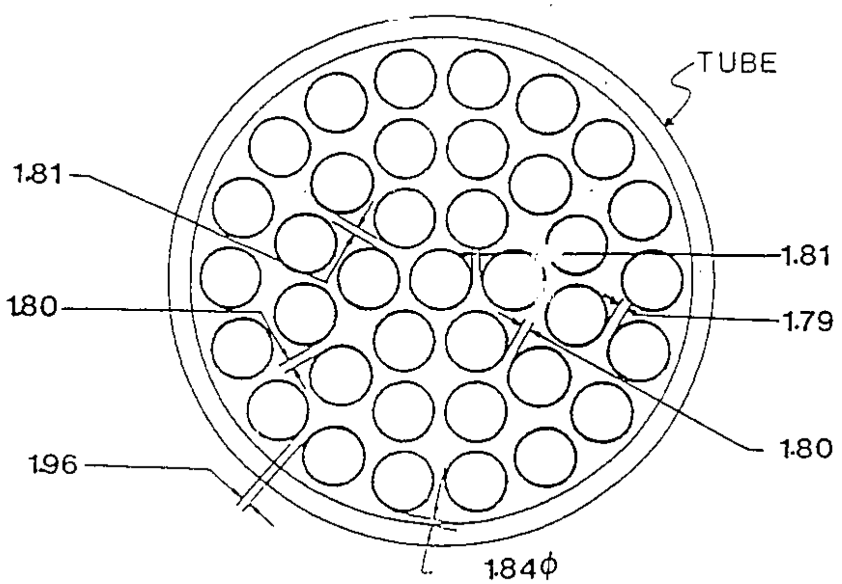

Figure 3.9: CANDU-Type 37 Rod Nuclear Fuel Bundle

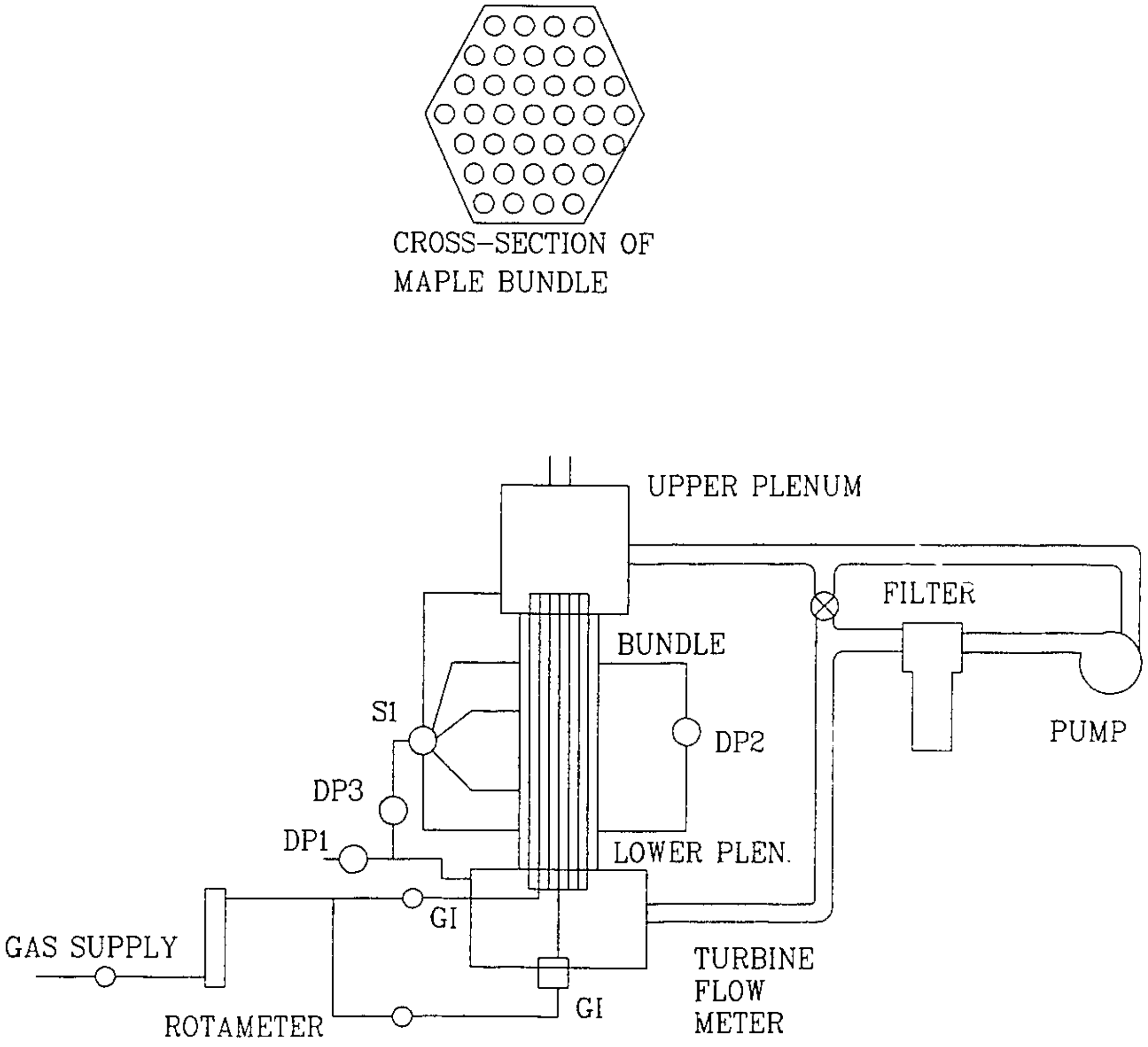

Figure 3.10: MAPLE-Type Nuclear Fuel Channel Flow Loop

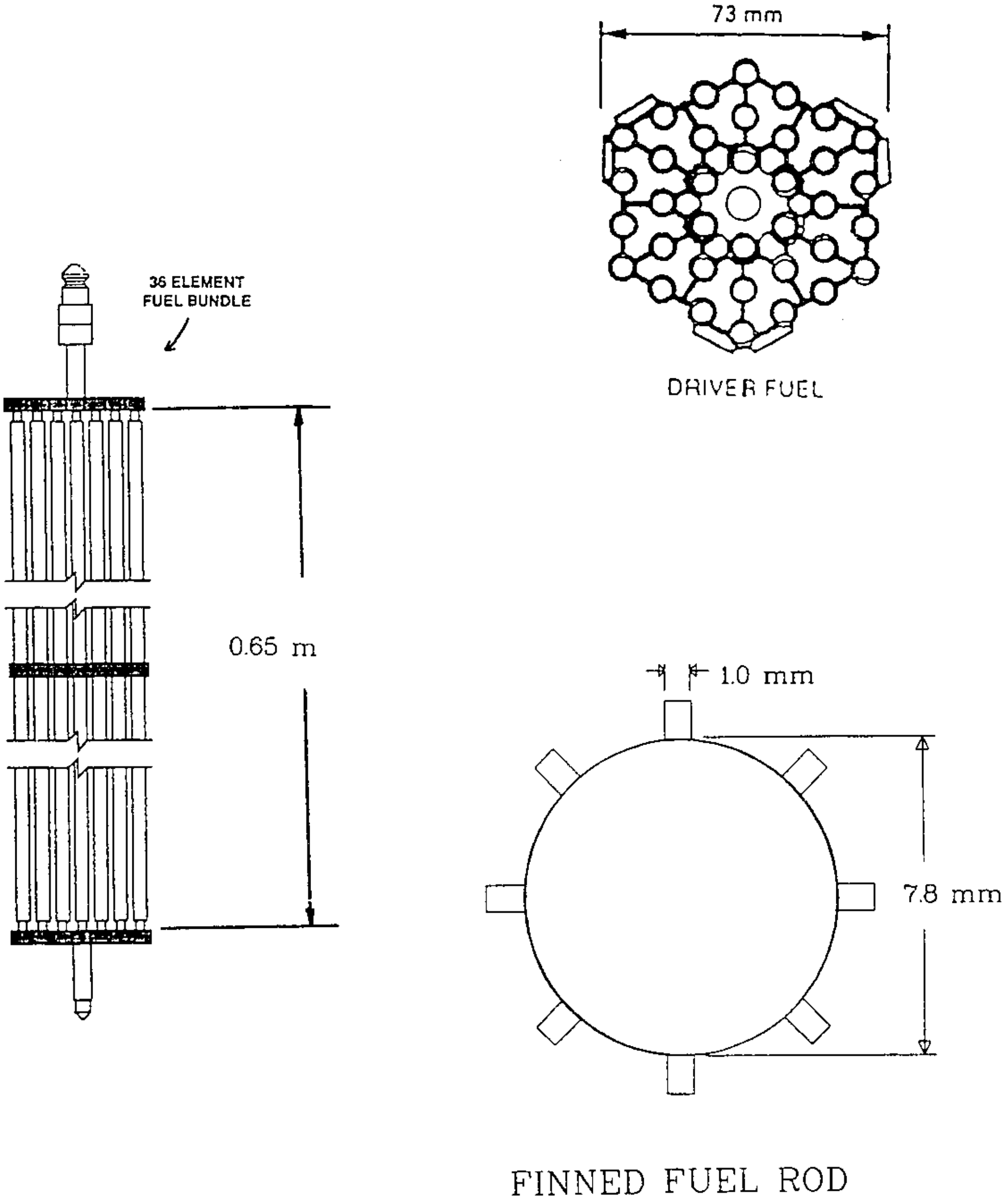

Figure 3.11: MAPLE-Type 37 Finned Rod Hexagonal Nuclear Fuel Bundle

before the finned hexagonal bundle exit, where this point corresponds to a normalized distance from the hexagonal flow channel entrance ($\frac{l_E}{D_h}$) of 13.8 for the hexagonal flow channel with a finned hexagonal bundle. Here, l_E is the distance from the entrance of the hexagonal flow channel to the observation point and D_h is the hydraulic diameter.

Chapter 4

4. Principle of RTNR and X-CT Void Fraction Measurement

4.1 Theoretical Basis for Two-Phase Flow Measurement

The determination of void fraction by the RTNR system is based on neutron attenuation by scattering and absorption phenomena as discussed in Chapter 2.

The attenuation equation shown in Equation 2.7 can be modified to include the void fraction and wall materials as follows:

$$I(x,y,z) = I_0 Bu(\mu y)\ \exp(-\sigma_{wall} N_{wall}(x,z) y_{wall})\ \exp(-\sigma_l N_l(x,z) y_l)\ \exp(-\sigma_g N_g(x,z) y_g) \quad \textbf{(4.1)}$$

The density of the gas (N_g) is small compared to the other densities. Thus, Equation 4.1 can be simplified to:

$$\frac{I(x,y,z)}{I_0} = Bu(\mu y)\ \exp(-\sigma_{wall} N_{wall}(x,z) y_{wall})\ \exp(-\sigma_l N_l(x,z)(1-\alpha(x,z)) y_t) \qquad \textbf{(4.2)}$$

,where y_t is the chordal length along the neutron path inside the flow channel and α is the void fraction.

For small path lengths or non-scattering materials, the build-up factor can be neglected and Bu(μy) becomes 1 in Equation 4.2. The wall attenuation terms can usually be neglected if neutron transparent materials such as Aluminium are used or we can remove this component during image processing. Equation 4.2 could then be used to calculate the chordal void fraction profile, α(x,z), except that the characteristics of the RTNR camera, such as gain and offset factors described in Chapter 3, are not included.

The chordal void fraction ($\alpha(x,z)$) does not truly represent the type of void migration under consideration as length averaging is inherent. However, weighting the void fraction with the water path length (chordal length)provides a cross-sectional averaged void fraction at each axial location. This cross-sectional averaged void fraction can then be expressed by Equation 4.3 as follows:

$$\bar{\alpha}(z)=\frac{\int_0^X \alpha(x,z)L(x)\,dx}{\int_o^X L(x)\,dx} \tag{4.3}$$

,where L(x) is the weighting function for chordal path length differences at each lateral position as shown in Figures 4.1 and 4.2.

The different chordal path length geometries studied in this work are pipe, annulus, CANDU-type nuclear fuel channels, and MAPLE-type nuclear fuel channels as described in Chapter 3. These path lengths are shown in Equations 4.4 to 4.7 respectively and in Figures 4.1 and 4.2.

$$L(x)=2\sqrt{R^2-x^2} \quad :\mathit{Pipe\ Flow\ Channel} \tag{4.4}$$

$$L(x)=2(\sqrt{R_1^2-x^2}-\sqrt{R_2^2-x^2}) \quad :\mathit{Annulus\ Flow\ Channel} \tag{4.5}$$

$$L(x) = 2\sqrt{R^2-x^2} - \sum_{i=1}^{n} 2\sqrt{r_i^2-(x-h_i)^2} \quad :\textit{CANDU Flow Channel} \tag{4.6}$$

$$L(x) = \textit{Hexagon} - \sum_{i=1}^{2} 2\sqrt{r_i^2-(x-h_i)^2} \quad :\textit{MAPLE Flow Channel} \tag{4.7}$$

Two techniques can be used to determine the radial void fraction profile. The first technique is a simple algorithm which measures the two-phase flow from the outer radius to the centre[47]. The void fraction is calculated for the outer layers and is assumed symmetrical about the axis. As the calculations proceed to the inner radii, the values are corrected with the values obtained from the outer radii previously calculated. The advantage of this algorithm is the simplicity of the calculation. However, the algorithm inherently accumulates the error during each calculation. This implies that the void fraction values obtained for the centre of the pipe could have a significant error in certain cases.

An Abel Inversion technique can also convert the radial component of the void fraction from the lateral void fraction profiles.[56] In the present version of the Abel Inversion technique, we assume that the geometry of the object is symmetrical in a cylindrical coordinate system as precisely the case in two-phase pipe flow. Knowledge of the radius of the pipe and inverting the lateral (x) void fraction obtains the void fraction in the radial (r) direction as follows:

$$\alpha(r) = -\frac{1}{\pi}\int_{r}^{R} \frac{\alpha(x)x}{\sqrt{x^2-r^2}}\,dx \tag{4.8}$$

By analyzing the profiles at each axial location, a 2D (two-dimensional) contour map of the void fraction can be generated for each image. Successive analysis results in temporal 2D contour images.

The bubble diameter is measured using the image processing system by examining the width of the void fraction profiles in the lateral(x) and axial(z) coordinates. The interfacial area for bubble flow is calculated using Equation 1.6 with the cross-sectional averaged void fraction and the average bubble diameter.

The bubble velocity is calculated using frame by frame analysis of the void fraction axial profiles.

4.2 Calibration of RTNR System

Several experiments are performed to calibrate the Real-Time Neutron Radiography System for void fraction measurement. The first set of experiments uses rectangular channels of known thickness and of various materials. The measured intensity is related to the thickness of the material to generate a calibration curve as shown in Figure 4.3.

Several materials were investigated using the RTNR system for determination of their material cross-sections. Pure substances of Aluminium, Copper, and Lead, and also compound substances such as steel, Lucite, and water were placed in the neutron beam path with various thicknesses. Enough material for water was examined to ensure build-up effects were significant.

Figure 4.3 shows the experimental data obtained for the determination of the material cross-sections. Figure (4.3) relates the non-dimensional neutron intensity to the attenuating thickness for materials of Aluminium(Al), Copper(Cu), Lead(Pb), Steel (St), Acrylic Resin (Lu) and water(H_2O). The non-dimensional intensity is related to the transmitted neutron intensity by Equation 4.9 below;

$$A(y)=\frac{GI(y)-GI_D}{GI_o-GI_D} \tag{4.9}$$

,where G is the gain factor for the image processing software and the RTNR camera target. I(y) is the transmitted neutron intensity for a thickness y. I_D is the dark current noise associated with the RTNR camera target, i.e. the output intensity of the camera when no neutrons are incident to the camera screen. I_o is the intensity

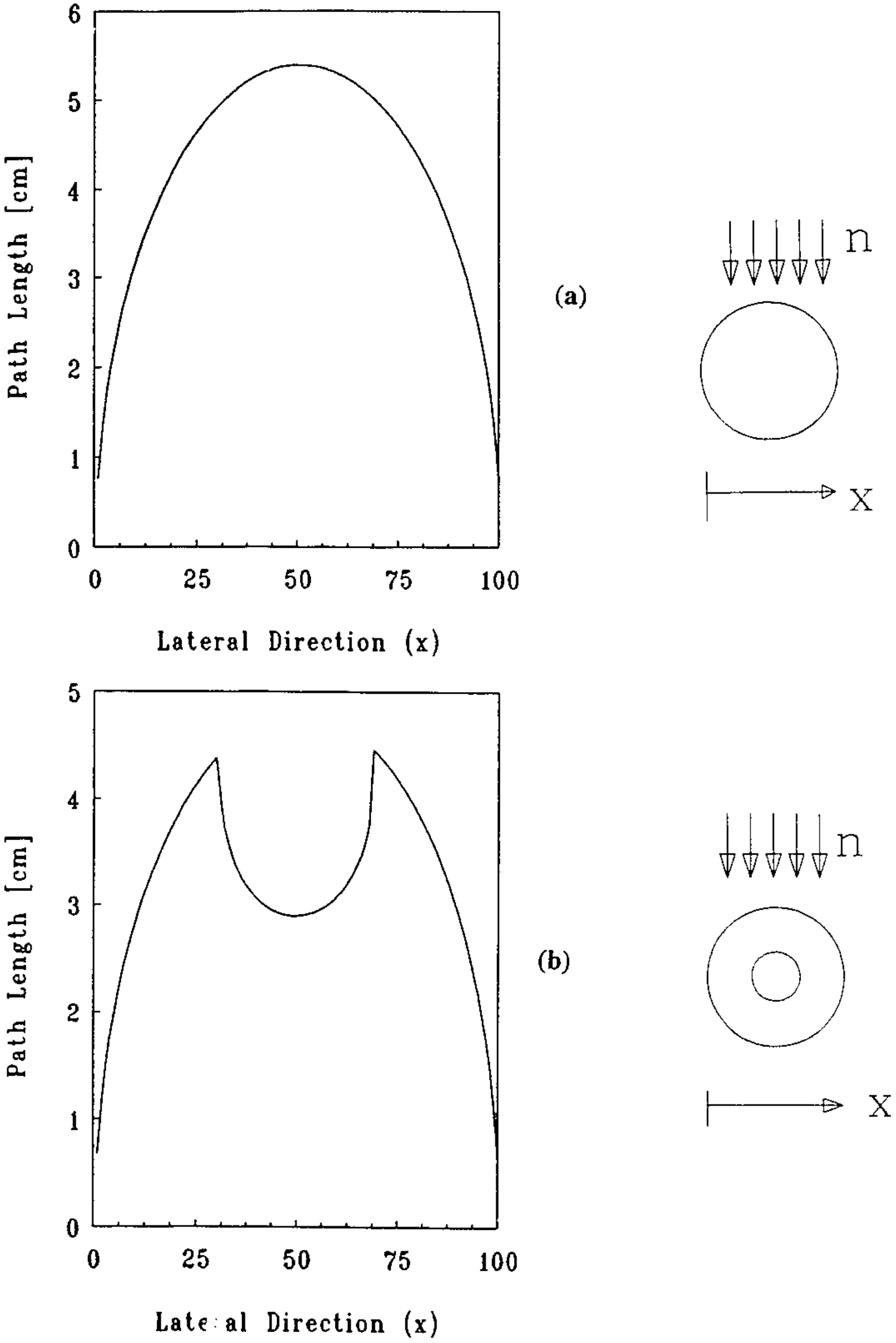

Figure 4.1: Chordal Path Lengths (a) Pipe Flow Channel 5.4 cm I.D.(b) Annulus Flow Channel 4.8 cm O.D., 1.9 cm I.D.

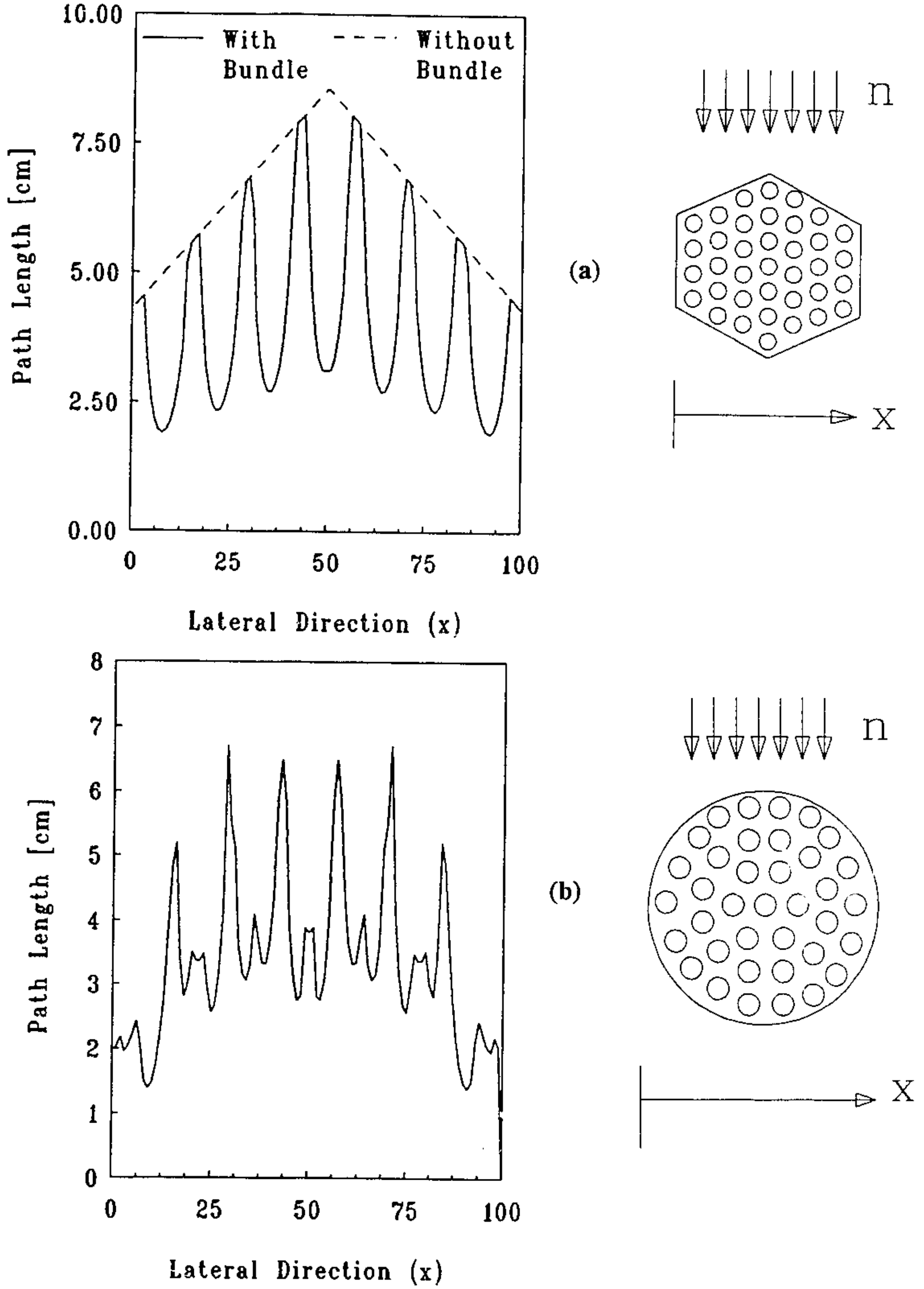

Figure 4.2: Chordal Path Lengths (a) CANDU Nuclear Fuel Flow Channel (b) MAPLE Nuclear Fuel Flow Channel

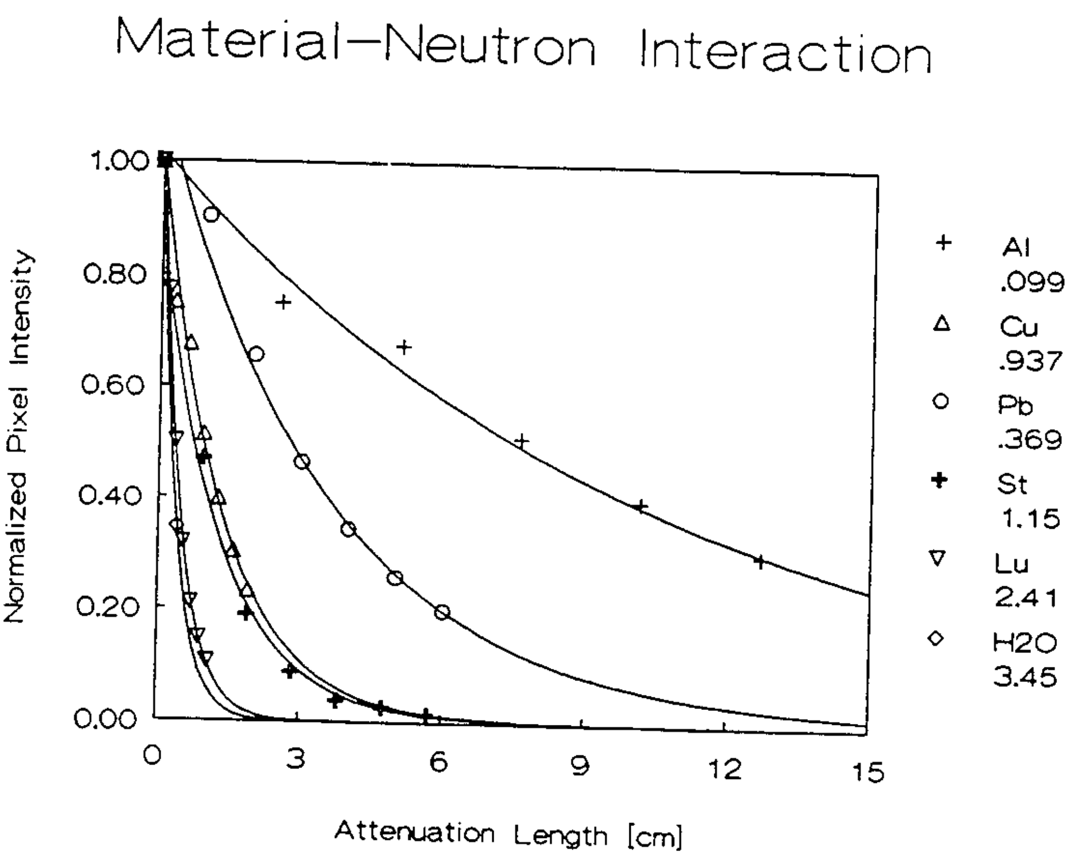

Figure 4.3: Neutron Attenuation Characteristics for Various Materials Imaged by the Real-Time Neutron Radiography System

of the incident neutron beam, i.e. the output intensity when a full neutron beam is incident on the camera system.

It has been observed that Aluminium and Lead have relatively poor neutron attenuating capabilities whereas materials such as Copper, Lucite, and water have strong neutron attenuation capabilities.

Essentially, these materials are fairly efficient at scattering thermal neutrons. Acrylic resin and water have high neutron scattering capabilities due to the presence of large amounts of Hydrogen.

Another experimental calibration approach uses the known neutron path length at each point across the flow channel. This approach produces a similar calibration relationship between the pixel intensity and the liquid thickness as shown in Figure 4.4.

The attenuating length can also be non-dimensionalized by multiplying the path length by the appropriate thermal neutron cross-section. All of the experimental data then collapses to one relationship with a small error possibly due to scattering phenomena. The slope of this curve represents the linear relationship between the neutron flux and the optical intensity produced by the camera and image processing system. Modifications to the camera or the software such as gain factors, changes in the neutron to photon converter screens, and dynamic range adjustments will affect the slope of this calibration curve. As such, a new calibration is required when any of these factors are changed.

Known thicknesses of light water and heavy water are used to calibrate the RTNR system. The results show the neutron flux exponentially decreases with increasing water thickness according to theory[57]. When the neutron flux has been attenuated from $10^6 (n)/(cm^2\text{-}s)$ to $10^4 (n)/(cm^2\text{-}s)$, the camera no longer responds linearly with the neutron flux in real-time. From the calibration study, it was found that the light water thickness was approximately 1.0 cm when the relationship between the neutron flux and the camera response changed from linear to non-linear. Thus, for increasing water thicknesses beyond 1.0 cm, the accuracy of measurement decreases. Two calibration curves are developed for the linear and non-linear regions as shown in Equations 4.10 and 4.11 respectively;

$$\frac{I(x,y,z)}{I(x,0,z)} = e^{-\beta \Sigma_t y} \tag{4.10}$$

$$\frac{I(x,y,z)}{I(x,0,z)} = 0.2568 \left(\Sigma_t y\right)^{-.3795} \tag{4.11}$$

,where Σ_t is the thermal neutron cross-section of the fluid, I(x,y,z) is the pixel intensity in the image at pixel location (x,z), $\beta = 0.5993$ is the RTNR system calibration constant, and y is the thickness of the fluid. The calibration curves are shown in Figure 4.4.

The lateral void fraction is then determined from the calculated water thickness (x_{RTNR}) and the known maximum water thickness (x_{Max}) as shown in Equation 4.12.

$$\bar{\alpha}(x,z) = 1.0 - \frac{x_{RTNR}}{x_{Max}} \tag{4.12}$$

For void fraction calibration, all results are static test cases. As such, the analysis does not include the motion effect. The error produced by motion depends on bubble size and bubble velocity and is only significant if the bubble velocity exceeds the velocity limitation imposed by the bubble size and exposure time. For example, a 10.0 cm bubble with a 33.0 ms exposure time will produce a significant error if the bubble velocity is greater than 10.0 cm/33.0 ms = 3.03 m/s. Here, the 10.0 cm bubble will have moved one full diameter and the void fractions obtained at the bubble location would not truly represent the bubble. In a time averaged sense, the void fraction is still correct.

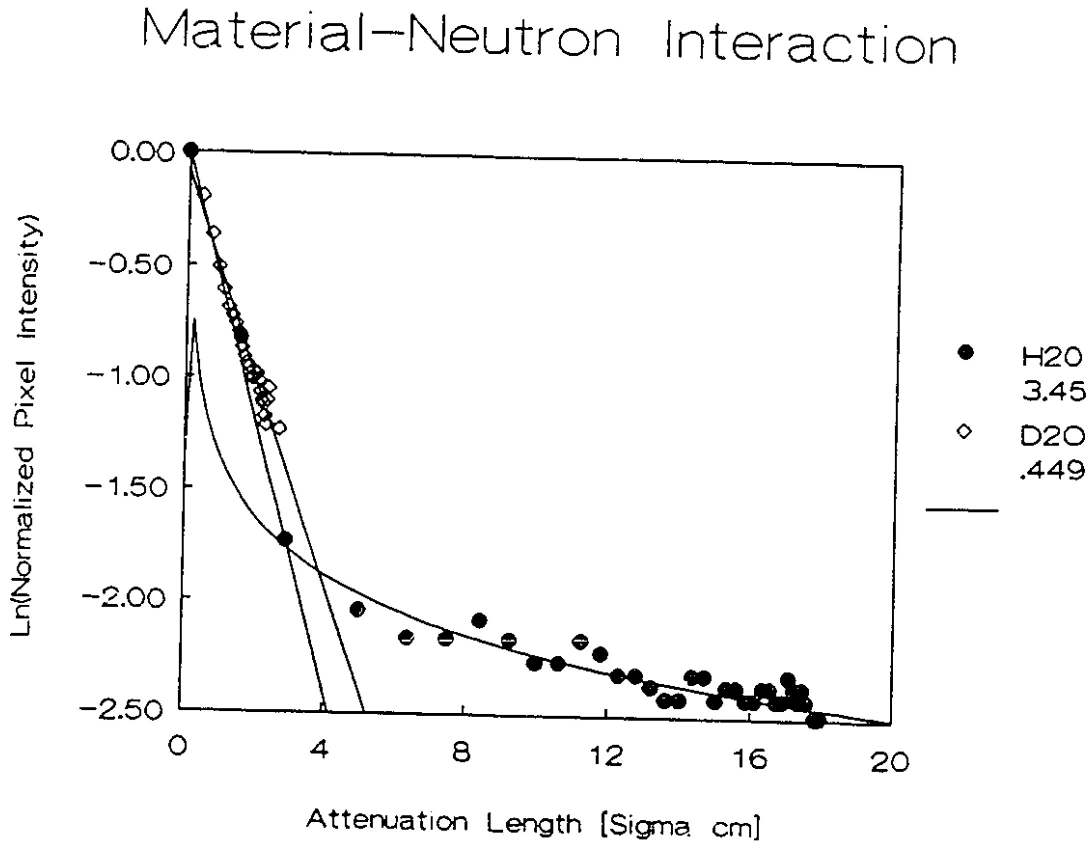

Figure 4.4: Calibration Curve for H_2O and D_2O for the Real-Time Neutron Radiography System

4.3 Image Analysis Techniques: Approaches and Software

Due to various limitations of the commercial software, specifically, the poor capability of customizing image processing routines for specific applications, customized software was written in a variety of language forms.

4.3.1 Image Correction and Enhancement

The image processing system allows for some key image manipulation such as frame averaging, filtering, image subtraction, and contrast imaging. The ability to average many frames and to pass the images through various filters greatly reduces the noise associated with the radiographic images. Work performed by Fujine et al.[58] shows in great detail the effects of frame averaging and image subtraction. Contrast imaging allows for the enhancement of the image to aid in visualizing either very weak or very strong attenuating materials. By combining these image processing features in the correct manner, it is possible to visualize various two-phase flow pattern fluid density maps.

The clarity and definition of the resultant image depends very much upon the methods of enhancement, the size of the test apparatus, and the neutron flux incident upon the neutron to photon converter. The effect of the enhancement techniques is to favour certain intensity ranges over others resulting in clearer imaging of certain ranges of material density. The size of the test apparatus affects the flux incident upon the neutron to photon converter. If thick material is present, the neutron flux will be significantly attenuated resulting in poor contrast in the final image. Altering the strength of the neutron beam can increase the image contrast depending upon the geometry and size of the test apparatus.

An original image produced by the Real-Time Neutron Radiography system is shown in Figure 4.5. Figure 4.5 shows an RTNR image of the annulus flow channel with no gas flow rate. The white region in the centre of the image is the gas inside the annulus flow channel and the black region immediately below is water. The two black regions to either side are boronated neutron shields manufactured from rubber doped with Boron. A time clock is shown in the upper left region of the image. The annulus flow channel is brightest in the centre of the image and gradually becomes darker closer to the edge of the image. This variation in intensity is due to target integration effects. A vertical line profile of the pixel intensity along the annulus centreline is shown immediately below the image where pixel 0 corresponds to the top of the image and pixel 479 corresponds to the bottom of the image. The intensity variation can clearly be seen. Below the line profile is a histogram of the annulus flow channel. The annulus flow channel is seen to occupy only a narrow range of the gray levels. As the left edge of the screen is too low in intensity, the frame grabber board cannot use the full range of gray levels for the annulus flow channel.

The image produced by the camera is offset by a background signal. This offset needs to be removed to ensure the image dynamic range can be enhanced. The software routine "TISUBT" removes the offset through subtracting a background image obtained when the RTNR system is on but no neutron beam is present. Once the offset is removed, the target integration and camera gain effects are removed using the software routine "TICORR". This routine uses an image obtained when a full neutron beam is applied to the camera and division operations to correct the non-linearity in the image.

Figure 4.6 shows the image shown in Figure 4.5 after image enhancement has been performed. The central region of the image no longer varies significantly in intensity although some non-linearity effects remain at the extreme edges of the image. The line profile is much flatter than shown in Figure 4.5, but the noise level has increased slightly. The histogram is now expanded and provides a better representation of the image.

For determination of the flow regime, the corrected images are analyzed by the IPPLUS software where contrast enhancement and image subtraction are performed.

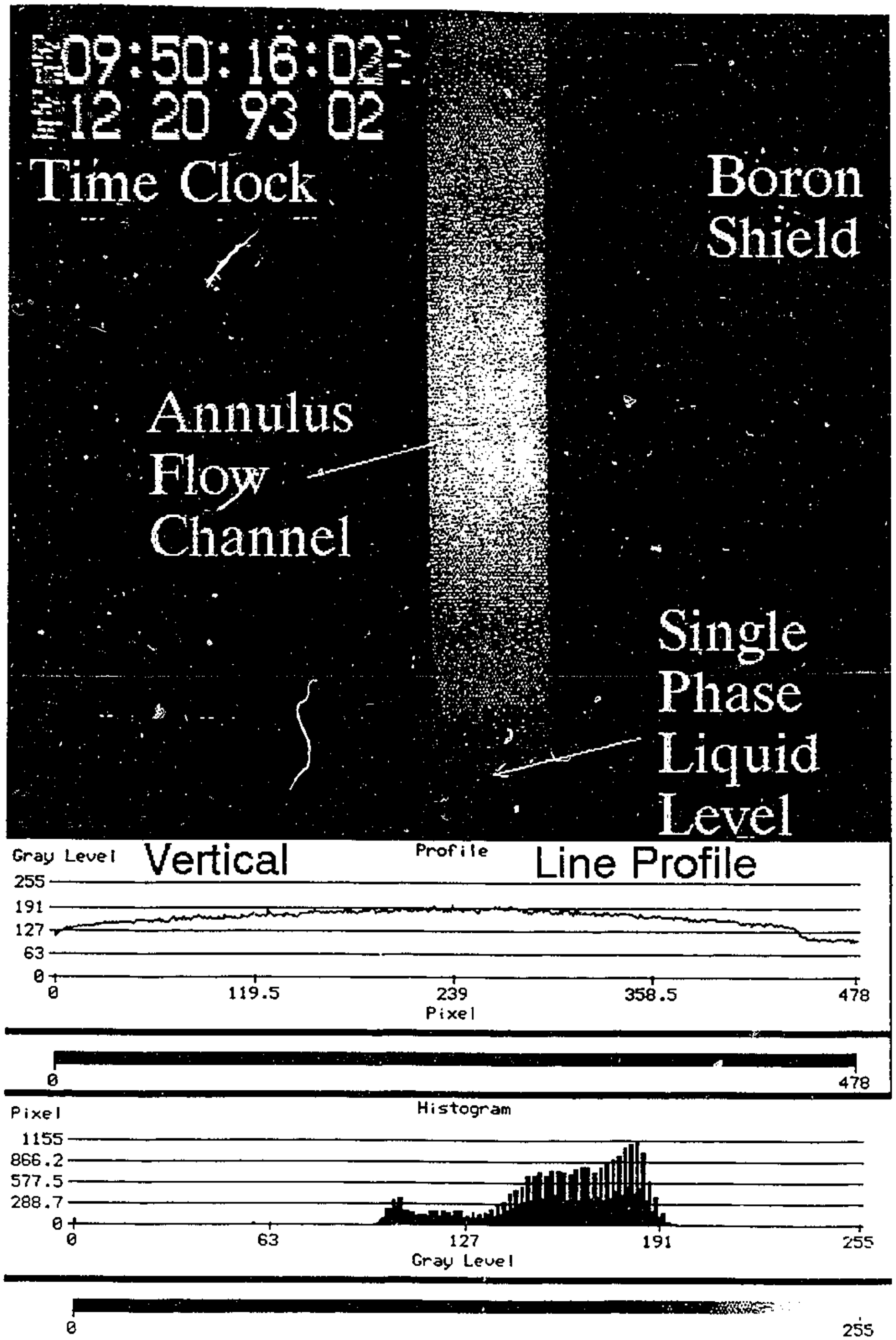

Figure 4.5: A Typical Original Image Obtained by the Real-Time Neutron Radiography System with a Vertical Line Profile Along the Centre Axis of the Annulus Flow Channel and a Histogram of the Annulus Flow Channel

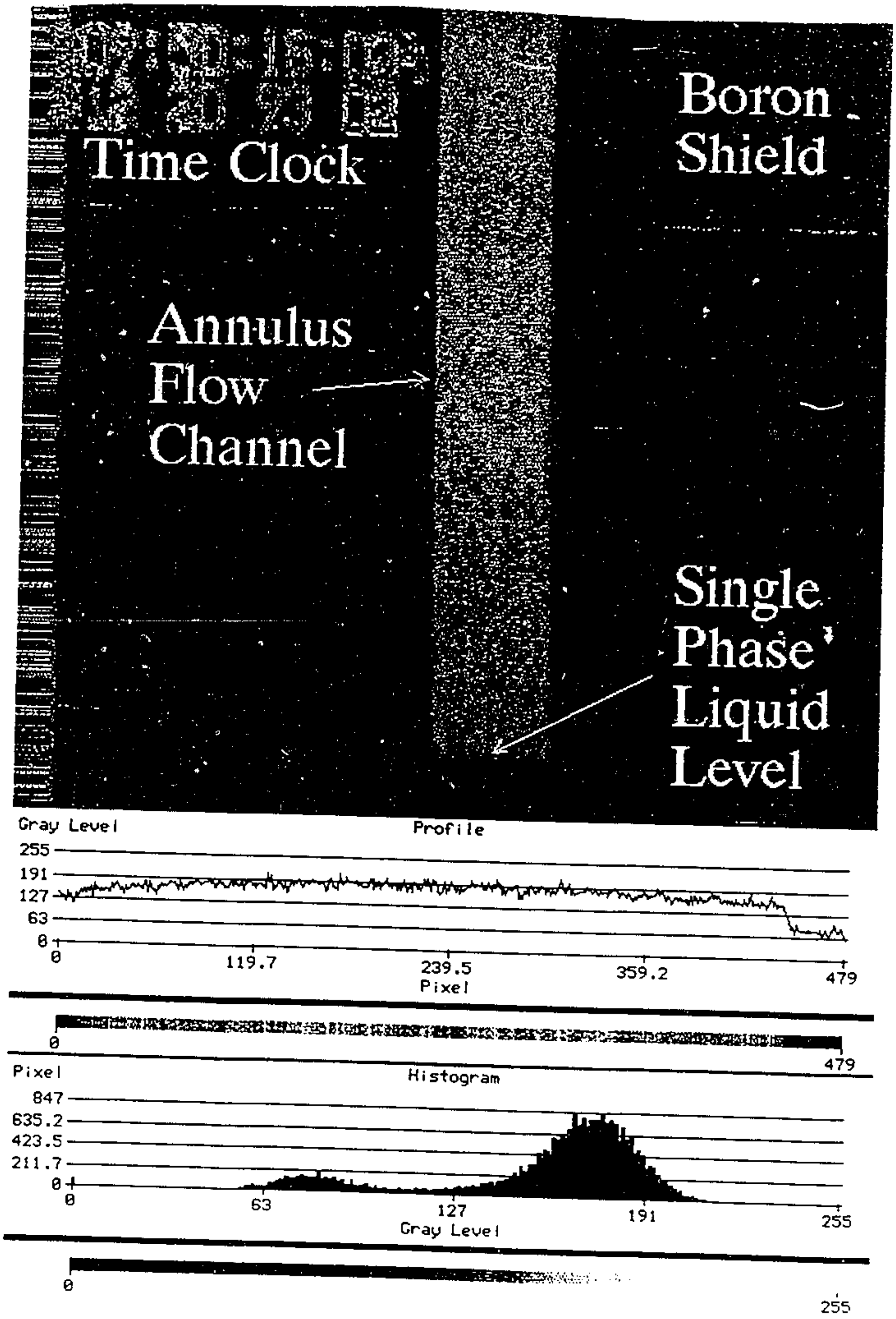

Figure 4.6: An Enhanced Image using Customized Software Routines with the equivalent Vertical Line Profile and Histogram of Figure 4.5

4.3.2 Two-Phase Image Analysis

For determination of two-phase flow parameters, customized software has been developed. Two-phase flow analysis of the images follows the flow chart shown in Figure 4.7. First, the images are enhanced and corrected as previously mentioned. Then the software routine "LINEPROFILE" is used to obtain the intensity values for each pixel into a data file for calibration. Once the calibration curve is obtained, the software routine "VOIDRTNR" is used to calculate the chordal, radial, and cross-sectional averaged void fractions for the flow channel.

Each type of void fraction is saved to a different data file for analysis. The cross-sectional averaged void fraction is plotted as a function of the axial coordinate (z). By examining the data sets of several images, we can obtain the cross-sectional averaged void fraction as a function of time. The Abel inversion technique is used to obtain the radial void fraction and is stored as a function of the axial coordinate. Contour maps can then be produced.

4.4 Theory of X-ray CT Scanner Operation and Reconstruction

The principle of an X-ray CT system is the material dependence of X-ray attenuation in the imaging plane.

X-ray computed tomography uses the attenuated X-ray beams measured by a series of detectors in a cross-sectional plane of the flow area. The data collected by these detectors is called projection data. A complete set of projection data is obtained either by rotating an X-ray source or by using more than one X-ray source to cover an angle greater than 180°.

Various reconstruction techniques exist for modern applications of tomography. Two main classes of reconstruction techniques are used today; they are the iterative reconstruction techniques and the analytical reconstruction techniques[59].

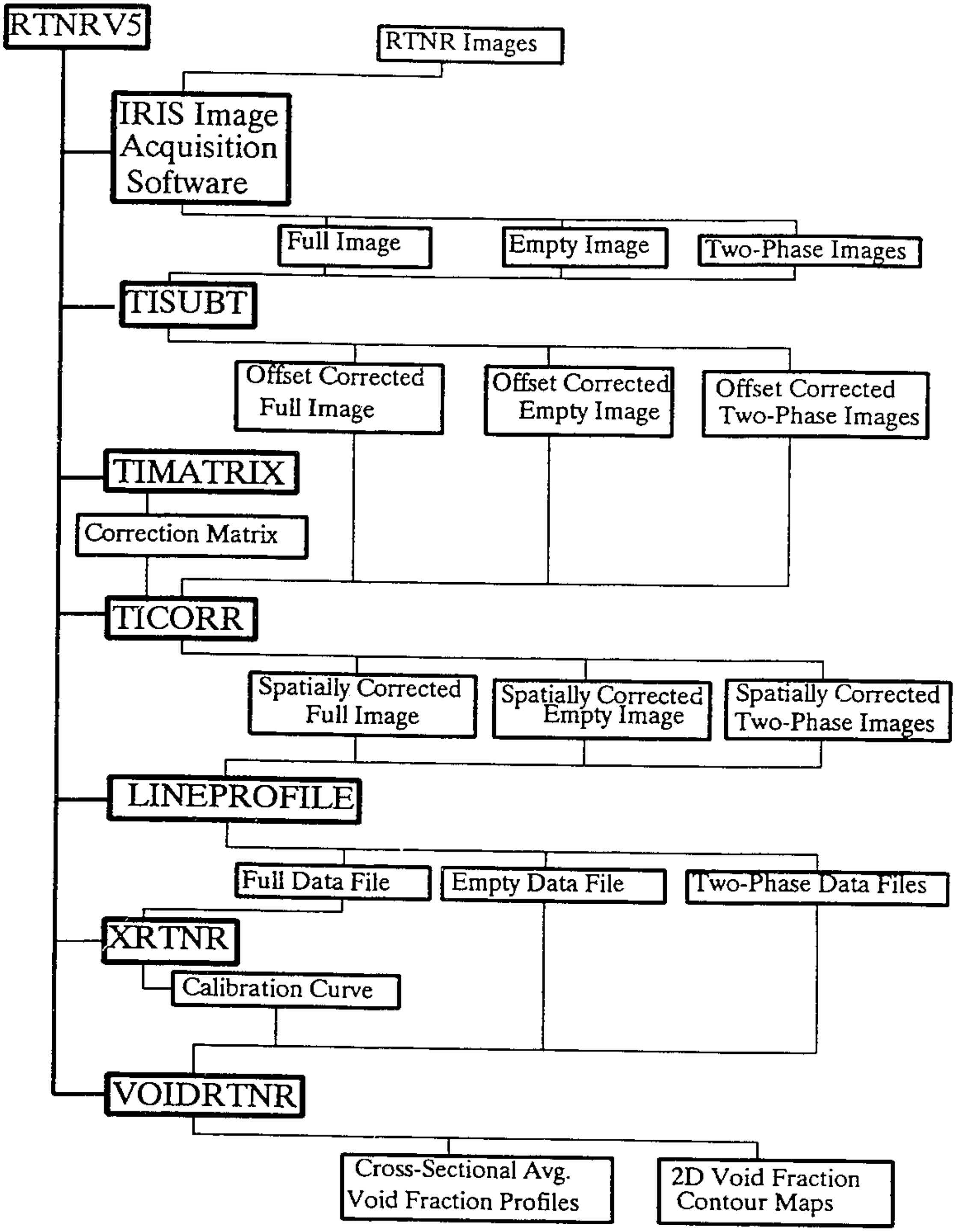

Figure 4.7: Flowchart of Software Routines for Two-Phase Flow Analysis by the Real-Time Neutron Radiography System

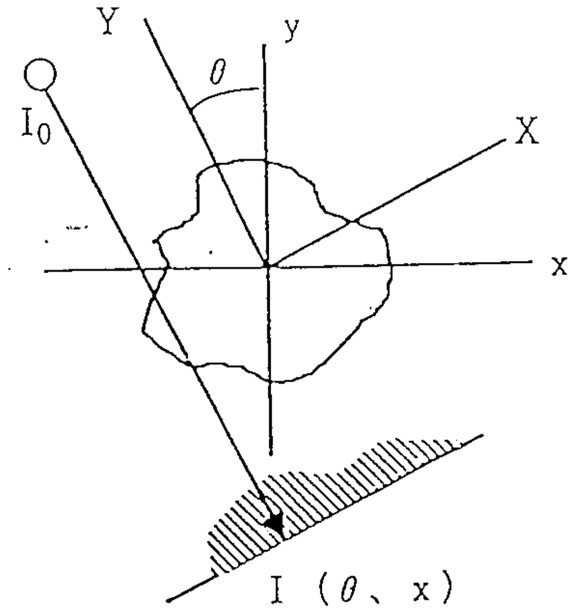

Figure 4.8: Reconstruction Algorithm Geometry for the High Speed X-ray CT System: Description of Coordinate Systems for Reconstruction

Iterative reconstruction techniques use successive approximations from an arbitrary initial image until satisfactory agreement with the projection data is obtained. This technique is usually more time consuming than analytical techniques and can be dependent on the choice of initial image data but does provide good reconstruction of the image.

Analytical methods use exact formulations as opposed to approximations in the reconstruction process. The High Speed X-ray CT system currently uses the two-dimensional Fourier transform technique as discussed below considering an object as shown in Figure 4.8.

The projection data represents the integrated attenuation of the X-ray beam by all the material present in the beam path between the source and the detector as shown in Equation 4.13 below;

$$I(\theta,X) = I_o \exp(-\int_{L_y} \mu(x,y)\, dY) \tag{4.13}$$

,where x and y are the Cartesian coordinates of the image plane, θ is the angle between the X-ray beam path and the y-axis in the Cartesian plane, μ(x,y) is the X-ray attenuation coefficient for the material at the coordinates (x,y) along the beam path also called the density function f(x,y), and I_o is the incident X-ray beam strength.

As the nature of the radiation interaction with matter is exponentially dependent on the material thickness, a ray projection function can be described as follows;

$$p(\theta,X) = -\ln\left(\frac{I(\theta,X)}{I_o}\right) = \int_{L_y} \mu(x,y)\, dY \tag{4.14}$$

The incident X-ray intensity can be determined by measuring the projection data for the case where no object is in the imaging plane or for two-phase flow, by measuring either an empty flow channel or a full flow channel. Measuring the incident intensity with an object in the imaging area is only practical when this object is common (stationary) to all images. Evaluation of the cross-sectional data at each point can then be evaluated as follows;

$$
\begin{aligned}
p_m(\theta,X)-p_b(\theta,X) &= -\ln\left(\frac{I_m(\theta,X)}{I_o}\right)+\ln\left(\frac{I_b(\theta,X)}{I_o}\right) \\
&= -\ln\left(I_m(\theta,X)\right)+\ln\left(I_b(\theta,X)\right) \\
&= \int_{L_y}\left(\mu_m(x,y)-\mu_b(x,y)\right)dY \\
&= \int_{L_y}\Delta\mu(x,y)\,dY
\end{aligned}
\tag{4.15}
$$

,where m signifies the measured projection for the object of interest and b signifies the base projection or the incident intensity.

A two-dimensional Fourier Transform represents the density function as follows;

$$
\begin{aligned}
f(x,y) &= \mu(x,y) \\
&= {}^2F^{-1}[f(u,v)]\int_0^{\pi}1F_w^{-1}[{}^1F_x[p(\theta,X)]\,|W|]\,d\theta \\
&= \int_o^{\pi}p(\theta,X)*\psi(X)\,d\theta
\end{aligned}
\tag{4.16}
$$

,where F denotes the Fourier transform, 1 refers to one-dimensional, 2 refers to two-dimensional, and ω is the filter function expressed as follows;

$$
|\omega| = {}^1F_x[\psi(X)] \tag{4.17}
$$

The Fourier transform is expressed as follows;

$$
f(\omega) = {}^1F[f(X)] = \int_{-\infty}^{\infty}f(X)e^{-2\pi i\omega x}dx \tag{4.18}
$$

$$f(x) = {}^{1}F^{-1}[f(\omega)] = \int_{-\infty}^{\infty} f(\omega)\, e^{2\pi i \omega x} d\omega \tag{4.19}$$

Combining the Fourier transform and the inverse Fourier transform, we can obtain the density function as follows;

$$f(x,y) = {}^{2}F^{-1}[f(u,v)] = \int_{-\infty}^{\infty}\int_{-\infty}^{\infty} f(u,v)\, e^{2\pi i(ux - vy)} dudv \tag{4.20}$$

,where u and v are the coordinates for the Fourier space.

Using these equations with knowledge of the X-ray source and detector geometry, it is possible to reconstruct a two-dimensional image of the cross-sectional plane occupied by the X-ray beams.

Additional software is used to convert the reconstructed images into binary images with a known threshold level. The binary image represents a void fraction distribution in the imaging plane. Summing the area occupied by the gas phase and dividing by the total area produces the cross-sectional averaged void fraction. Successive images can be used for three-dimensional reconstruction and interfacial area calculations.

Chapter 5

5. Pipe Flow Studies

As previously mentioned, two different experimental apparatus have been studied for measurement of two-phase flow parameters in pipe flow channels. The experiments are analyzed to determine the flow regime, cross-sectional averaged void fraction, void fraction distribution, bubble diameter, and interfacial area density.

5.1 Visualization of Two-Phase Pipe Flow

The first experiment involves the natural circulation flow loop. Comparison is made between the RTNR system (metal walls), a standard video system (glass walls), and an ultrasonic system (metal walls) for two-phase flow visualization. Image processing is used to enhance the detail of the RTNR images for analysis.

Figure 5.1 shows typical real time neutron radiographs obtained from two-phase flow in a natural circulation loop after correction for spatial non-uniformity due to integration across the camera target. These particular images represent the natural circulation loop with (a) the loop empty, (b) the loop half full with heavy water (D_2O), and (c) the passage of a liquid slug. It can be seen from the images that the resolution in the radial direction is poor across the test section due to the small diameter of the test section(only 15 pixels).

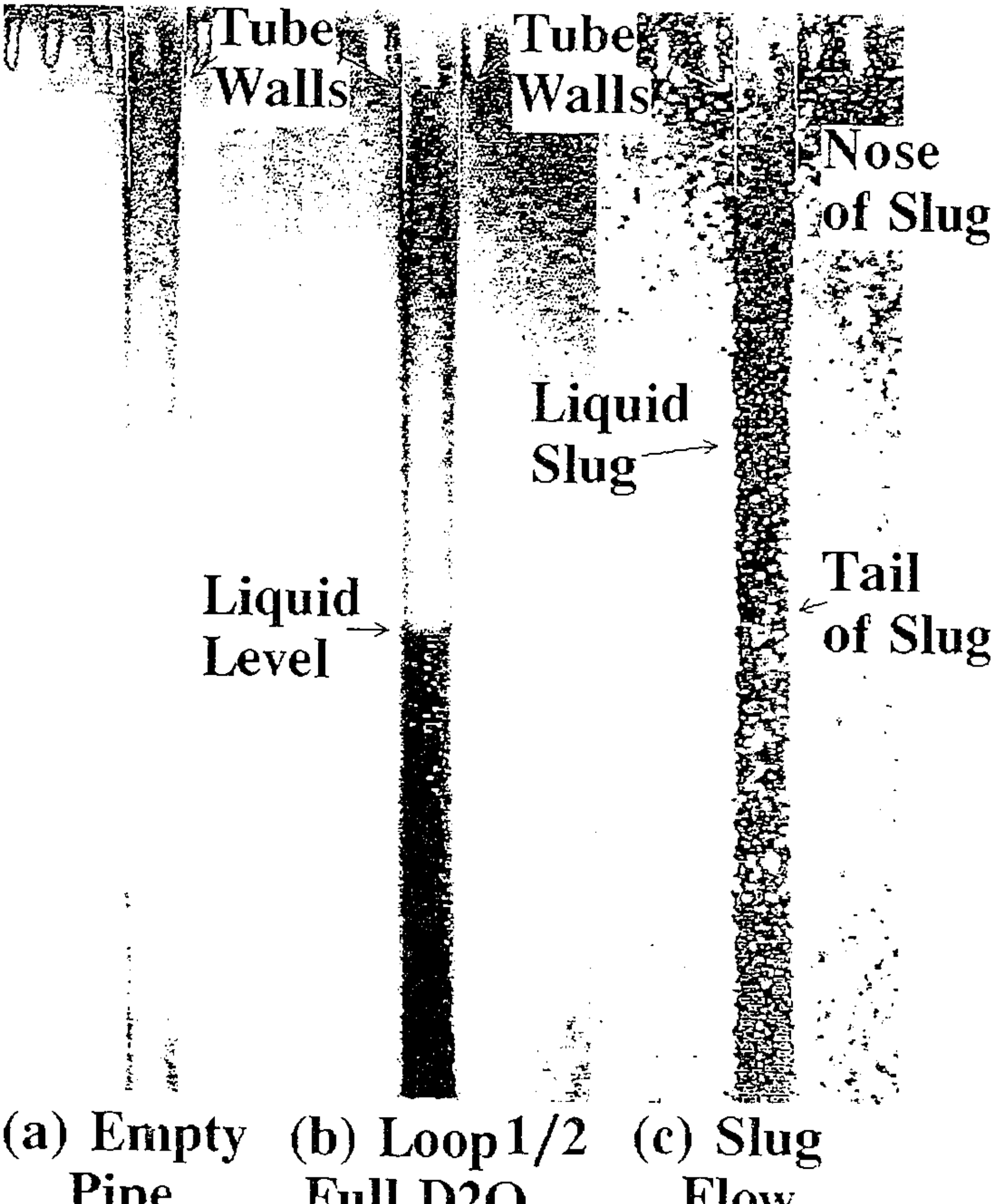

Figure 5.1: RTNR Images of Two-Phase Flow in a Natural Circulation Flow Channel: 1.0 cm ID, (a) Empty Channel, (b) Loop Half Filled with Heavy Water, (c) Typical Slug Flow

As stated earlier, the RTNR images need to be processed to reduce the noise and the effect of the background. To remove the background, an averaged image of the steel pipe completely filled with heavy water was used. The averaging removed the noise from the background image. Since the foreground image of the bubble consists of a single frame, the noise remaining in the subtracted image is still significant. To further reduce the noise a low pass convolution filter was applied to the subtracted image. A 1x7 vertical filter was used. First, the background noise variation was determined. Then all pixels with an intensity value below one standard deviation in the background noise level were changed to white (gray-scale value of 255). All those pixels with an intensity greater than one standard deviation were given an intensity of 0. This removes almost all the remaining noise in the image. Finally, a Roberts edge detection filter converts the image into the edge contour shown in Figure 5.2. Structure in the intensity map suggests the slug of air consists of several coalesced cap-shaped bubbles. This type of structure is often observed in the glass test section experiments and also in the ultrasonic results.

Ultrasonic techniques can be used to show the presence of bubbles and the distance from the wall to the bubble edge, i.e. film thickness. Only one edge of the bubble can be observed unless multiple transducers are used. Figure 5.3 shows a typical profile obtained by a single beam ultrasonic method.

For a low gas flow rate (<0.042 m/s, Re_g = 268) injected into the rig, small bubbles will be generated. Because of the mixer design and small diameter tube, dispersed bubbly flow does not exist. As the flow rate is increased, the bubbles begin to coalesce (0.064-0.127 m/s). Taylor bubbles or slug flow appears at air flow rates of about 0.212 m/s(Re_g = 135.3). This flow regime is relatively narrow and leads to a wide slug-churn transition. Above 2.12 m/s (Re_g= 135.3) the flow becomes annular. Figure 5.4 shows the flow regimes observed in terms of the inlet superficial gas velocity and the induced liquid superficial velocity. The results are compared with the flow regime map of Mishima and Ishii[60].

Although the current results were obtained for a natural circulation loop as opposed to a forced convection system, they are in good agreement with theoretical

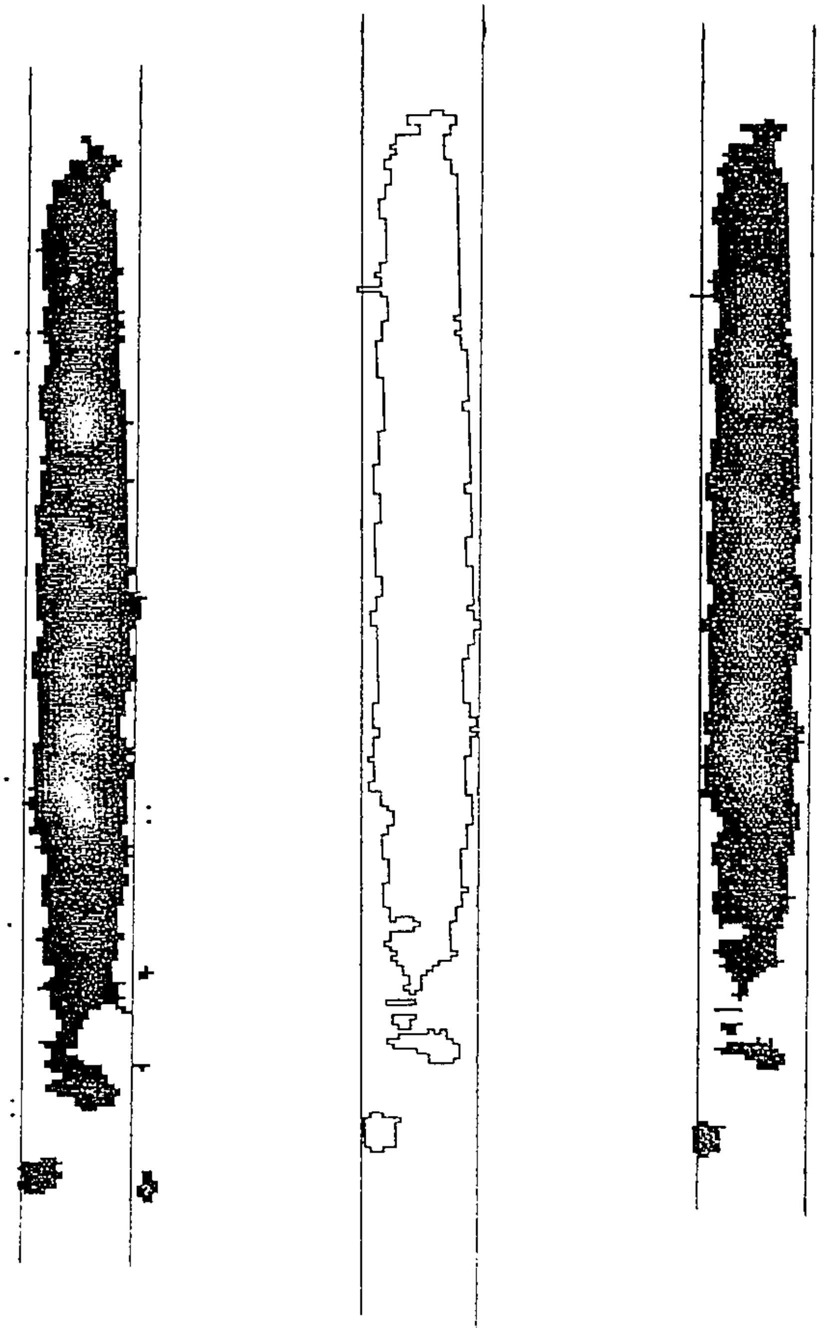

PROCESSED IMAGE

EDGE CONTOUR

CONTOURED IMAGE

Figure 5.2: RTNR Image of a Taylor Bubble after Image Processing

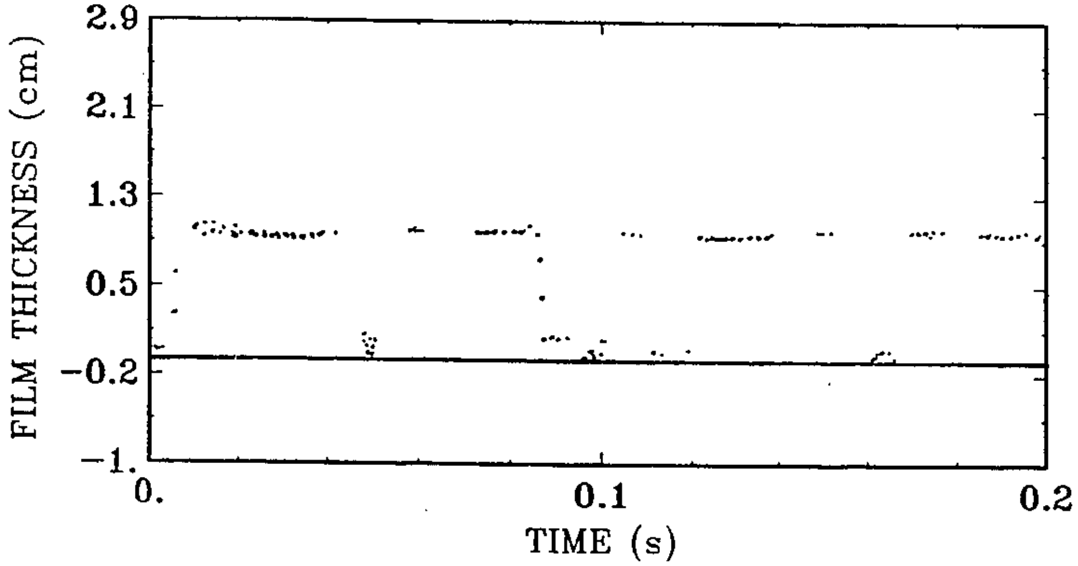

Figure 5.3: Ultrasonic Interface Measurement for Slug Flow; F-Full, E-Empty

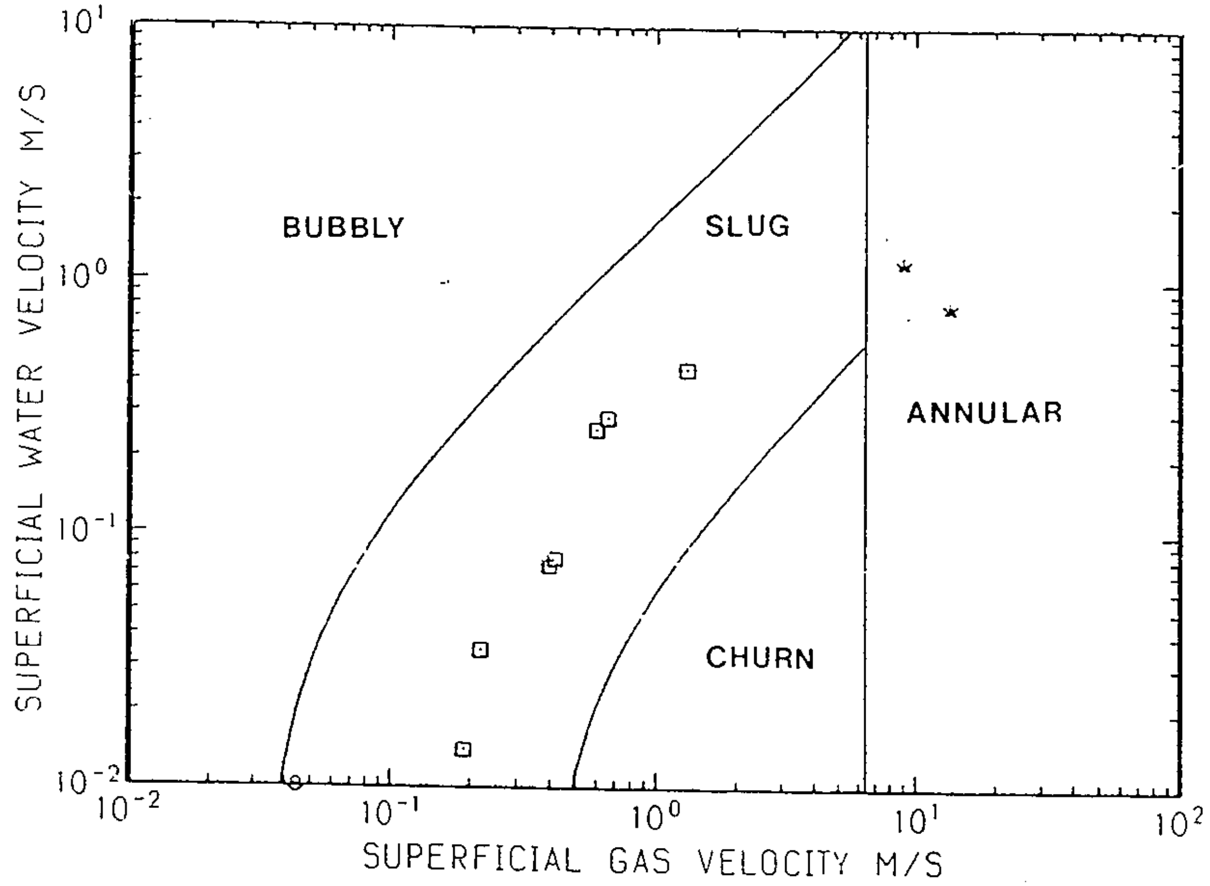

Figure 5.4: Flow Regime Map;(———) Mishima and Ishii's Map[60],(○) Experimental Slug Flow, (△) Experimental Churn Flow,(□) Experimental Annular Flow

predictions.

Figures 5.5a to 5.5d are radiographic images obtained using the RTNR system where Figures 5.5a and 5.5b show images of empty and static liquid level before gas injection respectively, and Figures 5.5c and 5.5d show images acquired during gas injection with different gas flow rates. Figure 5.5c shows an image for a moderate flow of 0.010 m/s ($Re_g=34.4$) depicting a quiescent system with a steady interface. Figure 5.5d results when the gas velocity is increased to 0.016 m/s ($Re_g=55.1$). The slight increase in gas velocity in this region has generated two distinct low and high void regions in a bubble column.[61] Although the smaller high void region is only noted when low water inventories are present, it is surmised that the high void region will always exist if large enough flow rates are injected into the bubble column. The high void region is noted to have visible bubbles without image enhancement techniques and recirculating flow. The low to high void region interface is clearly visible as indicated in Figure 5.5d. Agglomeration of bubbles is noted to occur in the high void region and bubble velocity is observed to be higher in the channel center than at the pipe walls. Bubbles near the wall are seen to move more slowly and even reverse direction.

5.2 Measurement of Cross-Sectional Averaged Void Fraction

The growth of the high void region in the bubble column is clearly seen in Figure 5.6 where the locations of the gas-high void and low-high void region interface are shown as a function of the superficial gas velocity. The high void region grows at a very slow rate to a certain gas velocity, at which time the high void region is enlarged dramatically. As the high void region develops, the bubble coalescence rate increases in the high void region due to a greater collision frequency and larger bubbles can be seen.

Axial time and cross-sectional averaged void fraction profiles is shown in Figure 5.7 for various gas flow velocities at an initial liquid level of L_0 = 31.07 cm. Figure 5.7 shows that while the time averaged liquid level increases with increasing

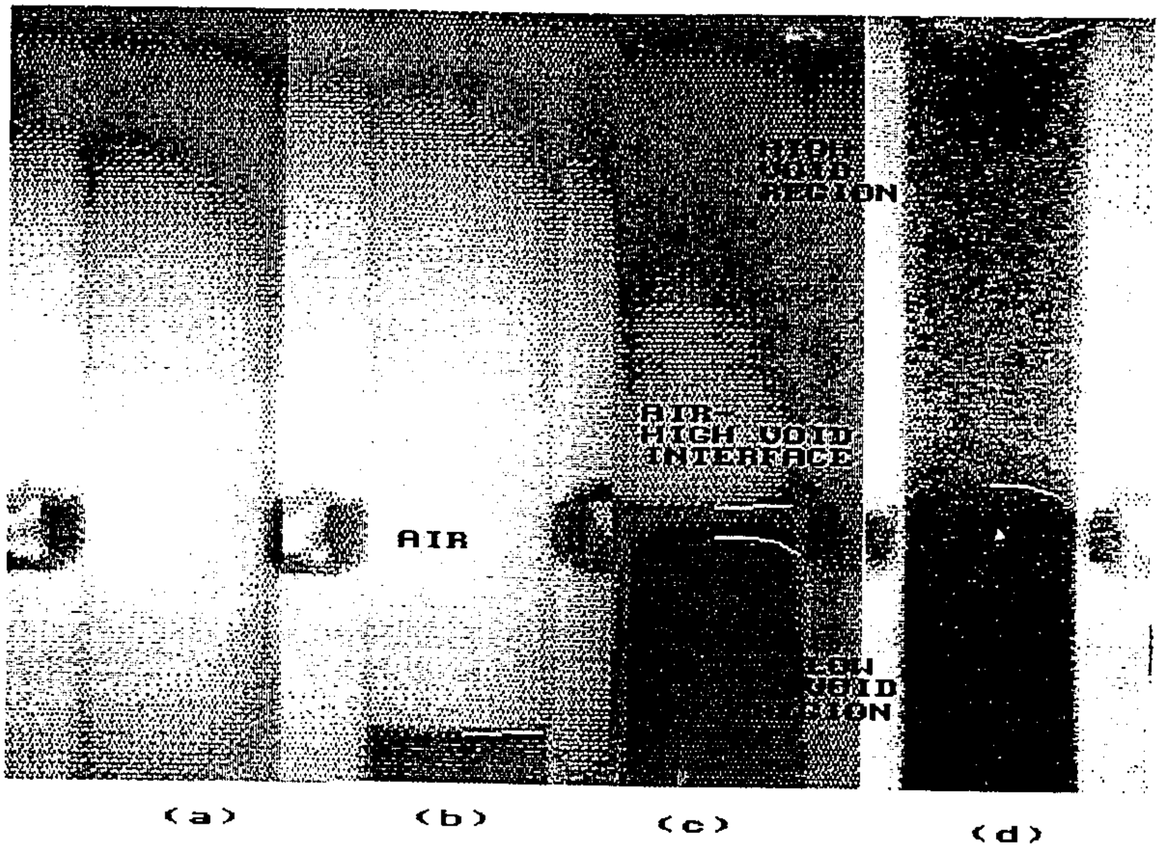

Figure 5.5: Real-Time Neutron Radiographs of a 5.4 cm ID Bubble Column: (a) Empty;(b) Liquid Level before Gas Flow;(c) U_g = 0.01 m/s;(d) Developed Low-High Void Region, U_{gs} = 0.016 m/s

superficial gas velocity, the void fraction decreases below superficial gas velocities of $U_{gs} \leq 0.015$ m/s ($Re_g = 51.7$) as have been observed by various researchers[44,45]. However, Figure 5.7 also shows more quantitatively that two distinct void regions exist above a superficial gas velocity of $U_{gs} \geq 0.015$ m/s as described before. In the low void region ($\alpha_g \leq 0.1$), the axial void profile is relatively uniform until a sudden stepwise change in void fraction separates the low and high void region. In the high void region, the axial void profile is again relatively uniform and independent of superficial gas velocity, e.g. $\alpha_g \approx 0.3$ for the experimental conditions in Figure 5.7. The stepwise void fraction change which separates the low and high void region may be due to the motion of rapidly moving bubbles from near wall to tube center (or vice versa) created by recirculating flow phenomena. This distinct void region also depends significantly on the initial liquid level as expected from the recirculation of flow in the bubble column. The presence of a high void region suggests the development of foam flow in the bubble column. Observations from the top of the bubble column indicate a large degree of bubble packing at the surface, yet these observations do not clearly indicate the presence of foam flow. Thus, the determination of the high void region as foam flow needs to be verified.

Volume averaged void fraction or liquid hold-up of a bubble column is usually determined from the time averaged liquid level measurement. The initial liquid level without flow and the liquid level with flow are measured with the RTNR system and used to calculate the volume averaged void fraction. The volume averaged void fraction can also be obtained by integrating the cross-sectional averaged void fraction profile along the axis.

The volume and time averaged void fraction determined from the RTNR measured liquid level, and the RTNR measured cross-sectional averaged void fraction profiles are shown in Figure 5.8. Figure 5.8 also shows that the RTNR method agrees well with the ultrasonically determined results obtained by Chang and Morala [28] at Z = 25 cm except where $U_{gs} \geq 0.015$ m/s (Re_g=51.7). Relatively good agreement between both methods is obtained, where the discrepancy in the higher void fraction condition may be due to the effect of the mixing section for the liquid

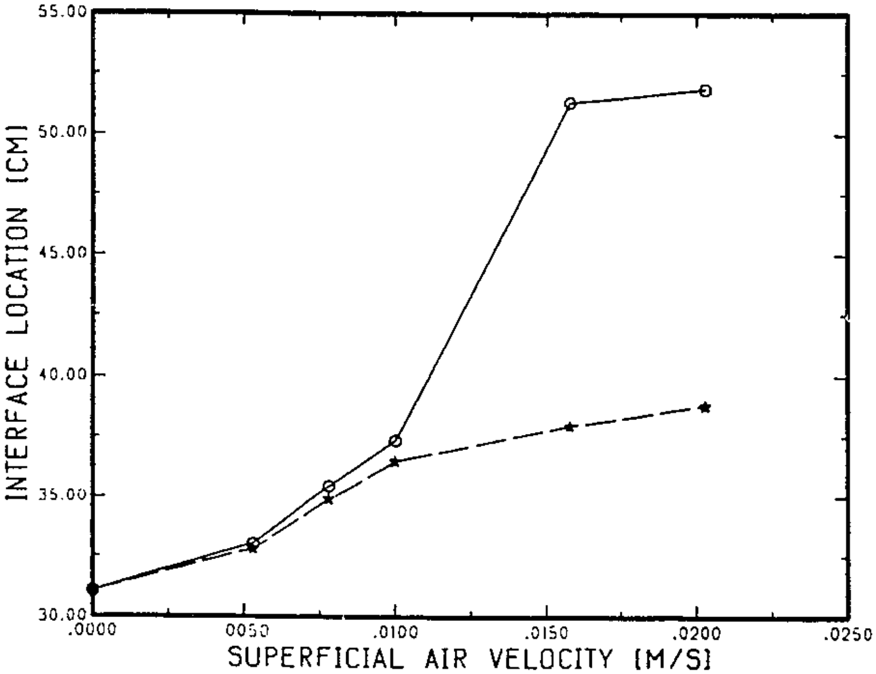

Figure 5.6: Locations of Gas-High Void Region and Low-High Void Region Interfaces for Various Superficial Gas Velocities: ○ Gas-High Void Interface; ★ Low-High Void Interface

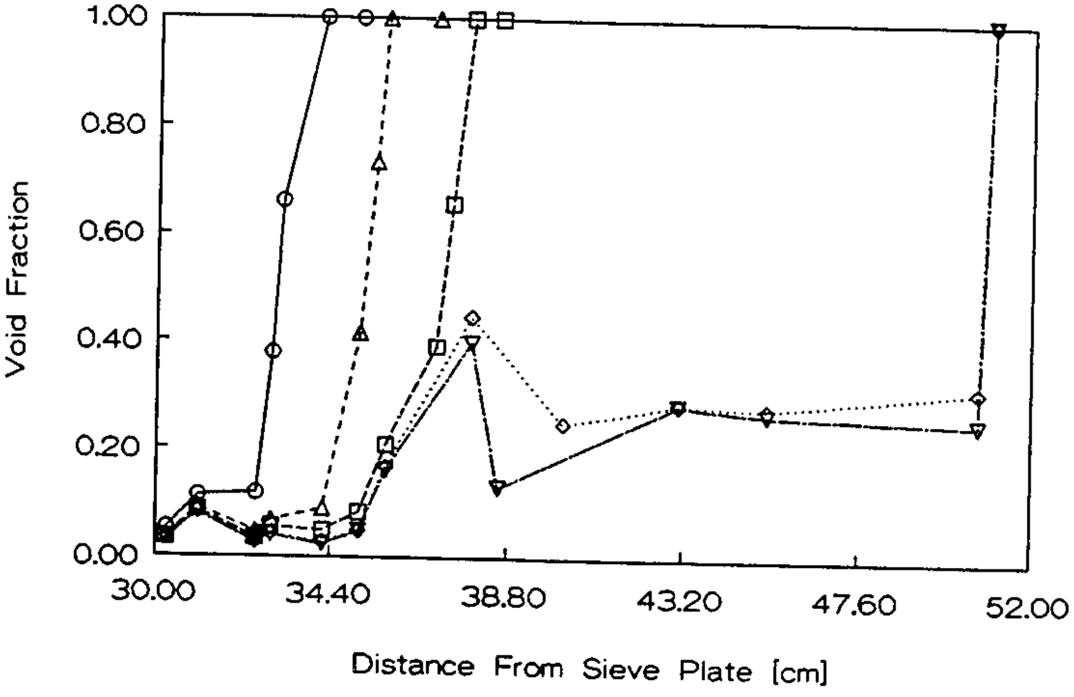

Figure 5.7: Axial Void Fraction Profiles in Bubble Column for Various Flow Rate: ○ U_{gs} = 0.005 m/s △ U_{gs} = 0.008 m/s □ U_{gs} = 0.010 m/s ◇ U_{gs} = 0.016 m/s ▽ U_{gs} = 0.020 m/s

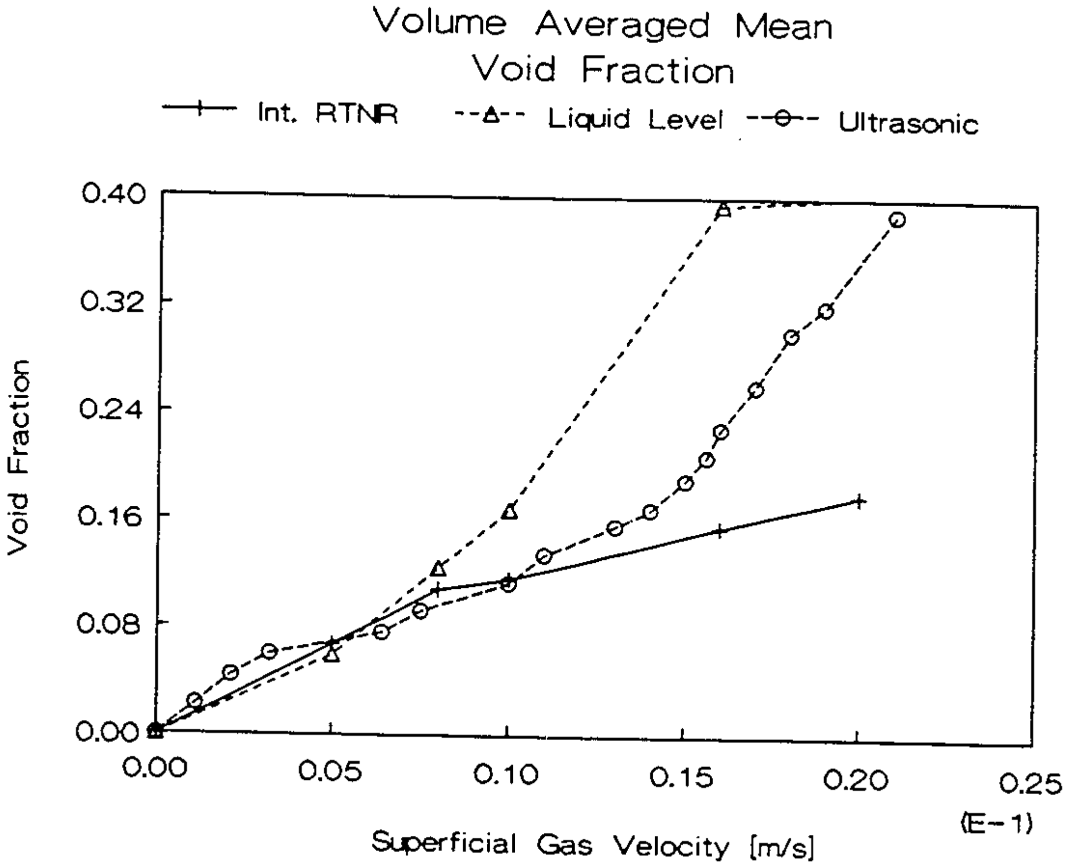

Figure 5.8: Volume Averaged Void Fraction Determined by Liquid Level Measurement and Neutron Attenuation Method via RTNR Technique as a Function of Superficial Gas Velocity: Ultrasonic Results From Chang and Morala[29]

level determined volume averaged void fractions as the water displaced from the mixing section cannot be accounted for in the calculation.

5.3 Measurement of Void Fraction Distribution

Contour (2D) and axonometric (3D) representations are generated for radial void fraction profiles at several axial locations. The contour plots can be difficult to interpret but do show the proper void fraction distribution trends for each type of flow regime. The axonometric plots provide a more easily understandable representation of the flow regime.

The contour and axonometric plots for the images shown in Figure 5.1b are shown in Figure 5.9 for the case where the natural circulation loop is half-filled with heavy water. The contour plot clearly shows the image half filled with water. The interface is well defined at 38.0 cm from the bubble sieve plate. The only discrepancy in the contour plot is the region above 38.0 cm. The wall region is considered to have a low void fraction value. This is due, in part, to a wet surface since the measurement is taken after flow. Another possibility is the edge spread function due to neutron scattering at the wall. Neutron radiographs are not inherently sharp at an interface due to these scattering effects[58]. The pipe centre region should ideally be equal to a void fraction of 1. The discrepancy, here, results from propagation of error from the wall during iteration of the algorithm and variation in the neutron intensity due to noise fluctuations.

Void fraction contour and axonometric plots for Figure 5.1c are shown in Figure 5.10. The image with a liquid slug shown in Figure 5.1c is more difficult to interpret. This results from analyzing an instantaneous image. The contour plot for the liquid slug clearly shows the liquid slug contains some entrained bubbles and is generally in the region between 39.0 cm and 48.0 cm. In comparison to the radiograph shown in Fig. 5.1c, the liquid slug image is not uniform in the radial direction and that shows the contour plot is correct.

The axonometric plot is somewhat clearer indicating the high void fraction

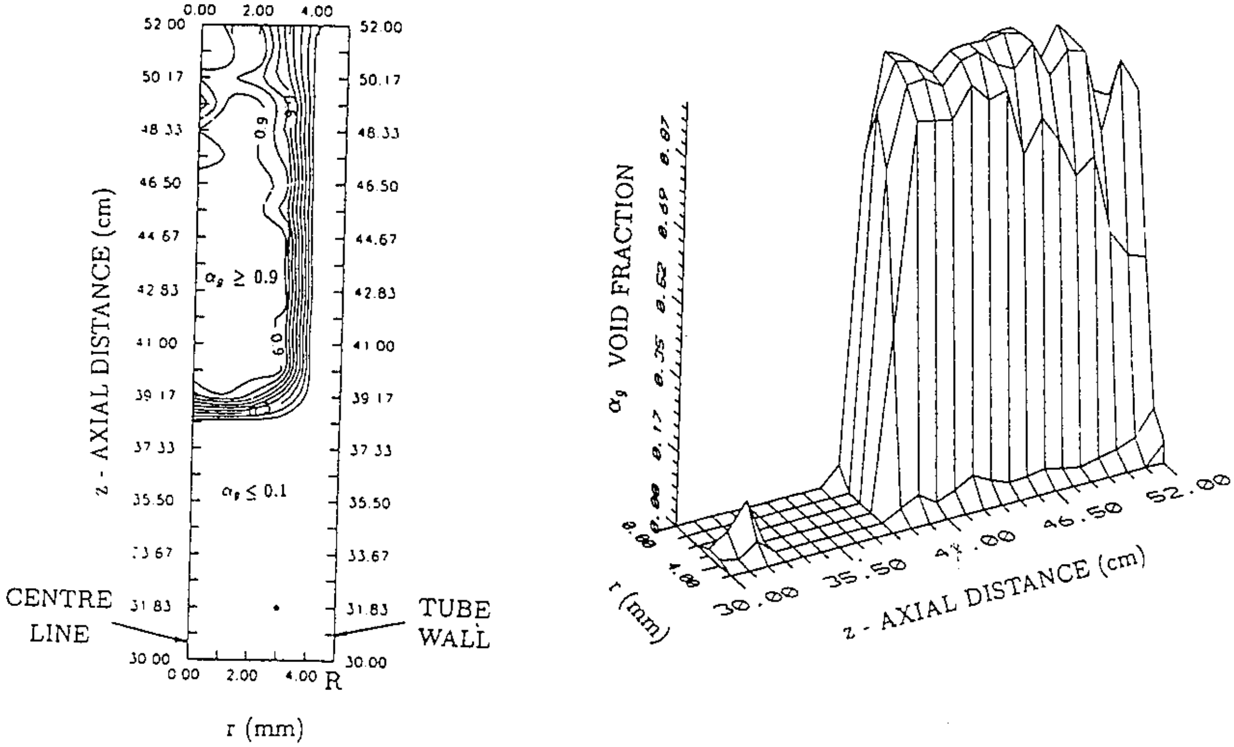

CONTOUR MAP

AXONOMETRIC MAP

Figure 5.9: 2D Void Distribution Contour and Axonometric Maps for Neutron Image in Figure 5.1b: Loop 1/2 Full with D_2O

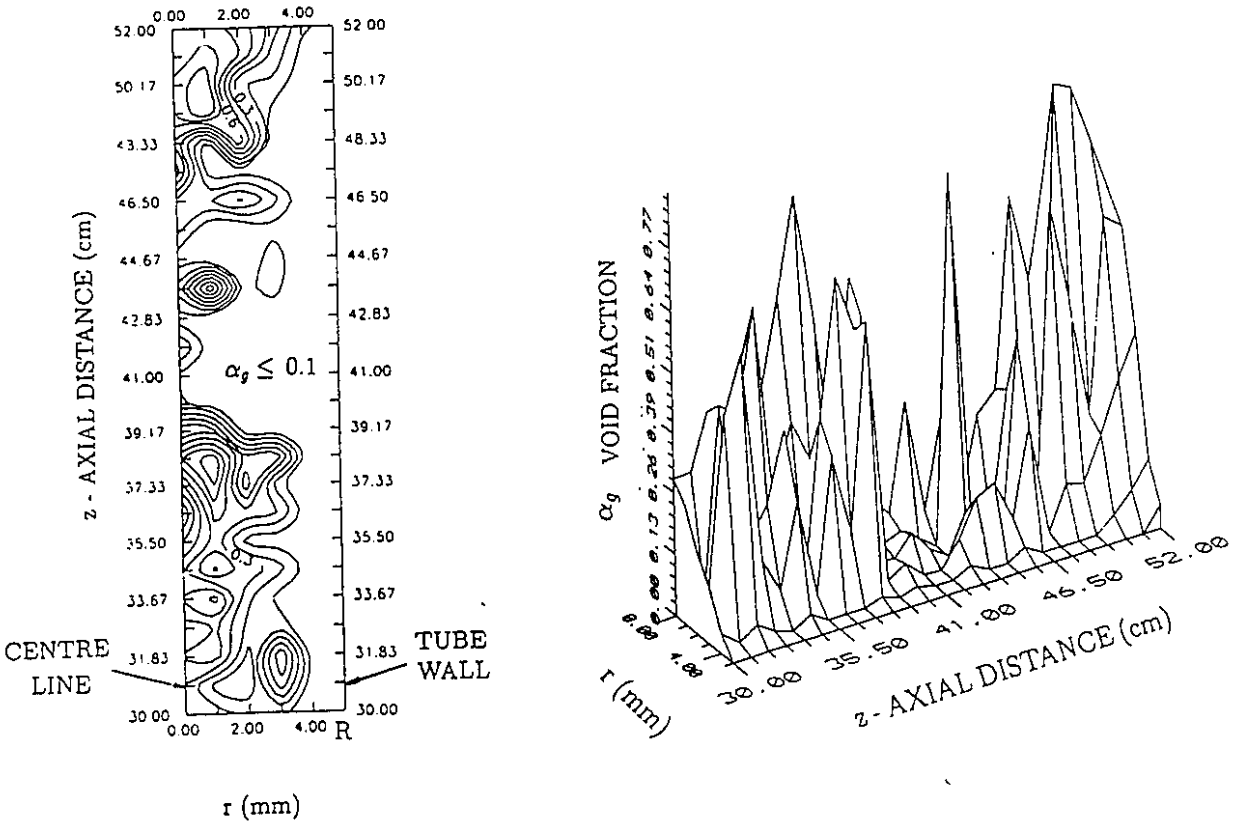

CONTOUR MAP

AXONOMETRIC MAP

Figure 5.10: 2D Void Distribution Contour and Axonometric Maps for Neutron Image for Slug Flow in Figure 5.1c

regions ahead of and behind the liquid slug. The void fraction values in those regions are near 80% and are typical of slug flow. The large spike in the liquid slug at 44.0 cm suggests the presence of a large entrained bubble. The smaller peak at 42.0 cm suggests a smaller sized bubble is present. The spiked nature of the void fraction after the liquid slug suggests the presence of large air bubbles on the verge of coalescence into a Taylor bubble. The region before the liquid slug could indicate the tail of a fully developed Taylor bubble. Fairholm et al. [62] suggest that a Taylor bubble visualized by RTNR will not appear as expected due the inherent time averaging (33 ms) while the camera integrates the neutron flux, since the gas-liquid interface could travel as much as 7.3 mm or 14.4 pixels in one image.

The contour plots can also provide information about the slug velocity and slug stability by examining the 2D information for successive images. Three 2D contour plots, each 132 ms apart, are shown in Fig. 5.11 with the presence of a liquid slug. The slug velocity is calculated based upon motion of the interfaces. In the first contour map, the liquid slug is fairly small with large regions of the image separated into distinct bubbles. The second contour map, 132 ms later, shows adjacent water has increased the size of the liquid slug and the large bubbly flow regions have coalesced into larger bubbles. The downstream interface has moved approximately 2.0 cm and the upstream interface has moved approximately 0.5 cm. The third void fraction contour map is obtained at 264 ms from the first contour map. The liquid slug has broken into several smaller regions and many bubbles have been created. The locations of the interfaces are not as clear as before. From visual observations of the neutron image, these liquid slugs occur at relatively high superficial gas velocities where most of the two-phase section is voided. The liquid slugs created are small and easily destroyed by the gas flow.

The bubble column could not provide as good quantitative results as the natural circulation loop since the calibration for light water is less accurate at large diameter flow tubes. The qualitative results do predict the axial and radial void fractions expected. Figure 5.12 shows an axonometric void fraction plot for a superficial air velocity of U_{gs} = 0.016 m/s (Re_g=58). The test section clearly shows

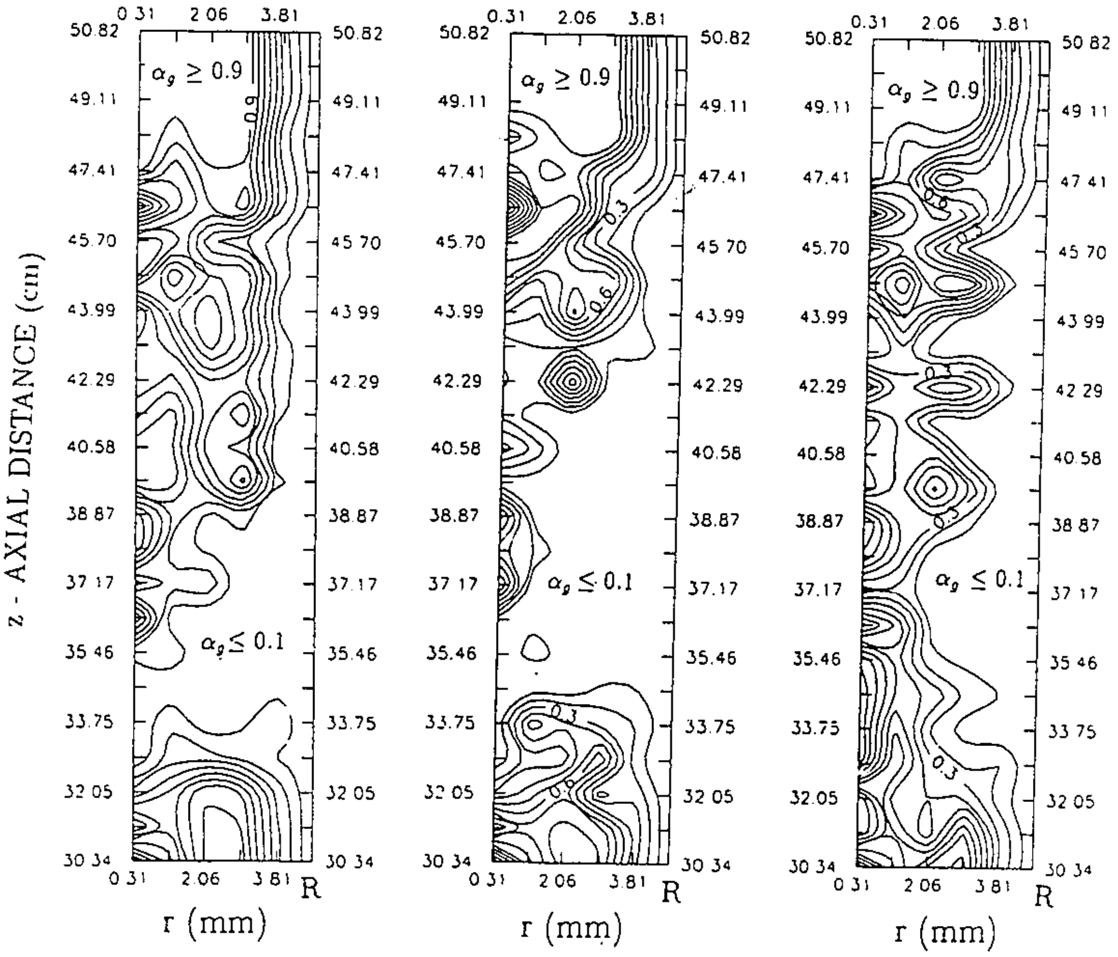

t = 0.0 ms t = 132.0 ms t = 264.0 ms

(a) (b) (c)

Figure 5.11: 2D Void Distribution Contour Maps for Three Neutron Images of a Liquid Slug Flow:(a) t = 0.0 ms;(b) t = 132.0 ms;(c) t = 264.0 ms

two distinct void fraction regions as discussed earlier. The radial and axial information shown in Figure 5.12 is not cross-sectionally averaged and is under slightly different flow conditions (different images). The axonometric plot shows the separation region between the high void region and the low void region. Although it is difficult to determine from the axonometric plot, the meniscus effects on the air-water interface present at the top of the pipe can be observed.

5.4 Measurement of Other Two-Phase Flow Parameters

This section discusses the measurement of bubble diameter and interfacial area using the RTNR technique in the bubble column with some comparison to the ultrasonic technique[29,63].

By using an enhanced imaging technique on each RTNR image with pixel to pixel analysis, the averaged bubble diameter can be determined. A typical enhanced image relative intensity profile along the cross-sectional plane is shown in Figure 5.13, where the bubble diameter can be determined from the pixel distance full width 1/10 maximum of the bubble peak.

Based on the above mentioned method, the mean bubble diameter, determined by the RTNR system, across the bubble column as a function of the superficial gas velocity is shown in Figure 5.14. Figure 5.14 shows that the mean bubble diameter increases slightly with increasing superficial velocity. This result agrees well with the mean bubble diameter determined by an ultrasonic transmission technique[29] measured at Z = 25.0 cm from the sieve plate, where the cross-sectional averaged bubble diameter slightly increases with increasing vertical axis position as shown in Figure 5.15.

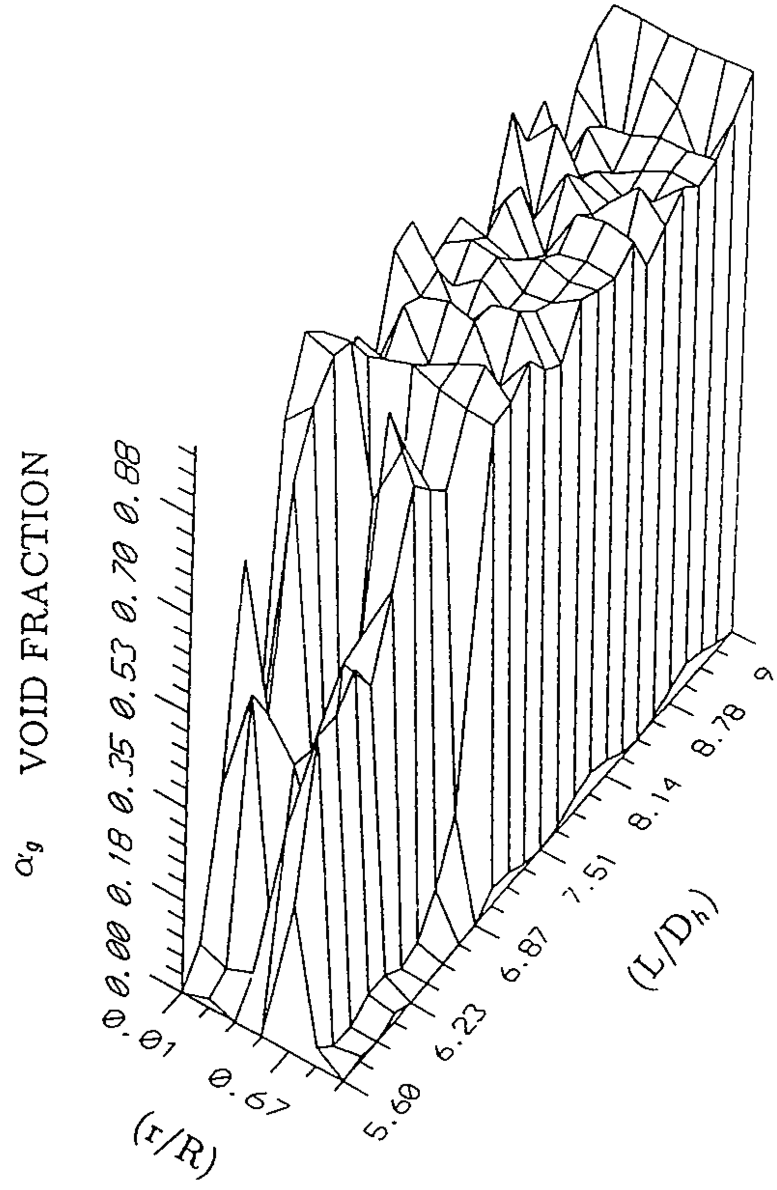

Figure 5.12: 2D Void Distribution Axonometric Map for Bubble Column at a Superficial Air Velocity of U_{gs} = 0.016m/s

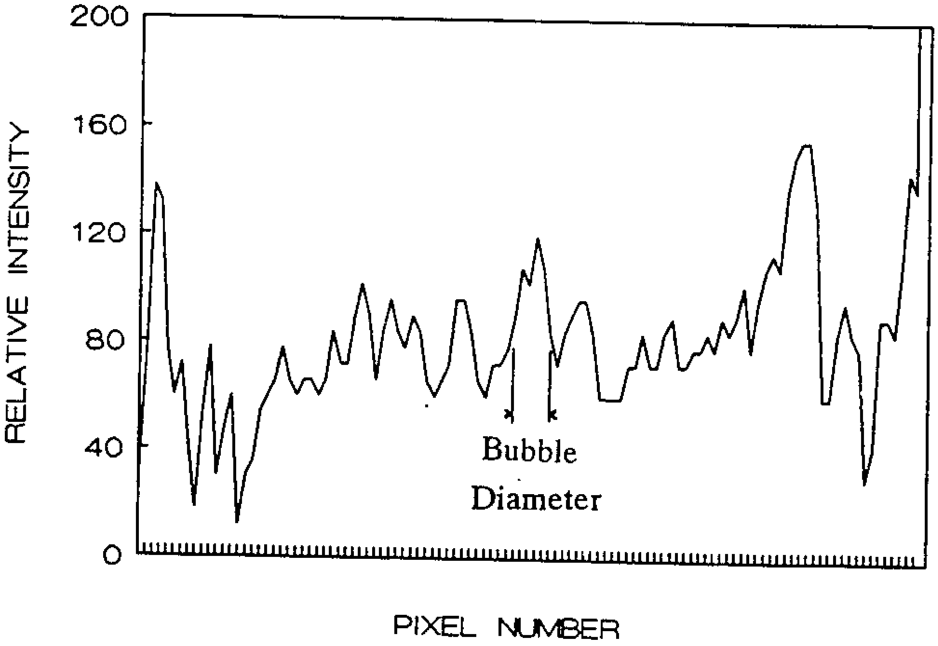

Figure 5.13: Typical Pixel to Pixel Analysis for Bubble Diameter Measurement

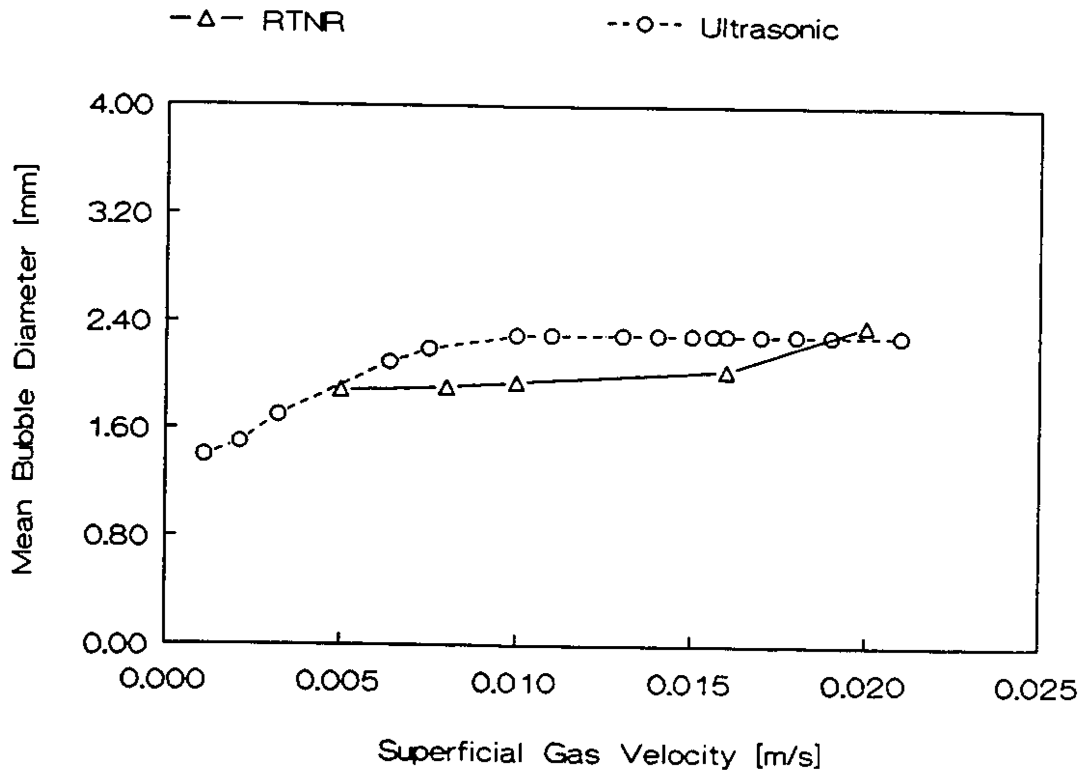

Figure 5.14: Averaged Bubble Diameter across Bubble Column for Various Superficial Gas Velocities

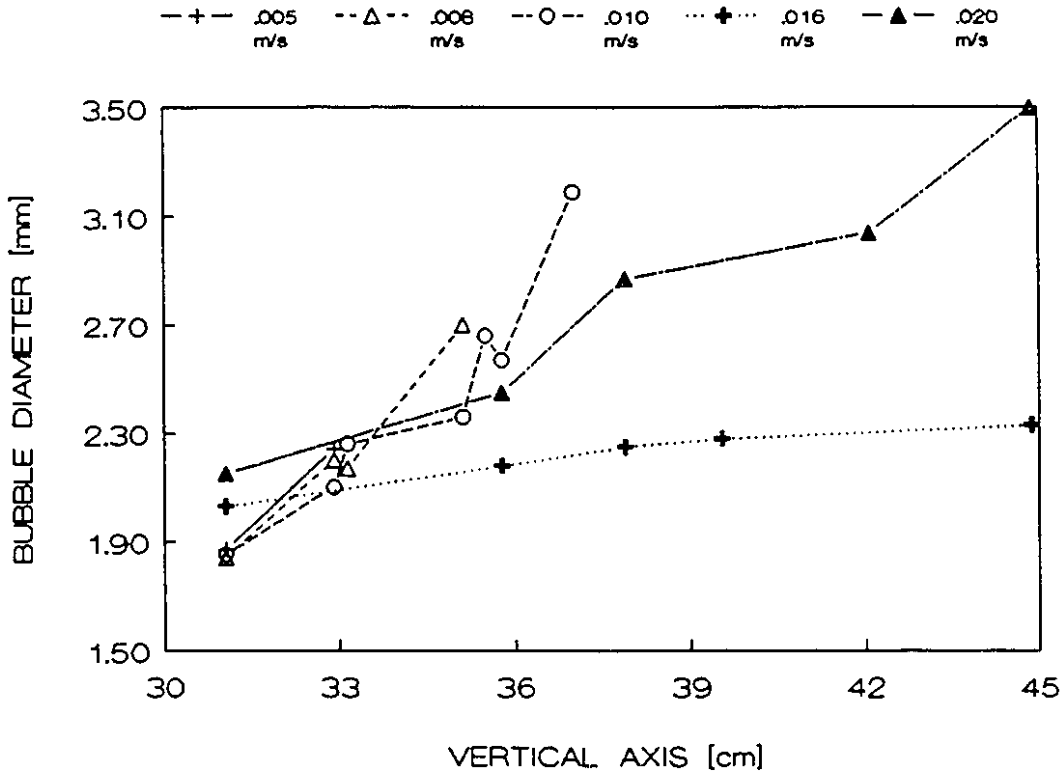

Figure 5.15: Axial Bubble Diameter Profiles for Various Superficial Gas Velocities

The cross-sectional averaged interfacial area density along the vertical axis as determined by Equation 1.6 is shown in Figure 5.16 for various superficial gas velocities. Figure 5.16 shows that the local cross-sectional averaged interfacial area density is approximately uniform in the low void region near the sieve plate and increases along the vertical axis until the gas-liquid interface for low superficial gas velocities. For higher superficial gas velocities where a distinct high void region is noted to exist, both the low and high void regions have an uniform interfacial area density region with the two regions separated by a relatively high interfacial area density peak as has been observed by Calderbank[45]. Since the mean bubble diameter along the vertical axis does not show any small peaks in this transition region, this interfacial area density peak may be due to the void fraction or bubble density peak as has been observed in Figure 5.7.

Interfacial area density averaged across the bubble column as a function of superficial gas velocity is shown in Figure 5.17. The results show that the interfacial area increases at low superficial gas velocities ($U_{gs} \leq 0.007$ m/s, $Re_g \leq 25$). As the mean bubble diameter becomes almost constant, the interfacial area increases only slightly with superficial gas velocity, where the interfacial area determined by the liquid level method again shows a discrepancy at larger gas velocity conditions due to the effect of the two-phase mixing section below the sieve plate. This observation agrees well with the interfacial area measured by the ultrasonic transmission technique as shown in Figure 5.17 [29].

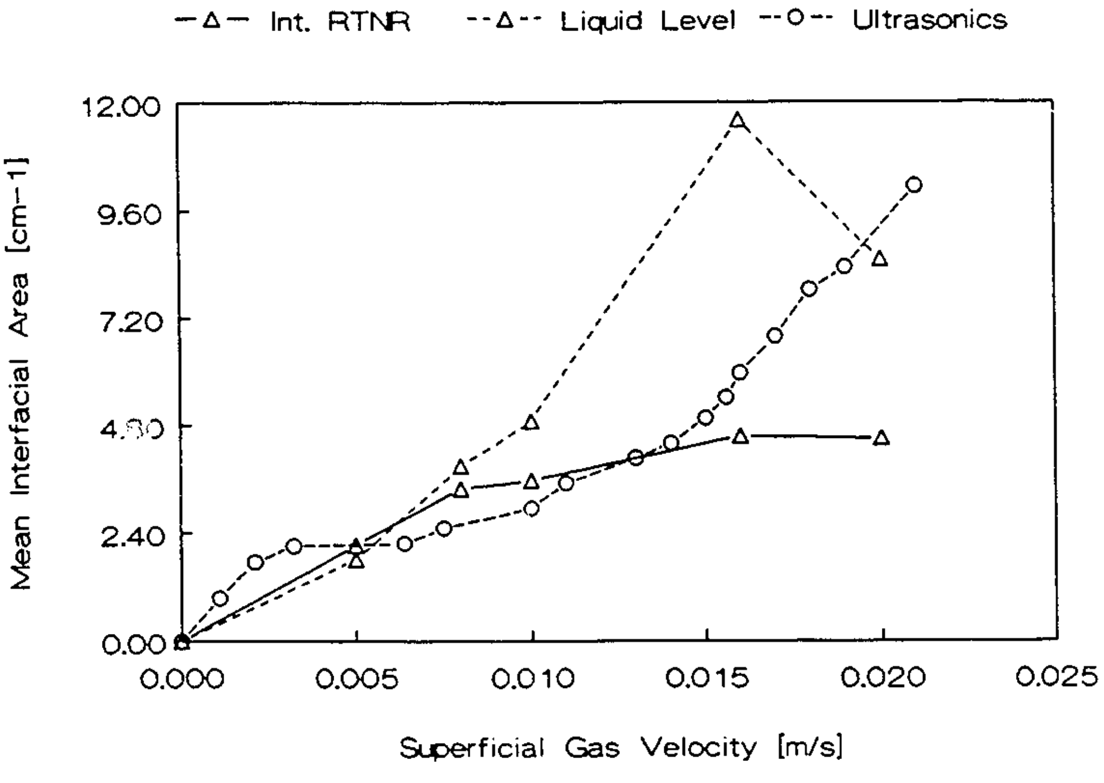

Figure 5.16: Axial Profiles for Interfacial Area Density for Various Superficial Gas Velocities

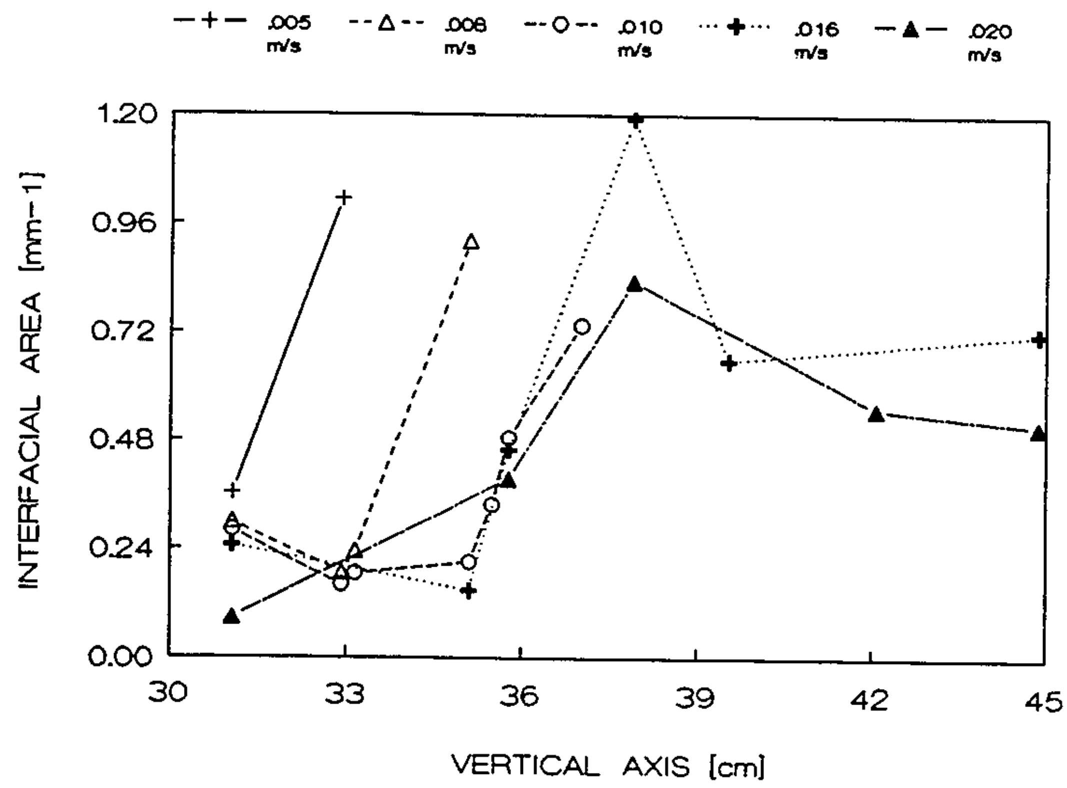

Figure 5.17: Interfacial Area Density averaged across Bubble Column as a Function of Superficial Gas Velocity

Chapter 6

6. Annulus Flow Studies

6.1 Visualization of Two-Phase Flow in a Vertical Annulus Flow Channel

Flow regimes for a vertical annulus flow channel are studied by three characterization techniques; a High-Speed X-ray CT system, a high shutter speed video camera system, and a Real-Time Neutron Radiography system. The annulus flow channel is operated in a bubble column mode with a static single-phase liquid level and gas injection in the bottom of the annulus flow channel.

Four possible flow regimes can exist in a vertical annulus flow channel as shown in Figure 6.1. They are bubbly flow, slug flow, churn flow and annular flow. Bubbly flow is characterized by small bubbles that can be spherical or non-spherical in shape. Small diameter bubbles tend to be more stable and spherical and larger bubbles tend to be non-spherical. These bubbles do not surround the inner tube of the annulus flow channel but may coalesce into larger bubbles due to collisions with neighbouring bubbles.

As the gas flow rate increases, the bubbles will become larger and increasingly irregular in shape. The bubble collision frequency will increase and the probability

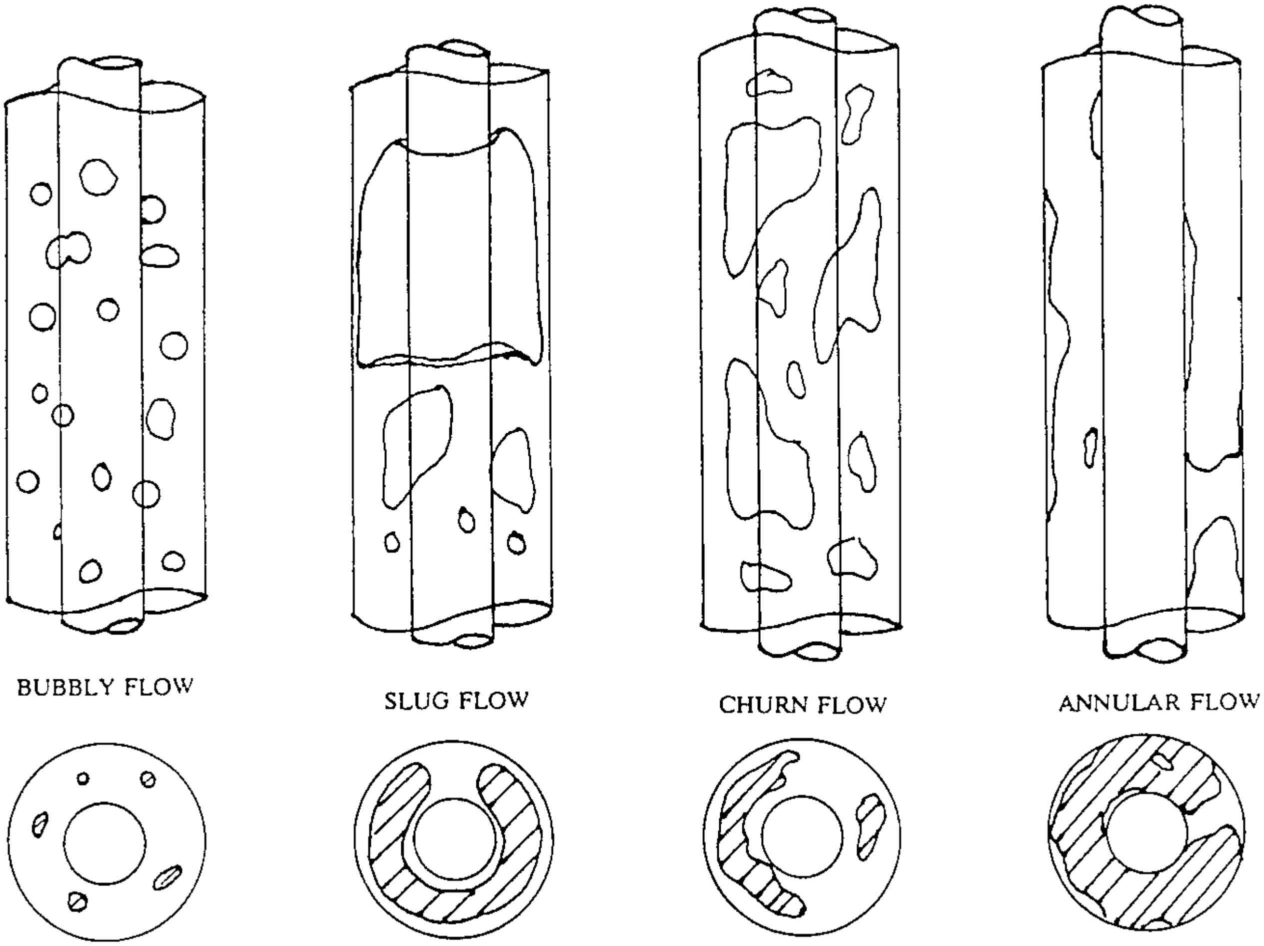

Figure 6.1: Pictorial Representations of Flow Regime for a Vertical Annulus Geometry

of bubble coalescence will increase. As the gas flow rate increases further, large bubbles now coalesce and occupy a significant part of the flow area. These bubbles represent slug flow where a large packet of bubbles has coalesced into one large bubble followed by a liquid slug with a much lower void fraction. As the large bubble moves upwards along the flow channel, the interface becomes increasingly smooth and the bubble represents a donut-shaped Taylor bubble with the central core occupied by the inner tube of the flow channel.

With further increases in the gas flow rate, the void fraction in the liquid slug increases and the stability of the formed Taylor bubble decreases. At a certain point, the gas flow rate is too high and the Taylor bubble formation cannot be maintained. This flow regime is called churn flow. Churn flow bubbles are highly irregular in size, shape, and distribution.

Substantial increases in the gas flow rate will push the liquid to the inner and outer walls of the annulus flow channel to form a thin film with a gaseous core. This flow regime is commonly called annular flow. However, the gas flow rates required for annular flow are too high for the experimental apparatus to measurably achieve and a simulated oscillatory film flow is produced instead. This flow regime is characterized by a very low liquid volume and represents an entrained liquid flow in a gaseous core where droplets are deposited on the walls in the upper part of the annulus flow channel. The droplets fall downwards and produce an oscillating film in the imaging region due to the countercurrent nature of the two-phase flow.

Of the four flow regimes mentioned, only the first three experiments are observed under measurable conditions. Annular flow has been achieved as a simulated oscillatory film flow but the gas flow rate is unknown for this test.

6.1.1 Visualization using the X-ray CT System

Figure 6.2 shows the results for a bubbly flow case where the single-phase liquid level elevation at the initiation of the test is 60.0 cm and the gas flow rate is 5.0 l/min. The images for cross-section number 222 to cross-section number 231 are

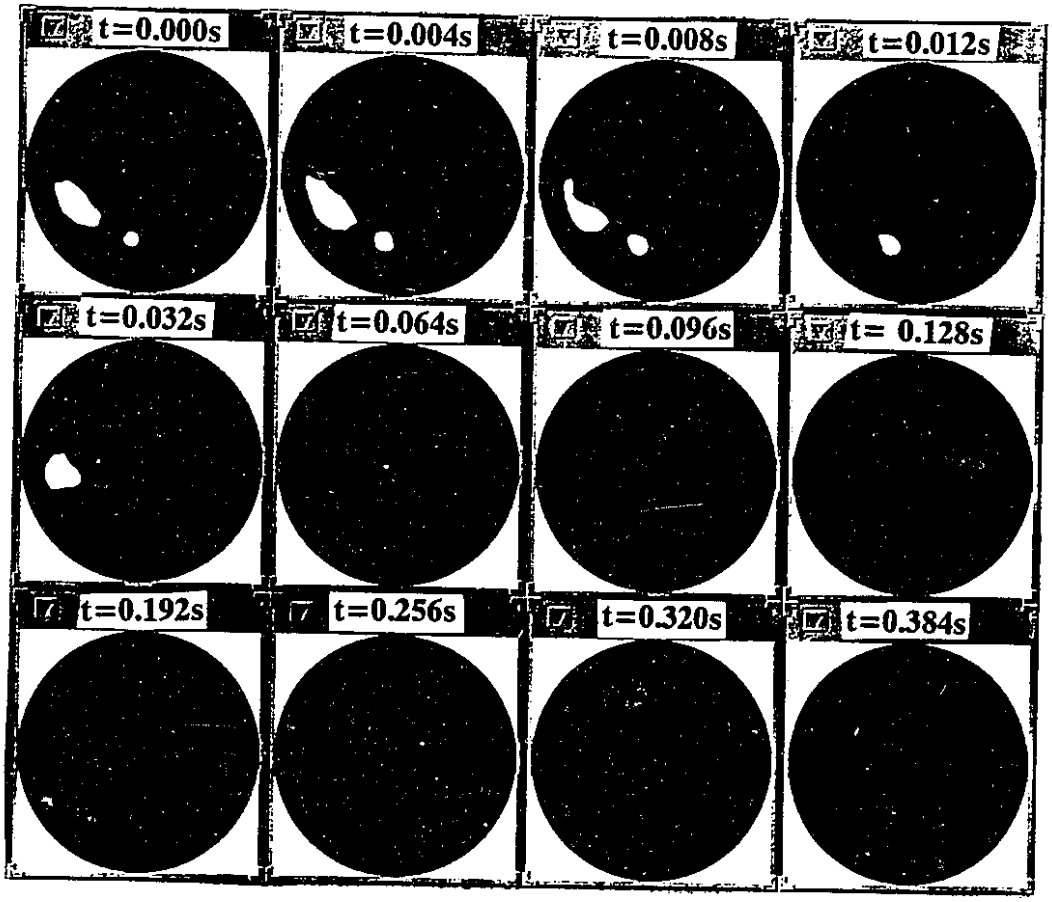

Figure 6.2: Reconstructed X-ray CT Images of Bubbly Flow for a Gas Flow Rate of 5.0 l/min and a Static liquid level Elevation of 60.0 cm:(Test 7WF05L60)

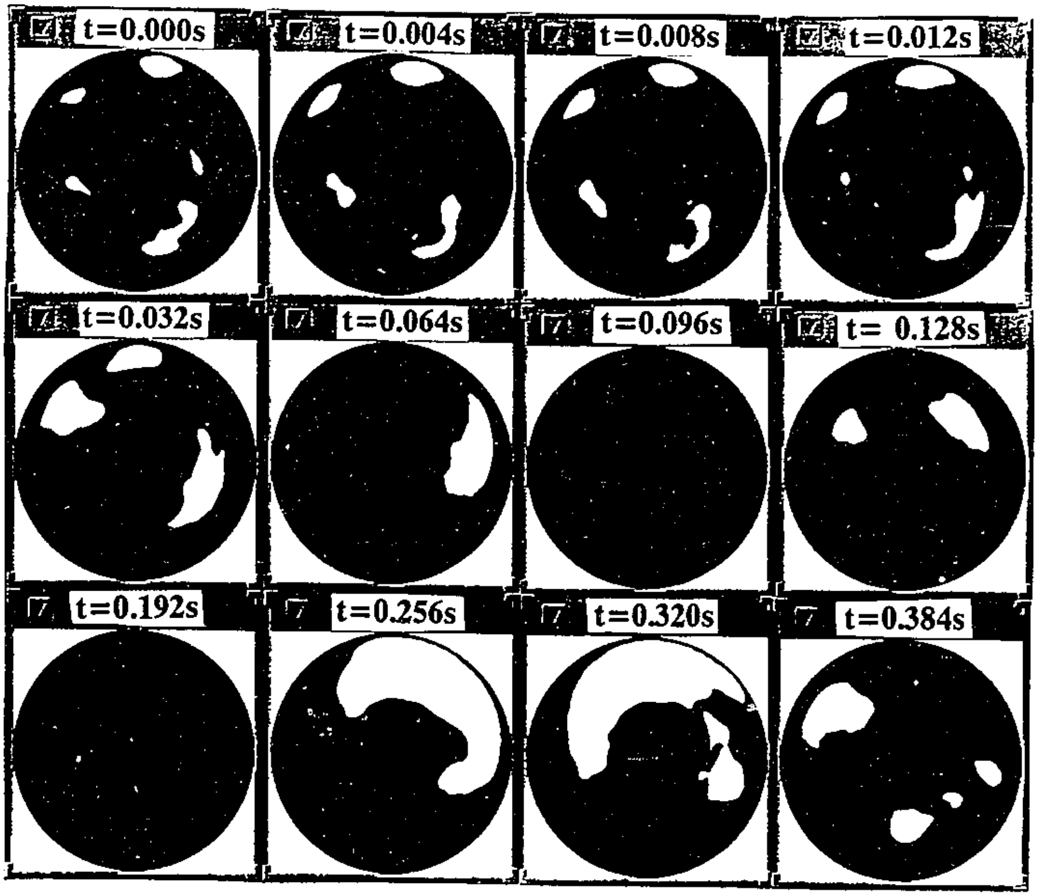

Figure 6.3: Real-Time Void Distribution of Developing Slug Flow for a Gas Flow Rate of 10.0 l/min (Re_g = 220) by an X-CT method at a Static liquid level Elevation of 60.0 cm (Test 5WF10L60)

shown in Figure 6.2. For this low gas flow rate case, the bubble sizes are seen to be small and well separated from each other. Also, circumferential motion is small. This is true for most of the cases studied where the gas flow rate is low.

Figure 6.3 shows the two-dimensional (r,θ) void fraction distribution for an undeveloped slug flow as determined by the X-CT system. Twelve images are shown for a gas flow rate of 10.0 l/min ($Re_g = 220$). The top row is separated by 4.0 ms, the middle row is separated by 32.0 ms, and the bottom row is separated by 64.0 ms. The top row of images show small bubbles entrained in a liquid slug. The middle row of images shows larger bubbles which have coalesced and will eventually be absorbed into the large bubbles typical of slug flow. The bottom row of images shows a large bubble preceded by a liquid slug and followed by entrained bubbles. The shape of the bubble is smooth along the outer edge but is still developing at the circumferential ends as the bubble traverses the flow channel.

Figure 6.4 shows the reconstructed X-ray CT images for a drift velocity Taylor bubble. Cross-section 416 to cross-section 450 show the passage of the nose of the Taylor bubble through the imaging area. Cross-section 580 to cross-section 600 shows the tail end of the Taylor bubble with small bubbles in the wake of the Taylor bubble.

Figures 6.5 and 6.6 show the temporal behaviour for a liquid film in an annulus test section under low liquid level and high gas flow rate conditions. Cross-section 238 is expanded and labelled as shown in Figure 6.5 and shows three important phenomena that can be observed using the X-ray CT system. Figure 6.5 shows an entrained droplet in the lower right area of the image, droplets attached to the inner tube wall in the lower right area of the image, and a liquid bridge between the inner tube and the outer tube. The liquid bridge is formed in cross-section 233. The liquid bridge grows and breaks up continuously but usually reforms in the same location. Also, the motions of the liquid droplets on the inner and outer tube surfaces tend to be in opposite circumferential directions.

Figure 6.6 shows the temporal behaviour for cross-sections 250 to 269. These cross-sections correspond to the temporal range of 0.988s to 1.068s as shown in

Figure 6.18. The liquid film is unstable due to the high gas flow rate and is constantly changing in size and in shape. The liquid film is shown to oscillate circumferentially. However, the great majority of the liquid film remains near the point of closest contact between the inner and outer tubes as the gas velocity is somewhat lower in this region due to the slight local restriction in flow area.

In the top part of each image is a liquid bridge between the inner and outer tubes of the annulus. As time progresses, the liquid on the outer tube moves in a counter-clockwise direction and the liquid on the inner tube moves in the clockwise direction. This results in a distortion to the liquid bridge due to the shear forces. However, the direction of flow is reversed at cross-section number 258 and the shear forces also switch direction. The liquid bridge does not retain enough surface tension and eventually breaks up in cross-section number 263.

The characterization of flow regime by the high speed X-ray CT system can be conducted by two methods. The first method, is to reconstruct the cross-section image data in a binary format where one colour represents the void (gas phase) and the other colour represents the liquid phase as shown in Figure 6.2. The second method is to determine the history of the cross-sectional averaged void fraction.

In the first method, the characterization of flow regime depends on the size and shape of the void regions and how they change in successive cross-sections. Bubbly flow is fairly simple to determine as the gas phase appears as small relatively circular regions scattered throughout the flow area. These regions will grow and shrink with successive cross-sections. Slug flow is characterized by the presence of a large sickle shaped void region that is attempting to surround the inner tube of the annulus flow channel. The walls are relatively smooth in each cross-section and the void fraction is greater than 30%. Although each cross-section has a relatively smooth interface, the changes in the interface location from one cross-section to the next can be dramatic. This is caused by the unstable nature of the bubble during slug flow in a bubble column. Churn flow is characterized by large irregular shaped bubbles with possibly an unsharp interface, and the successive cross-sections show dramatic changes to the interface location.

Figure 6.4: Reconstructed X-ray CT Images of a Taylor Bubble produced by Pulsed Gas Flow (Cross-sections 416 to 600) (Test 6WFSLUG)

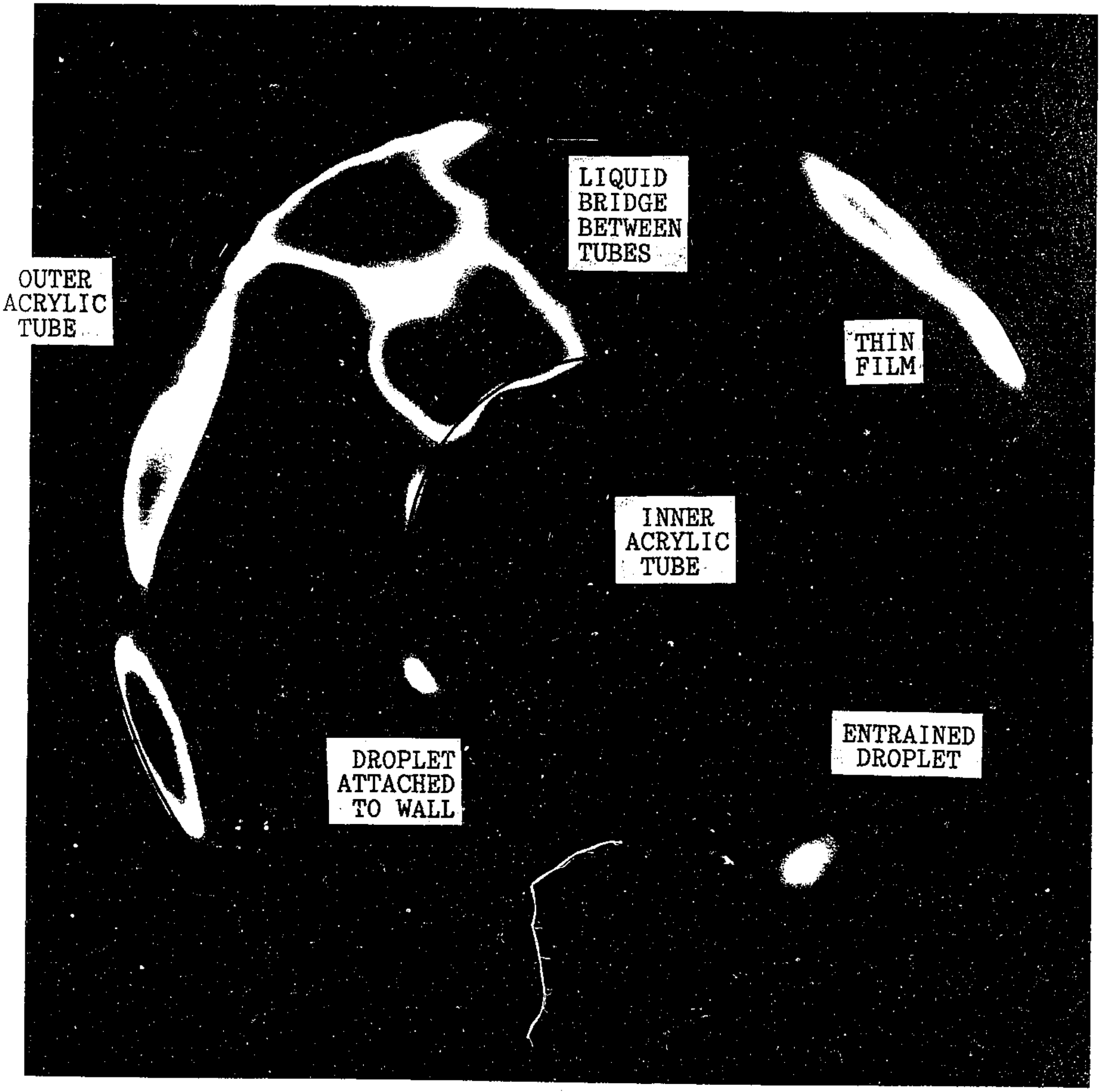

Figure 6.5: Enlarged Reconstructed Image of Cross-section 238 of Figure 4.6 showing Entrained Droplet, Droplets Attached to Walls, Thin Liquid Films, and a Liquid Bridge (Test 8WFMXL20)

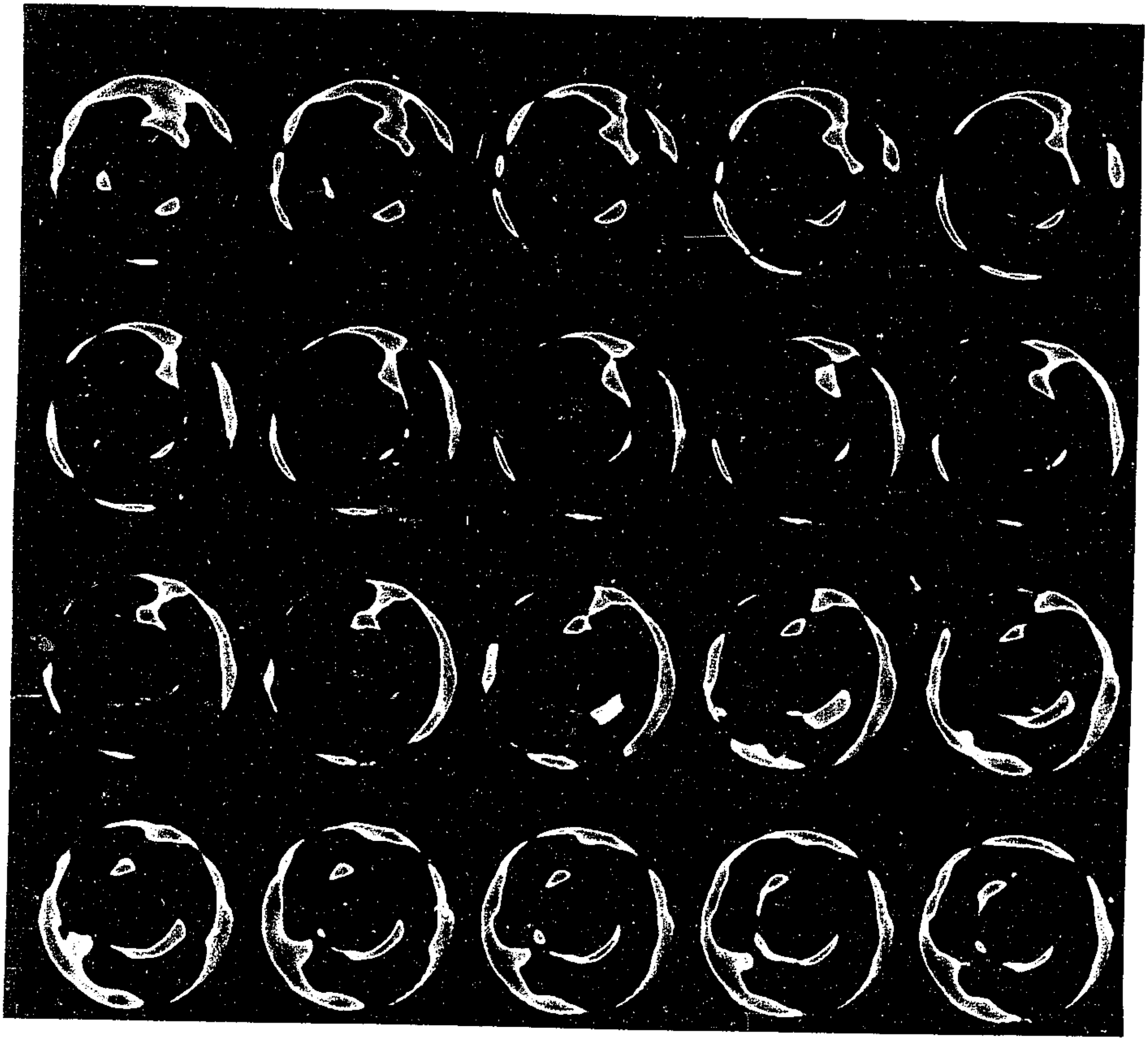

Figure 6.6: Reconstructed X-ray CT Images of Unstable Film Flow (Cross-sections 250 to 269); Liquid Bridge Collapse (Test 8WFMXL20)

The second method uses the waveform shown by the void fraction histories(Figures 6.14 to 6.18) to predict the flow regime similar to the capacitance void transducer waveform technique.[13] In this approach, bubbly flow is characterized by small void fraction peaks less than 20% in void fraction. Slug flow occurs when the void fraction peaks increase to greater than 30% and have a regular shape and frequency between bubbles. Churn flow is characterized by high void fraction peaks with irregular shape and an unstable frequency.

Generally, both methods produce results which agree well with each other. The first method is more accurate as this method produces a visual representation of the flow regime but is quite time consuming, especially when numerous images need to be examined. The second method is faster but the difficulty in interpreting the waveform can sometimes lead to erroneous results as shown by the low flow rate data for the 60.0 cm level. At less than 5.0 l/min, the reconstructed images show the flow regime to be bubbly flow since large bubbles exist that do not surround the inner tube. The void fraction histories for this flow condition show very large maximum void fractions with a strong repeatable nature like slug flow. This erroneous result occurs since the measurement location for this point is 65.0 cm. The dynamic liquid level is very close to the measurement location and the high speed X-ray CT system is measuring partly the bubbly flow below the interface and partly the bubble packing layer above the interface. The other bubbly flow regime data is in agreement because the high speed X-ray CT system is measuring the flow regime well below the dynamic liquid level.

Figure 6.7 shows the flow regime data obtained by the high speed X-ray CT method. The x-axis is the superficial gas Reynolds number as defined by Equation 6.1 and the y-axis is the non-dimensional static liquid level(L/D_h) from the sieve plate obtained by dividing by the hydraulic diameter. Two non-dimensional static liquid levels are observed at 23 and 30 which correspond to liquid levels of 60.0 cm and 80.0 cm. bubbly flow, slug flow, and churn flow are characterized by the high speed X-ray CT system. Figure 6.7 shows that the transition from bubbly flow to slug flow occurs close to a superficial gas Reynolds number of 110. The transition from slug

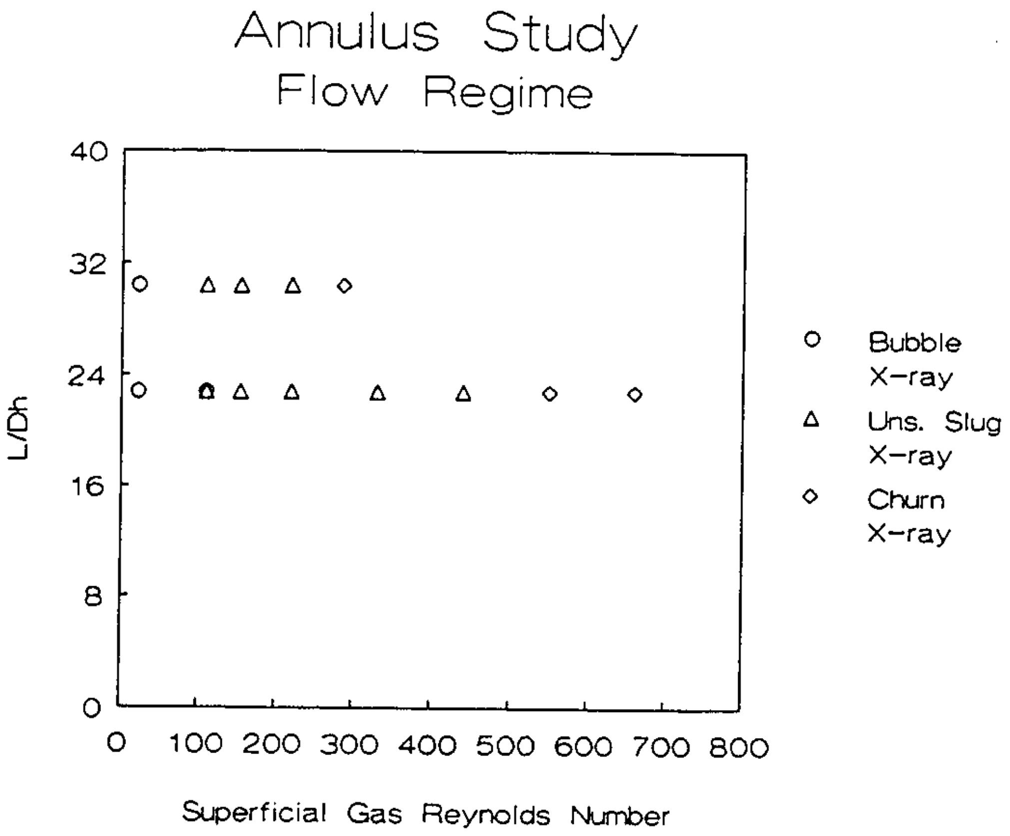

Figure 6.7: Flow Regime Observations by the High Speed X-ray CT Study

flow to churn flow depends strongly on both the superficial gas Reynolds number and the non-dimensional static liquid level.

$$Re_{gs}=\frac{\rho_g U_{gs} D_h}{\mu_g}$$

6.1.2 Visualization using the Optical Video System

The optical video system records an image of the gas-liquid interface inside the flow volume of the vertical annulus flow channel. A high shutter speed allows for the sharp determination of the gas-liquid interface. The recorded image is a planar image with respect to the vertical axis and shows the shape and distribution of the bubbles in the image.

Figure 6.8 shows three images obtained from the optical video camera for bubbly flow, slug flow, and churn flow respectively. For bubbly flow, small spherical bubbles are seen to move upwards in the annulus flow channel as shown in Figure 6.8 as black spots. The bubbles are randomly distributed and at low gas flow rates are usually of the same size order. Above the interface, liquid droplets can be seen on the glass wall.

Slug flow is seen as a liquid region preceding and following a gas bubble which occupies a majority of the annulus flow channel area with respect to other bubbles. In Figure 6.9, the gas bubble is present on all side of the inner tube except the side facing the camera. The gas bubble is approximately 6.0 cm in length with a rounded nose and entrained bubbles in its wake.

Churn flow is characterized by large irregular shaped bubbles. In the wake of such bubbles, a highly agitated liquid slug follows with numerous bubbles also irregularly shaped as shown in Figure 6.8.

Figure 6.9 shows a Taylor bubble produced by pulsed gas flow similar to the Taylor bubble imaged by the High-Speed X-ray CT system as shown in Figure 6.4. The Taylor bubble has a smooth nose and an abrupt tail with a significant amount

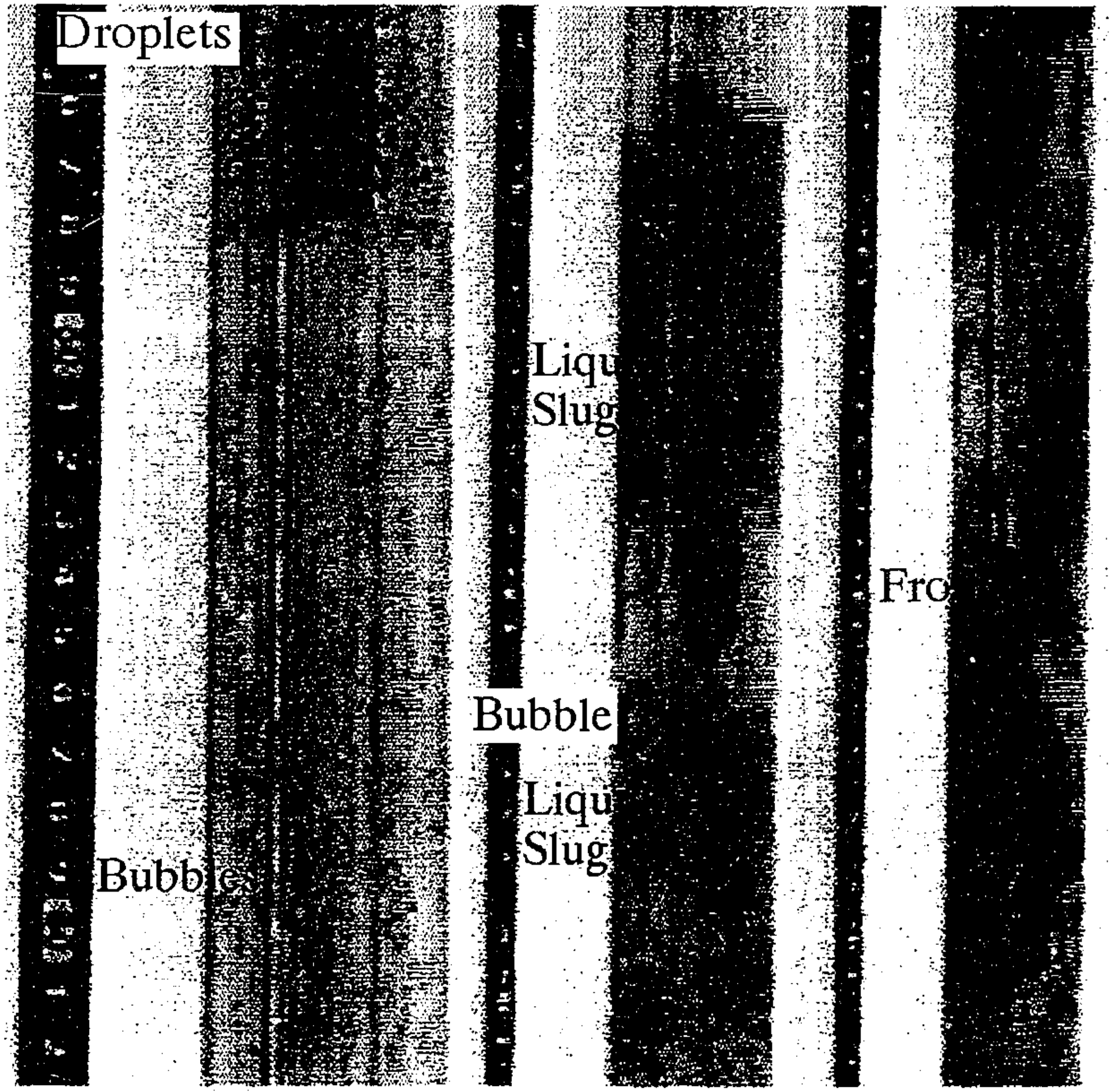

BUBBLY FLOW SLUG FLOW CHURN FLOW

Figure 6.8: Bubbly Flow, Slug Flow, and Churn Flow by Optical Video Study

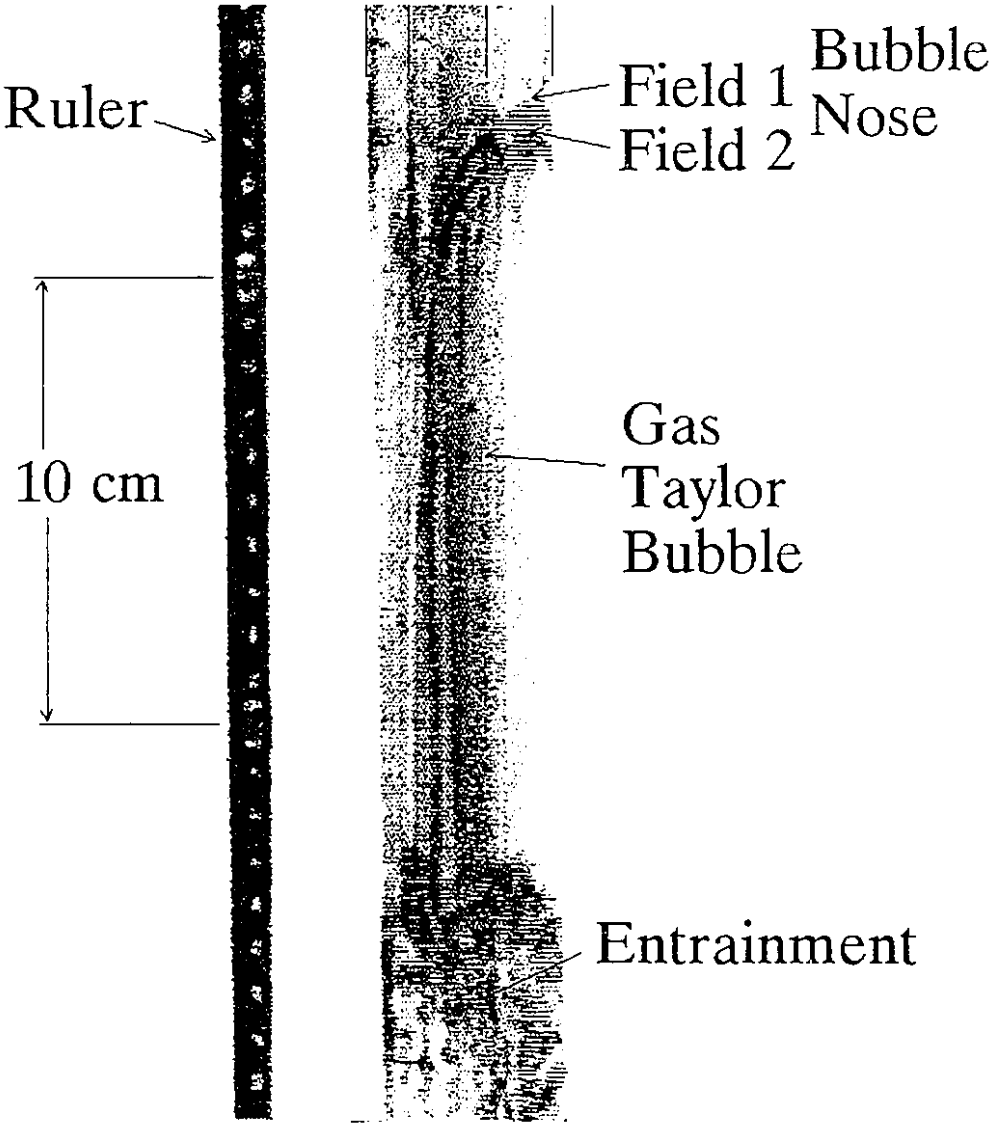

Figure 6.9: Taylor Bubble Visualized by Optical Video Camera

of entrainment. Two noses are apparent in Figure 6.10, they each belong to a field from a different frame and are 16.5 ms apart in time. A feature of most frame grabbers is to grab two fields for each frame as cameras and monitors use a 2:1 interlace to improve the image display quality. It is possible to actually acquire information from two different frames simultaneously. These two fields could be used to calculate the bubble velocity. Such a calculation gives the velocity of the Taylor bubble shown in Figure 6.9 as 0.32 m/s.

The flow regime observations for various gas flow rates and single-phase liquid levels is shown in Figure 6.10. The x-axis is the superficial gas Reynolds number in the annulus flow channel. The y-axis is the non-dimensional single-phase liquid level before gas is injected into the bottom of the channel. The optical video system observes similar flow regimes as does the High Speed X-ray CT system. The transition from bubbly flow to slug flow is seen to occur at increasing superficial gas Reynolds numbers as the non-dimensional static liquid level decreases. The slug flow to churn flow transition occurs at a Reynolds number near 400.

6.1.3 Visualization using the RTNR System

The experiments performed using light water (H_2O) did not show good contrast at low void fractions because the thermal neutron flux had been significantly attenuated. The visualization of bubbly flow and slug flow is difficult whereas churn flow is easier to visualize due to the greater void fraction. The heavy water (D_2O) experiments show a much improved ability to visualize the flow behaviour as the neutron beam is not attenuated as strongly as it is with light water.

The images produced by the Real-Time Neutron Radiography System show planar images of the projection of thermal neutrons through the test section as previously discussed. The image represents a density map of the liquid in the flow channel. The darker the intensity, the more liquid present at that point. Bubbles appear as lighter regions in the original image. The interface between the gas and the liquid is usually not sharp as the shutter speed is standard at 33 ms/image.

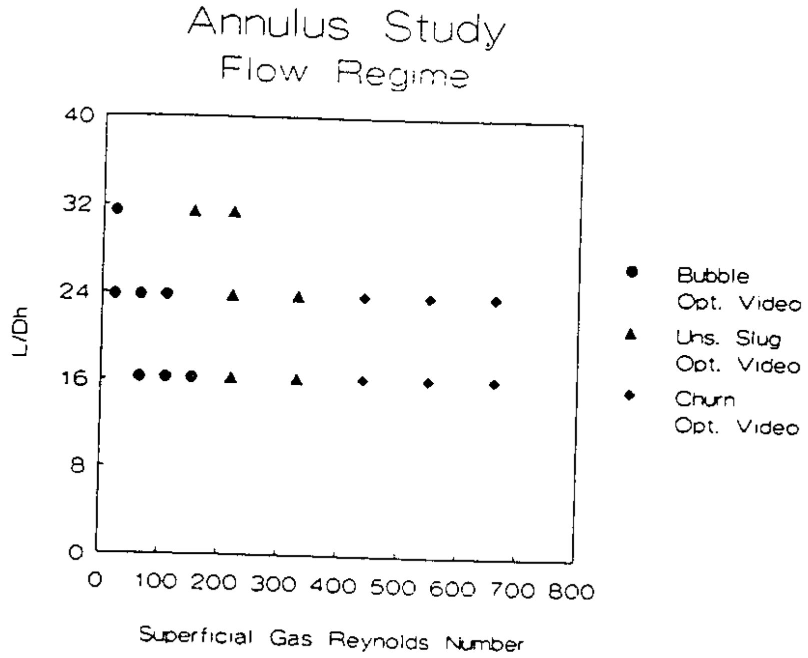

Figure 6.10: Flow Regime Observations by the Optical Video Camera Study

Bubble motion can be significant in this time period.

Bubbly flow is difficult to identify from simply viewing the image as the change in the intensity levels depends on bubble size and liquid content in the flow path. Usually, image processing and analysis are required to detect the presence of a dispersed lighter phase. Slug flow is identified by the presence of large bubbles passing through the image area with a steady frequency and following the same flight path. Churn flow is identified by a breakdown in the bubble shape, bubble frequency, and flight path. In fact, the bubble shape cannot be clearly defined due to the chaotic nature of the flow.

Figure 6.11 shows a typical image of slug flow produced by pulsing the gas flow. In this image, black corresponds to gas and white corresponds to liquid as the image has been reversed by image processing for easier visualization. The image shown in Figure 6.11 has been corrected for intensity offset and target integration using camera images for a full neutron beam and for no neutron beam. This correction results in subtle errors in the time clock and at the left edge of the image but does produce good quality in the centre of the images. The white regions to either side of the image are the boron rubber shields used to eliminate scattering phenomena and to reduce the effect of high frequency components at the tube walls.

Black lines mark the tube walls in Figure 6.11 to clarify the location of the inner and outer tubes. A white dashed line outlines the gas bubble to indicate it's approximate position. An arrow shows the location of the gas-liquid interface near the top of the image. Figure 6.11 shows that the gas bubble partially surrounds the inner tube and is centred to the right of the image. The gas bubble rises to the right of the image as the local flow area is slightly larger on this side or perhaps the annulus tubes have a slight inclination to the left.

Figure 6.12 shows the flow regime observations for the Real-Time Neutron Radiography system. Results for high non-dimensional static liquid levels (>16) show a small bubbly flow region, a slug flow region, and a churn flow region. At low non-dimensional static liquid levels(<16), the bubbly flow region extends to higher superficial gas Reynolds numbers and the churn flow region extends to lower

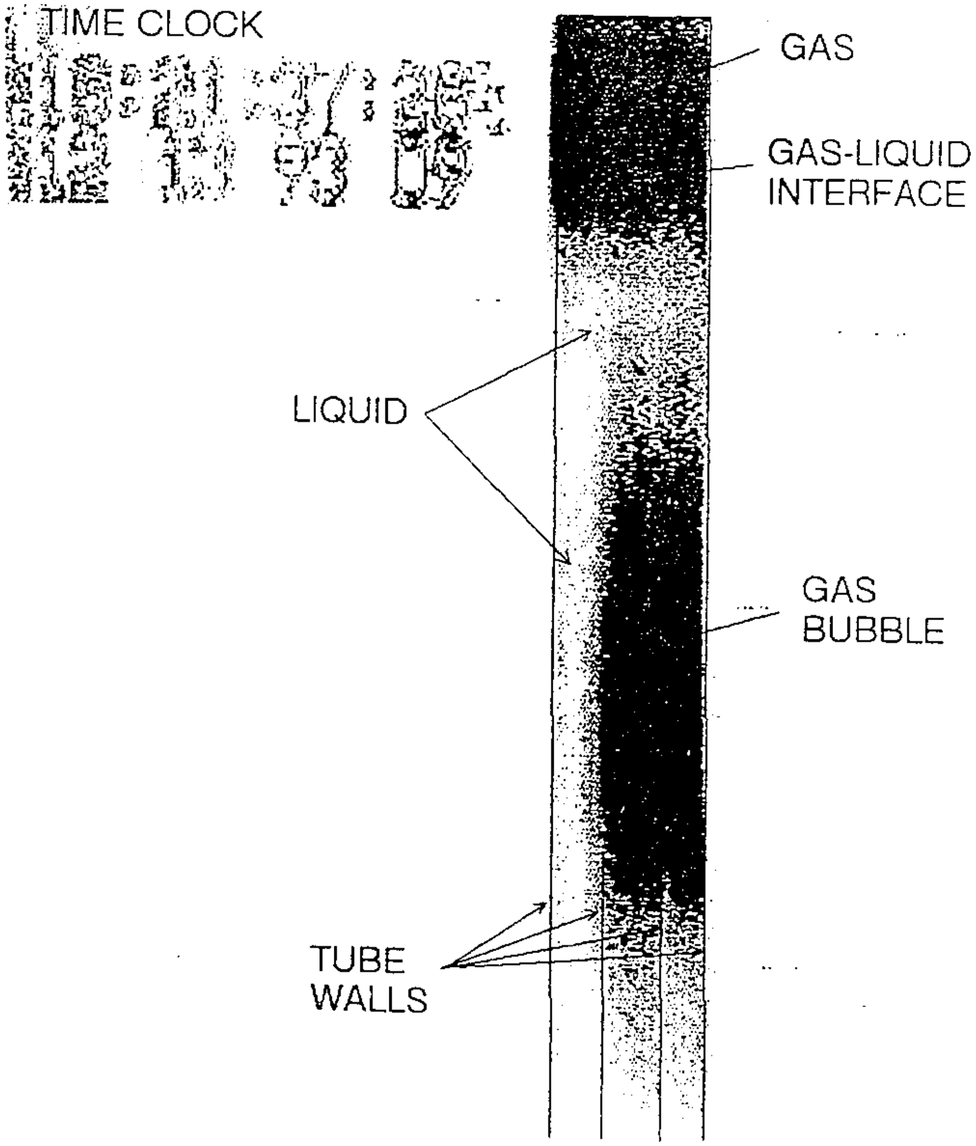

Figure 6.11: A typical Real-Time Neutron Radiograph after Image Correction showing a Taylor Bubble produced by Pulsed Gas Flow similar to Figures 6.4 (X-ray CT) and 6.9 (Optical Video Camera)

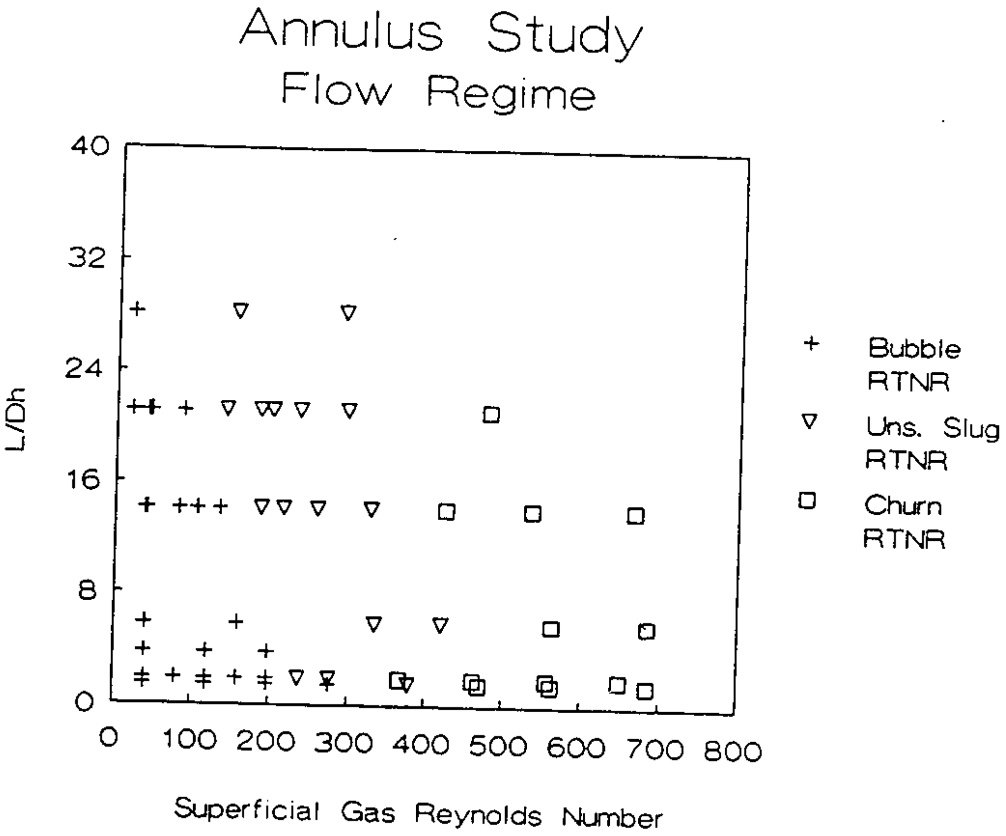

Figure 6.12: Flow Regime Observations by the Real-Time Neutron Radiography System

superficial gas Reynolds numbers. Also, for low non-dimensional static liquid levels, the residence time of each bubble in the test section is short and hence the bubble collision frequency becomes small. Thus, at higher superficial gas Reynolds numbers($0 < Re_g < 300$), the flow regime is still bubbly flow. As the superficial gas velocity increases further, the bubble collision frequency will increase to the point where large bubbles will be formed, however, at this point the bubbles will be unstable due to a high superficial gas Reynolds number and will develop into churn flow.

Figure 6.13 shows the flow regime experimental data obtained by all three techniques. In general, the agreement among the three techniques is quite good. There is some difficulty with the transition between bubbly flow and slug flow at the higher liquid levels. This is caused by the interpretation of the images produced by each technique. For bubbly flow, agglomeration of the bubbles into larger bubbles occurs for lower flow rates than shown for the transition to slug flow. These bubbles cannot be considered as slug flow as they are still too small. However, this means that the determination of the transition between bubbly flow and slug flow is quite difficult from observation of the images alone since the main criteria will be bubble size and shape.

6.2 Measurement of Void Fraction in Annulus Flow Geometry

This section will discuss the measurement of cross-sectional averaged void fraction by both advanced radiation techniques. Local void fraction measurement is not discussed here. The determination of local void fraction by the high speed X-ray CT system is simply visualization of binary images as shown in Figure 6.2. For the RTNR system, the local void fraction is inherently averaged along the neutron beam path length.

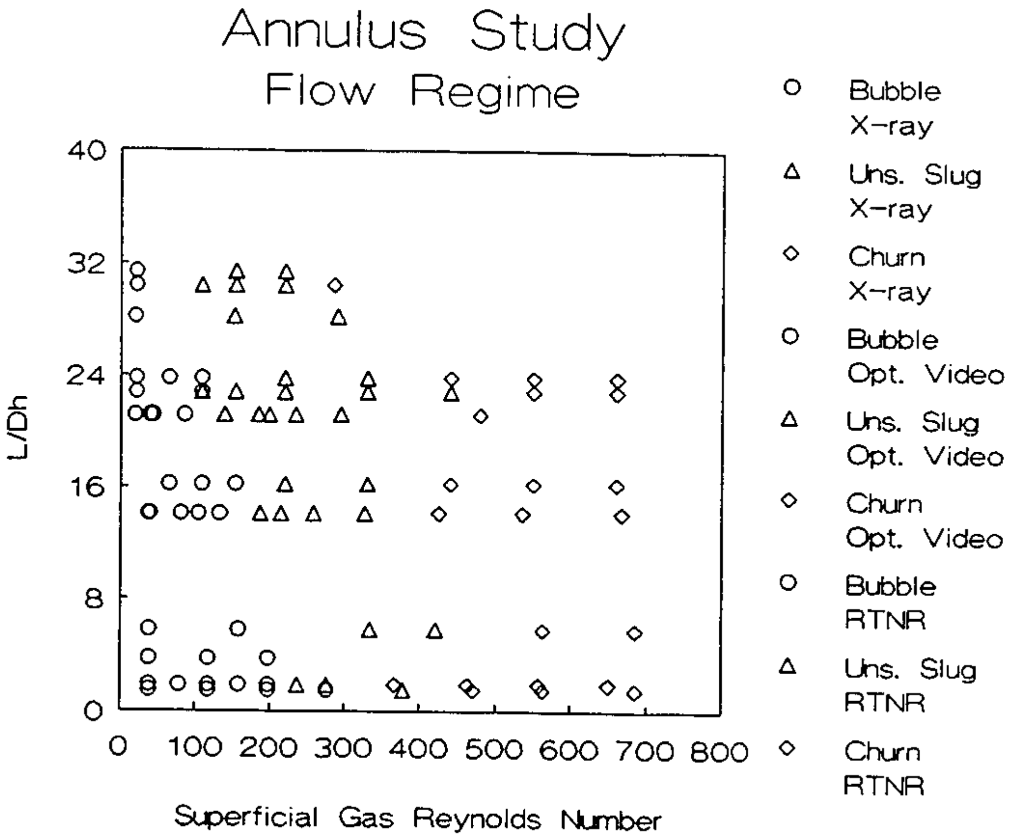

Figure 6.13: Flow Regime Observations in a Vertical Annulus Flow Channel by a High Speed X-ray CT system, an Optical Video Camera system, and a Real-Time Neutron Radiography system

6.2.1 Cross-Sectional Averaged Void Fraction Determined by X-ray CT System

Figures 6.14 to 6.18 show some of the cross-sectional averaged void fraction histories obtained by the X-ray CT system. The threshold level for each void fraction history is obtained using the derivative technique based upon the empty annulus flow channel data averaged for 100 image cross-sections. The experimental results range in void fraction from 0% to 100% and cover all flow regimes mentioned in the previous section.

Figures 6.14 and 6.15 show the cross-sectional averaged void fraction histories for a static liquid level elevation of 60.0 cm and steady-state gas flow rates of 15.0, and 25.0 l/min respectively. The X-ray imaging plane is located at an elevation of 65.0 cm relative to the inlet of the test section. Similar results are obtained for other gas flow rates studied in this work.[64]

Figure 6.14 shows the temporal variation of the cross-sectional averaged void fraction. Depending on the value of the transient maximum void fraction, we can categorize three distinct void waveforms as follows. The first type of void waveforms have transient maximum void fractions less than 10% representing small bubbles passing through the X-ray imaging plane. The second type of void waveform have transient maximum void fractions between 20% to 40%. The transient maximum void fraction range corresponds to bubbles that have a larger size than the first type of void waveform and are packed close together. These bubbles are in the process of agglomeration. The third type of void waveform have transient maximum void fractions greater than 50% and represent large bubbles after agglomeration is completed. The three distinct types of void waveforms occur repeatedly, hence the flow regime is in transition from bubbly flow to slug flow. With increasing gas flow rates, the frequency of the third type void waveforms increases while the frequency of first and second type void waveforms decreases. The experimental results show the occurrence of second type void waveforms decreases sharply at a gas flow rate of 20.0 l/min, hence an unstable slug flow is achieved. However, the bubbles in this

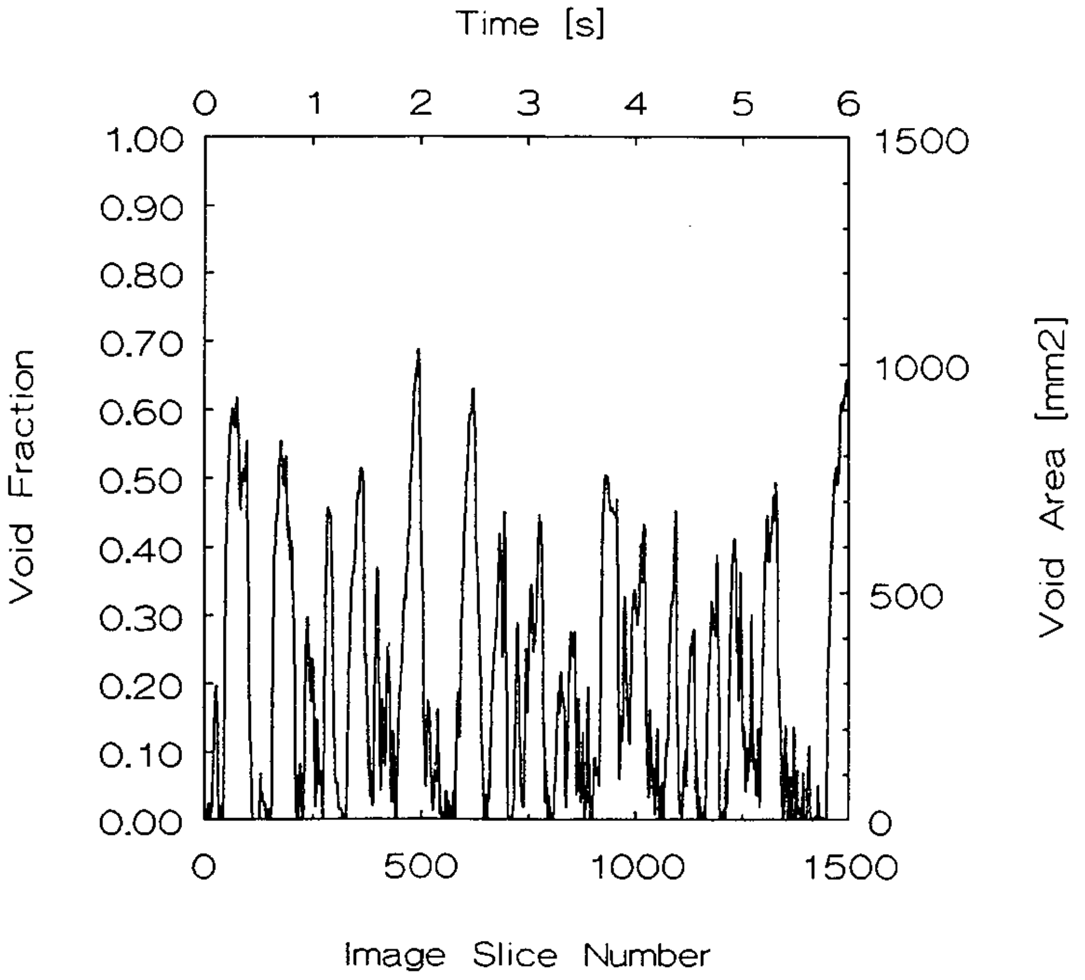

Figure 6.14: Void Fraction History of Two-Phase Flow in a Vertical Annulus Flow Channel for a Gas Flow Rate of 15.0 l/min and a Static liquid level of 60.0 cm

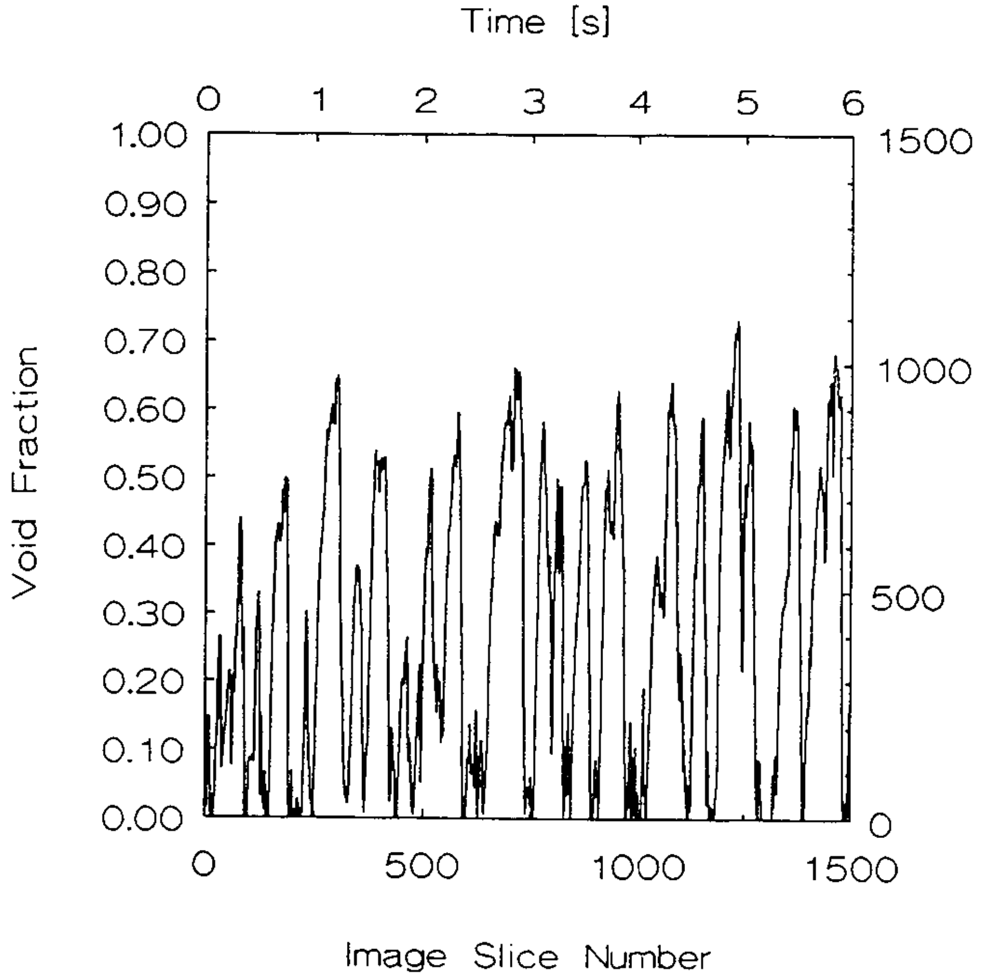

Figure 6.15: Void Fraction History of Two-Phase Flow in a Vertical Annulus Flow Channel for a Gas Flow Rate of 25.0 l/min and a Static liquid level of 60.0 cm

flow regime do not reach 80% void fraction which is usually considered the correct order of magnitude for slug flow. Visual observations show the length of the bubbles are quite short, hence, the two-phase flow is still under-developed. The experimental data also shows an increase in the bubble lengths and frequencies as the gas flow rate increases.

Figure 6.16 shows the cross-sectional averaged void fraction histories for a liquid level elevation of 60.0 cm and steady-state gas flow rate of 5.0 l/min. The X-ray imaging plane is set to an elevation of 60.0 cm (5.0 cm lower than for Figures 6.14 and 6.15). Reconstructed images for cross-section numbers 222 to 231 of Figure 6.16 are shown in Figure 6.3.

Figure 6.16 shows similar trends as Figures 6.14 and 6.15. The maximum cross-sectional averaged void fraction increases with increasing gas flow rate and the frequency of the second type void waveforms decreases with increasing gas flow rate.

Figure 6.17 shows the cross-sectional averaged void fraction history for a stable Taylor bubble slug flow regime. The liquid level elevation at the initiation of the test is 60.0 cm and the X-ray imaging plane is located at an elevation of 80.0 cm. The gas flow rate is a short duration pulse to produce uniform drift velocity Taylor bubbles.

Figure 6.17 shows a very interesting cross-sectional averaged void fraction history. At first, the void fraction is 100% as the static liquid level elevation is lower than the X-ray imaging plane elevation. As the gas pulses into the test section, the dynamic liquid level increases to a higher elevation. At approximately 800.0ms, the liquid level passes through the X-ray imaging plane and the void fraction drops sharply to 0%. At approximately 1.8s, the nose of the Taylor bubble passes through the imaging plane and the cross-sectional averaged void fraction increases sharply. The maximum void fraction observed for the Taylor bubble is approximately 83% and occurs near the tail. At approximately 2.5s, the tail of the Taylor bubble passes through the test section and the cross-sectional averaged void fraction decreases sharply. From 2.5s to approximately 3.25s, the void fraction changes rapidly, hence there is entrainment in the liquid slug. At 3.25s, an incompletely formed Taylor

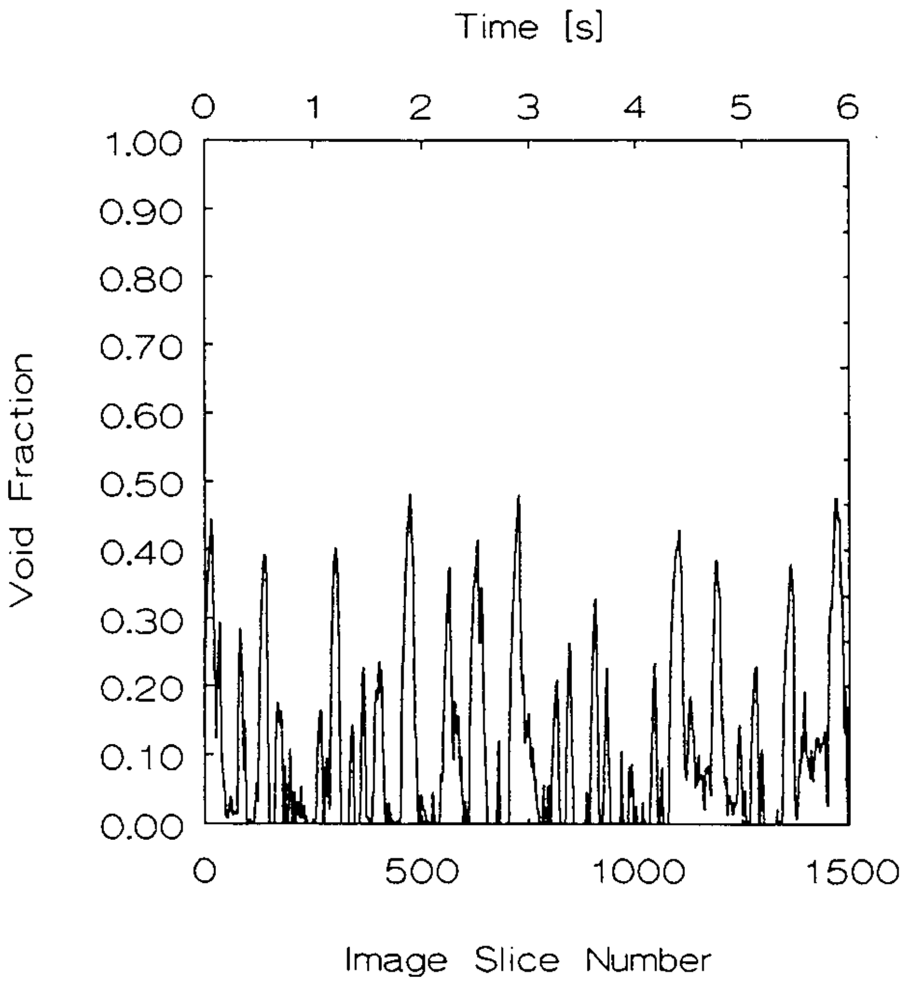

Figure 6.16: Void Fraction History of Two-Phase Flow in a Vertical Annulus Flow Channel for a Gas Flow Rate of 5.0 l/min and a Static liquid level of 60.0 cm and a Imaging Elevation of 60.0 cm

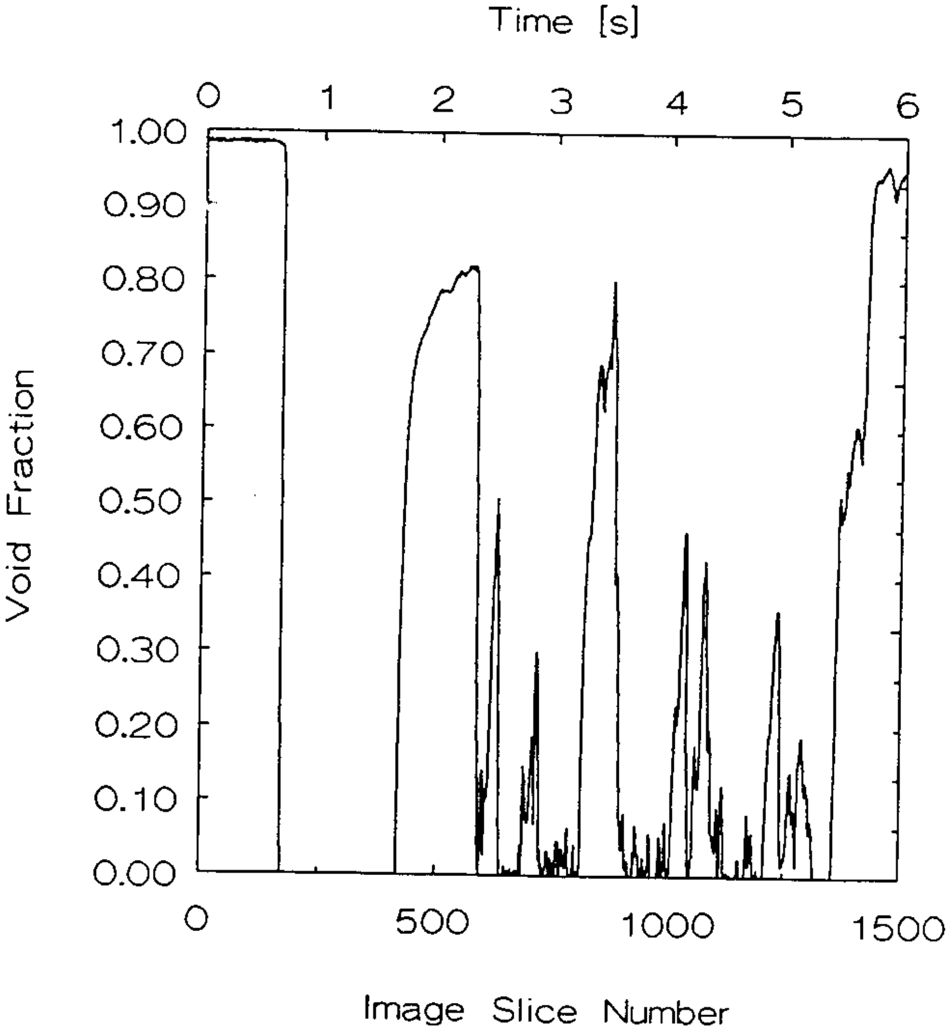

Figure 6.17: Void Fraction History of Two-Phase Flow in a Vertical Annulus Flow Channel for a Pulsed Gas Flow Rate to Produce a Drift Velocity Taylor Bubble and a Static liquid level of 80.0 cm

bubble enters the X-ray imaging plane followed by many bubbles of different sizes. At 5.5s, most of the gas injected into the test section has passed through the X-ray imaging plane. The cross-sectional averaged void fraction will increase again as the dynamic liquid level is decreasing in elevation and a packing of very small bubbles or froth is usually present very close to the dynamic liquid level. The rate of decrease of the elevation of the dynamic liquid level is very slow as the bubbles are quite small and are moving slowly.

Figure 6.18 shows the cross-sectional averaged void fraction histories for high gas flow rates (>30.0 l/min) and low liquid levels at an elevation of 20.0 cm respectively. The X-ray imaging plane is located at an elevation of 60.0 cm. The gas flow rate cannot be accurately measured here as the gas flow rates are beyond the range of the gas flow meter and the test cases display transient behaviour.

Figure 6.18 shows very high void fractions. The cross-sectional averaged void fraction at 0.0s is 100% as the dynamic liquid level is at an elevation of 20.0 cm, well below the detector level of 60.0 cm. For a gas flow rate greater than 30.0 l/min (Source Pressure 5.0 kg/cm^2), small droplets of liquid will be entrained into the gas flow. These droplets will pass through the X-ray imaging plane and deposit on both walls of the annulus test section. The droplets move circumferentially along either tube wall until they reach the region where the two tubes are closest to each other. At this point, the direction of the liquid is mostly downwards and the droplets may form to create a falling film. At close to 1.0s, the first such film is formed. Subsequent films are smaller as some liquid is carried over into the overflow tank and due to a constantly decreasing gas pressure. The gas pressure is decreasing as the air compressor tank is too small to maintain a constant pressure at such high gas flow rates. The increase in liquid volume ensures more liquid is moved upwards by the gas flow.

At approximately 1.0s, the void fraction decreases sharply. The liquid is pulled along by the gas as a film on both walls and the liquid oscillates up and down as a film in the X-ray imaging plane. In some cases, the liquid will bridge the gap between the inner and outer tube but the liquid bridge is usually broken very quickly

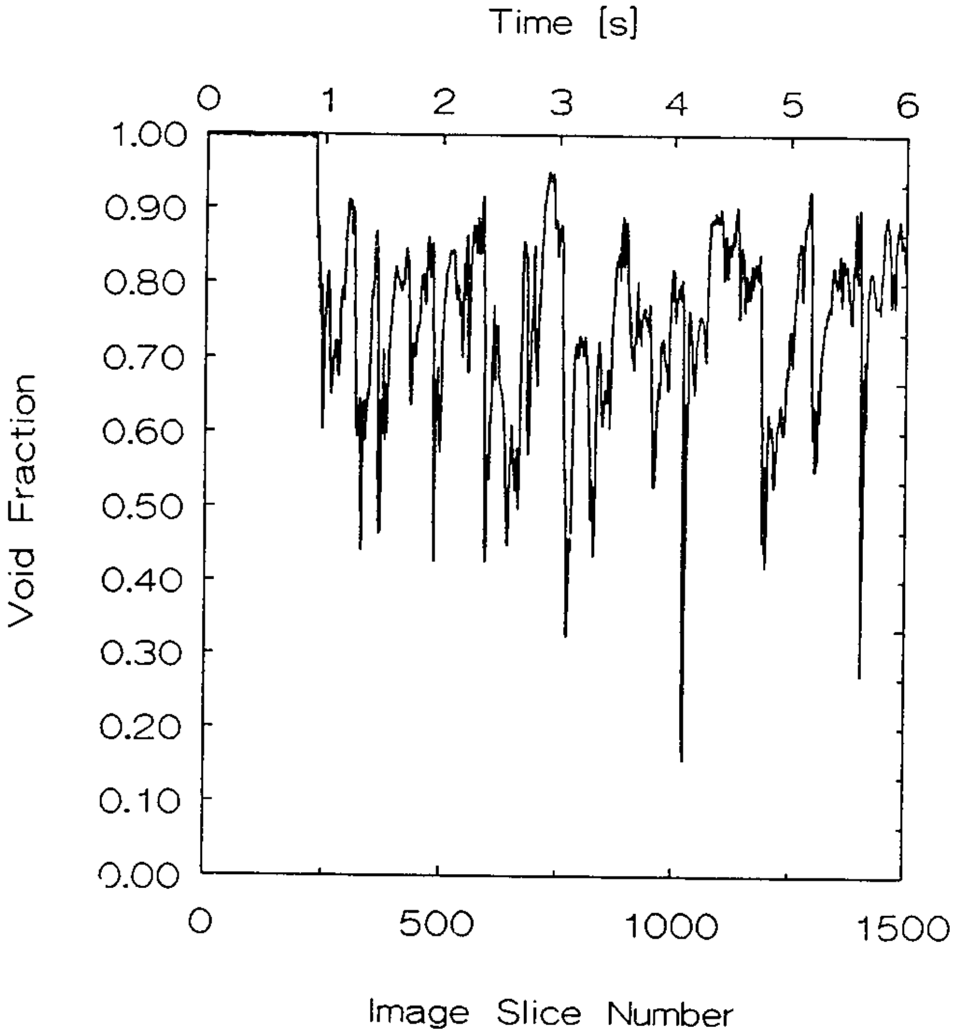

Figure 6.18: Void Fraction History of Two-Phase Flow in a Vertical Annulus Flow Channel for a Maximum Gas Flow Rate (>30.0 l/min) and a Static liquid level of 20.0 cm

afterwards. The nature of the flow is more violent than in the previous case and vibration of the inner tube is observed by the optical video system.

6.2.2 Cross-Sectional Averaged Void Fraction Determined by RTNR System

Several experiments have been performed to obtain cross-sectional averaged void fraction in an annulus flow channel. Figures 6.19 to 6.22 show cross-sectional averaged void fraction profiles along the vertical axis of the annulus flow channel for various gas flow rates and static liquid levels. Experimental results for heavy water (D_2O) are shown in Figures 6.19 to 6.21 and 6.22 for static liquid levels of 60.0 cm and 40.0 cm respectively. Experimental results for void fraction with light water (H_2O) as the working fluid have also been performed. For each figure, the x-axis is the vertical axis of the annulus flow channel and the y-axis is the cross-sectional averaged void fraction.

Experimental results of cross-sectional averaged void fraction at a static liquid level of 60.0 cm for gas flow rates of 2.0, 9.3, and 13.1 l/min are shown in Figure 6.19. Without gas flow (0.0 l/min), the void fraction at an elevation of z = 60.0 cm is approximately 50% as this is the location of the interface. The calculated void fraction never quite reaches 1.0 due to statistical noise inherent in the neutron beam. The cross-sectional averaged void fraction decreases with increasing vertical elevation (z) as the target integration effects cannot be completely corrected, especially at the edges of the image. As the gas flow rate increases, the liquid level increases and the void fraction gradient at the interface decreases. The cross-sectional averaged void fraction below the interface remains below 0.2. The interface between the gas and the two-phase flow increases beyond the viewing area with increasing gas flow rate. The void fraction at each point along the axis also increases with increasing gas flow rate. At 13.1 l/min, the cross-sectional averaged void fraction along the vertical axis increases non-linearly. This type of cross-sectional averaged void fraction profile shows slug or churn flow exists as large bubbles or groups of bubbles are travelling together. Figure 6.19 shows that axial void fraction profiles are non-monotonic along

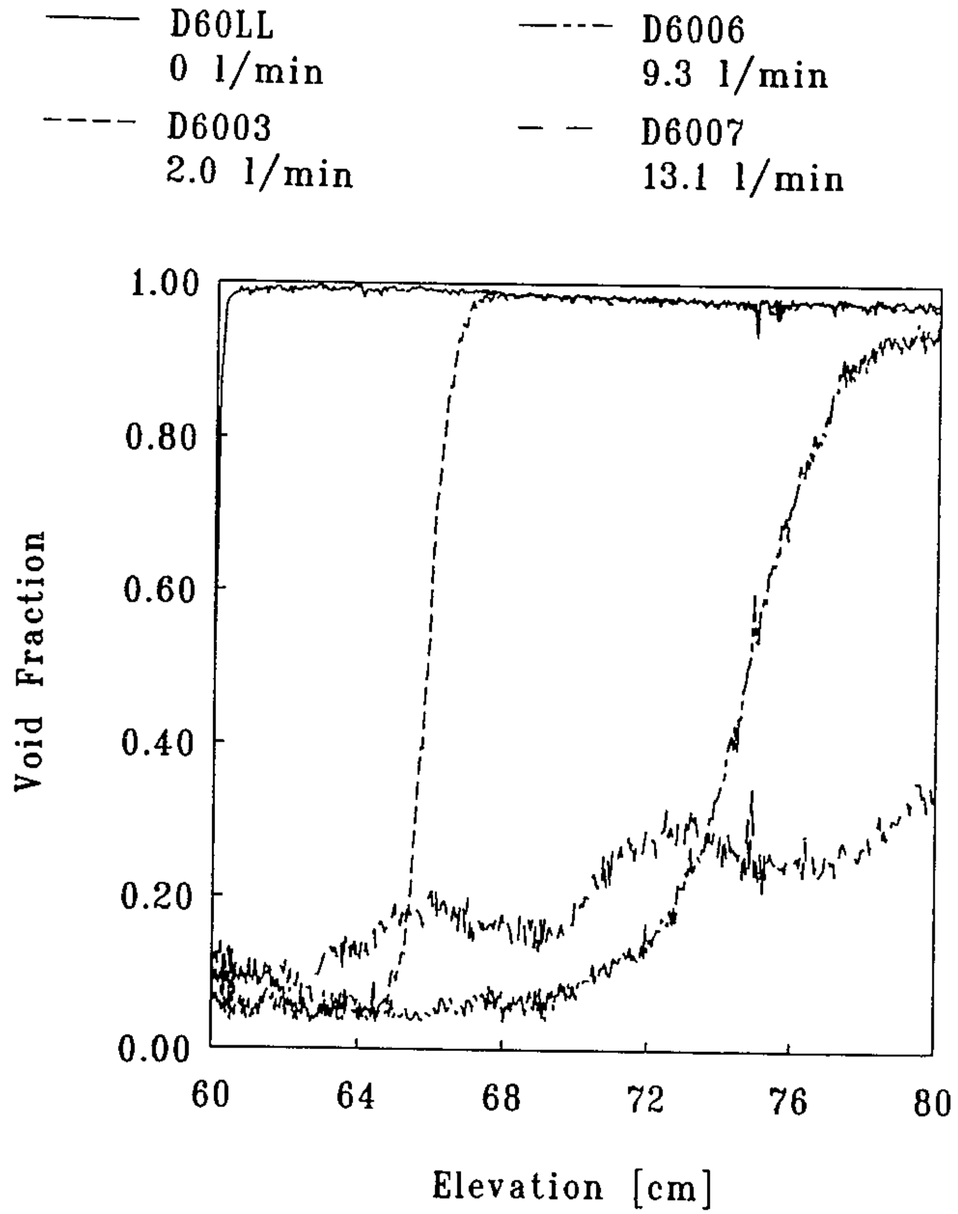

Figure 6.19: Cross-Sectional Averaged Void Fraction by RTNR system for a Static liquid level of 60.0 cm of D_2O and Gas Flow Rates from 0.0 to 13.1 l/min

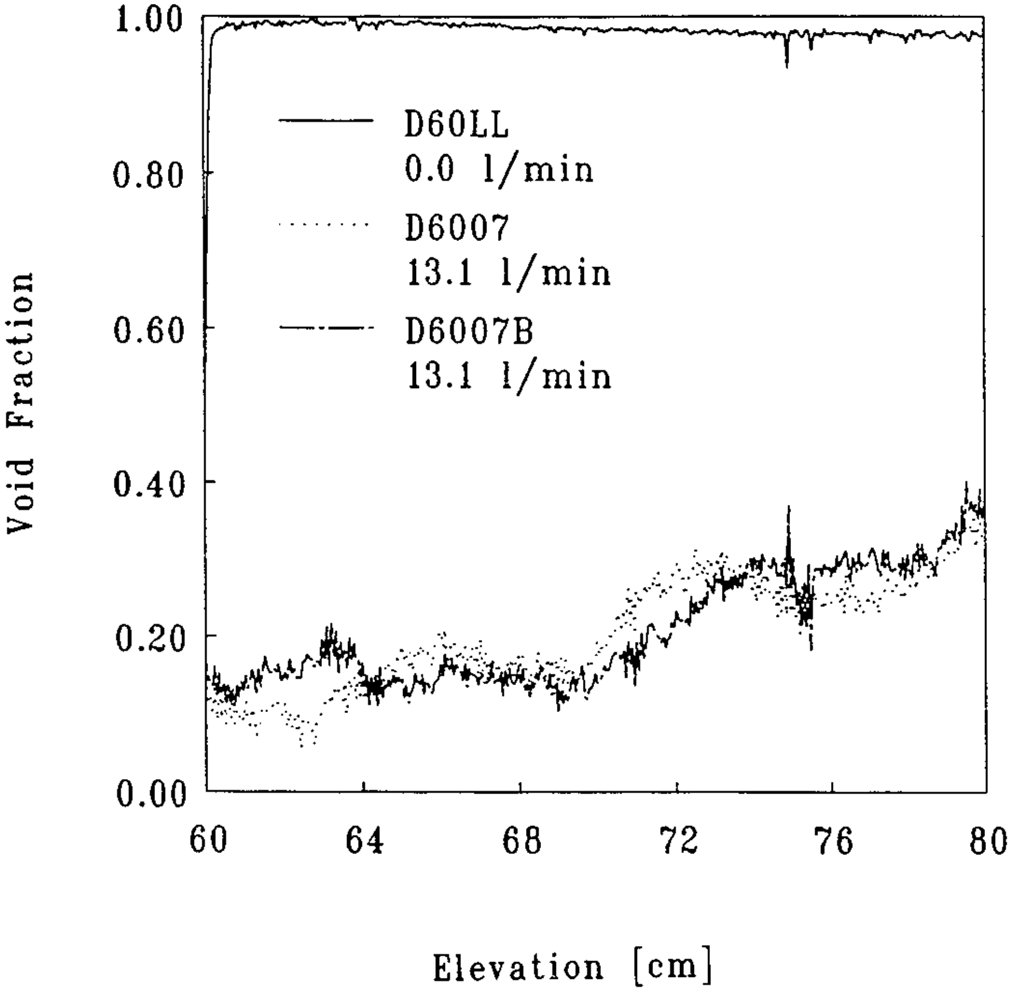

Figure 6.20: Two Cross-Sectional Averaged Void Fraction by RTNR system for a Static liquid level of 60.0 cm of D_2O for a Gas Flow Rate of 13.1 l/min where Test D6007B is Acquired approximately 10.0 s after Test D6007

the vertical axis, where the minimum void fraction is always observed at a given location depending on the gas flow rates inside the two-phase column.

Figure 6.20 shows two cross-sectional averaged void fraction profiles for a gas flow rate of 13.1 l/min at a static liquid level of 60.0 cm at different times. Here, the fluctuation in the cross-sectional averaged void fraction at a given elevation is 0.5 cm and the minimum to maximum void fraction fluctuation is approximately 20%. This means that the two profiles show the two-phase flow has a cyclic component typical of either slug flow or churn flow. The cross-sectional averaged void fraction fluctuations are shown to increase with increasing gas flow rate and increasing void fraction.

Axial void fraction profiles of pulsed gas flow is shown in Figure 6.21 for a 60.0 cm static liquid level. The cross-sectional averaged void fraction profile shown in Figure 6.21 is obtained from the image shown in Figure 6.11. The dynamic liquid level is shown to occur at a liquid level near 76.0 cm. The large Taylor bubble shown in Figure 6.11 appears as a broad peak with a maximum cross-sectional averaged void fraction of 0.6. The nose of the Taylor bubble is located near 72.0 cm and the tail is located near 62.0 cm. The gradual increase in void fraction along the Taylor bubble may be caused by two factors. The actual shape of the Taylor bubble is a well rounded elongated nose as shown in Figure 6.9 by the optical video camera system. The first factor is the interlaced scanning of the RTNR system which overlays two fields into one frame. Each frame is acquired in time 1/60 s apart. The bubble is in a different location in each field and the result is a distorted image. The second factor is caused by the inherent time averaging of the Real-Time Neutron Radiography system. The sampling time for the RTNR system is 33.0 ms and a bubble can travel over several vertical pixels in this time period.

Figure 6.22 shows the cross-sectional averaged void fraction for a static liquid level of 40.0 cm for gas flow rates of 19.91, 25.13, and 31.27 l/min. The elevation of the gas-liquid interface increases and blurs with increasing gas flow rate. The local void fraction increases with increasing gas flow rate. The noise level in the cross-sectional averaged void fraction increases with increasing gas flow rate. Although not

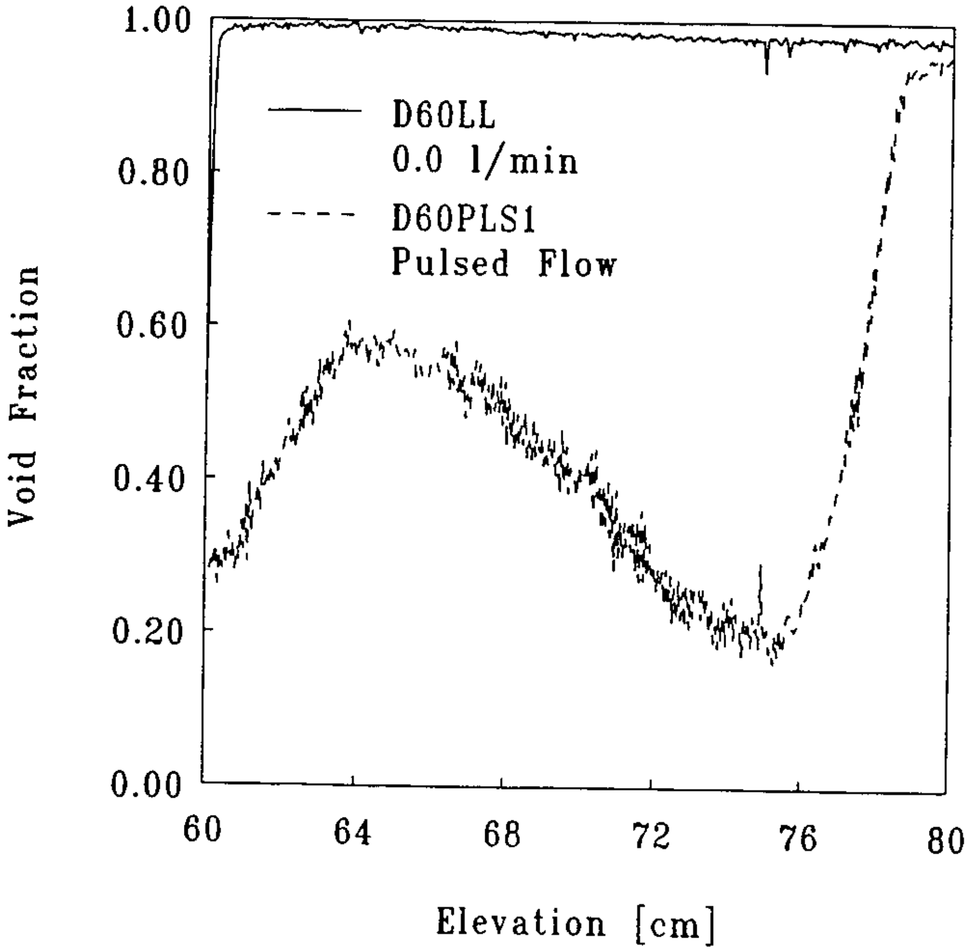

Figure 6.21: Cross-Sectional Averaged Void Fraction by RTNR system for a Static liquid level of 60.0 cm of D_2O with a Pulsed Gas Flow: Taylor Bubble of Figure 6.12

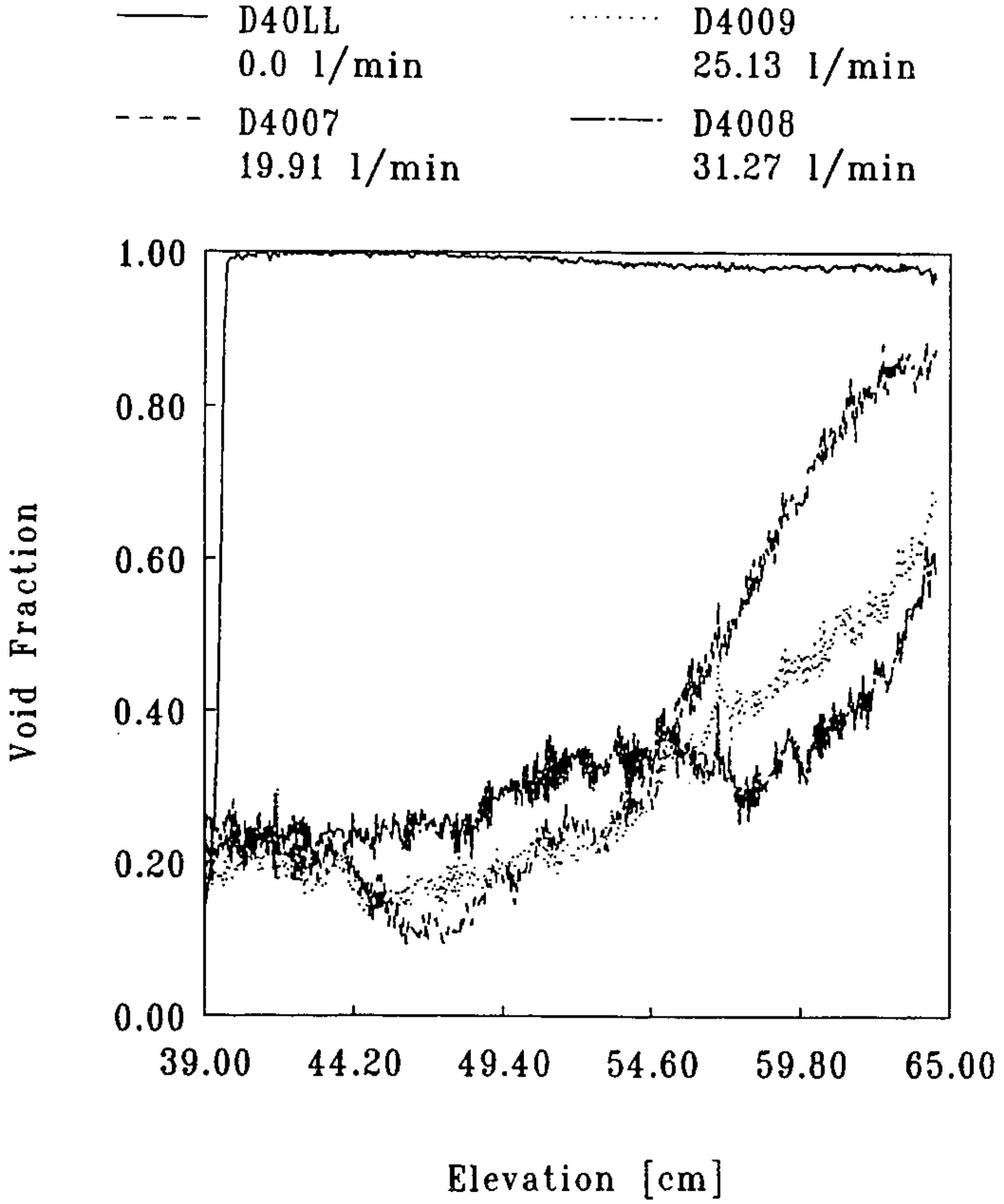

Figure 6.22: Cross-Sectional Averaged Void Fraction by RTNR system for a Static liquid level of 40.0 cm of D_2O for Gas Flow Rates from 19.9 to 31.3 l/min

shown in this figure, an oscillation is introduced after 5.0 l/min due to a change in flow regime. This means that the cross-sectional averaged void fraction profiles shown for gas flow rates above 5.0 l/min are specific to one image and do not represent time averaged results.

Figure 6.23 shows the dynamic liquid levels measured for each gas flow rate for two sets of experiments. The first experiment is performed at an initial liquid level of 40.0 cm and the second experiment is performed at an initial liquid level of 60.0 cm. The liquid levels are shown to increase with increasing gas flow rate although the measurements after 5.0 l/min cannot represent time averaged results. The results show that the dynamic liquid level has a decreasing slope with respect to the gas flow rate as the gas flow rate is increasing. This suggests the dynamic liquid level will eventually reach a maximum value at much higher gas flow rates than studied in this work but this is probably not correct. Instead, two relationships, one for smaller liquid levels and one for higher liquid levels, are more likely where the transition from one relationship to the next represents a flow regime change. Further measurements of dynamic liquid level are necessary to determine, if two relationships are needed for a more accurate representation and the transition criteria necessary.

6.2.3 Comparison of RTNR and X-CT Void Fraction Measurement Techniques

Direct real-time comparison of the cross-sectional averaged void fraction between the High Speed X-ray CT system and the Real-Time Neutron Radiography system is limited as the experiments cannot be performed simultaneously. Hence, time and cross-section averaged results are compared. Figures 6.24 and 6.25 show experimental results for time and cross-section averaged void fraction as related to the superficial gas velocity for both advanced radiation techniques at initial static liquid levels of 40.0 cm, 60.0 cm, and 80.0 cm. All High Speed X-ray CT measurements shown in Figures 6.14 to 6.18 are time averaged for the 6.0 s experiment time and are shown in Figure 6.24 and Figure 6.25 for 60.0 cm and 80.0

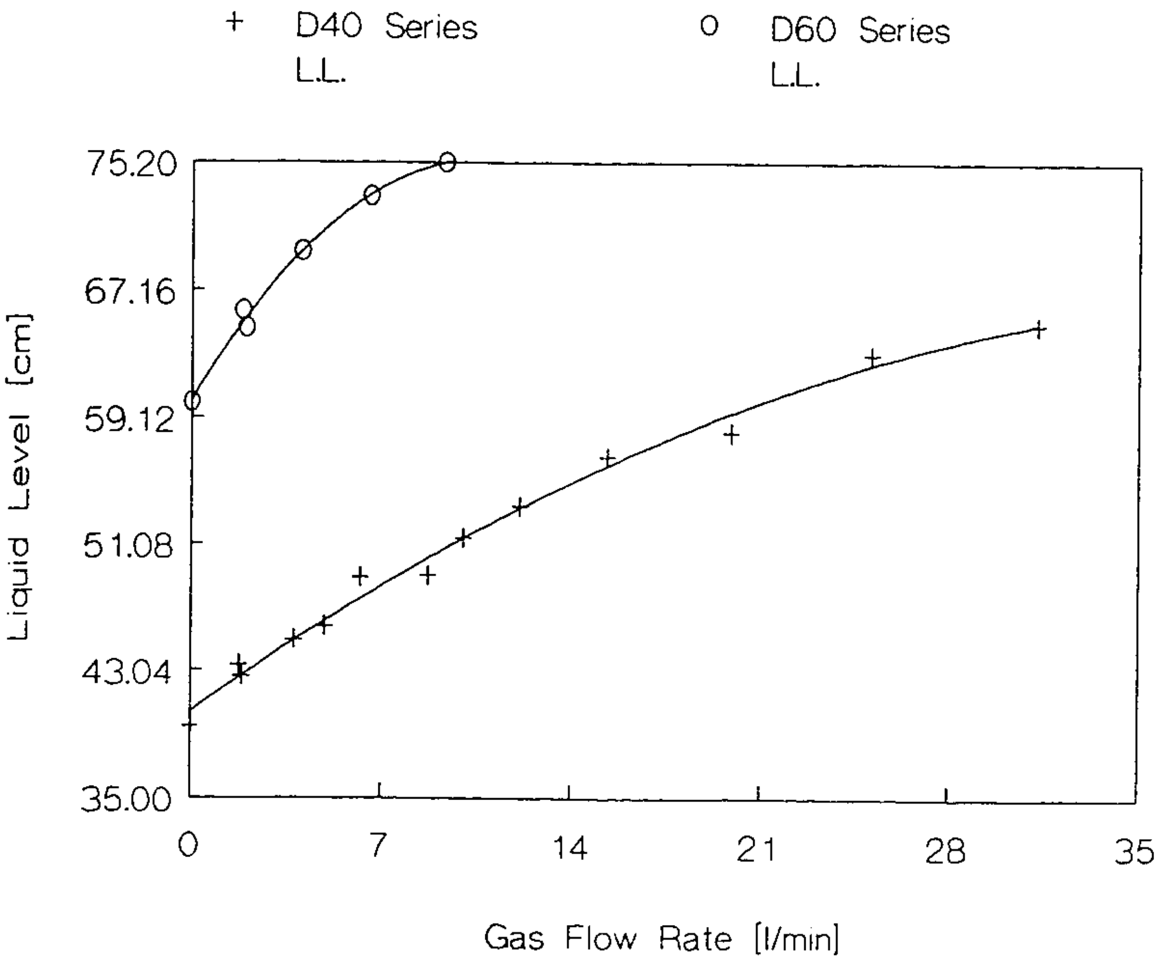

Figure 6.23: Dynamic liquid level Measurements for Various Gas Flow Rates obtained by Real-Time Neutron Radiography

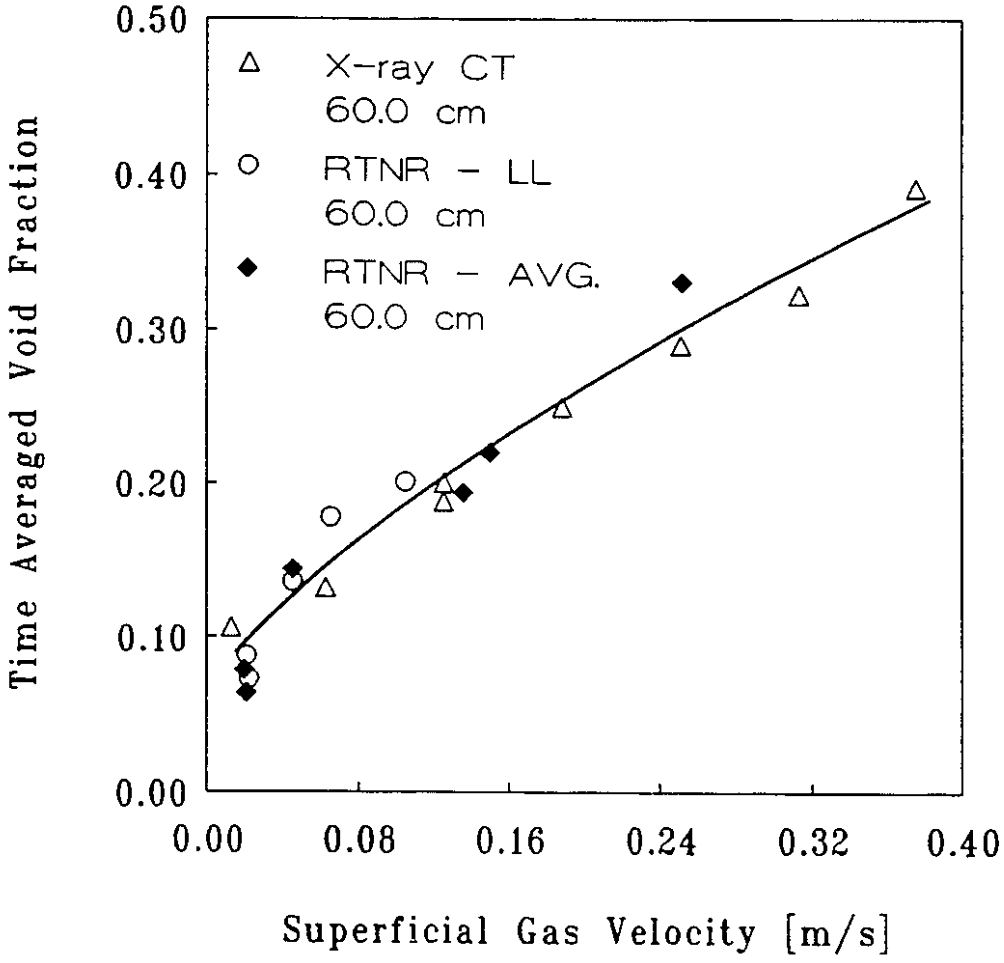

Figure 6.24: Time Averaged Void Fraction by Real-Time Neutron Radiography and High Speed X-ray CT Measurements: Static Liquid Level = 60.0 cm.

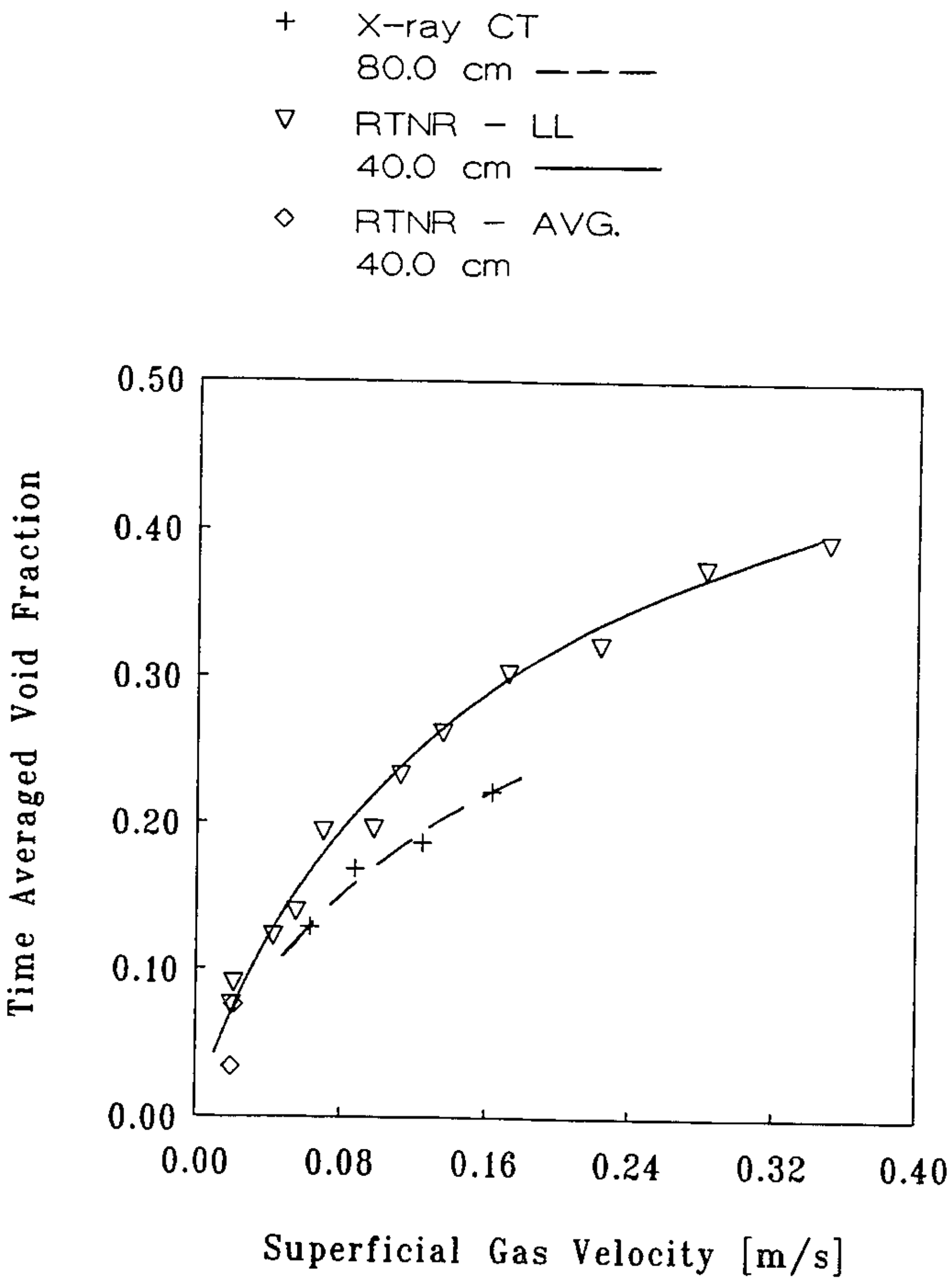

Figure 6.25: Time Averaged Void Fraction by Real-Time Neutron Radiography and High Speed X-ray CT Measurements: Static Liquid Level = 40.0 cm and 80.0 cm.

cm static liquid levels respectively. The dynamic liquid levels observed by the Real-Time Neutron Radiography system are used to calculate the time and volume averaged void fraction for a 40.0 cm static liquid level as shown in Figure 6.25. Time and volume averaged void fractions based on measured dynamic liquid levels for a 60.0 cm static liquid level are shown in Figure 6.24. Time and cross-section averaged void fraction observed by the Real-Time Neutron Radiography system is also shown in Figures 6.24 and 6.25 for a 60.0 cm and a 40.0 cm static liquid level respectively. The time and cross-section averaged void fractions for the 60.0 cm static liquid level are obtained at the same axial location (z=65.0 cm) for both the High Speed X-ray CT system and the RTNR system.

Figures 6.24 and 6.25 show the void fraction increases with increasing superficial gas velocity as more gas is remaining in the liquid volume. Between superficial gas velocities of 0.0 m/s and 0.1 m/s, the agreement between the void fraction determined by the RTNR system and the High Speed X-ray CT system has a 4% variation. Above a superficial gas velocity of 0.1 m/s, the agreement is still good but with an increased error. This discrepancy may be due to the fact that the higher superficial gas velocity results are for slug flow and churn flow whereas the void fraction results below 0.1 m/s are for bubbly flow. Slug flow and churn flow have a cyclic nature and the time averaging by the High Speed X-ray CT and RTNR systems may not be adequate or the liquid level measurements obtained by the RTNR system may need better time averaging. This means that a large temporal fluctuation as seen in slug flow may require much longer time averaging than in the present experiments. In either case, the agreement is adequate and these discrepancies can be minimized with more extensive analysis in the future.

Figures 6.24 and 6.25 also show the variation of the time and cross-sectional averaged void fraction is not significantly dependant on the static liquid level. This result is somewhat surprising but is best explained as the static liquid levels studied in this work do not represent a sufficient range for an observable effect upon the time and cross-sectional averaged void fraction.

6.3 Measurement of Void Fraction Distribution

6.3.1 Temporal Void Fraction Measurements

Figure 6.26 shows four axial profiles of the cross-sectional averaged void fraction for a gas flow rate of 22.5 l/min. These profiles show the passage of a large bubble as time progresses. The low void fraction values near an elevation of 60.0 cm are due to poor sensitivity at the edge of the camera view field. The void fraction maximum increases in magnitude and elevation as time increases.

This is shown more clearly in Figure 6.27. Figure 6.27 shows the temporal behaviour of the void fraction at elevations of 60.0, 65.0, 70.0, 75.0, and 80.0 cm. The void fraction ranges from close to zero to as high as 0.6 for each elevation. This is in keeping with slug flow behaviour and shows similar results as the X-ray CT system as shown by Figure 6.15. Figure 6.27 also shows the void fraction maximum at each location is changing in time. This shows the bubble propagation along the axial direction of the flow channel as will be discussed further.

The experimental results for cross-sectional averaged void fraction obtained by the Real-Time Neutron Radiography system (RTNR) and the High Speed X-ray Computed Tomography system (X-CT) are not directly comparable as the X-CT system measures only one location in time and the RTNR system measures several locations instantaneously.

One method for comparison is to convert the X-CT results into an equivalent distance. This can be achieved using the slice time and the superficial gas velocity as follows:

$$d_{eq}=U_{gs}t_{slice}=Q_gAt_{slice} \tag{6.1}$$

This equation achieves a calculated void fraction profile that shows the cross-sectional averaged void fraction for a simulated length. Unfortunately, this simulated

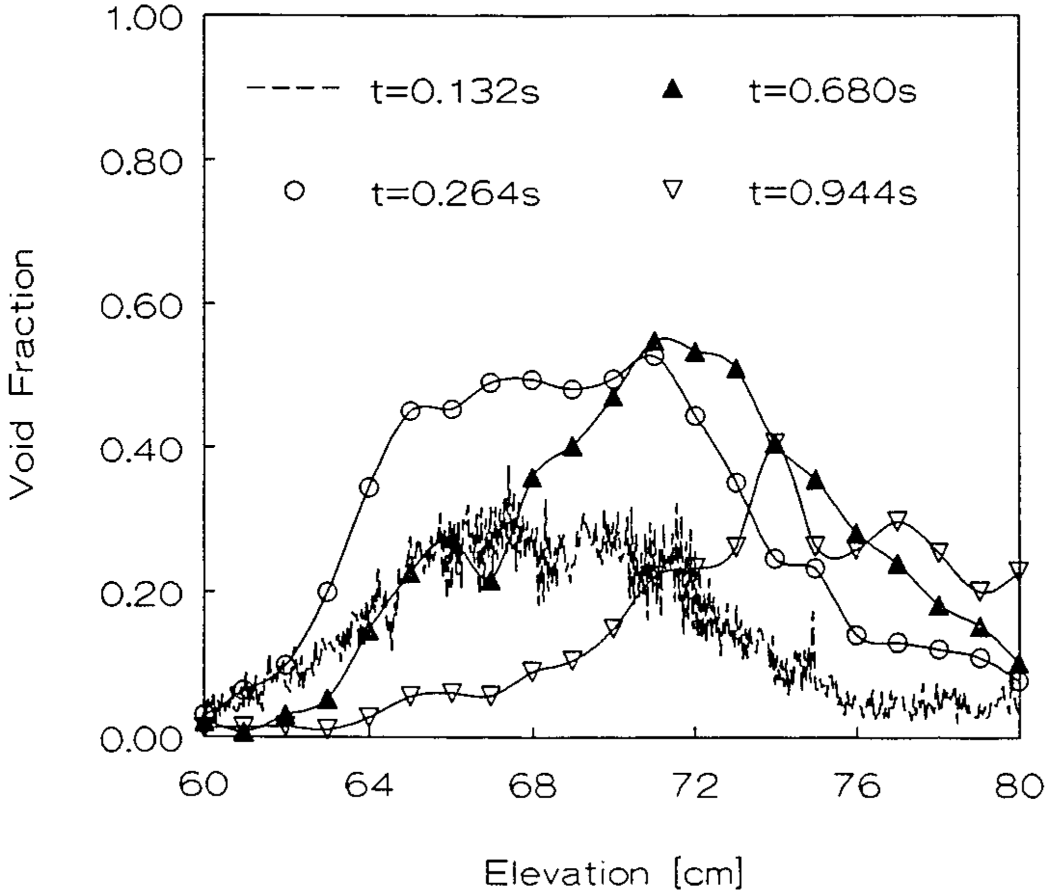

Figure 6.26: Cross-Sectional Averaged Void Fraction Profiles for a Vertical Annulus Flow Channel with a Gas Flow Rate of 22.5 l/min at Times 0.132 s, 0.264 s, 0.68 s, and 0.944 s.

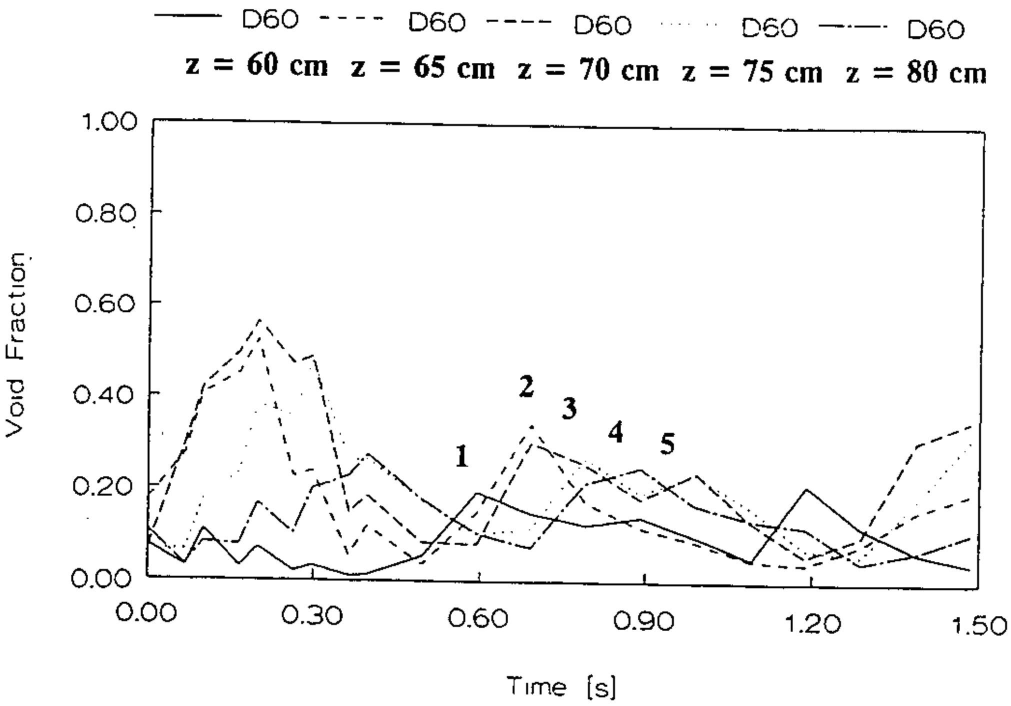

Figure 6.27: Void Fraction Fluctuations in a Vertical Annulus Flow Channel for a Gas Flow Rate of 22.5 l/min at axial Elevations of 60.0 cm, 65.0 cm, 70.0 cm, 75.0 cm and 80.0 cm.

void fraction profile will not be equivalent to the RTNR void fraction profiles for two reasons. The first reason is that the superficial gas velocity is used instead of the true gas velocity. The second reason is that flow development and liquid level are not accounted for. I.e. accelerational effects, different bubble velocities, and agglomeration will not be included.

Some work has been done to measure the fluctuations in the cross-sectional averaged void fraction in a vertical annulus flow channel by Real-Time Neutron Radiography(RTNR). The DT-2861 image processing board is used to acquire every fourth frame for a total of 16 frames. Every fourth image is 132.0 ms apart in time. Software is used to correct the images and calculate the cross-sectional averaged void fraction at each location along the axis.

Figure 6.28 shows temporal fluctuations in the cross-sectional averaged void fraction for a period of 2.0 seconds at a gas flow rate of 6.0 l/min. This test case is bubbly flow with some agglomeration of the bubbles occurring. Figure 6.28 shows the void fraction fluctuations for elevations of 60.0 cm, 65.0 cm and 70.0 cm where the static liquid level is 60.0 cm.

In general, the averaged void fraction increases as the elevation increases and the void fraction fluctuation varies from 5% to 12% depending on the gas flow rate and the elevation. Lower elevation fluctuations are small and do not show any aglommeration. Higher elevation void fraction fluctuations show the presence of large bubbles due to aglommeration.

Figures 6.29 and 6.30 show temporal fluctuations in the cross-sectional averaged void fraction at several different axial elevations for gas flow rates of 9.0 and 14.0 l/min respectively. In both cases, the void fraction fluctuations have periodic maximums indicating the passage of bubbles. In Figure 6.30, where slug flow occurs, the void fraction maximums are regularly spaced. In fact, it is possible to correlate the void fraction maximums from two different axial locations as shown by the arrows indicating the maximums which correspond to a single evolving bubble.

The observation of temporal and spatial variations in the void fraction is difficult from analyzing one or two axial locations. A software routine,

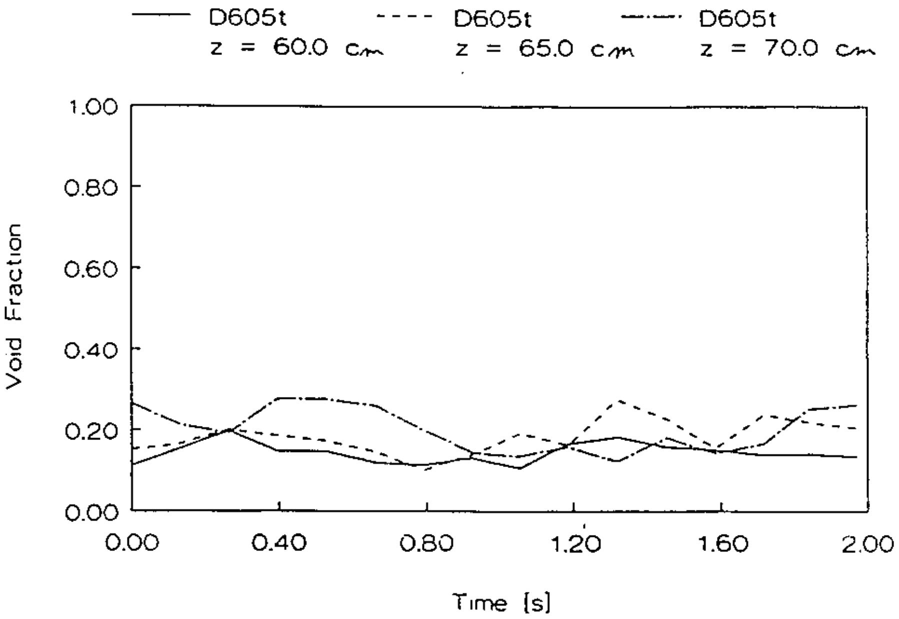

Figure 6.28: Void Fraction Fluctuations in a Vertical Annulus Flow Channel for a Gas Flow Rate of 6.6 l/min at axial elevations of 60.0 cm, 65.0 cm, and 70.0 cm.

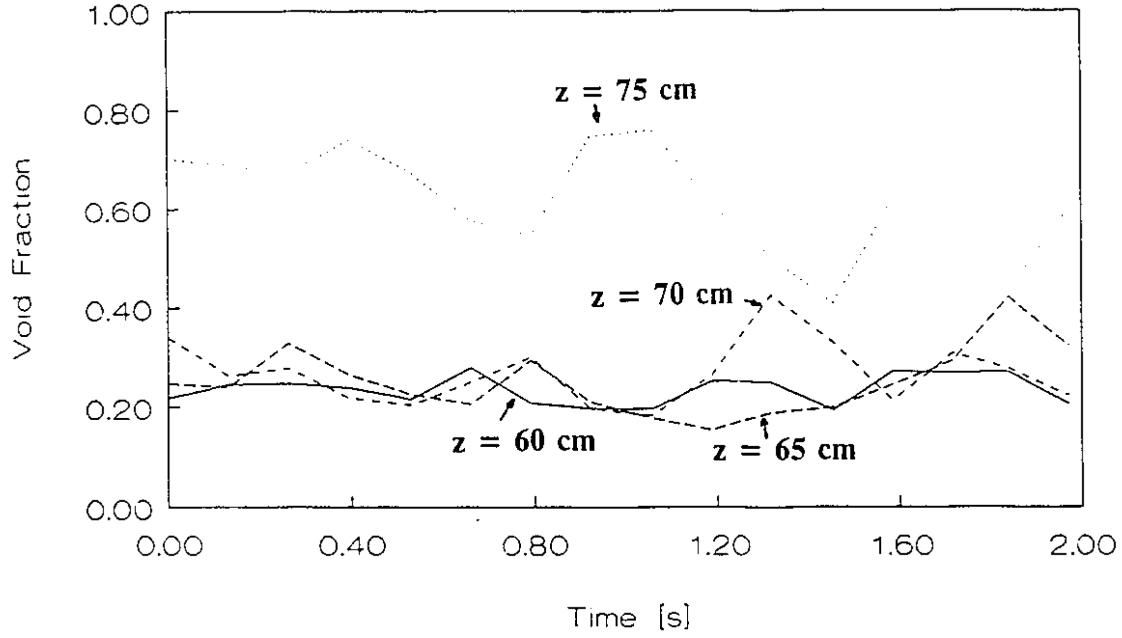

Figure 6.29: Void Fraction Fluctuations in a Vertical Annulus Flow Channel for a Gas Flow Rate of 9.0 l/min at axial Elevations of 60.0 cm, 65.0 cm, 70.0 cm, and 75.0 cm.

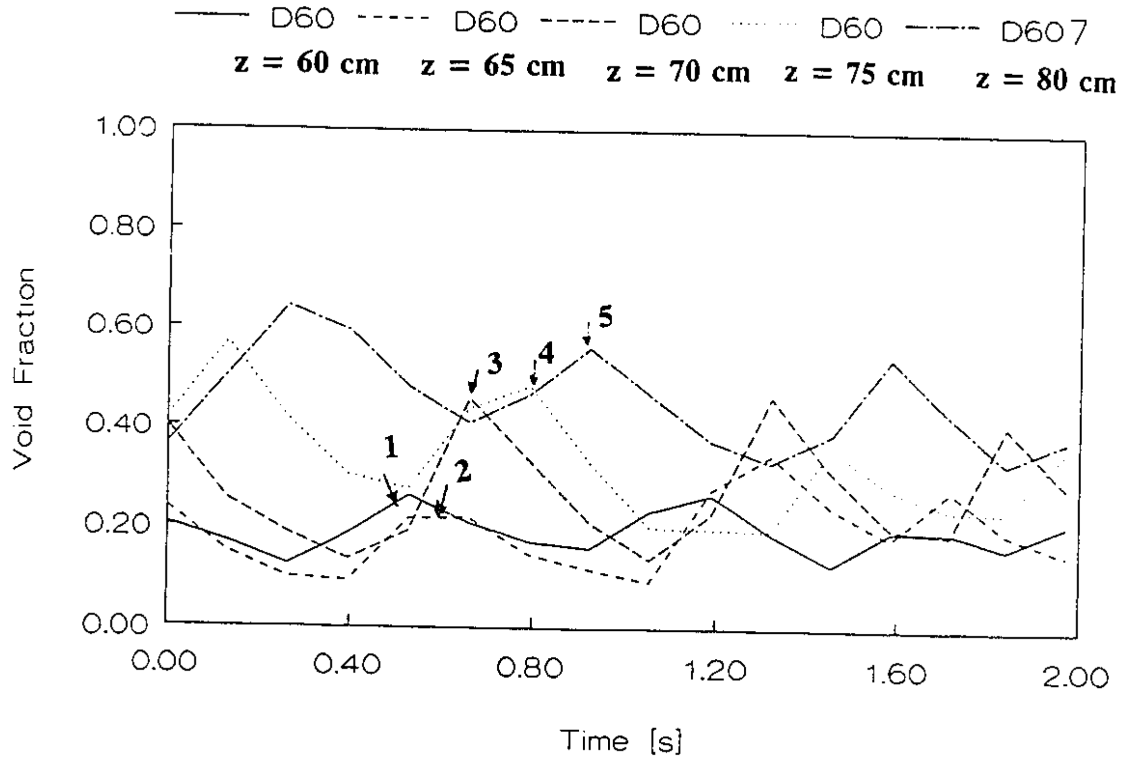

Figure 6.30: Void Fraction Fluctuations in a Vertical Annulus Flow Channel for a Gas Flow Rate of 14.0 l/min at axial Elevations of 60.0 cm, 65.0 cm, 70.0 cm, 75.0 cm and 80.0 cm.

ZTCONT.FOR, has been written which creates a data file for the *SURFER* contour plotting software. ZTCONT formats the data file such that time (t) is on the x-axis and axial location (z) is on the y-axis. The contour plot produced represents the cross-sectional averaged void fraction at each axial location in an RTNR image as a function of time. The software routine can only include 14 different files due to the nature of Fortran programming.

Figures 6.31, and 6.32 show void fraction contour maps in the z-t plane ($\alpha(z,t)$)for gas flow rates of 9.0, and 14.0 l/min respectively. Typically, Figure 6.31 is bubbly flow, and Figure 6.32 is slug flow. Figure 6.31 corresponds to the data shown in Figure 6.29 and Figure 6.32 corresponds to the data shown in Figure 6.30. In Figure 6.31, the void fraction contours do not significantly change in time, although some temporal variation in the void fraction contours is shown due to bubble coalescence. This is typical for bubbly flow. Figure 6.32 shows significant disturbances in the void fraction contours with respect to time truly indicating slug flow as the nature of the pattern is repeatable.

Figure 6.33 is a void fraction contour plot in the z-t plane for the cross-sectional averaged void fraction data shown in Figure 6.27 for a gas flow rate of 22.5 l/min. In this case, the contours are inclined at some angle instead of being horizontal as previously seen for bubbly flow. The angle of inclination represents the velocity of the bubble as the contours show the propagation of the bubble in space-time coordinates.

6.3.2 Void Fraction Distribution by RTNR System

The Real-Time Neutron Radiography system can reconstruct a void fraction contour map of two-phase flow for pipe and annulus flow channels.

Figure 6.34 shows four 2D void contour maps for a static liquid level of 60.0 cm of D_2O for gas flow rates of 2.0, 6.6, and 9.3 l/min and for the pulsed flow experiment shown in Figure 6.11. The x-axis is the radial access with the centreline of the annulus flow channel on the right and the outer tube radius (R_o) on the left.

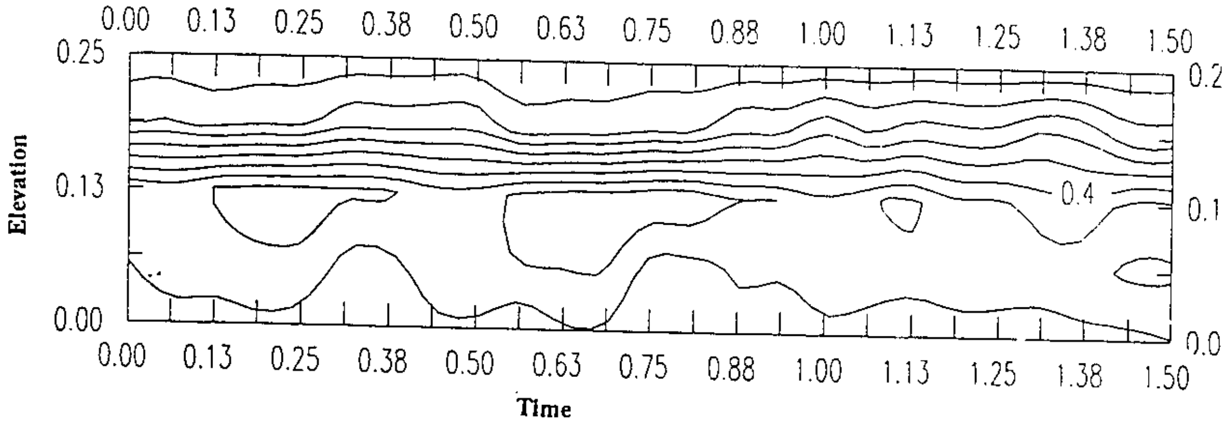

Figure 6.31: Axial-Time Contour Plot of Cross-Sectional Averaged Void Fraction at a Gas Flow Rate of 9.0 l/min.

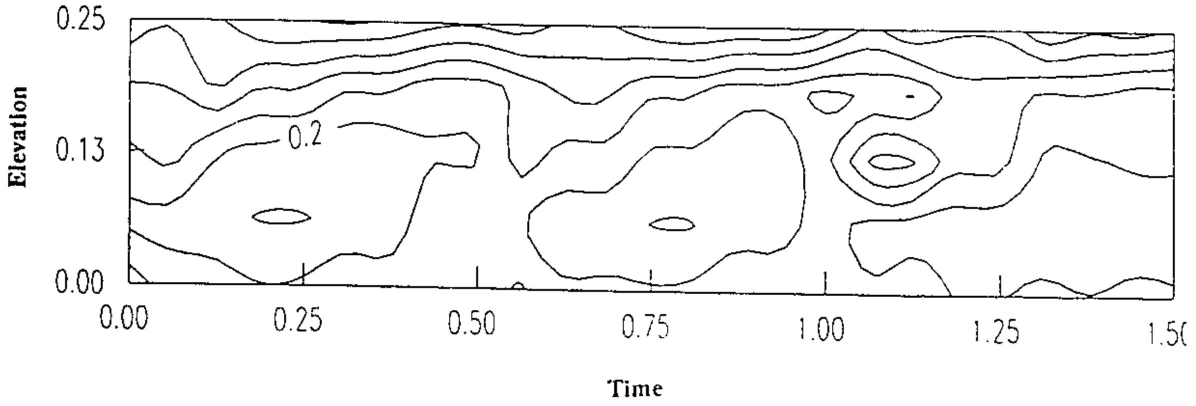

Figure 6.32: Axial-Time Contour Plot of Cross-Sectional Averaged Void Fraction at a Gas Flow Rate of 14.0 l/min.

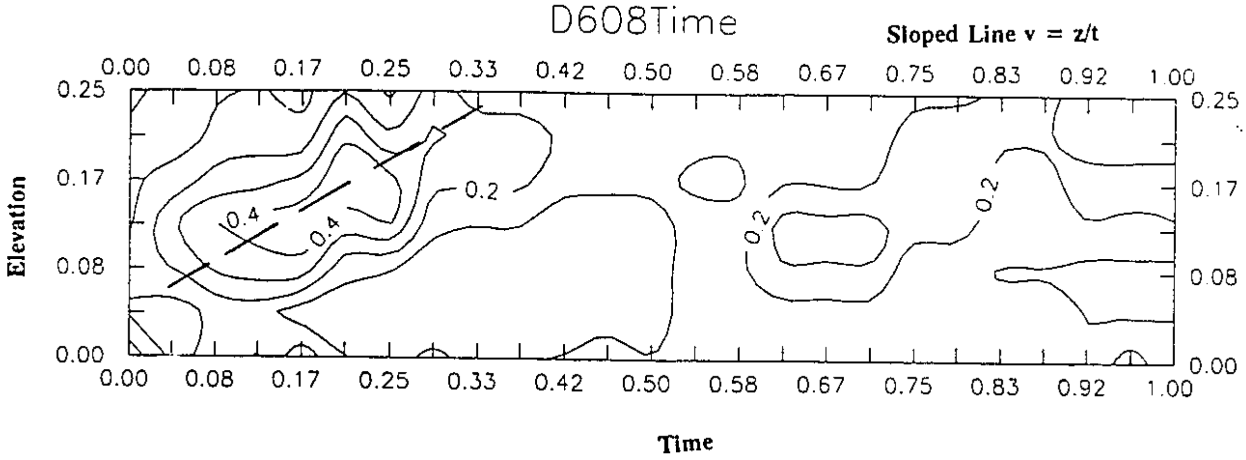

Figure 6.33: Axial-Time Contour Plot of Cross-Sectional Averaged Void Fraction at a Gas Flow Rate of 22.5 l/min.

The vertical dashed line is the location of the inner tube radius (R_i). The y-axis is the vertical axis of the flow channel from the gas injection point. In Figure 6.34a, the dynamic liquid level is shown near 65.0 cm. Above this point the void fraction is 1.0. The contour lines are in void fraction steps of 0.25 so that from right to left, the void fraction decreases as 1.0, 0.75, 0.5, 0.25, and 0.0 at the outer tube radius. Figure 6.34d shows the case of a Taylor bubble produced by pulsed flow. The Taylor bubble is located between 62.0 cm and 72.0 cm and is shown to occupy most of the flow channel area.

Figure 6.35 shows the 2D void fraction contour maps for a 60.0 cm static liquid level of D_2O for gas flow rates of 4.0 l/min and 13.1 l/min at two different points in time. This data is acquired from the same images that are used to calculate the cross-sectional averaged void fraction shown in Figure 6.20 for a gas flow rate of 13.1 l/min respectively. As shown in Figures 6.35a and 6.35b, the two-phase flow structure is not significantly changed. The dynamic liquid level occurs in approximately the same location and the void fraction is relatively unchanged in the flow channel. Figures 6.35c, 6.35d, and 6.20 show significant changes in the void distribution. This is apparent by studying the void distribution between 60.0 cm and 70.0 cm. Figure 6.35c shows a low void fraction region between 60.0 cm and 64.0 cm and a moderately high void fraction region between 66.0 cm and 70.0 cm whereas Figure 6.35d shows the opposite trends.

Figure 6.36 shows the 2D void fraction contour maps for heavy water with a static liquid level of 40.0 cm and gas flow rates of 5.0, 10.0, and 15.0 l/min. At 5.0 l/min, the interface is shown to be moderately flat with a small meniscus and very low void fraction in the two-phase region. At 10.0 l/min, the liquid level is no longer flat and increased wetting above the interface is noticed as shown in Figure 6.36b. Also, an increased turbidity in the two-phase region can be seen as the void fraction is no longer uniformly distributed. At 15.0 l/min, the interface is no longer sharp and the void fraction distribution is uneven.

Figure 6.37 shows the 2D void fraction contour maps with a static liquid level of 40.0 cm and gas flow rates of 6.25, 25.0, and 31.0 l/min. The experimental results

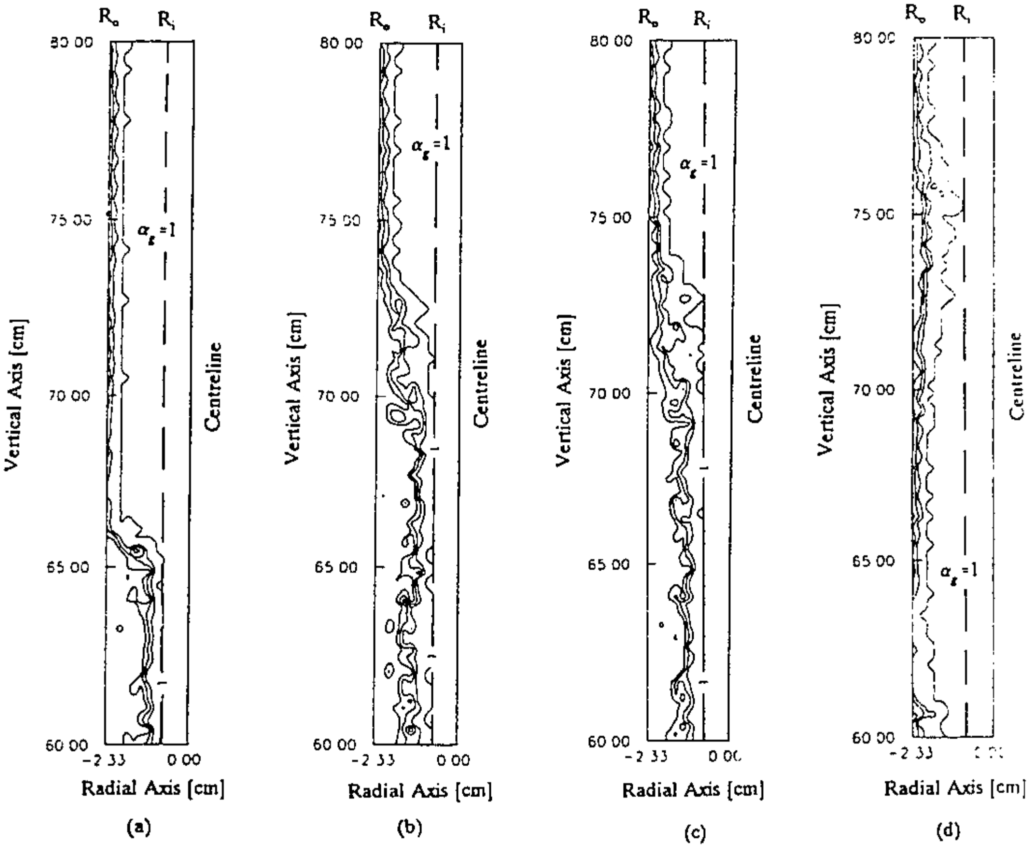

Figure 6.34: Void Fraction Contour Maps for a 60.0 cm Static Liquid Level of D_2O for Gas Flow Rates; (a) 2.0 l/min, (b) 6.6 l/min, (c) 9.3 l/min, (d) Pulsed Flow of Figure 6.12

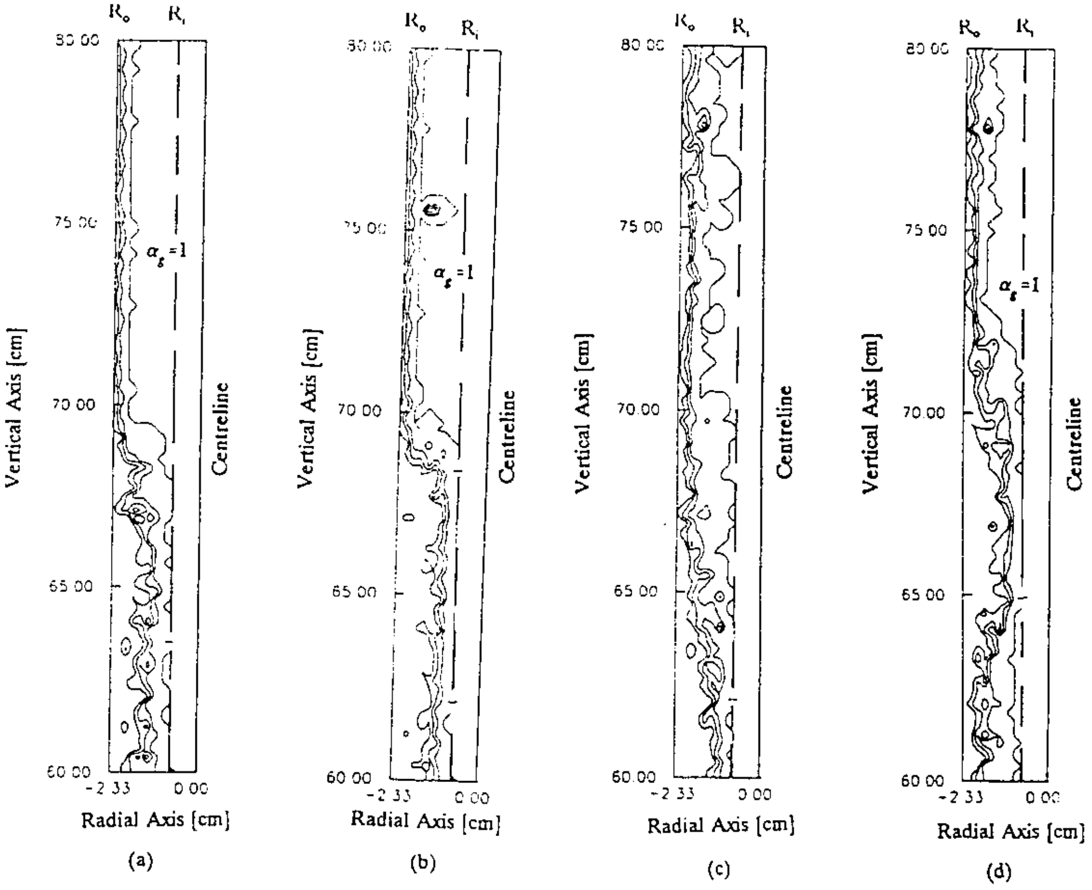

Figure 6.35: Void Fraction Contour Maps for a 60.0 cm Static liquid level of D_2O for Gas Flow Rates; (a) 4.0 l/min $t=t_o$, (b) 4.0 l/min $t=t_o + 10.0$ s, (c) 13.1 l/min $t=t_1$, (d) 13.1 l/min $t=t_1 + 10.0$ s

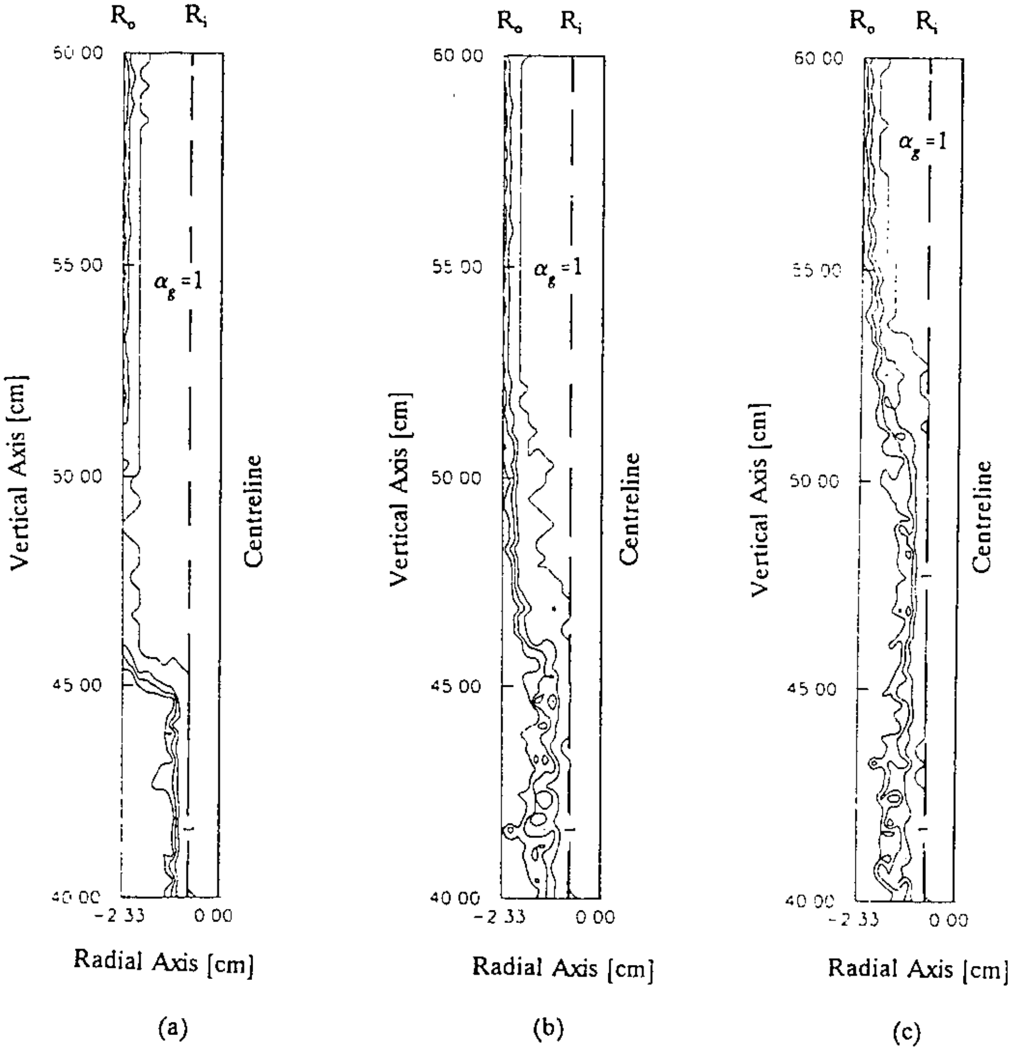

(a)

(b)

(c)

Figure 6.36: Void Fraction Contour Maps for a 40.0 cm Static liquid level of D_2O for Gas Flow Rates; (a) 5.0 l/min, (b) 10.0 l/min, (c) 15.0 l/min

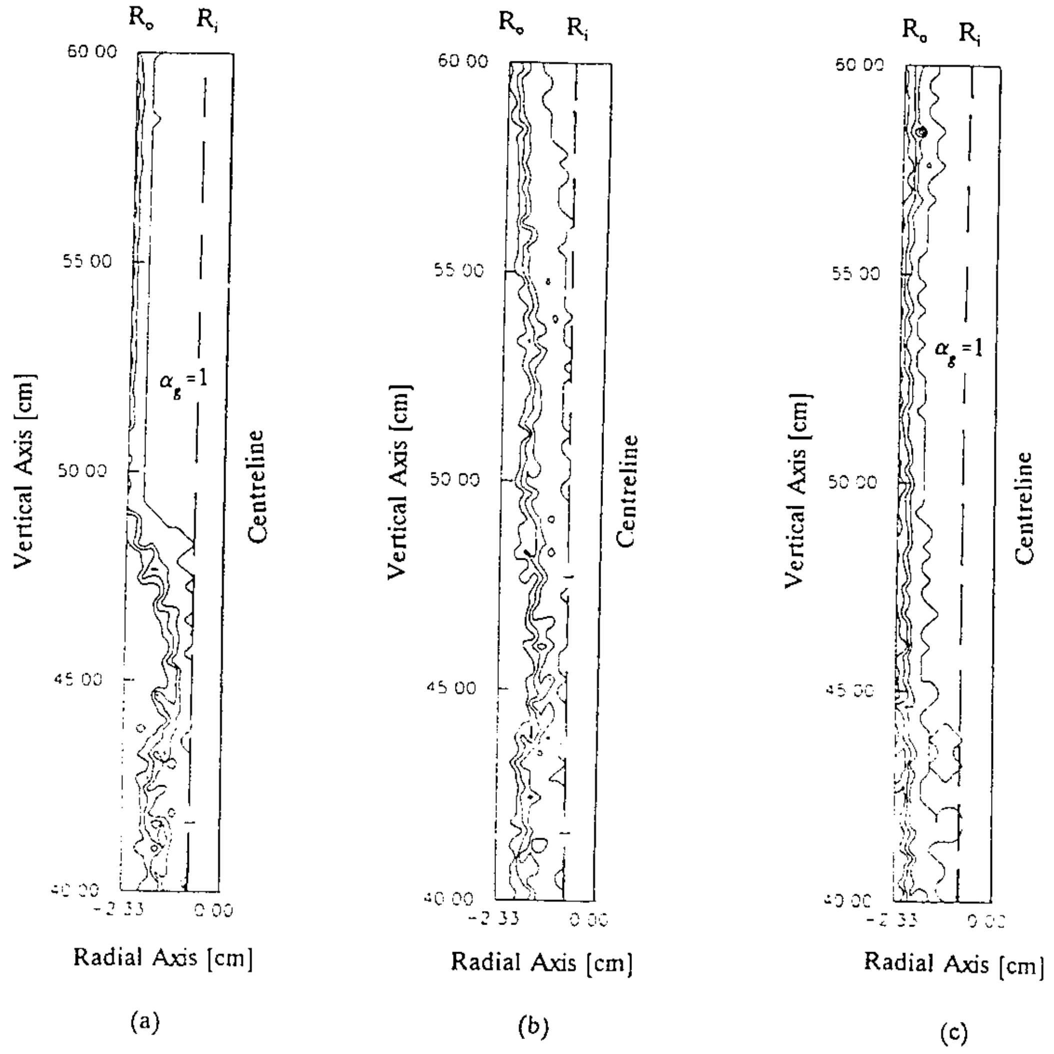

Figure 6.37: Void Fraction Contour Maps for a 40.0 cm Static liquid level of D_2O for Gas Flow Rates; (a) 6.25 l/min (b) 25.0 l/min, (c) 31.0 l/min

for a gas flow rate of 6.25 l/min are similar to the previous results of 5.0 l/min shown in Figure 6.36a except the meniscus is larger. At 20.0 l/min, the liquid level is beyond the viewing area and the void fraction is distribution unevenly. At 31.0 l/min, the gas flow rate is very high and the liquid is pushed to both the inner and outer walls.

The cross-sectional averaged void fraction profile associated with Figure 6.37 is shown in Figure 6.22. By examining all figures, a detailed understanding of the flow structure can be obtained.

Figure 6.38 shows the RTNR determined lateral void fraction (x-Coord.) in time as a contour map for a gas flow rate of 5.0 l/min at an elevation of 65.0 cm (same elevation for X-CT measurements) and is in the bubbly flow regime. The x-axis is the lateral position across the flow channel where 0.0 is the centre of the test section. The y-axis is time in seconds times 10. The strange unit is due to limitations in the plotting software. Each contour represents a step in void fraction of 2.5%. The maximum local void fraction in this figure is 12.5%. Two immediate observations are apparent. First, there is a large grouping or cluster of void near x=1.1 cm similar to results observed from the X-CT system (Figure 6.2) and elsewhere in the figure is several small isolated voids. Simply, this figure confirms the flow regime is bubbly flow and that at a gas flow rate of 5.0 l/min, the bubbles will travel both isolated and in clusters. Another important observation is that the bubbles are not moving laterally across the flow channel. This suggests the flow is relatively smooth and without strong eddy currents as we can observe in Figure 6.2. The X-CT images shown in Figure 6.2 cover a time span of 0.384 s. The data shown in Figure 6.38 covers a time span of 0.48 s.

Figure 6.39 shows the same data as Figure 6.38 but in a three-dimensional form. The magnitude of the void fraction and the void distribution is more clearly seen.

Figures 6.40 and 6.41 show the lateral void fraction as a function of time for a gas flow rate of 10.0 l/min(Re_g = 235) at an elevation of 65.0 cm and is in the slug flow regime. Each contour represent 10% void fraction and the maximum void

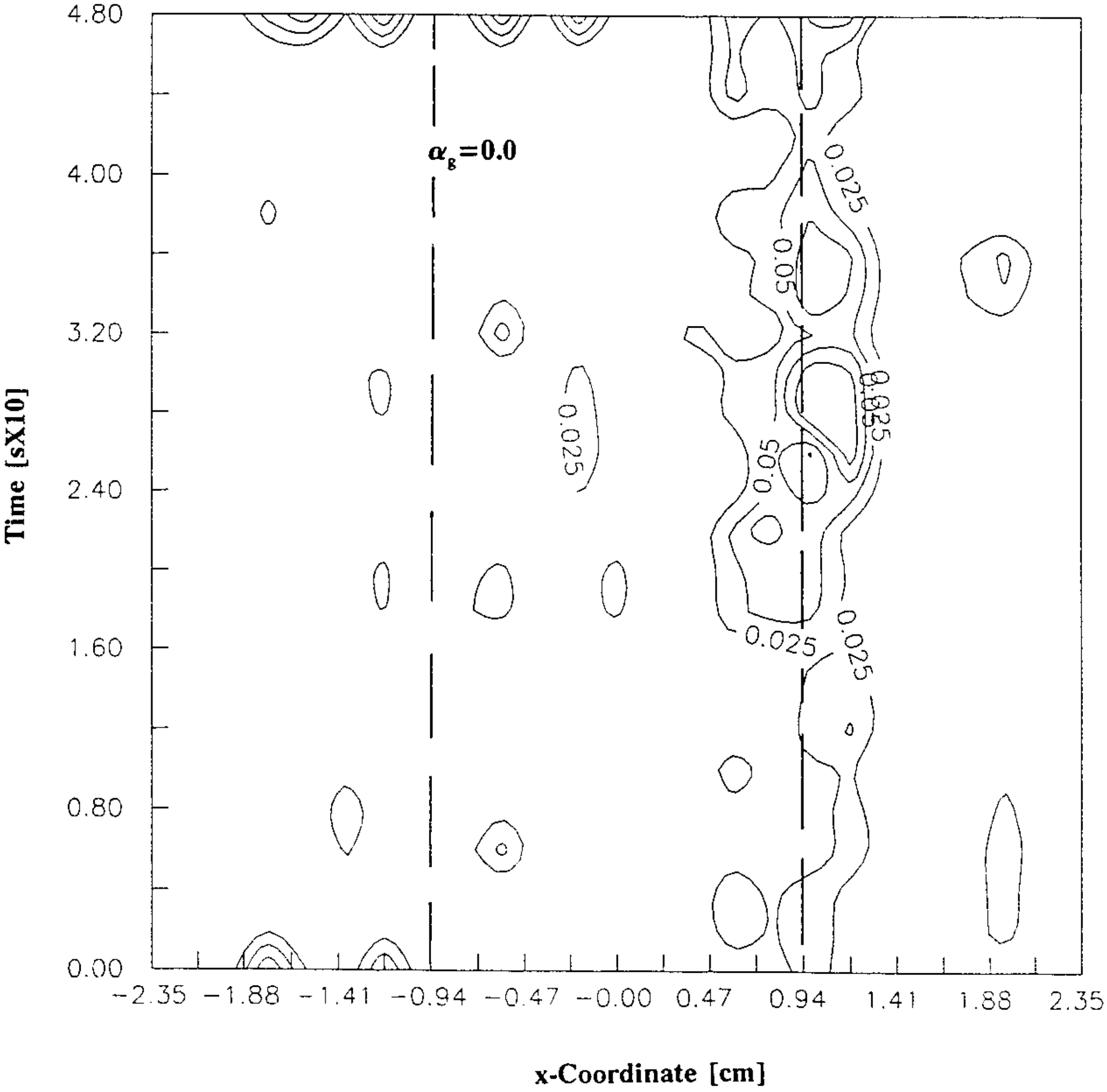

Figure 6.38: Contour Map of the Lateral Void Fraction in Time for a Gas Flow Rate of 5.0 l/min (Re_g = 105):Contour Level is 2.5% Void Fraction

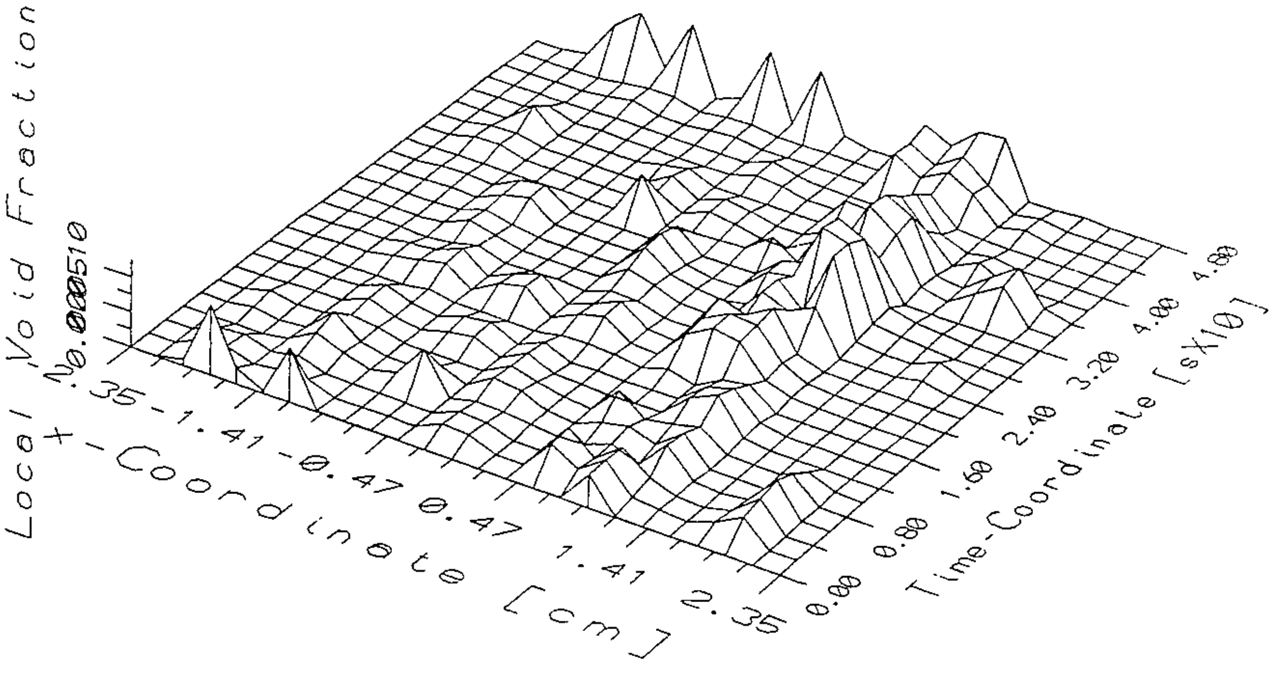

Figure 6.39: Three-Dimensional Representation of the Lateral Void Fraction Fluctuation in Time for a Gas Flow Rate of 5.0 l/min (Re_{gs} = 105)

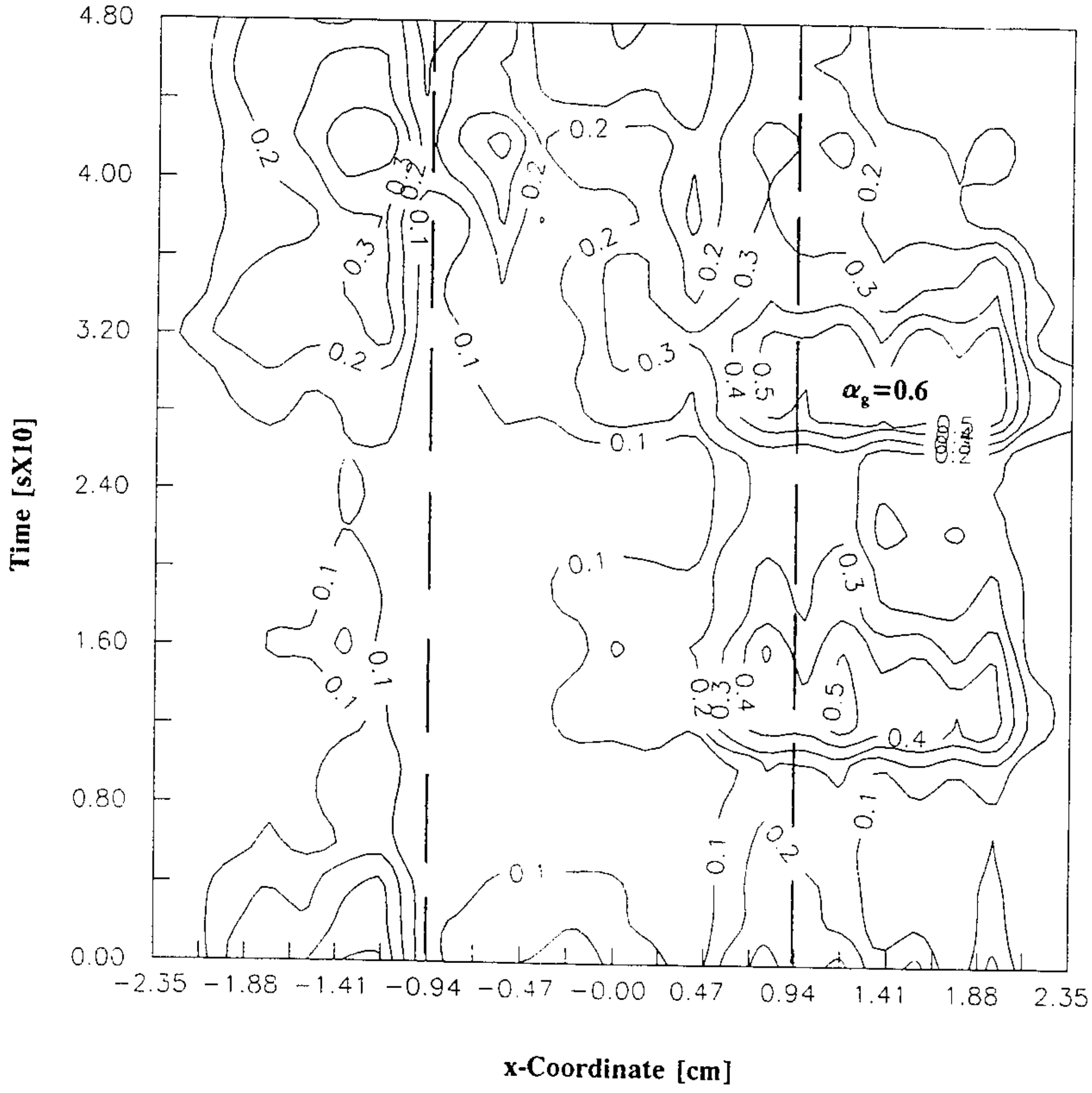

Figure 6.40: Contour Map of the Lateral Void Fraction (x,t) in Time for a Gas Flow Rate of 10.0 l/min (Re_{gs} = 235): Contour Interval is 10% Void Fraction

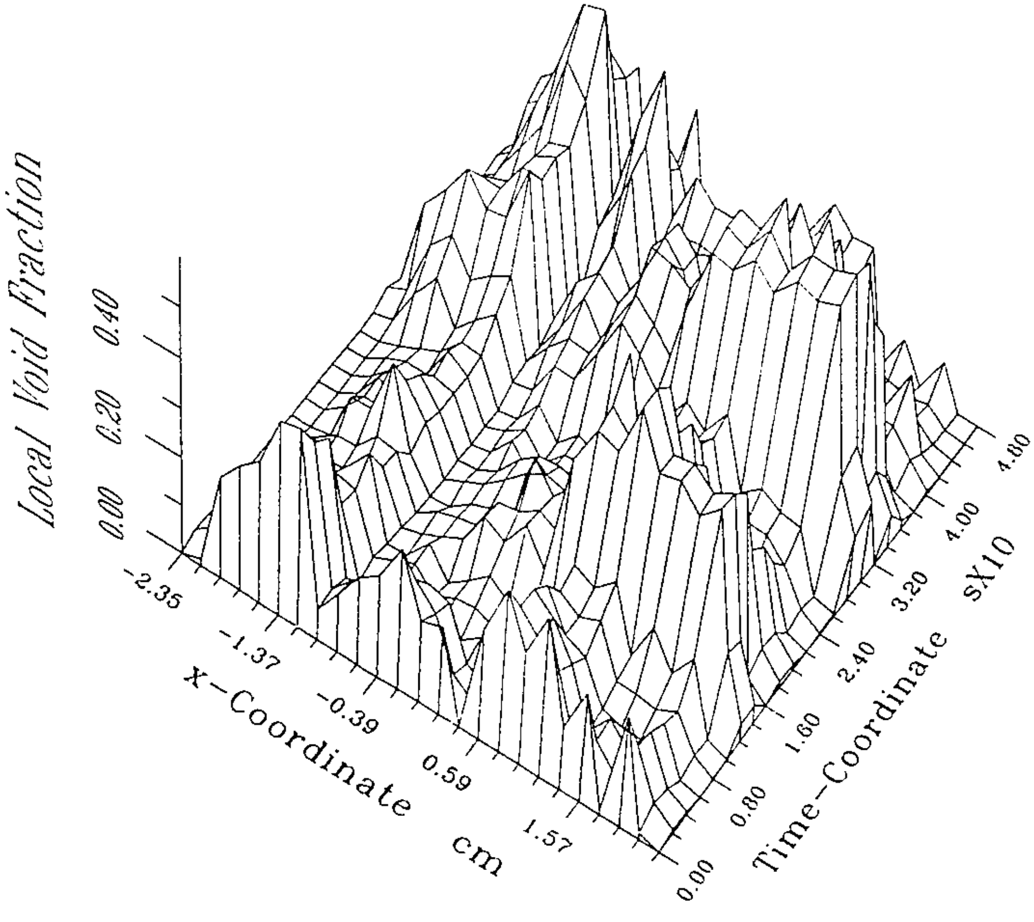

Figure 6.41: Three-Dimensional Representation of the Lateral Void Fraction Fluctuation in Time for a Gas Flow Rate of 10.0 l/min (Re_{gs} = 235)

fraction in the figure is approximately 60%. Two large bubbles, indicating slug flow, are shown at a lateral position of 1.5 cm and times of 0.14s and 0.3s. The majority of the void fraction is situated for positions of x > 0.4 cm. Large bubbles are also seen in other regions of the figure but they are not as regularly shaped as the two slug like bubbles which strongly shows the flow is still developing. The shape of the two large bubbles is very distinct with a sharp void fraction front and an irregular void fraction tail as we can observe from Figure 6.3. Figure 6.40 also shows the large slug flow bubbles as wrapping around the inner tube. This is shown by the bubble at 0.3 s, which has significant void fraction surrounding the tube, as well as the large bubbles in Figure 6.3 observed by the X-CT system. This suggests each bubble has significant entrainment typical of developing slug flow.

Figure 6.41 is the three-dimensional version of figure 6.40. The void fraction magnitude is clearly shown. Three very large bubbles exist along with several smaller ones. As in Figures 6.38 and 6.39, the lateral void fraction motion still does not exist even though we have entered the transition from bubbly flow to slug flow.

6.4 Measurements of Interfacial Area and Bubble Velocity

6.4.1 Bubble Velocity

Temporal studies of a large slug-like bubble are made for a static liquid level of 60.0 cm and a gas flow rate of 22.5 l/min. The cross-sectional averaged void fraction is calculated for each axial location at each image time. Temporal profiles of the cross-sectional averaged void fraction at certain locations are produced and analyzed to determine bubble location at each time frame.

The location of the bubble can be determined by several methods. One can use the void fraction maximum, the leading edge or start of void fraction rise, or the centroid of the void fraction temporal profile to determine the time at which a bubble passes a certain axial elevation. Although each technique should be capable of providing an approximate location of the bubble, using the void fraction maximum or the start of void fraction rise is too discrete and has a poor accuracy. Calculation of the void fraction centroid corresponds to the location of the bubble centroid and is not strongly influenced by the discrete nature of the temporal measurement.

Figure 6.42 shows the bubble centroid elevation as related to the time of bubble passage. Three bubbles were observed, however the third bubble had only entered the last image frame and not enough data is obtained to calculate the velocity. Bubble 1 shown by the + symbols is a relatively large bubble. Calculation of the average velocity from Figure 6.42 shows bubble 1 has a velocity of 0.693 m/s.

Bubble 2 is more difficult since the void fraction temporal profile is not always Gaussian shaped but sometimes has two maximum. In this case, the centroid of each maximum and the centroid of the entire profile is shown in Figure 6.42. The average velocity of bubble 2 is 0.875 m/s. The bubble velocities of the front and back maximums for bubble 2 are 1.025 and 1.676 m/s respectively.

Figure 6.43 shows the instantaneous velocity of bubbles 1 and 2 at several axial locations. The instantaneous velocity is obtained by using the time of passage between two axial elevations. The variation in the bubble velocity is significant as only the axial velocity is calculated and sometimes the bubbles will travel circumferentially instead of axially due to momentum changes. Another possible cause for the large variation in the bubble velocity is due to bubble acceleration.

The superficial velocity of the gas flow is 0.251 m/s. Using the X-ray CT time averaged void fraction for this gas flow rate, the local phase velocity is calculated to be 0.866 m/s. This velocity agrees well with the velocities measured above.

6.4.2 Three-Dimensional Reconstruction by High Speed X-ray CT system

Three-dimensional images can be reconstructed by the High Speed X-ray CT system using a marching cubes algorithm with knowledge of the object velocity.

Figure 6.44 shows three-dimensional reconstructed X-ray CT images for two-phase flow in an annulus channel. Figure 6.44a shows the reconstruction of bubble flow at a gas flow rate of 1.0 l/min and a static liquid level of 80.0 cm. Several small

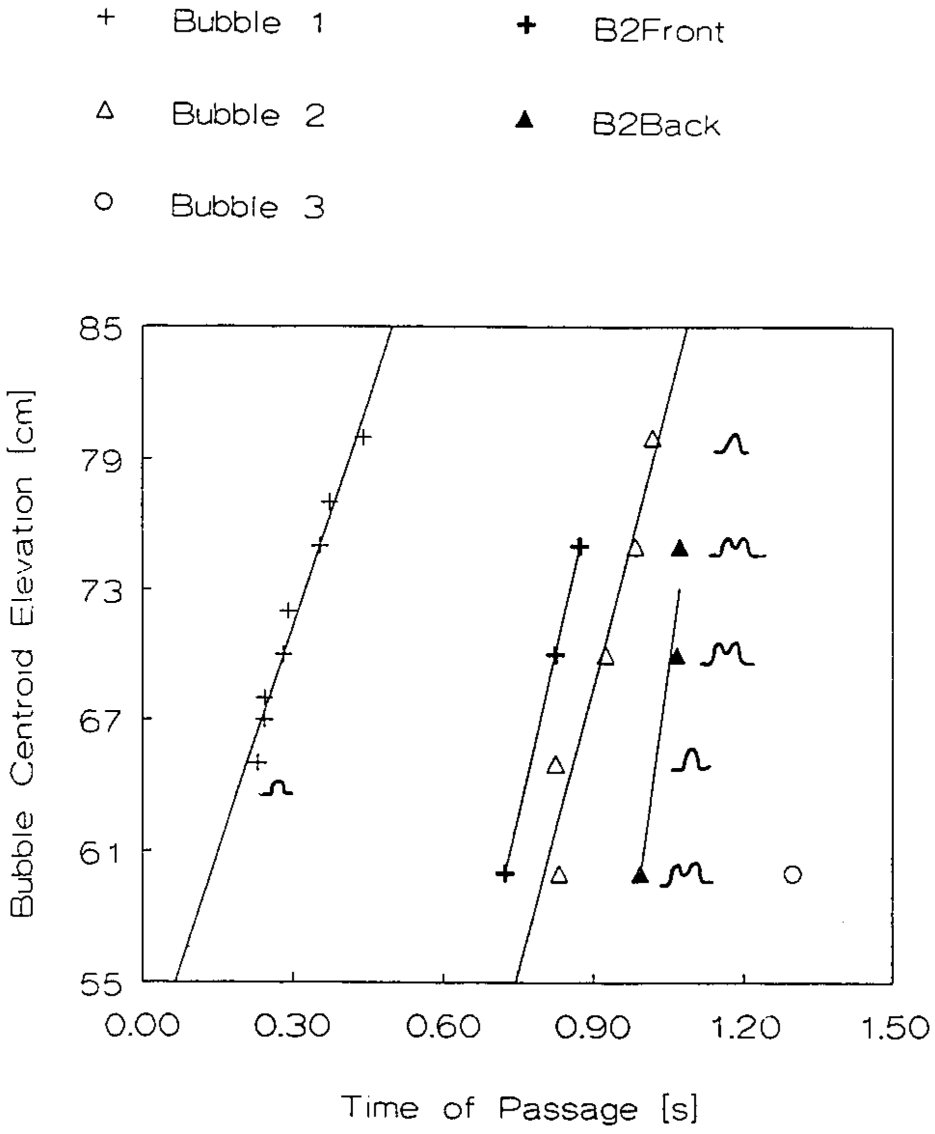

Figure 6.42: Relationship between Bubble Centroid Elevation and Time of Passage for a Gas Flow Rate of 22.5 l/min

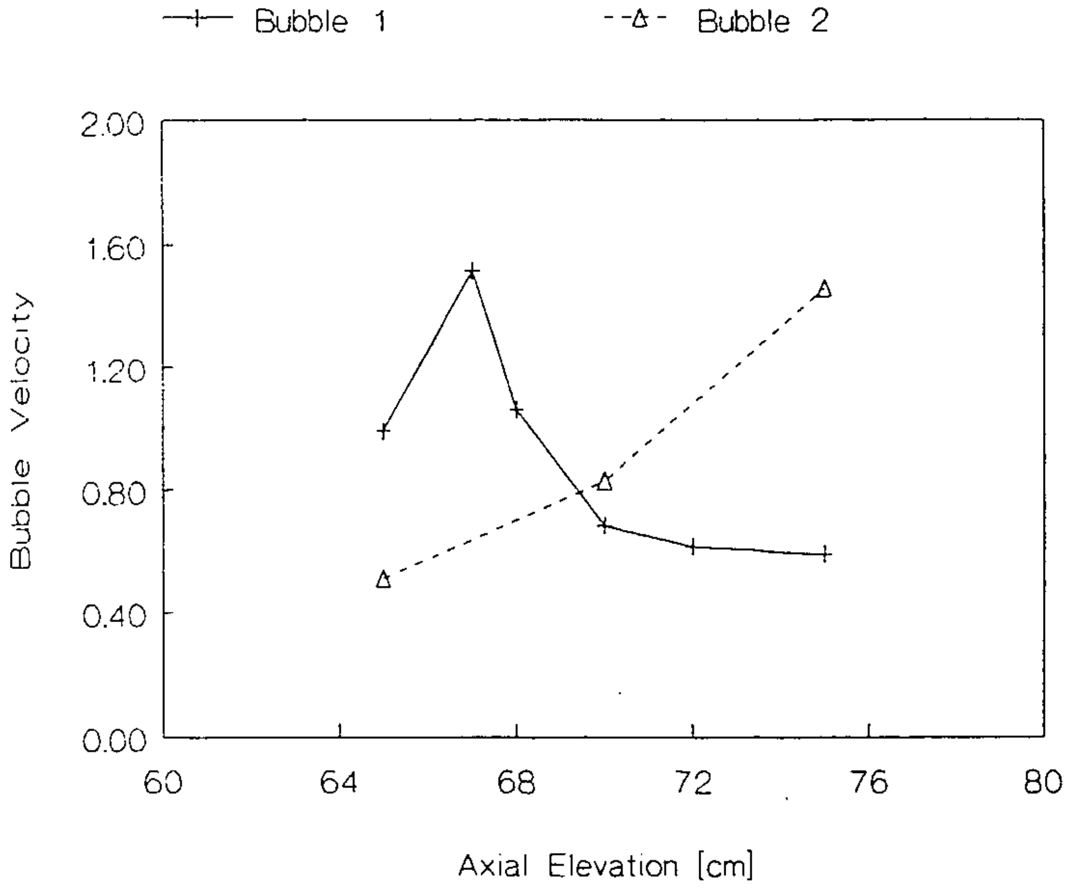

Figure 6.43: Instantaneous Bubble Velocity for a Gas Flow Rate of 22.5 l/min

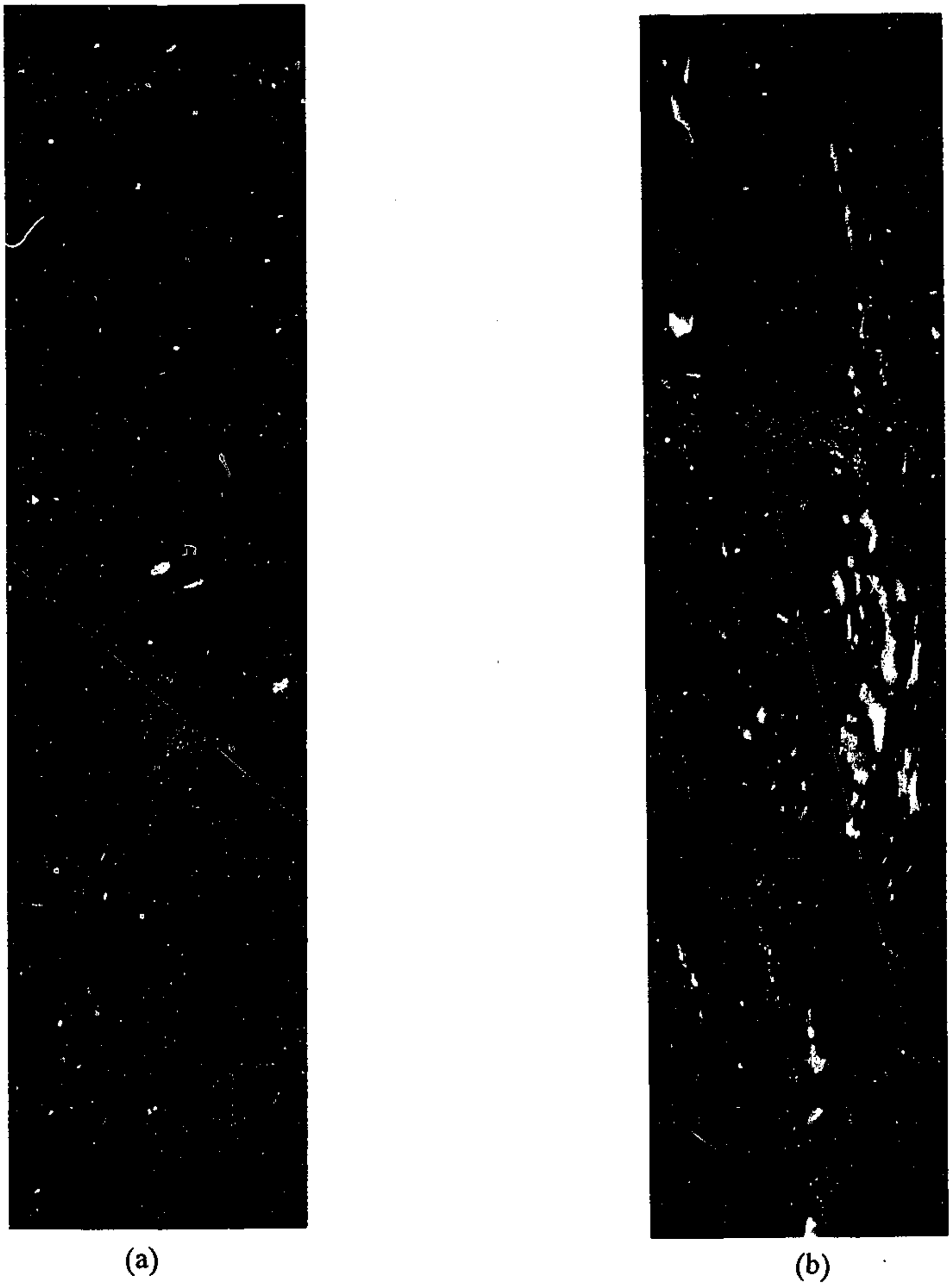

Figure 6.44: 3D Reconstructed X-ray CT Images of Air-Water Two-Phase Flow in a Vertical Annulus;(a) Bubbly Flow, (b) Observation of Coalescence

bubbles can be seen on the left side of the image and two long and thin bubbles can be seen on the right side of the image. The bubbles observed on the right side of the image as the two tubes of the annulus cannot be perfectly concentric. Thus the inner tube will be displaced slightly to one side, in this case, to the right, creating a larger local flow area to where the gas bubbles will migrate. The two long and thin bubbles are moving at a much slower velocity than is used to reconstruct the image and have a large component of their velocity in the circumferential direction. The reconstruction process does not account for circumferential motion of the bubbles nor for different bubble velocities.

Figure 6.44b shows the three-dimensional reconstruction of two-phase flow for a gas flow rate of 10.0 l/min and a static liquid level of 60.0 cm. The large dominant bubble is in fact several bubbles that the reconstruction process has confused as one. Two small bubbles appear as fingers in the centre of the image. These two bubbles have drifted together and coalesced into a large bubble and this new bubble has migrated towards another bubble and again coalesced. Unfortunately, the reconstruction process cannot distinguish between the two bubbles as only 1 imaging plane has been used in acquiring the experimental data.

Figure 6.45 shows reconstructed three-dimensional X-ray CT images for two-phase flow in an annulus flow channel for gas flow rates of 5.0 l/min, 7.0 l/min, 10.0 l/min, and 13.0 l/min. The static liquid level for these experiments is 80.0 cm. The vertical scale in each image is kept the same to obtain a relative visual relationship of the liquid slug lengths. At 5.0 l/min, the bubbles are evenly spaced with a small distribution in size. This flow rate corresponds to bubbly flow according to pipe flow models. At 7.0 l/min, the gas flow rate corresponds to slug flow. The size distribution of the bubbles has increased. Distinct regions of high void fraction and low void fraction can be observed. The large bubbles surround the centre tube but are still not completely developed. At 10.0 l/min, the liquid slug length has increased and the large bubbles show increased stability in shape. At 13.0 l/min, the liquid slug length further increases and the bubble length also increases.

Flow regime information can be obtained for two-phase flow in an annulus

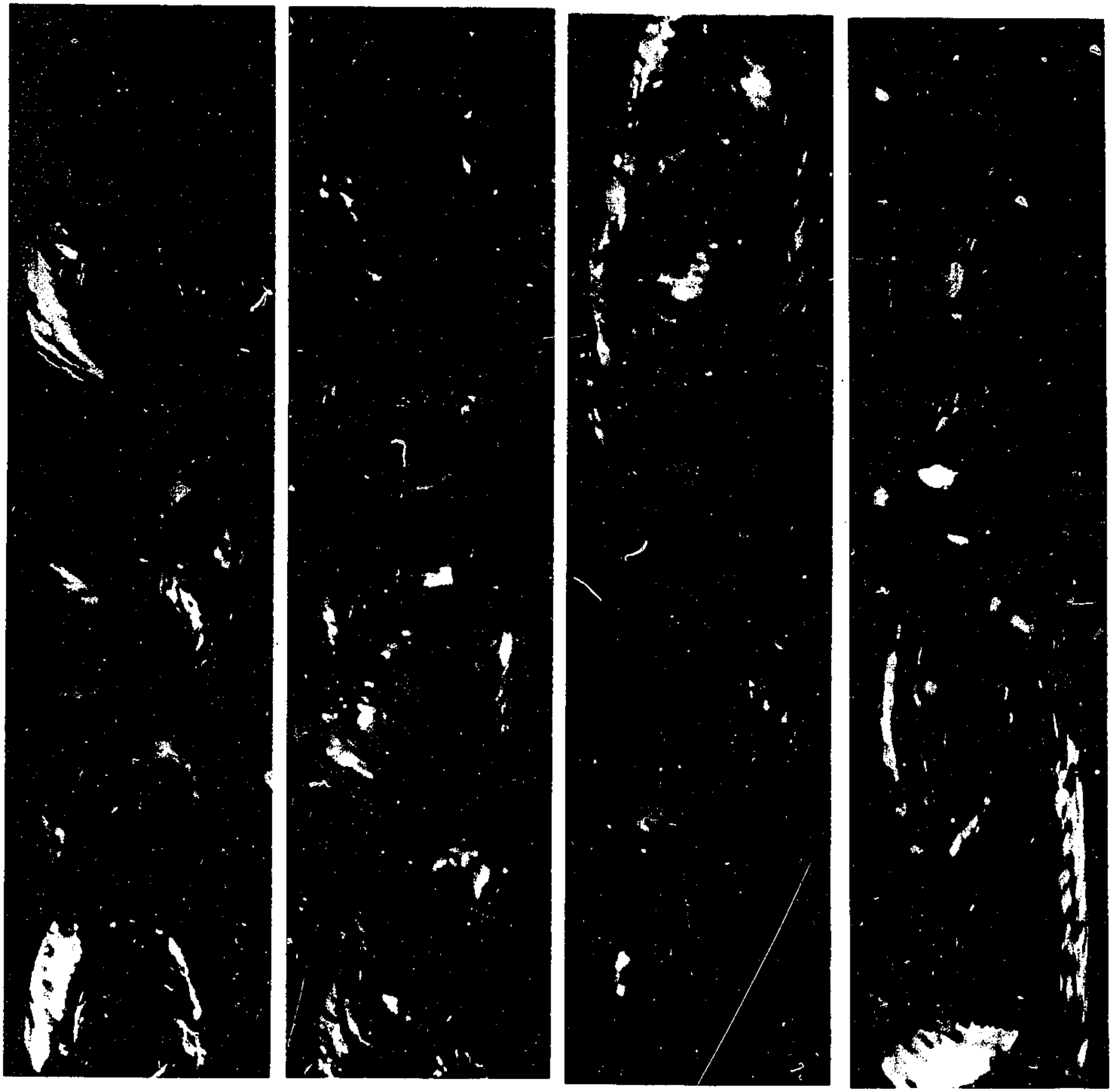

5.0 l/min 7.0 l/min 10.0 l/min 13.0 l/min

Figure 6.45: Vertical Air-Water Two-Phase Flow Observed by 3D Reconstruction by the High Speed X-ray CT system for various Gas Flow Rates

geometry and bubble coalescence and liquid film bridging can be observed.

6.4.3 Interfacial Area

Based on the phantom tests, the accuracy of the interfacial area measurement by the high speed X-ray CT system is influenced by the velocity of the objects. The interfacial area measurement is shown to be accurate to within 10% for velocities between 0.2 m/s and 1.5 m/s.

However, for bubbly flow, each bubble has a different velocity and only those bubbles whose velocities are close to the value used for the three-dimensional reconstruction process will produce accurate results.

Figure 6.46 shows the interfacial area measurements of two-phase flow in an annulus flow channel for gas flow rates of 5.0 l/min, 7.0 l/min, 10.0 l/min, and 13.0 l/min. The velocity used to reconstruct the three-dimensional images is calculated from the superficial gas velocity modified by the time averaged void fraction. The three-dimensional images for this data are shown in Figure 6.45. Most of the measured data is quite low and represents small bubbles. Measured values above 800 mm^2 represent large bubbles which surround the centre tube. The measured data cannot be considered exact as the velocity of each bubble is different and varies with the bubble size. Also, if a large circumferential velocity exists, the interfacial area will be calculated as larger than reality. However, the data does give an excellent indication of the interfacial area.

The Real-Time Neutron Radiography system has been shown to determine the interfacial area if both the cross-sectional averaged void fraction and the mean bubble diameter are known for bubbly flow as discussed in Chapter 5. Interfacial area measurements for slug flow or churn flow have not yet been made. Accurate measurement of the interfacial area by RTNR requires accurate determination of the location of the interface. This can be achieved through image processing techniques and can be combined with the 2D void fraction contour maps to project the third dimension.

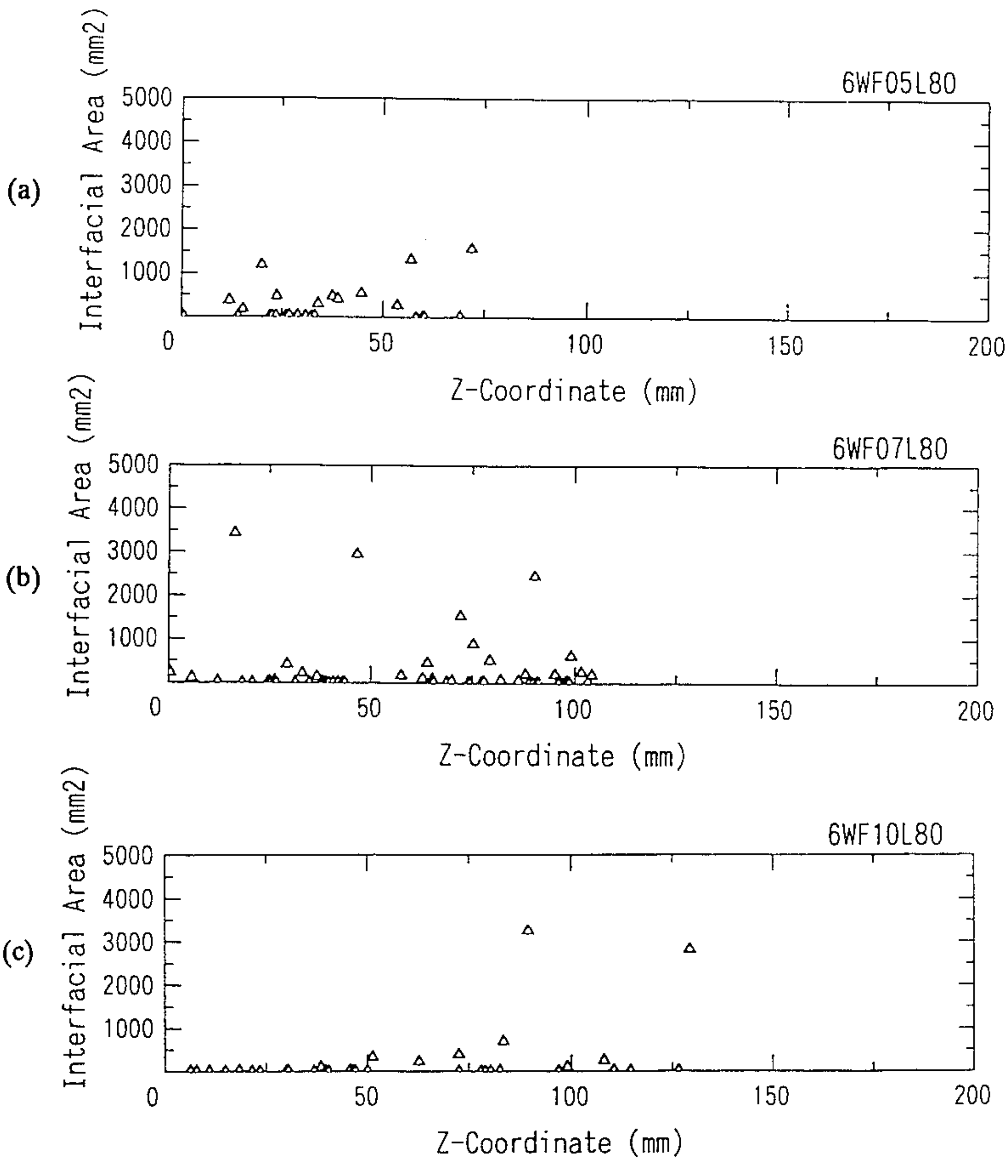

Figure 6.46: Experimental Results by High Speed X-ray CT system for Interfacial Area of Two-Phase Flow in a Vertical Annulus for various Gas Flow Rates; (a) 5.0 l/min, (b) 7.0 l/min, (c) 10.0 l/min

Chapter 7

7. Nuclear Fuel Channel Flow Studies

The addition of a rod bundle in flow channels complicates the nature of two-phase flow and phenomena such as void migration and recirculation phenomena becomes important. Void migration phenomena occurs when the void in one subchannel drifts to another subchannel. The subchannel to subchannel interactions are governed by the nature of the flow in each subchannel (α,U_g,U_l) and the resistance to drifting caused by the narrow gap between the rods and the effect of the fins. Recirculation phenomena can occur when flow reversal occurs in one or more subchannels and recirculation pathways are established inside the bundle. This phenomena is also governed by the nature of the two-phase flow in each subchannel and the resistance to cross flow.

In addition, the difficulty of measuring two-phase flow parameters increases as the location of the rods and rod movement may need to be accounted for and the neutron attenuation due to the wall and rod material is now significant.

In this chapter, two-phase flow parameters are measured by the RTNR system for nuclear fuel channels with rod bundles. Experimental results are presented for the MAPLE-type nuclear fuel channel and the CANDU-type nuclear fuel channel.

7.1 MAPLE-Type Nuclear Fuel Channel Flow Studies

The MAPLE-type nuclear fuel channel is described in detail in section 3.6.5. Experimental measurements of flow regime, void fraction, and bubble motion are observed and discussed.

7.1.1 Visualization of Two-Phase Flow

Typical RTNR images of a MAPLE-type bundle in a vertical hexagonal nuclear fuel channel is shown in Figure 7.1. Figure 7.1(a) shows the case where the MAPLE-type nuclear fuel channel is completely voided, i.e. without heavy water. Figure 7.1(b) shows the case where the MAPLE-type nuclear fuel channel is operated in the bubble column mode, and Figure 7.1(c) shows the case where the MAPLE-type nuclear fuel channel is operated under forced convection.

In Figure 7.1(a), seven rows of rods and the flow channel walls can be clearly seen as grey vertical bands. The light bands between the rods are the rows of subchannels. The central row, which has seven rods, is much darker in the image indicating a large amount of neutron attenuation. This is due to the high thermal neutron cross-section for the stainless steel support rod in the centre of this row. The thermal neutron cross-section for steel (Fe) is significantly higher than Aluminium as shown in Table 2.1.

Figure 7.1(b) shows the two-phase flow in the bubble column mode for a superficial gas velocity of 0.06 m/s. Near the top of the image is the gas-liquid interface with the interface elevation peak in the centre of the image. In reality, the liquid is climbing through the core of the flow channel due to surface tension affects within the core. When the MAPLE bundle is removed from the flow channel, the gas-liquid interface climbs the fuel channel walls instead and oscillates between the six sides of the fuel channel.

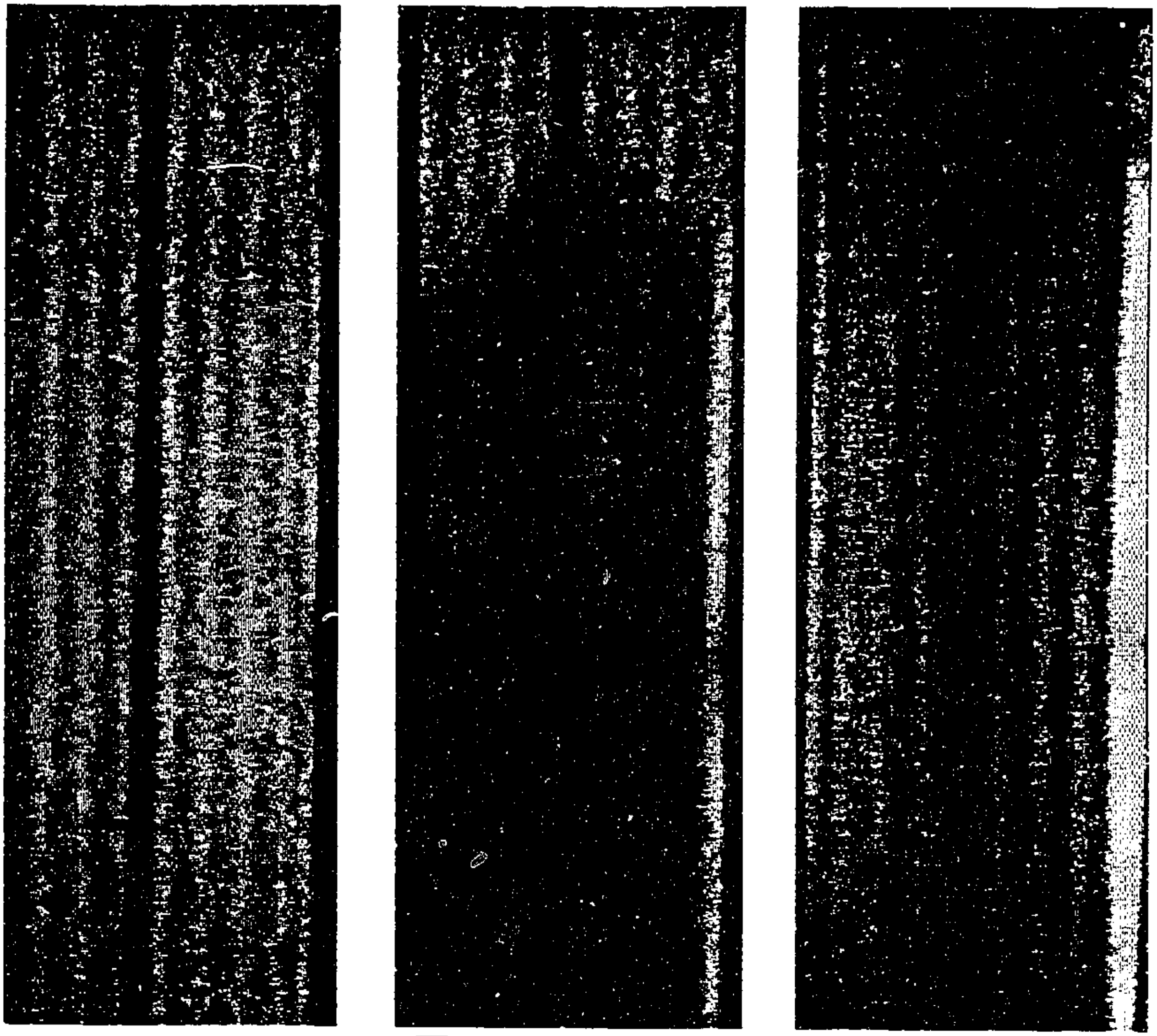

Empty Channel

(a)

Bubble Column Mode

(b)

Forced Convection

(c)

Figure 7.1: RTNR images of a MAPLE-Type nuclear Fuel Channel: (a) Empty Channel, (b) Bubble Column Mode U_{gs}=0.06 m/s, (c) Forced Convection U_{gs} = 0.38 m/s U_{ls} = 0.05 m/s.

The forced convection case is shown in Figure 7.1(c) for a superficial gas velocity of 0.23 m/s and a superficial liquid velocity of 0.10 m/s. In this case, a significant amount of gas travels upwards on the left side of the image. The large bubble penetrates into the second row of subchannels and completely surrounds the first row of rods.

Figure 7.2 shows the flow regime map for the MAPLE-type nuclear fuel channel determined by the RTNR system with the aid of image processing at a developing length (L/D_h) of 33.6 from the inlet of the hexagonal flow channel. The theoretical model of Harvel et al. [65] is also shown in Figure 7.2 for comparison, where this model is experimentally confirmed in a transparent test section with the identical rod bundle.

Figure 7.2 shows that the flow regime observations by the RTNR system and the theoretical model by Harvel et al.[64] agree quite well with slight discrepancies at the flow regime transition boundaries. These discrepancies can be accounted by two factors. The first factor is simply that the working fluid in the RTNR case is heavy water as opposed to light water, however, the fluid property differences are not significant. The second factor is that neutrons can penetrate through the entire bundle and properly visualize the two-phase flow in the bundle core whereas in previous work, the transparent test section did not allow for optical visualization into the core of the rod bundle beyond one row of subchannels. Although the capacitance void fraction transducer used in the previous work [65] on the transparent test section was able to measure the void fraction, the presence of the metal bundle influenced the capacitance transducer.

7.1.2 Measurement of Void Fraction

Measurement of chordal void fraction, cross-sectional averaged void fraction, time averaged void fraction, and void fraction fluctuations are discussed in this section.

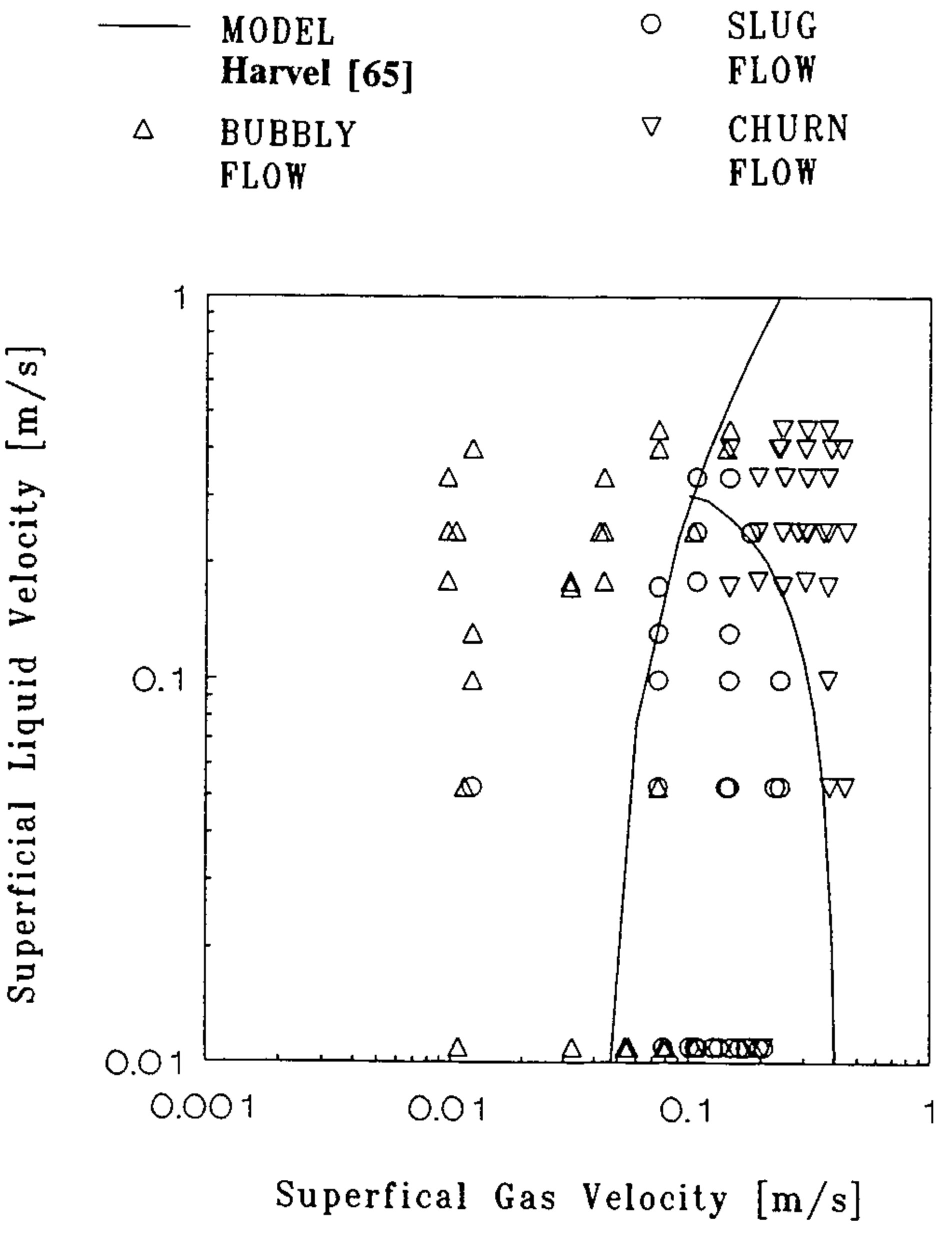

Figure 7.2: Flow Regime Map for Two-Phase Flow in a MAPLE-Type Nuclear Fuel Channel

Figure 7.3 shows the cross-sectional averaged void fraction for the MAPLE-type nuclear fuel channel for superficial gas velocities of 0.01, 0.03, 0.06, and 0.08 m/s when the experimental apparatus is operated under a bubble column mode, i.e. no net liquid flow rate. The cross-sectional averaged void fraction is shown for elevations from 35.0 cm to 48.0 cm with respect to the inlet of the hexagonal flow channel. The observed behaviour for the MAPLE-type nuclear fuel channel in a bubble column mode is similar to the two-phase behaviour in the pipe flow channel (Figure 5.7) and the annulus flow channel (Figure 6.19). The two-phase liquid level is seen to increase with increasing superficial gas velocity and the void fraction gradient at the gas-liquid interface decreases with increasing superficial gas velocity due to bubble packing.

Figure 7.4 shows the cross-sectional averaged void fraction profile with elevation of the flow channel for superficial gas velocities of 0.01, 0.03, 0.04, 0.11, 0.19, and 0.31 m/s at a superficial liquid velocity of 0.18 m/s. As expected, the cross-sectional averaged void fraction increases with increasing superficial gas velocity but the non-monotonic nature of the void fraction with respect to elevation previously observed in bubble column experiments is not apparent. Now, the void fraction is more or less constant or slightly increasing with elevation except in the case where a large bubble passes through. This suggests the void fraction is better dispersed throughout the bundle when there is a net liquid flow and that the non-monotonic nature of the void fraction previously observed in pipe, annulus, and MAPLE bundle bubble columns is due to recirculation phenomena.

Figure 7.5 shows experimental results for superficial gas velocities of 0.04, 0.11, 0.15, 0.19, 0.25, and 0.31 m/s but for a higher superficial liquid velocity of 0.34 m/s. In this case, the cross sectional averaged void fraction is significantly lower than that shown in Figure 7.4 which suggest the cross-sectional averaged void fraction decreases with increasing superficial liquid velocity and the influence of elevation upon the void fraction decreases, i.e., the possibility of recirculation phenomena and void migration are reduced.

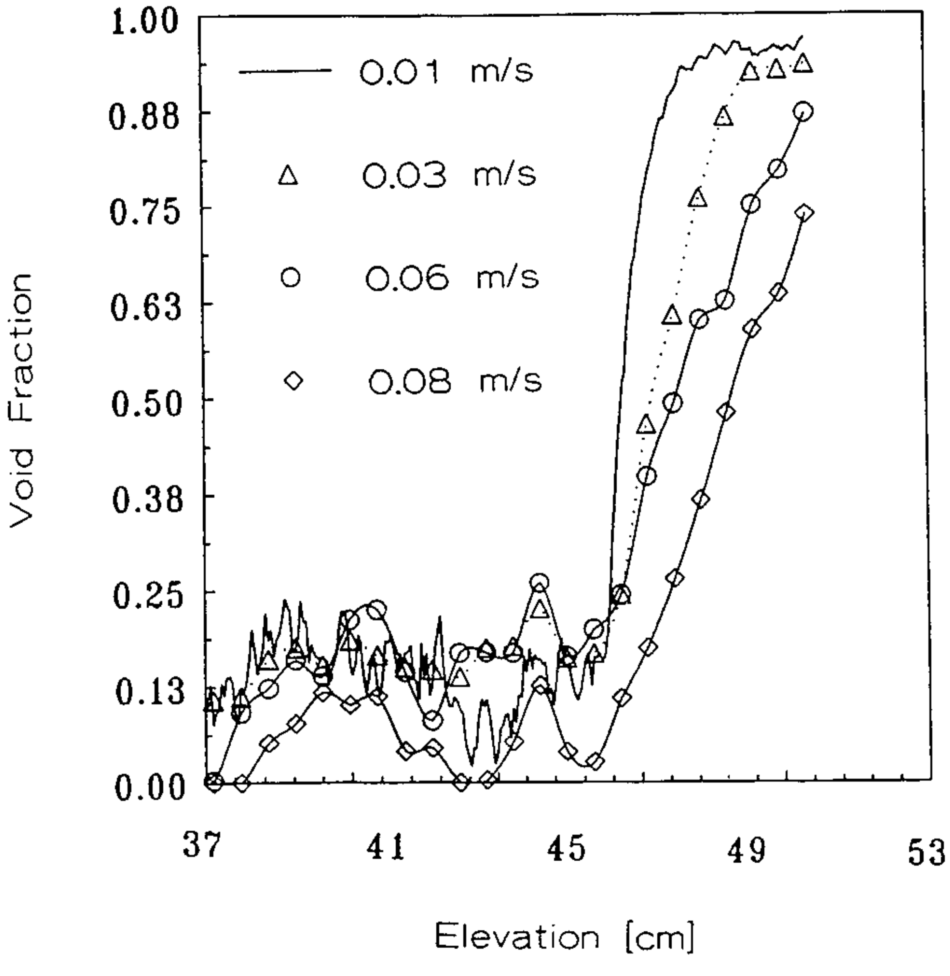

Figure 7.3: Cross-Sectional Averaged Void Fraction Profiles for a MAPLE-Type Nuclear Fuel Channel Operated in a Bubble Column Mode

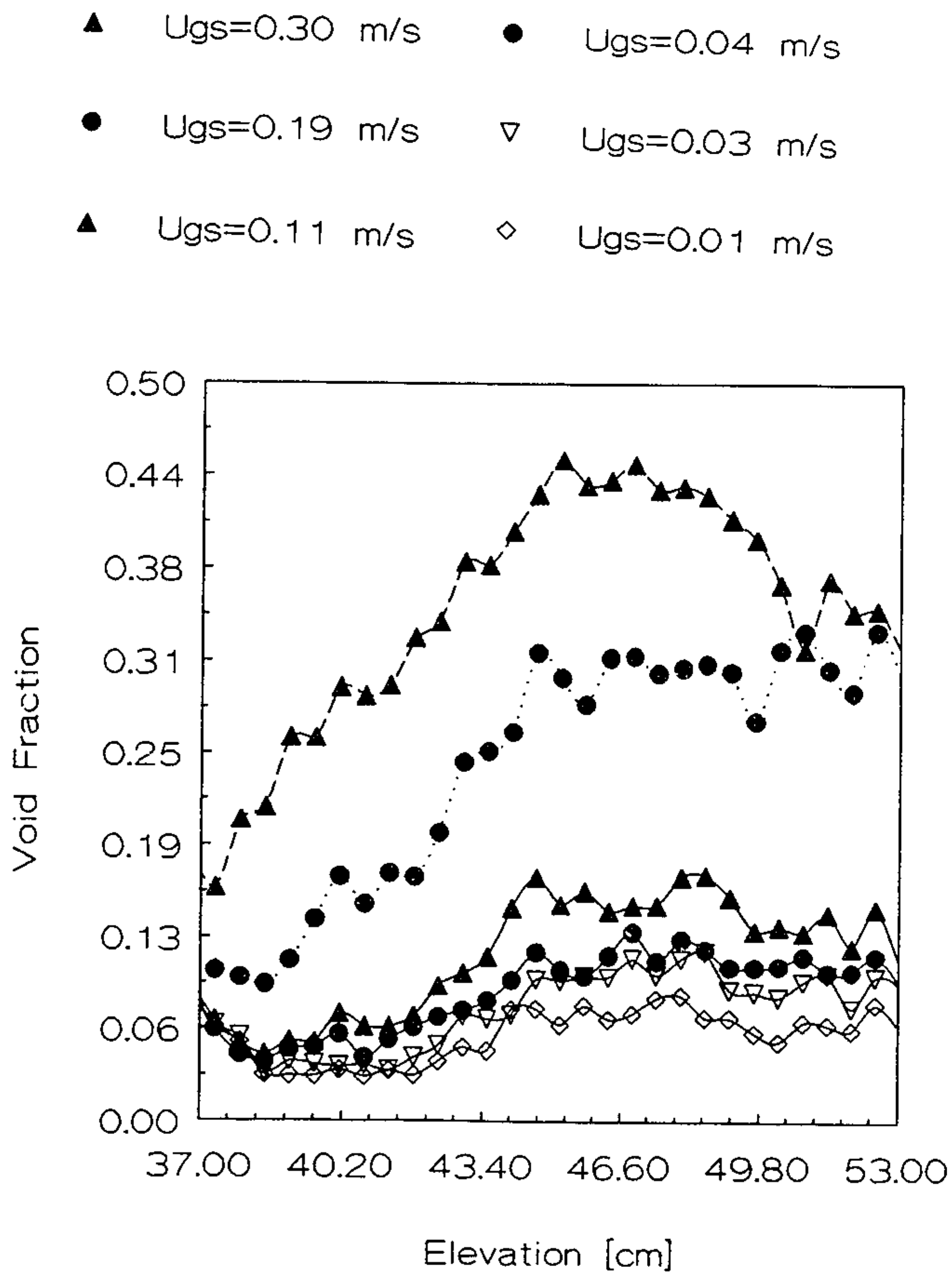

Figure 7.4: Cross-Sectional Averaged Void Fraction Profiles for a MAPLE-type Nuclear Fuel Channel under Forced Convection; U_{ls} = 0.18 m/s.

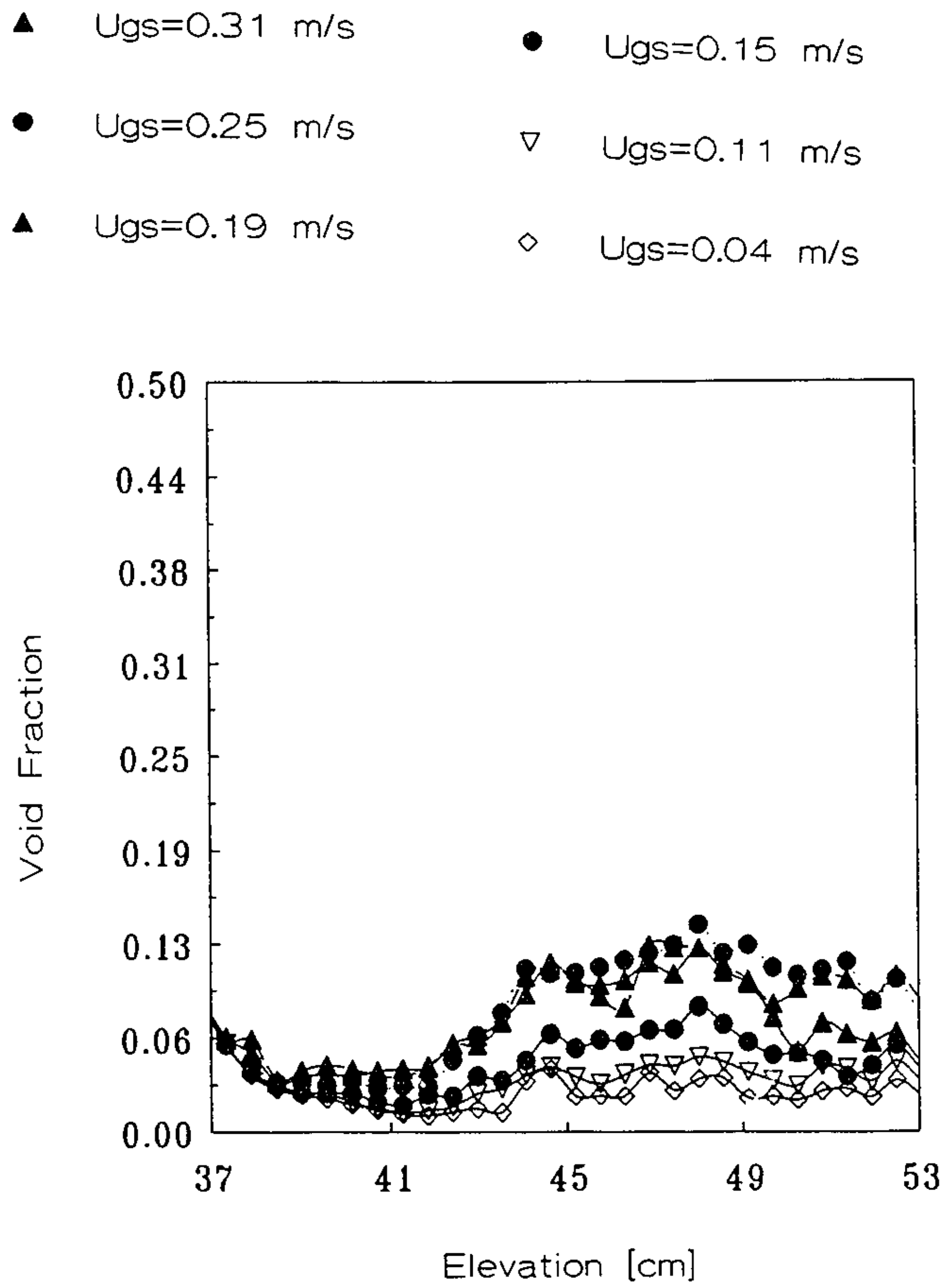

Figure 7.5: Cross-Sectional Averaged Void Fraction in a MAPLE-Type Nuclear Fuel Channel under Forced Convection; U_{ls} = 0.34 m/s.

Fig 7.6 shows the time and cross-sectional averaged void fraction ($<\bar{\alpha}>$) as a function of the superficial gas velocity at elevations of 45.0, 50.0, and 55.0 cm for a superficial liquid velocity of 0.05 m/s and at an elevation of 45.0 cm for a superficial liquid velocity of 0.10 m/s. The time averaged void fraction shows a slight increase with increasing superficial gas velocity. At elevations from 45.0 cm to 50.0 cm, the effect of elevation is indeterminate, yet from 50.0 cm to 55.0 cm, the void fraction increases with increasing elevation. This could be caused by the bundle resisting agglomeration and void migration phenomena at the entrance to the bundle.

The superficial gas velocity has a significant influence of the time and cross-sectional averaged void fraction between 0.08 m/s and 0.25 m/s. For superficial gas velocities above 0.25 m/s, the time and cross-sectional averaged void fraction remains constant.

The superficial liquid velocity is seen to have a stronger effect at lower superficial gas velocities than at higher superficial gas velocities, however more analysis is required to confirm this observation.

Figure 7.7 shows void fraction fluctuations ($\bar{\alpha}(t)$) for elevations of 45.0, 50.0, and 55.0 cm at a superficial liquid velocity of 0.10 m/s and a superficial gas velocity of 0.34 m/s. Although the superficial gas velocity is quite high and slug flow is observed, the magnitude and frequency of the void fraction fluctuation remains small due to the presence of the bundle. Also, at an elevation of 45.0 cm, the void fraction fluctuation is larger due to entrance effects in the bundle.

7.1.3 Measurement of Void Distribution

The instantaneous void fraction distribution ($\alpha(x,z)$) in a MAPLE-type bundle is shown in Figure 7.8 for a superficial gas velocity of 0.34 m/s and a superficial liquid velocity of 0.10 m/s. Several large bubbles are observed where the contour lines reach 60% void fraction and regions of mostly water can be observed where void fraction contours of 20% are shown. These isolated regions are elongated in the

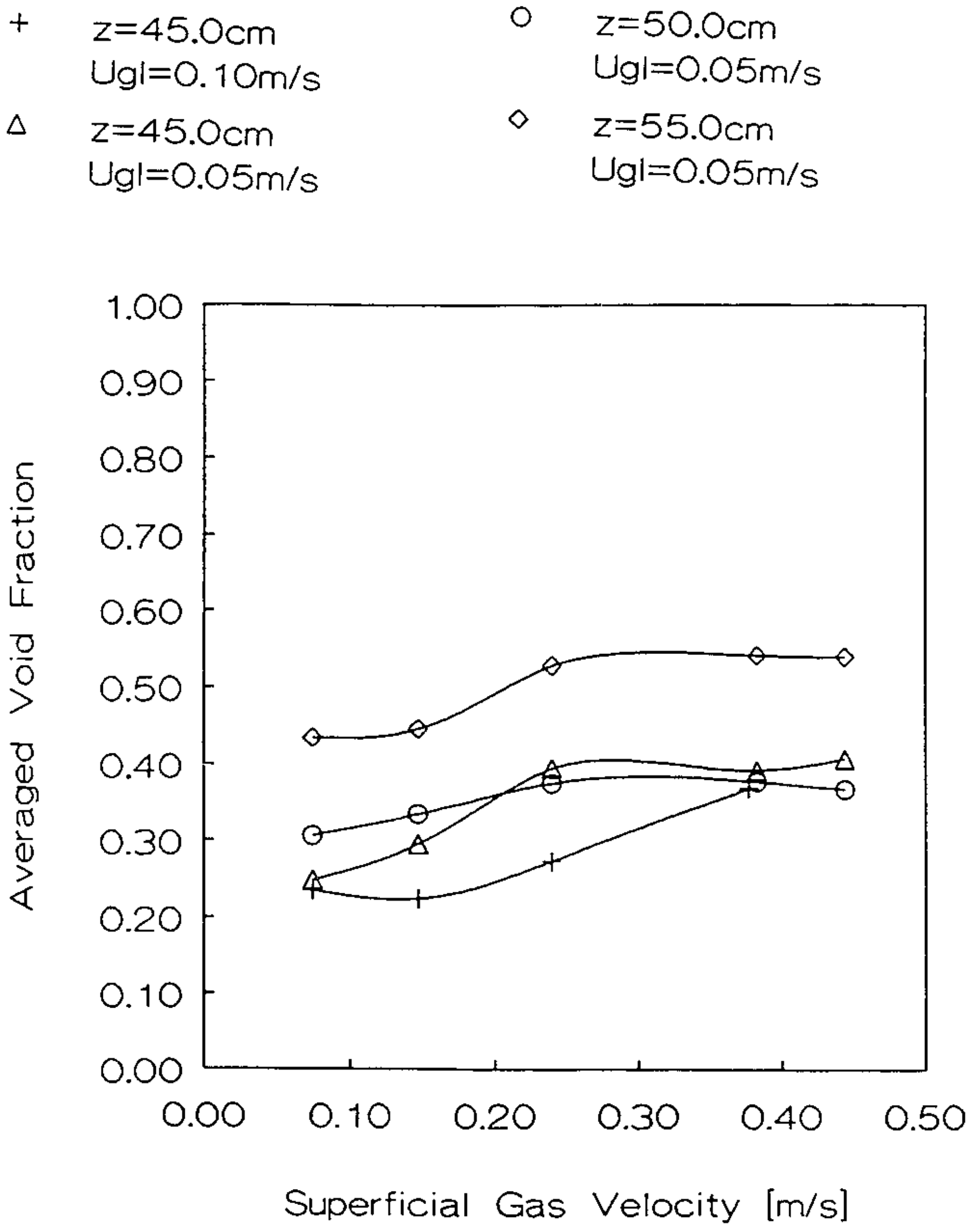

Figure 7.6: Time Averaged Void Fraction for various Superficial Gas Velocities in a MAPLE-Type Nuclear Fuel Channel

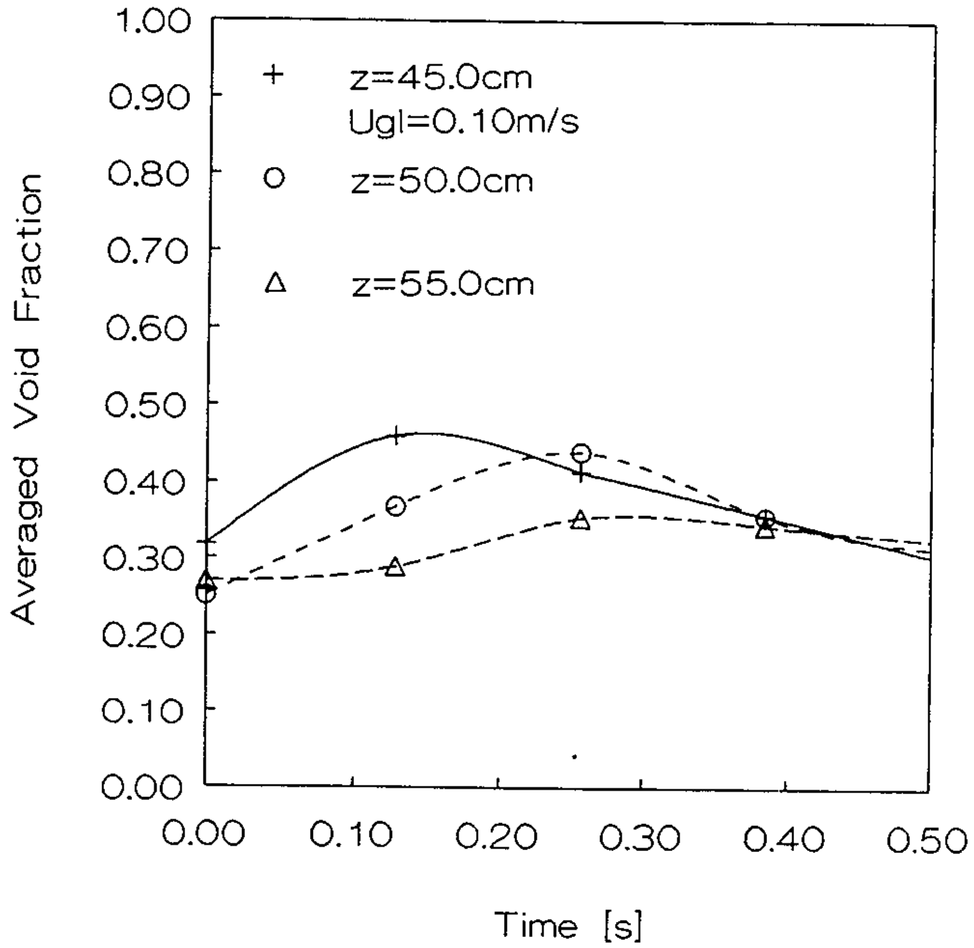

Figure 7.7: Void Fraction Fluctuation in a MAPLE-Type Nuclear Fuel Channel

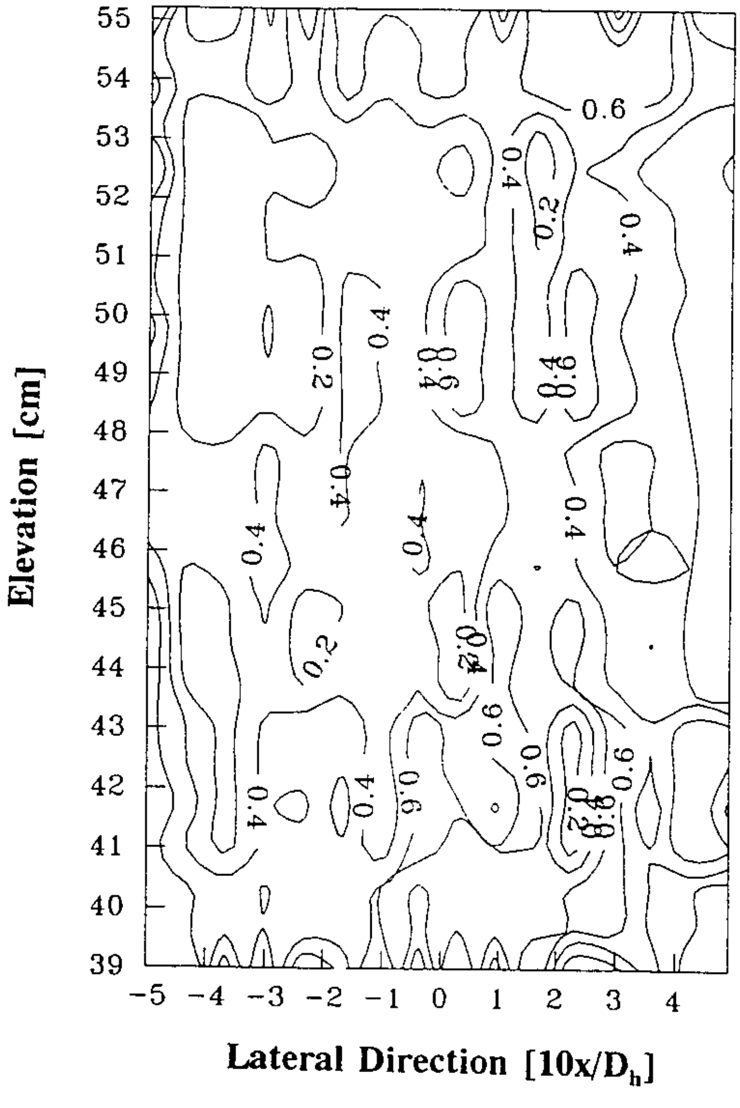

Figure 7.8: Instantaneous Void Fraction Distribution in a MAPLE-Type Nuclear Fuel Channel: U_{gs} = 0.34 m/s, U_{ls} = 0.10 m/s.

direction of flow as the rods in the bundles are restricting the width of the bubbles and liquid pockets to contain them within one subchannel.

One exception is shown at elevations from 40.0 cm to 45.0 cm at a lateral position of 2.0 cm. The 60% void fraction contour shows a shift in the lateral position towards the core of the bundle as the elevation increases. Essentially, the bubble is irregular in shape and is in the process of migrating from one subchannel to another.

The lateral void fraction distribution ($\alpha(x,t)$) in time is shown in Figure 7.9 for a superficial gas velocity of 0.23 m/s and a superficial liquid velocity of 0.10 m/s. In this test case, the gas flow is observed to be entirely on the left side of the image which corresponds to lateral positions of -3.5 cm to -2.2 cm. The penetration of the gas into each subchannel is very small and essentially is confined to the first row of subchannels and between the bundle and the channel wall. Figure 7.9 shows the lateral void fraction in this region to range from 0.4 to 1.0. The 40% void fraction contour also varies with time in the lateral coordinate. This shows a small fluctuation in the gas flow. The void fraction fluctuation suggests the gas is attempting to migrate into the next subchannel but is resisted by the narrow gap between the rods and the fins on each rod. The end result is a vertical interfacial wave. Unfortunately, due to the coarseness of the data with respect to time (Only 7 different times used), the contour plotting software produces an exaggeration for the 30% contour line. With additional temporal analysis, these results can be improved.

The experimental analysis shows that the void fraction and void fraction distribution in a MAPLE-type nuclear fuel channel can be determined even though the presence of 37 finned rods complicates the flow geometry.

7.2 CANDU-Type Nuclear Fuel Channel Flow Studies

The CANDU-type nuclear fuel channel is described in detail in section 3.6.4. Experimental measurements of flow regime, void fraction, and bubble motion are observed and discussed.

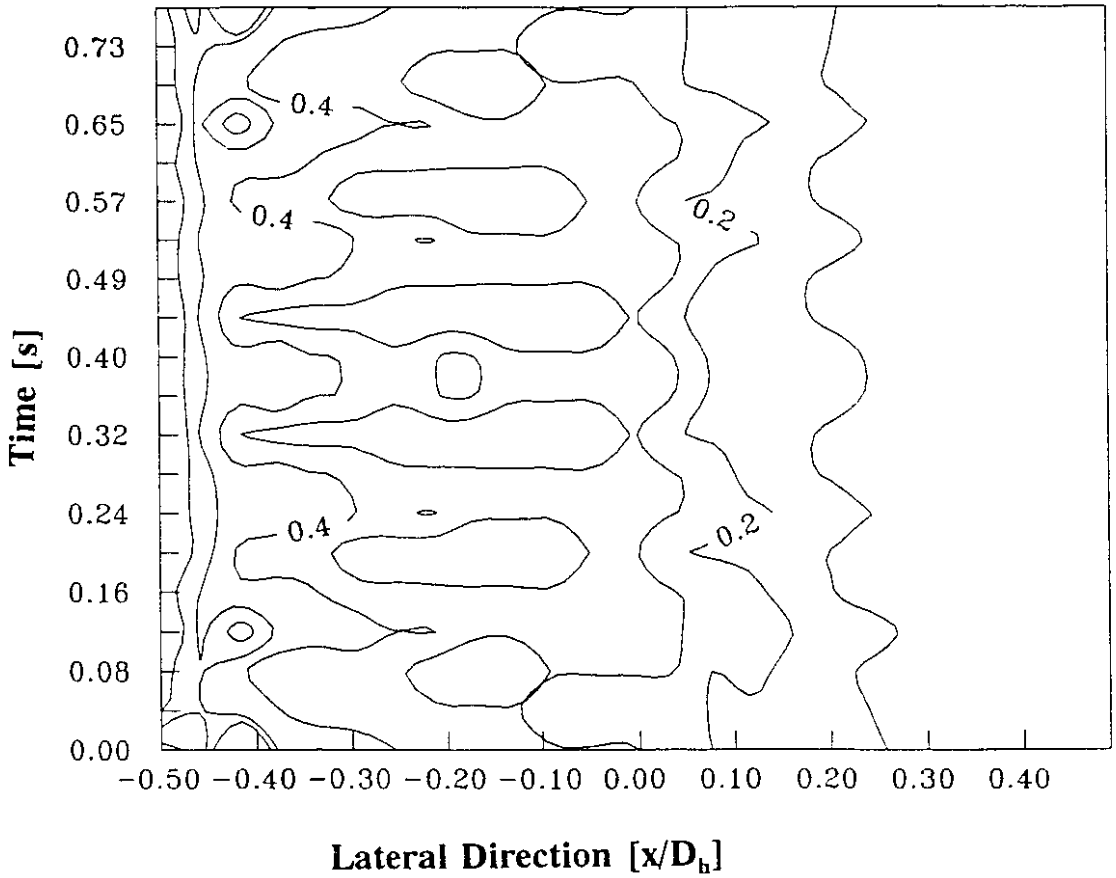

Figure 7.9: Lateral Void Fraction Distribution in a MAPLE-Type Nuclear Fuel Channel

7.2.1 Visualization of Two-Phase Flow

Three RTNR images of two-phase flow in a CANDU-type nuclear fuel channel are shown in Figure 7.10. Figure 7.10(a) shows the case where the CANDU-type nuclear fuel channel is completely voided. Figure 7.10(b) shows the case for a superficial gas velocity of 0.18 m/s and a superficial liquid velocity of 0.15 m/s. Figure 7.10(c) shows the case for a superficial gas velocity of 0.50 m/s and a superficial liquid velocity of 0.15 m/s. In each image, two black horizontal lines indicate the wall of the flow channel. Figure 7.10(a) shows the horizontal rods of the CANDU-type 37 rod bundle as dark grey horizontal bands. Black lines are added to this image to define the rod locations. Figure 7.10(b) shows a large amplitude wave which is just leaving the viewing area. This wave does not touch the top of the flow channel and travels through the core of the bundle. Some dark regions above the interface represent droplets attached to the rods. Figure 7.10(c) shows a nearly flat interface. This flow is in the middle of an elongated bubble before a plug of liquid is formed. Liquid droplets on the rods above the gas-liquid interface are not observed due to the higher gas velocity. Although Figure 7.10(b) shows a lower interfacial height than Figure 7.10(c) where a higher gas velocity is present, this does not reflect any dependence on the gas velocity as both images are instantaneous and the interfacial height is observed to be a strong function of time.

Figure 7.11 shows the experimental flow regime map obtained by the RTNR system in this study. The dashed curve represents the stratified smooth to intermittent flow regime transition boundary as determine by Osamusali et al.[66]. There is significant discrepancy between Osamusali et al.'s model [66] and the present experiments. The additional new flow regime called the "Large Amplitude Stratified Wavy Flow"(LASW) is defined.

The flow regimes for this experiment are defined as follows. Stratified smooth flow is defined as a smooth interface and stratified wavy flow is defined as a small amplitude wave not more than one subchannel in height. The difference between

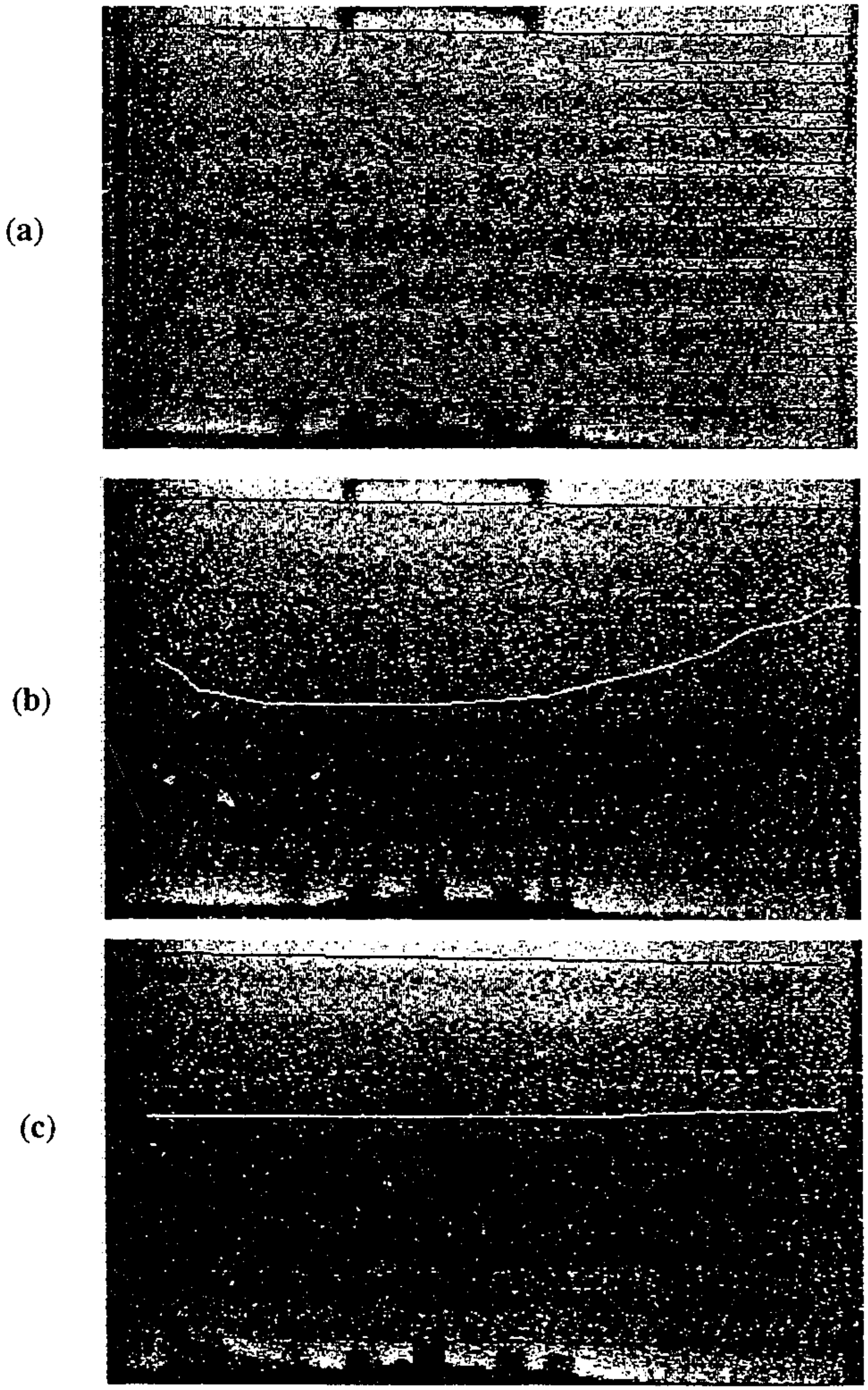

Figure 7.10: RTNR images of Two-Phase Flow in a Horizontal CANDU-Type Nuclear Fuel Channel: (a) Completely Voided Channel, (b) U_{gs} = 0.18 m/s, U_{ls} = 0.15 m/s, (c) U_{gs} = 0.50 m/s, U_{ls} = 0.15 m/s

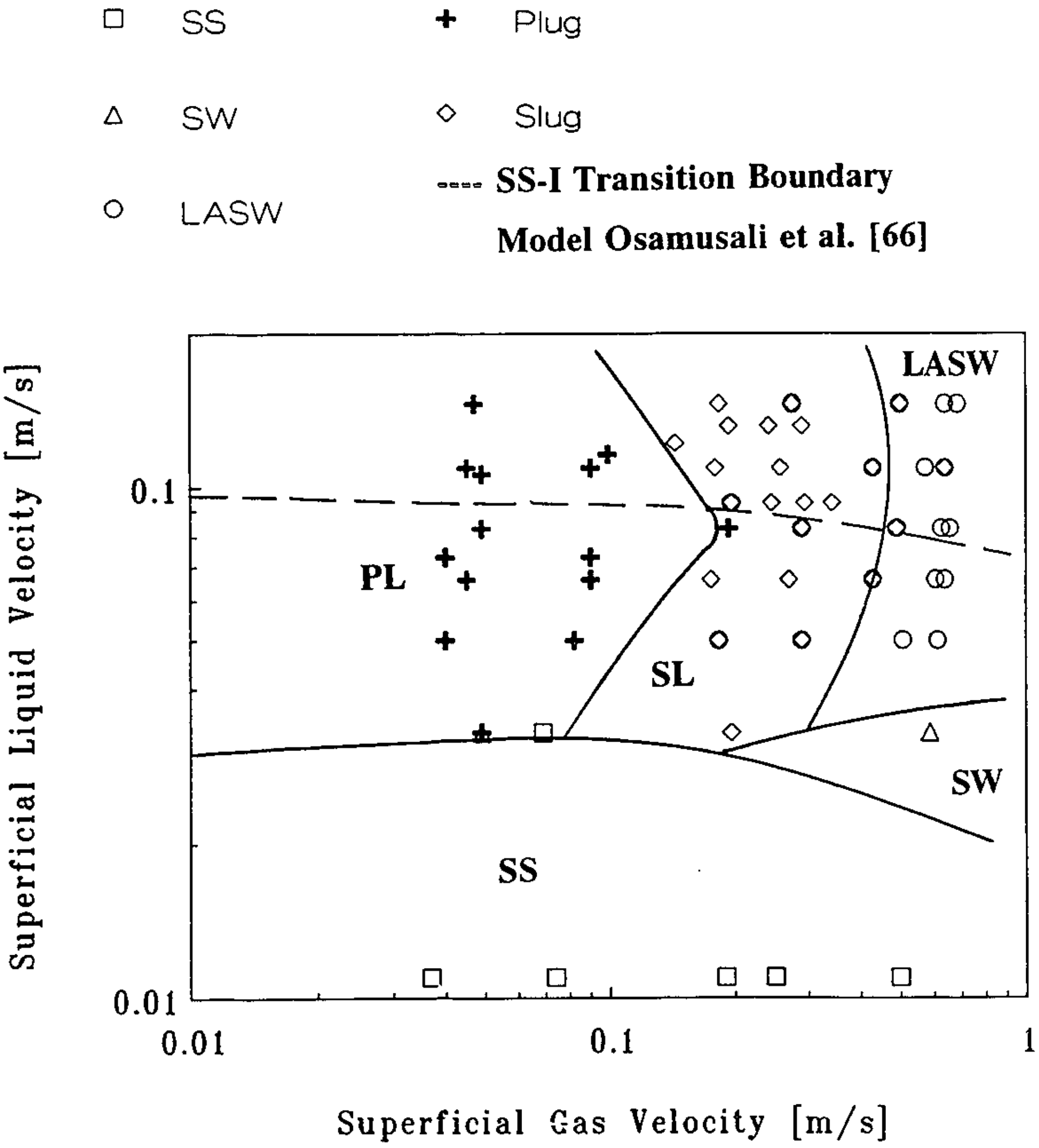

Figure 7.11: Flow Regime Map for a Horizontal CANDU-Type Nuclear Fuel Channel determined by RTNR: SS - Stratified Smooth, SW - Stratified Wavy, LASW - Large Amplitude Stratified Wavy, PL - Plug, SL - Slug, (- - - -) Theoretical SS-I Transition Boundary by Osamusali et al. [66]

slug flow and plug flow has been defined by the stability of the interface. Smooth interfaces were defined as plug flow(Elongated bubbles). Unsmooth, erratic, wispy, or violent interfaces which still produced a wave that connected to the top of the flow channel are called slug flow.

At high gas velocities, a new flow regime has been defined as large amplitude stratified wavy (LASW). Whether this flow regime is an extension of stratified wavy or a mixture of stratified wavy and plug flow is unclear. The characteristics of this new flow regime are as follows. LASW has a significant amplitude at least 50% the height of the liquid level compared to when the wave does not exist, i.e. at least two subchannels in height. LASW is a pulsed wave similar to plug flow and is not a continuous wave. Typical shape for LASW wave is gaussian. Most importantly, the LASW wave does not connect with the top of the flow channel and does not pass the top most row of rods. Under steady state conditions, pulse frequency appears to be constant. In between the pulses, the flow pattern is the normal stratified wavy with amplitude less than one subchannel.

Originally, the new flow regime was defined as the development or transition from stratified wavy to plug flow. This may still be the case, however, the experimental measurements obtained for LASW do not agree well with known flow regime maps. For example, according to previous work for pipe flow, all of the experimental measurements of LASW should be stratified smooth. Also, according to the model of Osamusali et al. [66], approximately 60% of the measured LASW data points should be stratified smooth and the other 40% should be plug flow. Previous observations of stratified wavy in the CANDU-type bundle were observed through a transparent test section and using a capacitance void fraction transducer. These observations showed that the stratified wavy flow was of a small amplitude and did not exceed one rod width at the gas flow rates studied in this work. An LASW wave could not be observed by the human eye as the metal outer rods would obstruct the view into the bundle core. The capacitance void fraction transducer is significantly influenced by the metal rod bundle so that only a small amplitude stratified wavy flow regime may be observed even though a large amplitude wave is travelling through the core of the bundle.

The discrepancies between the present experimental observations and the flow regime map from previous experimental work[66] as shown in Figure 7.11 are difficult to explain. For example, the experimental apparatus used by Osamusali et al.[66] and in the current work are nearly identical. The rod bundles, metal flow channels, gas-liquid mixing chamber, pump, and gas and liquid flow meters are identical. The transparent test section and the large reservoir tank used by Osamusali et al.[66] had been removed and replaced with a metal "T" section as shown in Figure 3.8. This was necessary due to space limitations in the beam port facility (Figure 3.1) and the need to close the loop as much as possible to reduce heavy water losses. The effect of the "T" section and the constrained space in the beam port facility is two-fold. The first effect is that the experimental observations obtained in this work are made at a shorter developing length than performed by Osamusali et al.[66] In this work, the experimental measurements are made for developing lengths (L/D_h) of 40. Osamusali et al. determined their measurements at an equivalent L/D_h of 50. The second effect by the "T" section is that the reservoir is smaller and during a plug-like flow, the "T" joint becomes completely filled with water which then has a pressure feed back into the system. These effects mean that the flow regimes observed in this work are not as developed as in previous work and that the boundary conditions at the exit of the flow channel change with flow regime. Since, in previous work, the pressure at the flow channel outlet was consistently near atmospheric pressure and definitely constant, the energy involved in the LASW flow regime would dissipate faster and the flow regime would change to stratified smooth or stratified wavy flow.

Entrance phenomena is not considered important since previous work by Osamusali et al. [67] showed that the entrance flow regime had a negligible effect except at low superficial gas velocities. Even under low superficial gas velocities, the effect of the entrance flow regime cannot explain the discrepancies found in the present work.

Another key factor in the generation of the LASW wave is cross flow phenomena which allows liquid to travel upward in the bundle across the subchannels aided by rod surface tension effects. As a wave travels through the bundle, the liquid in the subchannel migrates upwards and contacts the rods above the wave. Surface tension effects assist the growth of the wave and the wave climbs to higher and higher rods. However, the bundle is circular, which has the effect of pushing the fluid towards the centre of the core as the circumferential direction has the least resistance to cross-flow.

The presence of the LASW flow regime may be due to a combination of undeveloped flow phenomena, boundary conditions, and circumferential cross flow occurring in the bundle. The rods in the bundle may act as a dampener to the vertical flow and hinders the development of the wave into plug or slug flow by changing the momentum of the fluid in the circumferential direction.

7.2.2 Measurement of Void Fraction

The horizontal two-phase flow inside the CANDU-type nuclear fuel channel appears quite different than the case shown by the analysis for the vertical MAPLE-type nuclear fuel channel. Figure 7.12 shows the cross-sectional averaged void fraction along the axis of the flow channel for superficial gas velocities of 0.18, 0.50 and 0.64 m/s. As in the previous case shown in Figure 7.4, the cross-sectional averaged void fraction is not significantly dependent on the axial position, however in this case, the void fraction does not necessarily increase with increasing superficial gas velocities and is significantly time dependent.

Figure 7.13 shows the cross-sectional averaged void fraction profiles for various times with a superficial gas velocity of 0.50 m/s and a superficial liquid velocity of 0.15 m/s. Each curve is separated in time by 32.0 ms. The void fraction fluctuation is shown to be on the order of 15%. Detailed analysis shows that there is a small interfacial wave moving slowly along the axis.

Observation of the interfacial wave motion is shown in Figure 7.14 which indicates the void fraction fluctuation for three different axial positions as a function

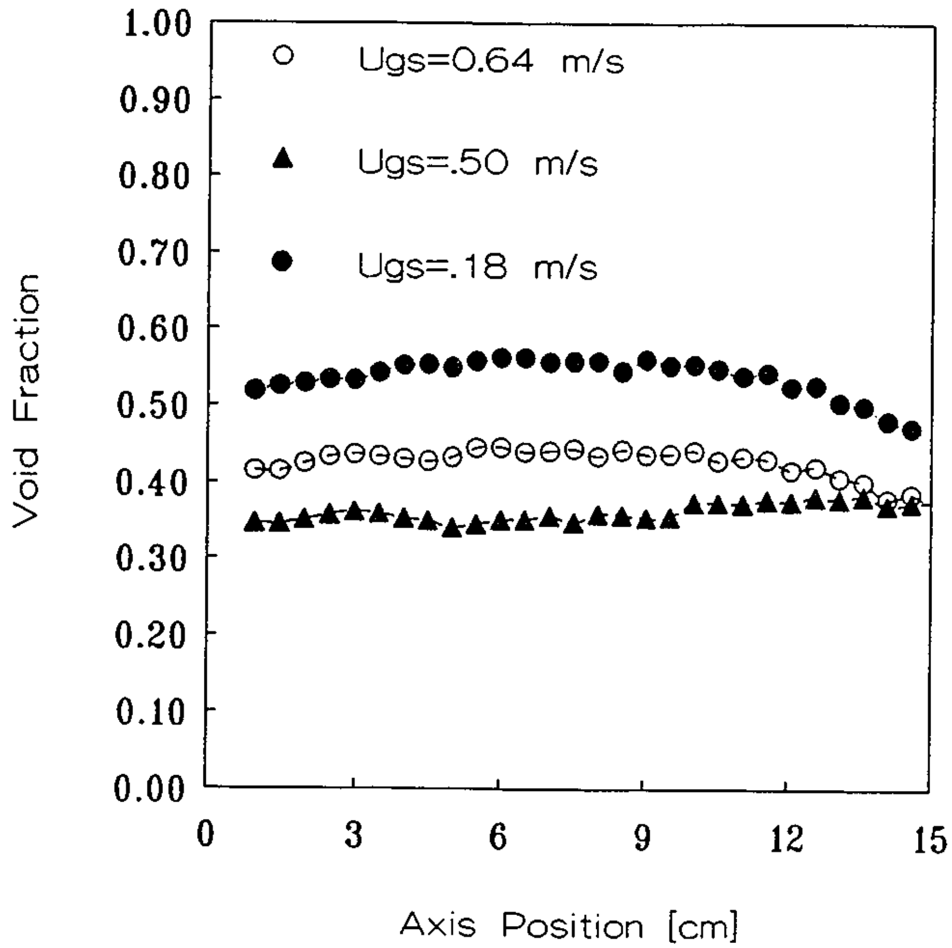

Figure 7.12: Cross-Sectional Averaged Void Fraction in a Horizontal CANDU-Type Nuclear Fuel Channel

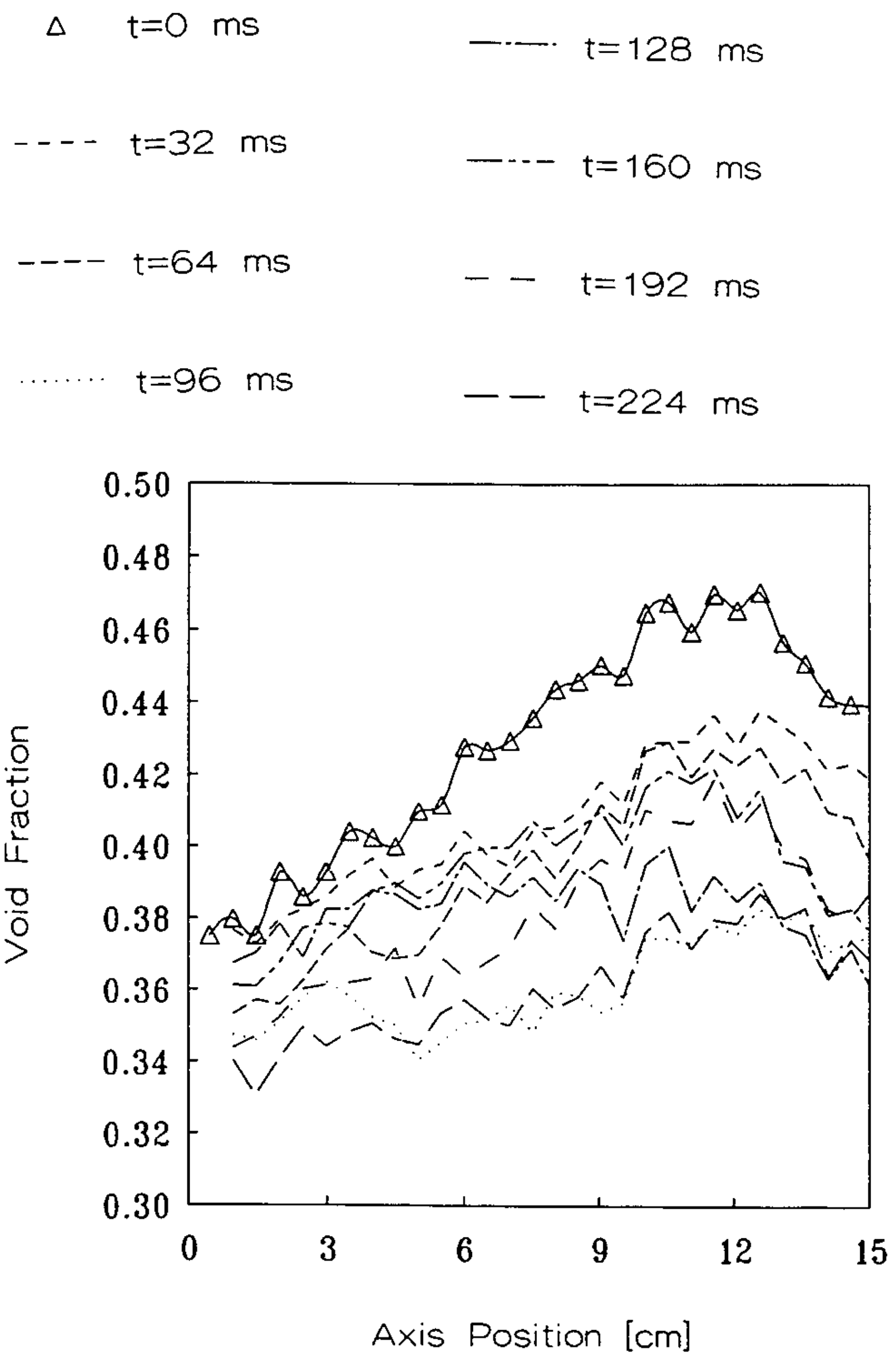

Figure 7.13: Cross-Sectional Averaged Void Fraction in a CANDU-type Nuclear Fuel Channel for a Superficial Gas Velocity of 0.50 m/s and a Superficial Liquid Velocity of 0.15 m/s

of time, where the gas and liquid superficial velocities are the same as for Figure 7.13. The magnitude of the fluctuation is approximately 15% and the periodicity of the wave is approximately 180 ms. As the void fraction fluctuation is constant with axial position, the wave can be considered steady state in time and space.

Figure 7.15 shows similar cross-sectional averaged void fraction waveforms for superficial gas velocities of 0.5 m/s and 0.64 m/s at a constant superficial liquid velocity of 0.15 m/s. Both the periodicity of the interfacial wave and the magnitude of the mean void fraction is influenced by the superficial gas velocity. As the superficial gas velocity increases, the periodicity of the wave decreases and the magnitude of the fluctuation increases. This suggests that each wave size increase as the superficial gas velocity increases. More analysis is necessary to determine if this effect extends over large ranges of superficial gas velocities.

7.2.3 Measurement of Void Distribution

Figure 7.16 shows the void fraction distribution in a CANDU-type nuclear fuel channel for a LASW flow regime. The upper part of the bundle has lateral coordinates greater than 0.0. Under this condition, the LASW wave is just leaving the viewing region as shown by the 80% void fraction contour increasing to higher lateral positions from axial positions of 11.0 to 15.0 cm. For the remainder of the viewing region, the interfacial wave is generally constant at a lateral position of 2.5 cm.

Figure 7.17 shows the lateral void fraction as a function of time for an LASW wave where the lateral void fraction information is taken for an axial position of 10.0 cm (centre of the viewing area). This figure shows the large change in the interface position, and small water droplets on the upper rods. There are some erroneous results in the image as shown for lateral position $0.5D_h$. This is the top of the nuclear fuel channel and scattering effects are disturbing the calculations for the void fraction. Also, there may be some droplets attached to the upper surface which are not removed by the passage of gas.

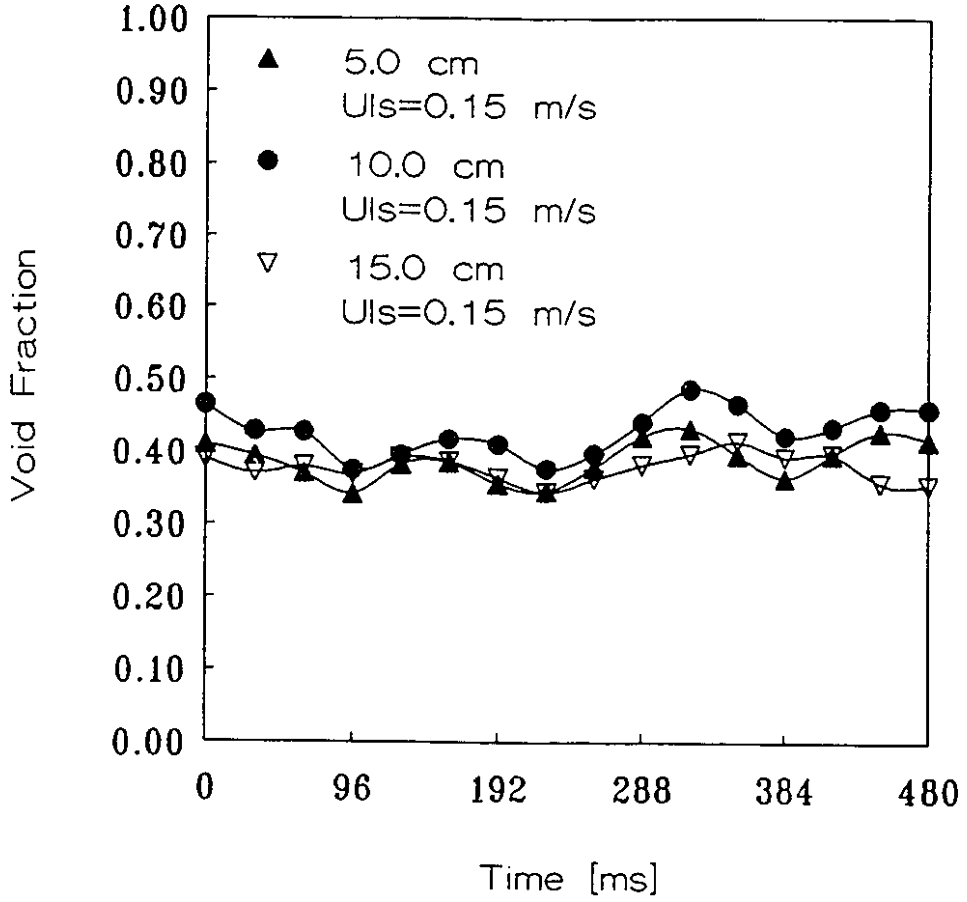

Figure 7.14: Void Fraction Fluctuation at Several Axial Positions in a CANDU-type Nuclear Fuel Channel

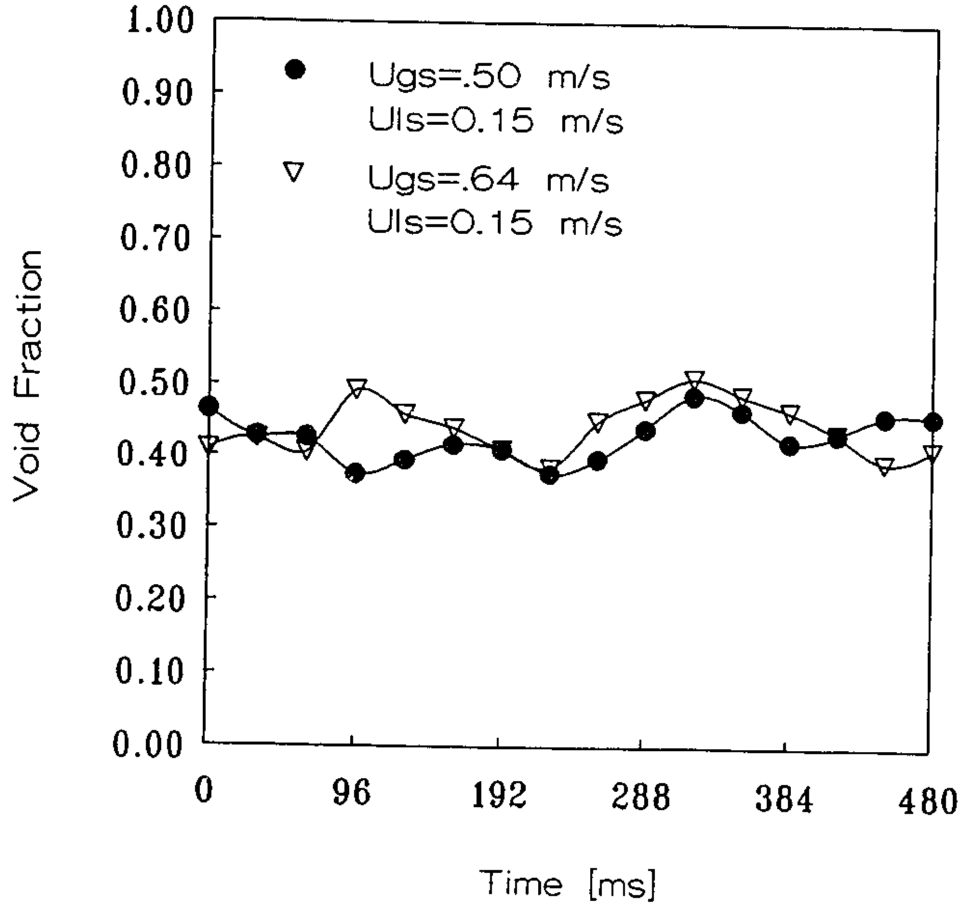

Figure 7.15: Void Fraction Fluctuation for Various Superficial Gas Velocities in a CANDU-type Nuclear Fuel Channel

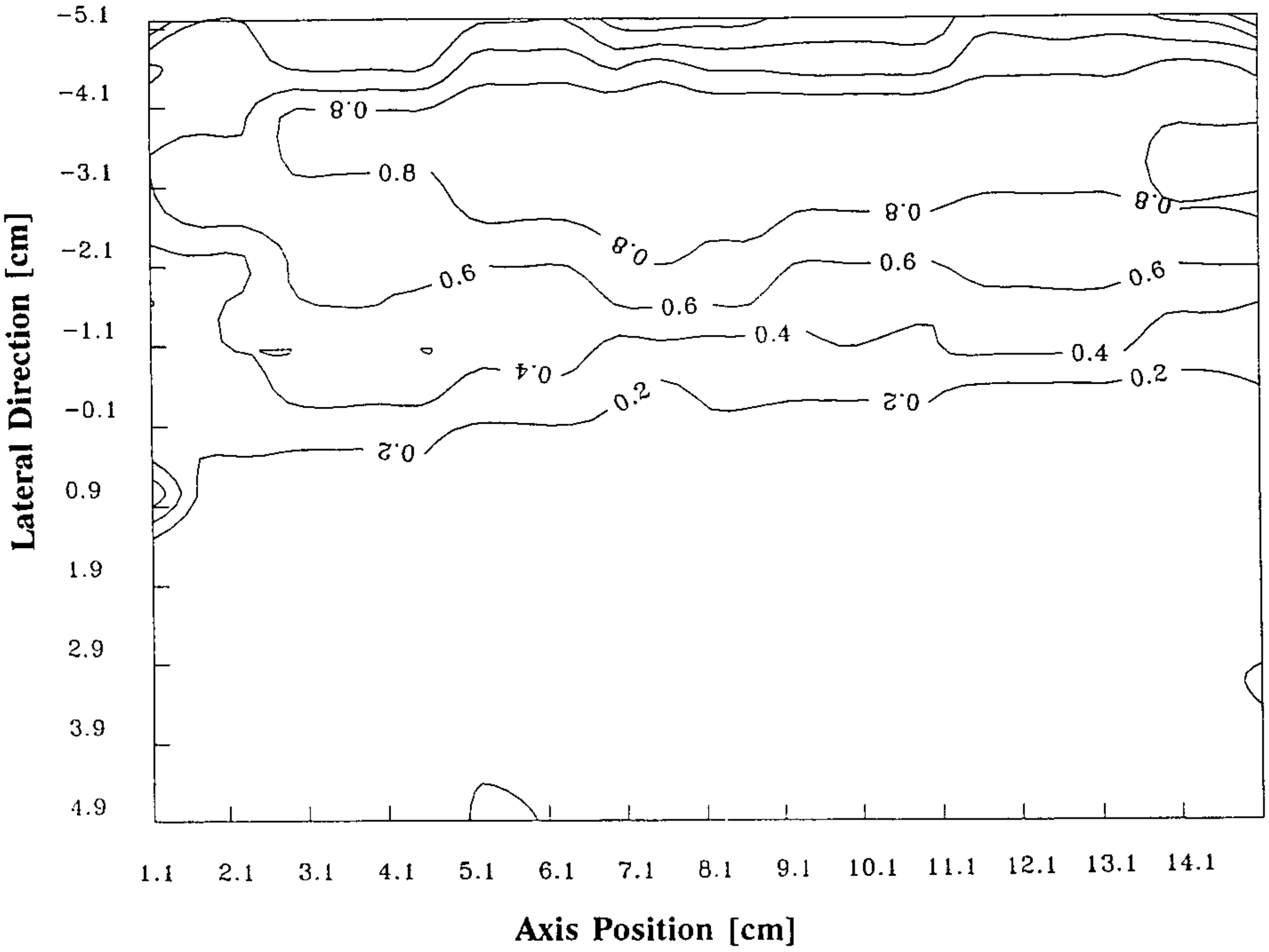

Figure 7.16: Instantaneous Void Fraction Distribution in a CANDU-type Nuclear Fuel Channel: $U_{gs} = 0.18$ m/s, $U_{ls} = 0.15$ m/s

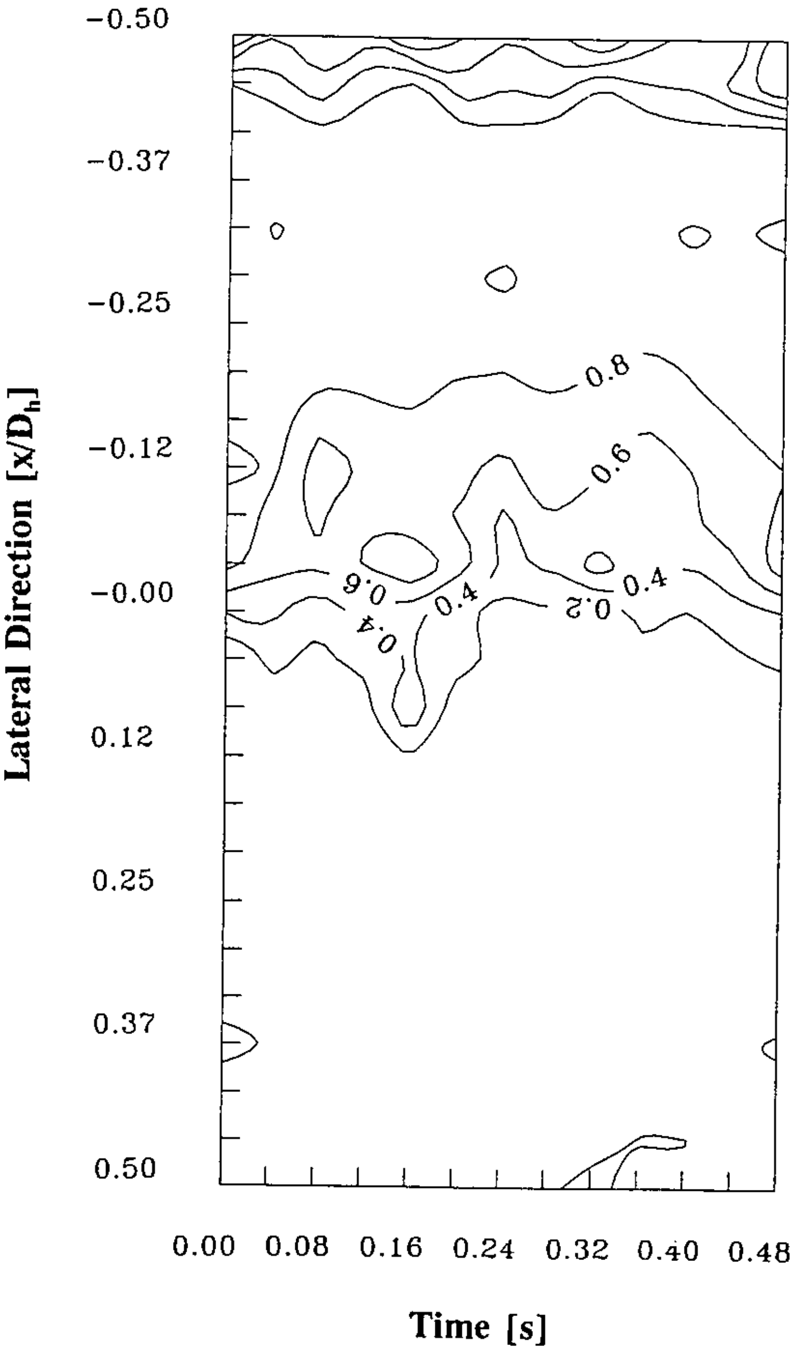

Figure 7.17: Lateral Void Fraction Distribution in a CANDU-type Nuclear Fuel Channel: U_{gs} = 0.18 m/s, U_{ls} = 0.15 m/s

Essentially, the flow regime, void fraction, void fraction distribution, and interfacial wave motion has been determined for the CANDU-type nuclear fuel channel. The presence of the rods have shown a significant effect on the flow regime and hence the void fraction distribution.

Chapter 8

8. Concluding Remarks

The measurement of two-phase flow parameters by a Real-Time Neutron Radiography system has been conducted for several different flow geometries. This work has culminated in obtaining detailed information regarding the characteristics of this system, and two-phase flow behaviour in complex flow geometries. The conclusions of this work can be separated into three areas. They are the RTNR system's performance, application of the RTNR system to two-phase flow, and measurement of two-phase flow phenomena.

8.1 Concluding Remarks for RTNR System Performance

There are now several RTNR systems and neutron radiography facilities around the world. Each one differs slightly in design, and detail of each system or facility is not presented here. However, all systems and facilities have similar limitation and capabilities which affect the performance of the RTNR system. These limitations and capabilities are summarized as follows:

- The RTNR system is sensitive to neutron fluxes greater than 10^4 n/cm^2-s depending on design of the converter screen.

- The signal to noise ratio increases and the target integration effects decrease with increasing neutron flux.

- The RTNR system has a non-linearity when neutron fluxes decrease below $10^4 n/cm^2 - s$, and this non-linearity has a significant effect on the image quality and accuracy of neutron detection.

- Most RTNR systems are affected by gamma radiation which appears as speckle noise in the image.

In summary, the good performance of an RTNR system depends on achieving a strong enough neutron flux for the desired application, and reducing gamma radiation and neutron scattering in the radiation beam, i.e. beam purity.

In spite of the fact that other facilities are currently demonstrating this technology for various applications at higher neutron fluxes($\geq 10^8$ n/cm^2-s), where the signal to noise ratio is excellent and the radiation dose is high, the present work has successfully shown application of this technique under moderate neutron fluxes(10^5-10^6 n/cm^2-s).

8.2 Concluding Remarks for RTNR Two-Phase Flow Measurement Techniques

This work has demonstrated that the RTNR system can be applied to measure two-phase flow phenomena for various flow geometries and different wall materials. The quantity of material used, type of material used, and the effect of neutron buildup are observed to significantly influence the RTNR two-phase flow measurement technique. The quantity or type of material affects the results when a significant amount of material or a highly attenuating material is used. Under these conditions, the attenuation of the neutron beam will be reduced below the real-time limit and the non-linear response of the RTNR system must be corrected.

Thus, in this work, it was shown that light water can only be used in small thicknesses or under large neutron fluxes. Other fluids such as heavy water are more suited for research at large fluid thicknesses and lower neutron fluxes.

Neutron build-up or scattering effects may also need to be considered if the application involves material with a significant scattering component such as light water.

Specific advantages for the RTNR system are the ability to measure two-phase flow phenomena in a non-intrusive manner, through metallic wall materials, and in $3^1/_2$ dimensions. non-intrusive measurement is important as this allows for detailed knowledge of the two-phase flow parameters without disturbing the flow. The ability to measure through opaque metallic flow systems allows for the measurement of two-phase flow parameters under low to high pressure, and low to high temperature conditions such as steam-water flow in a nuclear fuel channel (10.0 MPa, 300C). In addition, the $3^1/_2$ dimensions $(x,\int dy,z,t)$ measured provides extremely detailed information in complex geometries such as nuclear fuel bundles.

8.3 Conclusions for RTNR Two-Phase Flow Measurements

The following conclusions are obtained from the studies performed in this work for each flow geometry investigated. They are summarized as follows:

Pipe Flow

- Flow regimes observed by RTNR, video and ultrasonic pulse-echo techniques in the natural circulation loop agree well with each other, and the obtained flow regime map agrees well with Mishima and Ishii's model in-spite-of the natural circulation nature of the flow.

- Unlike optical visualizations, RTNR not only can determine two-phase interfaces in a metal tube as a two-dimensional edge contour, but also additional three dimensional interfacial geometry information can be obtained from the intensity contour map. However, this additional information is only obtainable through intensive image processing and analysis methods.

- The cross-sectional averaged void fraction at each axial location can be determined by Real-Time Neutron Radiography. The volume averaged void fraction of a bubble column determined by neutron attenuation agrees fairly well with the volume averaged void fraction by the RTNR determined liquid level method and with volume averaged information obtained by ultrasonic techniques.

- The instantaneous void fraction profile can be obtained in a relatively large section of the pipe(20cm X 20cm) and provide relevant information regarding the location and shape of interfaces.

- Bubble size and shape along the flow channel can be determined. Mean bubble diameter averaged across the bubble column only slightly increases with increasing gas velocity.

- Two distinct high and low void regions are noted to co-exist in a bubble column for higher gas velocities at low water volume conditions. This high void region represents a change in flow regime and the development of a new recirculation zone.

- The interfacial area at each axial location can be determined by the RTNR method, and results confirm non-monotonic axial interfacial area profiles as have been observed in earlier investigations. Interfacial area averaged across the bubble column increases with increasing gas velocity as expected.

- The RTNR technique has been shown to produce time dependent two-dimensional void fraction profiles for bubble and slug flow regimes.

- The error in void fraction measurement increases with increasing water thickness when the light water thickness is greater than 1.0 cm.

- The inclusion of the temporal component provides detailed insight into the migration of void fraction during steady-state global conditions and transient phenomena and allows for the determination of interfacial and slug velocities.

Annulus Flow

- The RTNR system, High Speed X-CT system, and the optical video system agree well for the characterization of two-phase flow regime in an annulus bubble column.

- The flow regime map for a vertical annulus flow channel operated as a bubble column has been determined. The flow regime map is found to be primarily dependent upon the gas Reynolds number(i.e. Superficial Gas Velocity), but is also influenced by the non-dimensional initial static liquid level.

- At low non-dimensional initial static liquid levels, slug flow is virtually non-existent in a vertical annulus flow channel.

- Both the RTNR system and the High Speed X-CT system can measure the cross-sectional averaged void fraction in a vertical annulus flow channel and account for the presence of the inner pipe.

- The behaviour of the void fraction determined by the RTNR system as a function of elevation and gas flow rate is non-monotonic in nature.

- The time and cross-sectional averaged void fraction as determined by the RTNR system and the High Speed X-CT system agree within 4% of each other.

- Circumferential bubble motion is easily observed in the X-CT system at high gas flow rates whereas axial and lateral bubble motion is observed in the RTNR system. Bubble development (agglomeration and shape change) is observed using the RTNR system which cannot be observed by the X-CT system.

- The X-CT system has a much better temporal resolution than the RTNR system but the RTNR system can still provide good temporal analysis and measurement of void fraction distributions, since both systems show qualitatively similar behaviour for two-phase interfacial motion and void distributions. For example, the RTNR system still shows the same periodic nature to the temporal void fraction as observed by the High Speed X-CT system even though the temporal resolution is decreased.

- Both the RTNR system and the X-CT system show that the lateral and circumferential void fraction motion does not occur for superficial gas Reynolds numbers less than 220 which shows a relatively low turbulence in the flow channel.

Nuclear Fuel Channels

- Although the influence of the rod bundle in a MAPLE-type nuclear fuel channel and a CANDU-type nuclear fuel channel complicates the geometry, knowledge of the rod locations and image processing techniques are sufficient to correct this influence and obtain the two-phase flow information.

- The flow regime map for the MAPLE-type nuclear fuel channel agrees well with the model by Harvel et al.[65]. This agreement confirms the fact that the MAPLE-type nuclear fuel bundle is the dominant influence on the flow regime and that the type of channel wall material used is unimportant.(aluminium in RTNR, lucite in previous work)

- The non-monotonic relationship between the cross-sectional averaged void fraction and elevation is observed only in the bubble column modes suggesting this relationship is a strong function of recirculation phenomena.

- The cross-sectional averaged void fraction in a MAPLE-type nuclear fuel channel increases with increasing superficial gas velocity and decreases with increasing superficial liquid velocity.

- The time and cross-sectional averaged void fraction in a MAPLE-type nuclear fuel channel is not influenced by elevation at the entrance to the bundle but does increase with increasing elevation above 50.0 cm from the inlet to the flow channel.

- The MAPLE-type bundle under vertical co-current two-phase flow restricts the flow into the subchannels and inhibits void drift phenomena although some void migration is observed from one subchannel to the next.

- Wavy Interfaces are observed in a MAPLE-type nuclear fuel channel at a superficial gas velocity of 0.23 m/s, i.e. above the drift velocity, and at a superficial liquid velocity of 0.10 m/s where these wavy interfaces are related to void migration attempts from one row of subchannels to another.

- A new flow regime has been defined for two-phase horizontal flow through a CANDU-type 37 rod nuclear fuel bundle. This flow regime is a large amplitude stratified wavy flow pattern (LASW) and is a product of cross flow and dampening forces in the bundle. The interfacial wave associated with the LASW flow pattern typically has a gaussian shape.

- Interfacial wave amplitude in stratified wavy flow is restricted to the height of one subchannel whereas LASW interfacial waves have amplitudes greater than two subchannels. No interfacial waves with amplitudes greater than one subchannel height and less than two subchannel heights have been observed.

- Increasing the superficial gas velocity does not necessarily increase the instantaneous void fraction in a horizontal CANDU-type nuclear fuel channel due to flow regime effects.

- The periodicity of an interfacial wave and the magnitude of the void fraction fluctuation in a CANDU-type nuclear fuel channel are observed as functions of the superficial gas velocity but not as a function of the axial position.

Detailed information regarding the flow regime, void fraction, void fraction distribution, bubble diameter, bubble velocity, and interfacial area have been obtained in complex two-phase flow geometries.

Chapter 9

9. Recommendations for Future Work

In order to establish a RTNR two-phase flow measurement technique, experimental data has been compiled for measurement of two-phase flow in pipe, annulus, and rod bundle nuclear fuel channels. Although vertical pipe flow has been extensively studied in this work, only a narrow experimental range of the results has been analyzed for the annulus and rod bundle nuclear fuel channel experiments except measurements of flow regime, void fraction, and void fraction distribution. Analysis of other two-phase flow parameters such as bubble diameter, bubble velocity, interfacial area, and interfacial velocity have been only briefly examined to demonstrate the capability of the RTNR system for nuclear fuel channels with rods. Hence, a significant amount of work remains to examine in detail these other two-phase flow parameters and what influence, if any, a nuclear fuel bundle will have on these parameters.

Remaining analysis of the annulus experiments include additional bubble velocity measurements. These measurements can be used to improve the three-dimensional reconstruction in the X-CT software and to determine the interfacial area of each bubble. It is then possible to correlate the void fraction, bubble velocity, and interfacial area in the annulus flow channel.

A more fundamental approach that remains is to examine each chordal void fraction in detail as determined by the X-CT system for a direct comparison with the RTNR technique. The effect of the circumferential angle can be determined and temporal void distributions similar to those obtained by the RTNR system can be determined.

For the MAPLE-type nuclear fuel channel, void migration phenomena can be studied in more detail. The effect of elevation, superficial gas velocity, and superficial liquid velocity remain to be correlated. Bubble velocity measurements and their dependence on flow regime, void fraction, and superficial gas and liquid velocities can be determined. With this knowledge, a more mechanistic model for the flow regime in a MAPLE-type nuclear fuel channel can be determined.

Experiments on the CANDU-type nuclear fuel channel have shown that cross-flow plays an important role in flow regime transitions. Measurements of interfacial area and cross-flow can be performed to develop a new mechanistic model for the flow regime and determine the source of the discrepancy with existing models.

In addition, laboratory scale experiments can be performed with the RTNR system to analyze transient phenomena and heat transfer phenomena such as steam generation and condensation studies. Results from these laboratory scale experiments can be used to develop new and improved interfacial correlations for constitutive relationships used in modelling of two-phase flow.

The RTNR system and the neutron beam port used in this work require further improvements to achieve a high signal to noise ratio. These improvements fall into three categories: upgrading the neutron flux in the beam port, increasing sensitivity to neutrons in the RTNR camera, and improved image processing techniques. Increasing the power of the nuclear reactor to 5.0 MW and modifying the beam port tube will increase the neutron flux. Development of higher sensitivity neutron to photon converters will allow for operation at lower neutron flux levels and improve the linearity in the RTNR system over a wider range of neutron fluxes. The use of a logarithmic video amplifier will improve the linearity of the RTNR system by modifying the RTNR camera output video signal. Finally, more advanced image processing algorithms can be developed to improve image analysis. One important example is to develop an interface tracking algorithm which would determine the two-phase interface location in each image and track the movement of the interface for successive images.

The neutron source used in this work (MNR) is not portable. The development of an inexpensive portable neutron source with similar neutron flux levels is important for applications beyond laboratory scale experiments.

For the High Speed X-ray CT system, an increase in the number of sources and/or detectors would increase the size of the imaging area. An increase in the source-detector X-ray beam path density would improve the spatial resolution. Additional measurement planes would allow for the measurement of each bubbles velocity and the velocity distribution thus improving the three-dimensional reconstruction and the measurement of interfacial area. With more than one imaging plane, the marching cubes algorithm can be easily modified to produce a more accurate three-dimensional reconstruction of the object. Also, with additional imaging planes, visualization of counter-current and reversing flows would be possible.

The use of multiple imaging planes increases the cost and complexity of the High Speed X-ray CT system. A simpler method is to use a minimum number of imaging planes with a two-dimensional source-detector array for velocity measurement. The source-detector array for velocity measurement would use one wide beam X-ray source with nine X-ray detectors. Five of the detectors would be placed circumferentially about the measurement channel on the same axial plane as the X-ray source. These detectors would measure the θ component of the bubble velocity. Four other detectors would be placed axially along the length of the channel in line with one of the circumferential detectors. Together, these five detectors would measure the axial component of the bubble velocity. The advantage of this approach is that the cost and complexity of the High Speed X-ray CT system is reduced and the 3D reconstruction improved. The major disadvantage is that only a small number of the bubbles will actually be measured for velocity and the reconstruction will only be accurate for these bubbles.

The scanning rate is limited by the number of X-ray sources but can be improved by simultaneously firing several sources at one time. These improvements to the X-ray CT system are best incorporated into a new model due to the difficulty of modifying the current system, however certain experiments can be performed to identify the feasibility of these improvements. For example, by using an appropriate lead shield, alternate detectors can be set to measure at different axial elevations. The spatial resolution of each cross-section would decrease but the ability to measure bubble velocity can be tested. The outputs of the detectors can be artificially added to test the concept of multiple source simultaneous firing. Based on these experiments, design parameters can be obtained.

The High Speed X-ray CT system acquires the experimental data quickly enough (4.0 ms), yet the analysis time is extremely long. Approximately 1 minute of real time is required to reconstruct 1 image. The memory size required for each data file is also large. A typical experiment for the vertical annulus study required 45.0 Megabytes of memory, most of which are unnecessary images.

References

1. G. Hewitt, *Measurements of Two-Phase Flow Parameters*. Academic Press, New York, 1978.
2. S. Banerjee, and R.T. Lahey, Jr. "Advances in Two-Phase Flow Instrumentation", *Advances in Nuclear Science and Technology*. **13**, 227-414, 1981.
3. Y. Taitel, and A.E. Dukler, "A model for predicting flow regime transitions in horizontal and near horizontal gas-liquid flow",*AIChE Journal.*,**22**(1), 47-53, 1976.
4. J.M. Mandhane, G.A. Gregory, and K. Aziz, "A flow pattern map for gas-liquid flow in horizontal pipes", *Int. J. Multiphase Flow*, 1, 537-553, 1974.
5. L. Lightstone, S.I. Osamusali, and J.S. Chang, "Gas-Liquid Two-Phase Flow in Symmetrically Dividing Horizontal Tubes",*AIChE Journal*, **37**(1), 111,122, 1991.
6. Y. Taitel, D. Bornea, and A.E. Dukler, "Modelling Flow Pattern Transitions for Steady Upward Gas-Liquid Flow in Vertical Tubes",*AIChE Journal*, **26**(3), 345-354, 1980.
7. K. Sekoguchi, H. Fukui, M. Tsustui, and N. Nishikawa," Investigation into the Statistical Characteristics of Bubbles in Two-Phase Flow: Fundamentals of the Instrumentation using the Electric Resistivity Probe Technique",*Bulletin of the JSME*, **18**:391-396, 1975.
8. I. Kataoka, M. Ishii, and A. Serizawa, "Local Formulation of Interfacial Area Concentration and it's Measurements in Two-Phase Flow", *Report ANL*, 84-68, 1984.

9. M. Ishii and S.T. Revankar, "Measurement of Local Interfacial Area and Velocity in Bubbly Flow", In ANS Proceedings of *1991 National Heat Transfer Conference*, pp. 181-189, 1991.

10. P. Andreussi, A. Di Donfrancesco, and M. Messia, "An Impedance Method for the Measurement of Liquid Hold-up in Two-Phase Flow", *Int. J. Multiphase Flow*, **14**(6):775-785, 1988.

11. N.A. Tsochatzidis, T.D. Karapantsios, M.V. Kostoglou, and A.J. Karabelas, "A Conductance Probe for Measuring Liquid Fraction in Pipes and Packed Beds", *Int. J. Multiphase Flow*, **18**(5):653-667, 1992.

12. K. Brunner and J.S. Chang, "Flow Regime Transitions under Strong Electric Fields in a Horizontal Two-Phase Flow", *Conference Record of 1980 IEEE Industrial Applications Society*, pp.1042-1047, 1980.

13. J.S. Chang, R. Girard, R. Raman, and F.B.P. Tran, "Measurement of Void Fraction in Vertical Gas-Liquid Two-Phase Flow by Ring type Capacitance Transducers", *Mass Flow Measurements-1984*, ASME Press, New York. pp. 93-99, 1984.

14. L. Cimorelli, and R. Evangelisti, "The Application of the Capacitance Method for Void Fraction Measurements in Bulk Boiling Conditions", *Int. J. Heat and Mass Transfer*, **10**, 277-278, 1967.

15. G.A. Irons, and J.S. Chang,"Particle Fraction and Velocity Measurements in Gas-Powder Streams by Capacitance Transducers", *Int. J. Multiphase Flow*, **9**, 289-297, 1983.

16. M. Sugaya, N. Hayashi, and J.S. Chang, "Effects of Highly Charged Powder on Solid Fraction Measurement by Capacitance Transducers in Solid-Gas Two-Phase Flow", *Trans. IEE Japan*, **110**-A(3)197-205, 1990.

17. J.S. Chang, T.A. Myint, B. Donevski, A.A. Berezin, G.A. Irons, and W.K. Lu,"Determination of the Interfacial Parameters in Gas-Solid Two-Phase Pipe Flow by Capacitance Transducers", *Particulate and Multiphase Processes - Colloidal and Interfacial Phenomena*, (T. Ariman and T. Nejat Veziroglu, Eds.) Hemisphere Publishing Corporation, Springer-Verlag, pp.173-187, 1985.

18. S.M. Huang, A.B. Plaskowski, C.G. Xie, and M.S. Beck,"Tomographic Imaging of Two-Component Flow using Capacitance Sensors", *Journal of Physics E, Scientific Instruments*, **22**(3), 173-177, 1989.

19. C.G. Xie, A.B. Plaskowski, and M.S. Beck, "Eight-electrode Capacitance System for Two-Component Flow Identification", *IEE Proceedings Pt. A*, **136**,

184-190, 1989.

20. A.D. Seagar, D.C. Barber, and B.H. Brown, "Electrical Impedance Imaging", *IEE Pt. A.*, **134**(2), 201-210, 1987.

21. J.T. Lin, L. Ovacik, O.C. Jones, J.C. Newell, M. Cheney, and H. Suzuki, "Use of Electrical Impedance Imaging in Two-Phase Gas-Liquid Flows", *ANS Proceedings 1991 National Heat Transfer Conference*, pp.190-198, 1991.

22. G.A. Irons and J.S. Chang, "Dispersed Powder Flow through Vertical Pipes", *Powder Technology*, **34**, 233-242, 1983.

23. K. Brodowicz, J.S. Chang, B. Donevski, I. Sekovanic, and W. Tofiluk, "Gas-Solid Two-Phase Flow Patterns, Pressure Drop, and Void Distribution in an Inclined Flow Tube", *Experimental Heat Transfer, Fluid Mechanics, and Thermodynamics,* (R.K. Shah, E.N. Ganic, and K.T. Yang, Eds.), Elsevier, New York, pp.1338-1342, 1988.

24. K. Sekoguchi, M. Takeishi, K. Hironaga, and T. Nishiura, "Velocity Measurement with Electrical Double-Sensing Devices in Two-Phase Flow", In *Measuring Techniques in Gas-Liquid-Solid Two-Phase Flows* (J.M. Delhaye, and G. Cognet, Eds.), Springer-Verlag, Berlin, pp.455-477, 1983.

25. K. Sekoguchi, H. Fukui, M. Tsutsui, and K. Nishikawa, "Investigation into the Statistical Characteristics of Bubbles in Two-Phase Flow: Application and Establishment of Electrical Resistivity Prove Method", *Bulletin of the JSME*, **18**, 397-404, 1975.

26. J.K. Keska and R.D. Fernando, "An Experimental Study of Liquid Film Thickness Measurements in a Two-Phase Flow", *AIChE Symposium Series: Heat Transfer*, San Diego, **88**(288), 34-43, 1992.

27. M.R. Ozgu and J.C. Chen, "A Capacitance Method for Measurement of Film Thickness in Two-Phase Flow", *Rev. Sci. Instr.*, **44**(12), 1714-1716, 1973.

28. H.C. Kang and M.H. Kim, "The Development of a Flush-Wire Probe and Calibration Method for Measuring Liquid Film Thickness", *Int. J. Multiphase Flow*, **18**(2), 423-437, 1992.

29. J.S. Chang and E.C. Morala, "Determination of Two-Phase Interfacial Areas by an Ultrasonic Technique", *Nuclear Engineering and Design*, **122**, 143-156, 1990.

30. L. Matikainen, G.A. Irons, E.C. Morala, and J.S. Chang, "Ultrasonic System for Detection of Transient Liquid-Gas Interfaces using the Pulse-Echo

Techniques", *Rev. Sci. Instr.*, **57**, 1661-1666, 1986.

31. A.M.C. Chan and S. Banerjee, "Design Aspects of Gamma Densitometers for Void Fraction Measurement in Small Scale Two-Phase Flow", *Nuclear Instruments and Methods*, **190**, 135-148, 1981.

32. G.F. Knoll, *Radiation Detection and Measurement*, John Wiley, New York, 1989.

33. K. Hori, K. Miyazaki, T. Kurosu, S. Sugiyama, J. Matsumoto, and Y. Akiyama, "In Bundle Void Fraction Measurement of PWR Fuel Assembly", *Proceedings Second ASME/JSME Nuclear Engineering Conference*, Book No. 10343A, 1993.

34. T. Narabayashi, T. Tobimasu, H. Nagasaka, and T. Kagawa, "Measurement of Transient Flow Pattern by High Speed Scanning X-ray Void Fraction Meter", *Measurement Techniques in Gas-Liquid Flows*, pp.259-280, Springer-Verlag, 1984.

35. S. Morooka, T. Ishizuka, M. Iizuka, and K. Yoshimura, "Experimental Study on Void Fraction in a Simulated BWR Fuel Assembly", *Nuclear Engineering Design*, **114**: 91-98. 1989.

36. T. Narabayashi, T. Ishiyama, H. Miyano, and H. Nei, "Measurement of Void Distribution in High Pressure Steam-Water Two-Phase Flow using High-Speed X-ray Scanner", *Proceedings of First International Conference on Multiphase Flows*Vol. 1, Sept. 24-27, Tsukuba, Japan,pp. 241-246, 1991.

37. T. Mitsutake, S. Morooka, K. Suzuki, S. Tsunoyama, and K. Yoshimura, "Void Fraction Estimation within Rod Bundles based on Three-Fluid Model and Comparison with X-ray CT Void Data", *Nuclear Engineering and Design*, **120**:203-212, 1990.

38. K. Hori, K. Kawanishi, H. Hamamura, M. Ochi, and M. Akai, "A High Speed X-ray Computed Tomography Scanner for Multipurpose Flow Visualization and Measurement", *Proceedings of Fourth International Topical Meeting on Nuclear Thermalhydraulics, Operations, and Safety*,pp. 43-D-1 - 43-D-6, April, 1994.

39. A. Inoue, T. Kurosu, M. Yagi, S. Morooka, A. Hoshide, T. Ishizuka, and K. Yoshimura, "In-Bundle Void Measurement of a BWR Fuel Assembly by an X-ray CT Scanner: Assessment of BWR Design Void Correlation and Development of New Void Correlation", *ASME/JSME Nuclear Engineering Conference*, Book No. 10343A,pp. 69-76, 1993.

40. K. Mishima, K. Yoneda, S. Fujine, K. Kanda, H. Nishihara, "An Application of Neutron Radiography and Image Processing Techniques to Gas-Liquid Two-Phase Flow in a Narrow Duct",*Annu. Rep. Res. Reactor Inst., Kyoto Univ.*, **22**, 133-141, 1989.

41. J.M. Cimbala, D.E. Hughes, S.H. Levine, and D. Sathianathan, "Application of Neutron Radiography for Fluid Flow Visualization", *Journal of Nuclear Technology*, **81**, 435-445, 1988.

42. A.H. Robinson and S.L. Wang, "High Speed Motion Neutron Radiography of Two-Phase Flow", *Neutron Radiography*, pp. 653-659, 1983.

43. J.D. Jones, J.T. Lindsay, C.W. Kauffman, A. Vulpetti, and B.D. Peters, "Real-Time Neutron Imaging applied to Internal Combustion Engine Behaviour", *SAE Technical Paper Series*, 1985.

44. T. Sridhar and O.E. Potter, "Interfacial Areas in Gas-liquid Stirred Vessels", *Chemical Engineering Science*, **35**:683-695, 1980.

45. P.H. Calderbank,"The Interfacial Area in Gas-Liquid Contacting with Mechanical Agitation", *Trans. Inst. Chem. Engrs.*,**36**:443, 1958.

46. M.J. Lockett, and A.A. Safekourdi, "Light Transmission through Bubble Swarms", *AIChE Journal*, **23**(3):395-398, 1977.

47. R.F. Mudde, R.A. Bakker, and H.E.A. van den Akker, "Noise Analysis of Transmitted Light Beams for Determining Bubble Velocity and Gas Holdup Profiles in a Bubble Column", *Chemical Engineering Science*, **47**(13/14):3631-3638, 1992.

48. R.C. Chen and L.S. Fan, "Particle Image Velocimetry for Characterizing the Flow Structure in Three-Dimensional Gas-Liquid-Solid Fluidized Beds", *Chemical Engineering Science*, **47**(13/14):3615-3622, 1992.

49. E.M.A. Hussein, "Optimal Design of Neutron Scatterometers for Void Fraction Measurement", *Proceedings of International Conference on Multiphase Flows*:Vol. 2, Tsukuba, Japan, pp. 243-246, 1991.

50. P. Kehler, "Pulsed Neutron Measurement of Single and Two-Phase Liquid Flow", *IEEE Transactions on Nuclear Science*, **NS-26**(1):1627-1631, 1979.

51. K. Yoshii, K. Miya, and N. Katoh, "Television Imaging System for Fast Neutron Radiography using Baby Cyclotron", *Journal of Nuclear Science and Technology*, **30**(12):1275-1282, 1993.

52. W.E. Dance and S.F. Carollo, "High Sensitivity Electronic Imaging System for Reactor and Non-Reactor Neutron Radiography", Neutron Radiography, 2, pp. 415-422, 1986.

53. L.E. Bryant and P. McIntire, *NonDestructive Testing Handbook Vol.3: Radiography and Radiation Testing,* American Society for Non-Destructive Testing, 1992.

54. G.J. Yates, J.J. Bujnosek, S.A. Jaramillo, R.B. Walton, T.M. Martinez, and J.P. Black, "Radiation Effects on Video Imagers", IEEE Transactions on Nuclear Science, 33 (1):279-282, 1986.

55. T. Sokolowski, "Neutron Dose Measurements by Means of a Tissue Equivalent Proportional Counter", M.Sc. Thesis, McMaster University, 1989.

56. G. Arfken, *Mathematical Methods for Physicists*, pg. 875, Academic Press, Toronto, 1985.

57. A.A. Harms and D.R. Wyman, *Mathematics and Physics of Neutron Radiography*, D. Reidel, Dordrecht, 1986.

58. S. Fujine, K. Mishima, K. Yoneda, K. Yonebayashi, K. Yamamoto, M. Sobajima, S. Ohtomo, K. Kanda, H. Nishihara,"Visualization on Gas-Liquid Two-Phase Flow in a Narrow Rectangular Duct", *Neutron Radiography (3)* pp. 513-521,1990.

59. R.A. Brooks and G. Di Chiro,"Theory of Image Reconstruction in Computed Tomography" *Radiology*, 117:561-572, 1975.

60. K. Mishima, and M. Ishii, "Flow Regime Transition Criteria for Upward Two-Phase Flow in Vertical Tubes", *Int. Journal Heat and Mass Transfer*, **27**:723-737, 1984.

61. J.S. Chang and G.D. Harvel, "Determination of Gas-Liquid Bubbly Column Instantaneous Interfacial Area and Void Fraction by a Real-Time Neutron Radiography Technique", *Chemical Engineering Science*, 47(13/14): 3639, 1992.

62. W.H. Fairholm, G.D. Harvel, J.C. Campeau, and J.S. Chang, "Visualization of Two-Phase Interfaces in a Natural Circulation Loop by a Real-Time Neutron Radiography Imaging System", *ANS 1991 National Heat Transfer Conference*, pp. 199-206, 1991.

63. J.S. Chang, Y. Ichikawa, G.A. Irons, E.C. Morala, and P.T. Wan, "Void Fraction Measurement by an Ultrasonic Transmission Technique in Bubbly Gas-Liquid Two-Phase Flow", *Measuring Techniques in Gas-Liquid Two-Phase*

Flows,(J.M. Delhaye and G. Cognet Ed.s), Springer-Verlag, New York, pp. 319-335, 1984.

64. G.D. Harvel, K. Hori, K. Kawanishi, and J.S. Chang, "Real-Time Cross-Sectional Averaged Void Fraction Measurements in Vertical Annulus Gas-Liquid Two-Phase Flow by Neutron Radiography and X-ray Tomography Techniques", *2nd International Conference on Multiphase Flow*, Kyoto, Japan,(In Press) 1995.

65. G.D. Harvel, "Two-Phase Flow Regime Map for a MAPLE Nuclear Rector Type Finned Hexagonal Bundle Flow Channel", M.Eng. Thesis, McMaster University, 1991.

66. S.I. Osamusali, and J.S. Chang," REGIME-4 code for prediction of flow regime transition in a horizontal pipe, annulus, and bundle flow under gas-liquid two-phase flow", *Proceedings of 8th Ann. Canadian Nuclear Society Meeting*, pp. 125-134, 1987

67. S.I. Osamusali and Jen-Shih Chang, "Two Phase Flow Regime Transition in a 37-Rod Nuclear Fuel Bundle Horizontal Flow", *Third International Topical Meeting on Nuclear Power Plant Thermalhydraulics and Operations*, Seoul, Korea,pp. A1-137 - A1 -143, 1988.

Appendix A

A. Contributions to Knowledge

The development of a Real-Time Neutron Radiography system for measurement of two-phase flow parameters in nucler fuel channels is the main focus of this work. This work has several contributions to knowledge including:

- Development of the RTNR system for application to two-phase flow measurement at low neutron flux levels.
- Measurement of two-phase flow parameters such as void fraction, void fraction distribution, bubble diameter, bubble velocity, and interfacial area by the RTNR diagnostic technique.
- Application of the RTNR system to complex nuclear fuel channels with rod bundles.

Several papers and conference presentations which have been published or accepted based on this work are listed as follows:

[1] G.D. Harvel and J.S. Chang, "Chapter 13: Electrostatic Multiphase Flow Measurement Techniques", Handbook of Electrostatic Processes, J.S. Chang, J.M. Crowley, and A.J. Kelly Editors, pgs. 271-294, Marcel Dekker Inc., New York, 1995.

[2] G.D. Harvel, J.S. Chang and V.S. Krishnan, "Determination of Time Dependent Void Fraction Distribution in Bubbly Two-Phase Flow by a Real-Time Neutron Radiogaphy Technique", *Journal of Nuclear Technology*, **109**(1):132-141, 1995.

[3] Jen-Shih Chang and G.D. Harvel,"Determination of gas-liquid bubbly column instantaneous interfacial area and void fraction by a real-time neutron radiography method", *Chemical Engineering Science* ,**47**(13/14):3639, 1992.

[4] G.D. Harvel, K. Hori, K. Kawanishi, and J.S. Chang, "Real-Time Cross-Sectional Averaged Void Fraction Measurements in a Vertical Annulus Gas-Liquid Two-Phase Flow by Neutron Radiography and X-ray Tomography Techniques", 2nd International Conference on Multiphase Flow'95 - Kyoto, Japan,(In Press) 1995.

[5] G.D. Harvel, K. Hori, K. Kawanishi, and J.S. Chang, "Cross-Sectional Void Fraction Distribution Measurements in a Vertical Annulus Two-Phase Flow by High Speed X-ray Computed Tomography and Real-Time Neutron Radiography Techniques", NURETH-7, Saratoga Springs, New York, USA, 1995. (To be Submitted).

[6] G.D. Harvel, J.S. Chang, and V.S. Krishnan, "Determination of Time Dependent Void Fraction Distribution in Bubbly Flow by a Real-Time Neutron Radiography Technique", In Proceedings of NURETH-6, Grenoble, France, 1993.

[7] G.D. Harvel and Jen-Shih Chang,"Determination of time dependent void distributions using a real-time neutron radiography method in gas-liquid two-phase flow", Published in Proceeding of 6th Miami Int. Heat Transfer Conference, 1992.

[8] W. Fairholm, G.D. Harvel, J.C. Campeau, and J.S. Chang, "Visualization of two-phase interfaces in natural circulation by real-time neutron radiography imaging", In 1991 National Heat Transfer Conference, pages 199-206, ANS Proceedings, July 28-31 1991.

[9] J.S. Chang, J.C. Campeau, G.D. Harvel, S.I. Osamusali, S.H. Wang, and M.P. Butler, "Real-time neutron radiography for visualization of interfacial geometry and phase distribution in two-phase flow", U. Muller, K. Rehme, and K. Rust, editors, Proceedings Fourth International Topical Meeting on Nuclear Reactor Thermal-Hydraulics, pages 413-417, NURETH-4, Karlsruhe, 1989.

[10] Glenn Harvel, "Determination of void fraction in two-phase flow by a real-time neutron radiography method", Proceedings CNA/CNS Student Nuclear Conference, McMaster University, Hamilton, Ontario, March 27th 1992.

[11] Glenn Harvel,"Real-time neutron radiography with application to two-phase flow diagnostics", Proceedings CNA/CNS Student Nuclear Conference, pages 130-137, University of Manitoba, Winnipeg Manitoba, March 31st 1989.

[12] G.D. Harvel and Jen-Shih Chang,"Determination of time dependent void distributions using a real-time neutron radiography method in gas-liquid two-phase flow", Proceedings of Condensed Papers, 6th Miami Int, Heat Transfer Conference, Pg. 160, Clean Energy Research Institute, University of

Miami, December 10-12, 1990.

[13] G.D. Harvel and Jen-Shih Chang, "Real time neutron radiography of two phase flows",1st International Conference on Multiphase Flows, Tsukuba, Japan, Sept. 24-27 1991.

[14] G.D. Harvel and J.S. Chang, "Diagnostics and image analysis for the determination of two-phase flow interfacial parameters", Third Workshop on CANDU and Advanced Reactor Thermalhydraulics, page 2, McMaster University, Hamilton Canada, October 3rd 1990.

Regarding McMaster University's policy on the ownership of intellectual property and graduate student work, it is understood that both of my supervisors, Dr. J.S. Chang and Dr. V.S. Krishnan, and myself co-own the intellectual property rights and copyright for the work presented in this thesis and completed during graduate work. In addition, Dr. K. Hori and Mitsubishi Heavy Industries, Ltd, co-own the intellectual property rights to Chapter 6.